Stanley James KUBINA Ph.D.

Radiation characteristics of vehicle-mounted antennas

RADIATION CHARACTERISTICS OF VEHICLE-MOUNTED ANTENNAS AND THEIR APPLICATION TO COMPREHENSIVE SYSTEM DESIGN

by

Stanley James Kubina, B.Eng.(Eng.Phys.), M.Eng.

A thesis submitted to the Faculty of Graduate Studies and Research in partial fulfillment of the requirements for the degree of Doctor of Philosophy.

Department of Electrical Engineering,
McGill University,
Montreal, Quebec.

August, 1972.

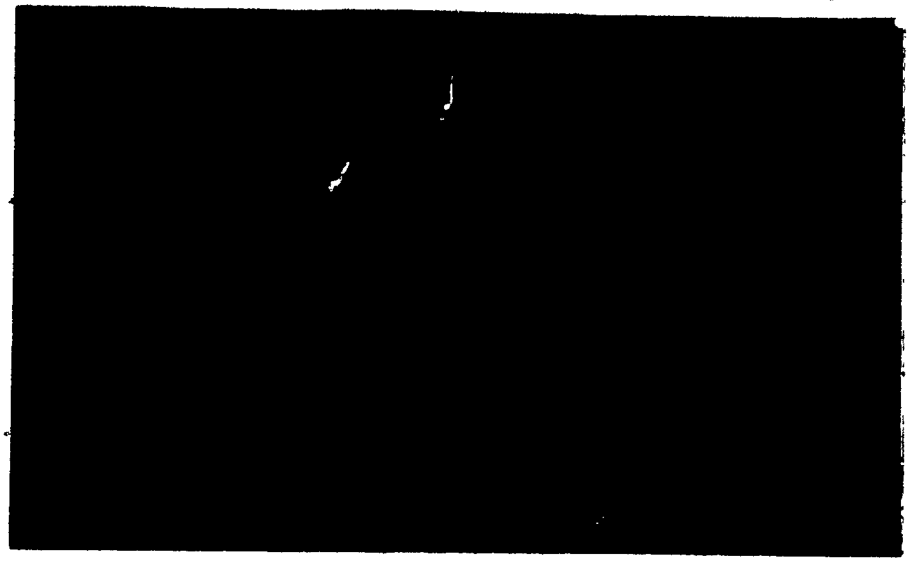

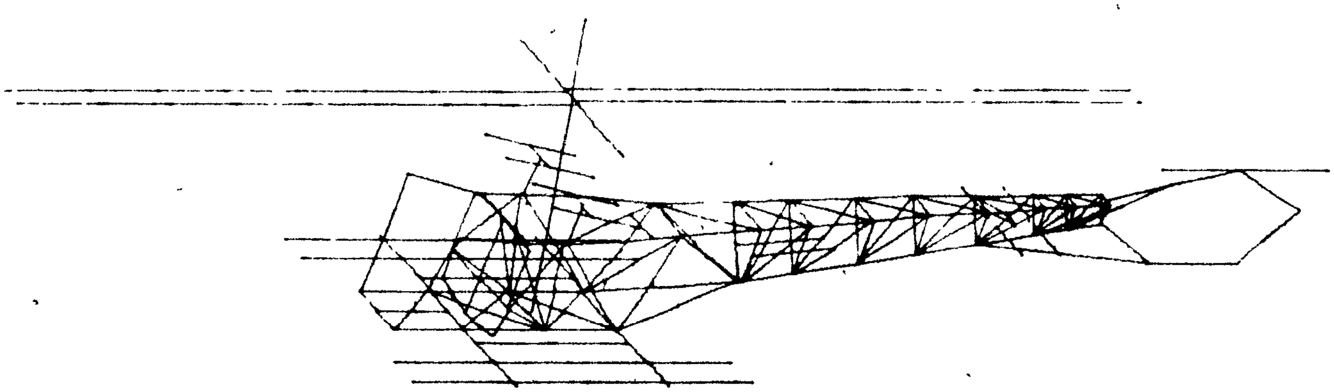

ABSTRACT

This thesis deals with three aspects of vehicle antennas: their comparative evaluation, the measurement of their radiation patterns and the prediction of their patterns by the technique of wire grid modelling.

The communications performance of sample helicopter antennas is evaluated in the HF frequency band, by traditional techniques and by a newly developed method. The method highlights significant performance differences directly related to operational performance specifications.

The development of a novel compact anechoic test facility is described. Results are presented of pattern measurements on models of a folded dipole, a ground rod antenna and a monopole on a helicopter and are compared with results obtained by others.

The application of numerical techniques using wire grid modelling establishes the importance of correctly modelling the source, indicates how thick elements can be represented in directive arrays, and shows that with complex bodies, increasing the number of elements does not necessarily produce pattern convergence. A satisfactory helicopter model is obtained and used to compute the effect of rotor modulation.

It is concluded that an interactive computer analysis and design procedure might now be formulated but that continuing experimental study, such as current distribution measurements, will be necessary to further future development of wire grid modelling guidelines necessary to establish the technique as a routine procedure.

ACKNOWLEDGEMENTS

The work of this thesis extended over several years during which the author has become indebted to many individuals for their kind assistance and encouragement.

To his wife, who waited so long for the convergence to normal family life, a gentle thank you. The author's entire family became an inevitable participant in this work: Mr. Charles Kubina, the author's father and son James helped in the construction of the anechoic chamber; daughter Camille helped in the laborious digitization of patterns and Lucy-Ann tried with the typing; son John Charles offered his joyful spirit. Their assistance is gratefully acknowledged.

At Loyola of Montreal, the president, the Very Rev. Father Patrick Malone and Dean George Joly encouraged the author's research work. His colleague, Mr. Ed Cerny was generous with his expert programming efforts. The author's students helped in many ways: Mr. Robert Kuley, most cheerfully with construction and assembly of the anechoic chamber and data reduction; Mr. Steve Fabiszewski with the construction team; Mr. James Bridgeman with draughting and especially Mr. Shing Kwong Lee with his meticulous CALCOMP graphics and programming.

At McGill, the author enjoyed the fruitful discussions and willing assistance of Dr. W. Wolde-Ghiorgis, his research colleague. Mr. Andrej Skalina helped with the measurements, with his skilful artwork and invaluable general assistance. Mr. John Foldvari and his colleaques constructed the inner arch support and all the antenna models. Mr. Stanley Henry maintained the electronic instrumentation.

Dr. J.Y. Wong of the National Research Council kindly supplied the model of the CHSS-2 helicopter and copies of his publications. Dr. G. A. Thiele of Ohio State graciously made his computer programs available. Messrs. Brian White and Dave Bell of Canadair Ltd. loaned some of their equipment and offered the use of their range. Mr. C. B. Seager of United Aircraft provided the drawing of CHSS-2 antennas.

To all of the above, the author would like to extend his sincere thanks.

Particular thanks are due to Miss Louise Smith for her expert typing on the ATS system of the draft and final copy.

The research work was supported financially by the Defence Research Board under Grant 5540-32. Material assistance was also provided by Hydro Quebec through project engineer, Mr. Paul Robertson.

This project was carried out under the direction of Dr.T.J.F. Pavlasek. He is the co-designer of the antenna test facility, a director with a discerning and especially light touch, generous with his time, skill and knowledge. His many contributions are much appreciated.

TABLE OF CONTENTS

Page

CHAPTER I

INTRODUCTION

1.1 Purpose of the Study

Avionic systems on aerospace vehicles require a variety of antenna types, operating over a wide frequency range. A typical arrangement on a commercial airliner is shown in Figure 1.1. The antennas of particular interest for this work are the low frequency, high frequency (HF) and very high frequency (VHF) antennas. The location of these antennas on a vehicle of

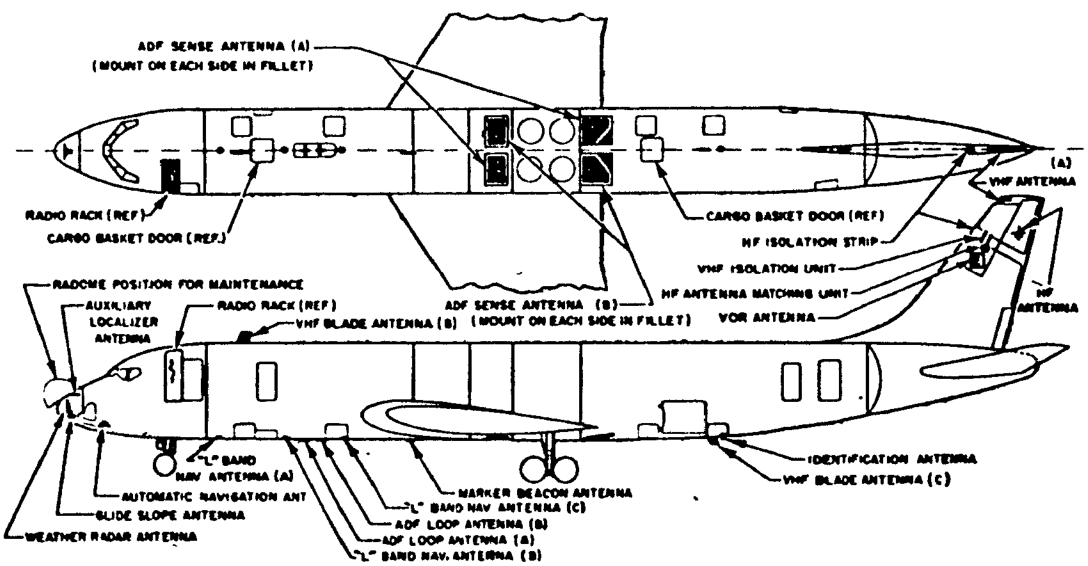

FIGURE 1.1. ANTENNAS ON DC-8 AIRCRAFT.

complex shape influences their radiation patterns. At the higher frequencies they are especially affected by the nearby geometry of the airframe. In the case of rotary wing aircraft such as helicopters, the susceptibility of the antennas to the influence of the rotating airfoils is an important consideration. Figure 1.2 shows an example of an antenna system on a medium-size helicopter.

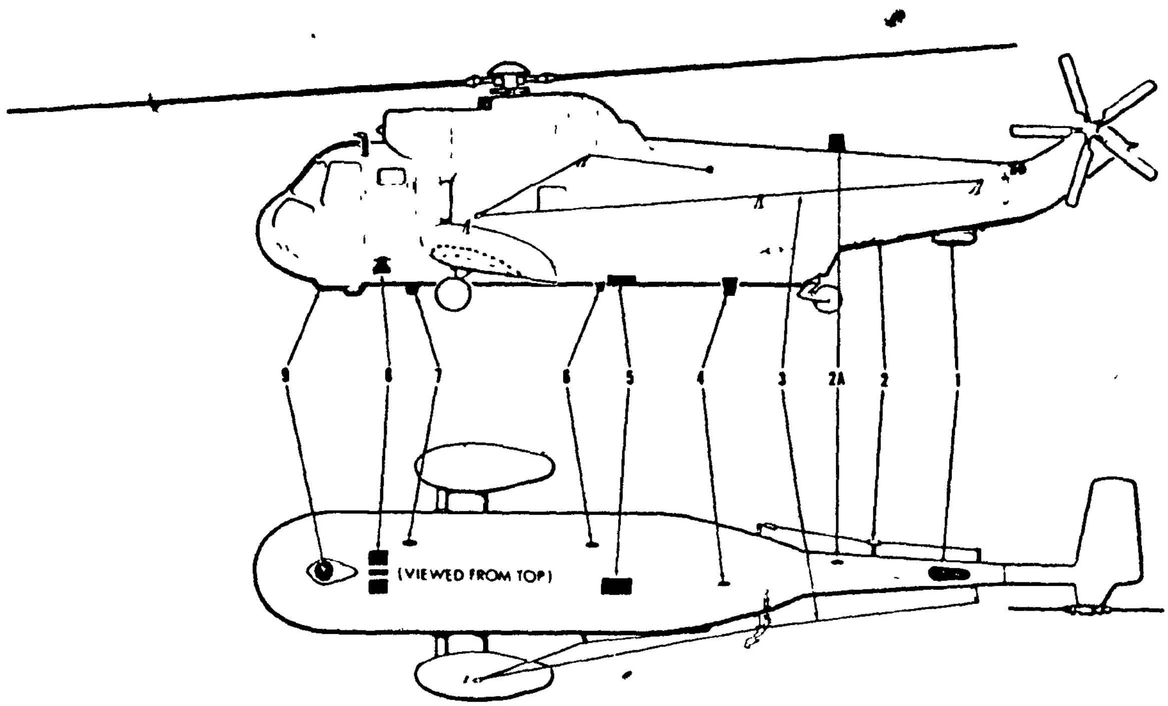

1 L.F. AUTOMATIC DIRECTION FINDER - LOOP
2 L.F. AUTOMATIC DIRECTION FINDER - WIRE(SENSE)
2A U.H.F. TRANSMITTER - RECEIVER (ALTERNATE)
3 H.F. TRANSMITTER - RECEIVER - WIRE
4 U.H.F. TRANSMITTER - RECEIVER (NORMAL)
5 RADAR ALTIMETER
6 I.F.F. RADAR IDENTIFICATION SET
7 TACAN NAVIGATION SET
8 DOPPLER RADAR
9 U.H.F. DIRECTION FINDER

FIGURE 1.2. ANTENNAS ON SIKORSKY CHSS-2 HELICOPTER.

The radiation characteristics of the antennas on vehicles are usually analyzed with respect to their contribution to the overall performance of the respective avionic system, such as communications, navigation, search and rescue etc. Clearly, until the radiation characteristics are related to system performance, it is difficult to evaluate antennas of different characteristics or locations or the seriousness of rotor effects in the case of helicopters.

Some reflection upon the design, development and production cycle of aerospace vehicles leads one to appreciate that radiation characteristics of antennas and their consequent effect on system performance should be known early in the design phase if some attempt at optimization is to be made prior to production committment of the vehicle. These considerations also recur during the useful life of aircraft, when new systems are introduced or antennas need to be relocated due to other installation changes.

Analytical techniques using closed form solutions of electromagnetic equations have been applied to representative simple shapes [1] of vehicles where possible. Scale model techniques [2] allow measurements representative of a full-scale system to be made. Performance criteria have been developed [3] for many systems and are being used. It has been found all too often, that a closed form solution is too crude and that measurements may be too costly or require too much time or pose some other practical difficulties. In addition, the performance criteria used so far do not always provide adequate resolution to differentiate between the performance of antenna systems. In helicopters, an understanding of rotor modulation effects is desired before these can be minimized by known design measures or by developing new ones. Problems of this type have been examined in this work and two specific cases are presented in this thesis.

(a) Several HF wire antennas for a medium-size helicopter (CHSS-2) were analyzed and their ratings compared using recognized performance criteria. The results of this analysis are presented in Chapter II. It was found that these criteria did not provide sufficient differentiation among similar antennas. Furthermore, the relationship of the performance criteria to operational usage is somewhat obscure. A new method has been proposed here, which bears a direct relationship to operational performance specifications while maintaining all the essential features of the criteria used heretofore.

The closer study of antennas and rotor modulation effects could not be realized without a measurement facility for near and far fields. A novel facility has been designed, built and tested. This facility and results are described in Chapter III.

Work on this problem suggested the need for an alternate modelling technique which would be more readily available and which would also provide some insight into rotor modulation effects and hopefully provide a data base for good performance analysis as well. Wire-grid modelling methods were examined, used and extended with the objective of becoming central to a new comprehensive methodology for the analysis and design of vehicle antennas. Measurements and wire-grid modelling were effectively applied in the case of a small helicopter (Bell 47G-4A).

(b) Because of their manoeuvrability, helicopters can be used for airborne field strength measurements of ground station antennas. For this application, however, three main antenna characteristics are desired:

(i) Known gain and unique polarization,

(ii) Omnidirectionality or uniformity in azimuth,

(iii) Freedom from rotor modulation effects.

To study the possibility of achieving these characteristics in an antenna system for the Bell 47G-4A helicopter at HF and VHF frequencies, a combination of analytical, experimental and wire-grid modelling techniques was used. The details of the program are presented elsewhere [4], but the modelling of the two antenna types for use at VHF frequencies is described in this work. It is believed that the results demonstrate the usefulness and sometimes the necessity of such a combined approach. An experimental and wire-grid modelling study of a monopole on the helicopter is also described. It is shown that the rotor modulation effect can be predicted by wire-grid modelling techniques. The computed patterns themselves, are in substantial agreement with experimental results and thus provide the data base sought by aerospace vehicle antenna designers for performance evaluation purposes.

Various elements of the combined approach are detailed in such a manner as to demonstrate the method of their application to complex problems. As the applications are developed, and the individual elements are elaborated, the essential unity of the proposed approach, from systems criteria to antenna characteristics back to system performance will be evident.

1.2 Vehicle Antenna Evaluation and Figures of Merit

It is notable that the first paper in the first issue of the I.R.E. Transactions on Airborne Electronics is Granger's paper entitled: "Systems Considerations in Aircraft Antenna Design" [5]. Granger's paper seeks a quantitative answer, for HF liaison antennas, to the question of how well an antenna system meets the requirements of its application. Several antennas having widely varying patterns and impedances over this relatively wide band, can possibly satisfy the requirements and, making comparisons, the engineer is confronted with a vast quantity of data. Granger proposed a figure of merit in terms of "antenna system efficiency", defined as the fraction of total power radiated in useful directions. An extensive investigation of antenna evaluation methods was carried out at Stanford Research Institute during 1949-53 under Granger's direction although most of the results were not published in the open literature until 1958 [7], [8], [9]. Based on a study of high frequency communications practices of commercial carriers and military communications requirements, the useful sector was defined as that 30° above and 30° below the horizontal plane. The antenna system efficiency criterion and methods for its derivation were incorporated in the military specification for aircraft HF liaison antennas [6] and this has become a standard for the aircraft industry.

1.2.1 Antenna System Efficiency

The antenna system efficiency is thus defined as the ratio of the power radiated into the solid angle included between 30° above and below the horizontal plane through the aircraft, to the total power input at the transmission line terminals. A definition of the co-ordinate system in common use and the polarization components is shown in Figure 1.3.

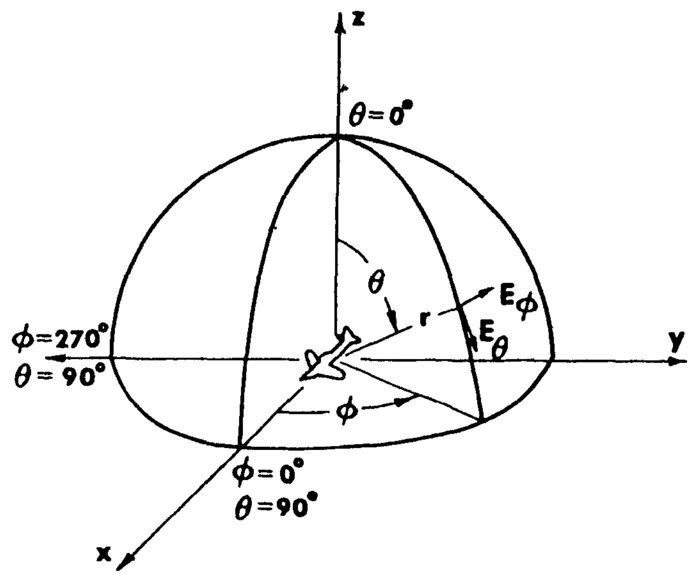

FIGURE 1.3. CO-ORDINATE SYSTEM USED FOR PATTERN MEASUREMENTS.

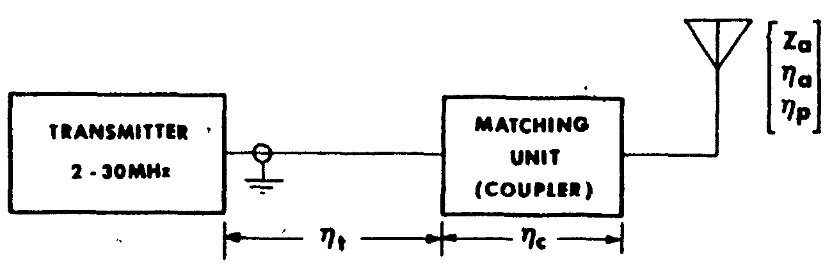

FIGURE 1.4. ELEMENTS OF THE ANTENNA SYSTEM.

A schematic of the system being considered is shown in Figure 1.4. The antenna system efficiency η_s, can be expressed as

$$\eta_s = \eta_p \, \eta_a \, \eta_c \, \eta_t \tag{1.1}$$

where

η_p = antenna pattern efficiency

η_c = antenna coupler efficiency

η_a = antenna efficiency

η_t = transmission line efficiency

The last three terms of (1.1) are a measure of the power transfer efficiency between transmitter and free space. The antenna pattern efficiency can be expressed as the ratio of the power radiated in the desired sector to the total power radiated

$$\eta_p = \frac{1}{4\pi} \int_{\Omega_u} G(\Omega) \, d\Omega \tag{1.2}$$

where

$G(\Omega)$ = antenna power gain function

Ω_u = useful solid angle sector

These factors are computed over the frequency range of interest, 2-30 MHz. The radiation pattern efficiency, η_p is usually obtained from model radiation pattern measurements (see Section 1.3) and the power transfer efficiency from model measurements or computational estimates [6].

Several investigators have applied this criterion. Among these, Moore [8] reports on the antenna system efficiency of antennas and is also called a "coverage factor" [14] in more recent spacecraft work.

Starting with the Shannon expression for channel capacity

$$C = W \log_2 \left(1 + \frac{S}{N}\right) \text{ bits/sec} \qquad (1.3)$$

where

S, N are signal and noise power densities

W = bandwidth in Hertz,

Lucke derives an expression for the average information capacity of the circuit of which the antenna forms a part. The average is taken over all the situations under which communication may take place. Thus

$$\overline{C} = \int p\,(\xi)\,\log_2\left[1 + \left(\frac{S}{N}\,(\xi)\right)\right] d\,\xi \qquad (1.4)$$

where

$\overline{C}$ = average information capacity, and stands for the aggregate of all the variables on which the signal to noise ratio S/N (ξ) at the receiving end depends.

The variable ξ is distributed with a probability density $p(\xi)$ and the integration is carried out over the volume for which $p(\xi)$ is defined, i.e. the volume for which several types of antennas on a C-54 aircraft, Wong [10] presents the radiation pattern efficiency of several antennas on the CL-28 aircraft and Kubina [3] reports on the antenna system efficiency of an isolated fin-cap antenna on this aircraft and its model and full-scale testing.

1.2.2 Other Factors of Merit

The work at Stanford Research Institute included examination of other evaluation methods. Long range communications at HF frequencies is of course also dependent on ionospheric conditions, atmospheric noise, time, place, distance and frequency. Lucke [9] reported on a communication theory approach incorporating Shannon's [12] formula for channel capacity in terms of bandwidth and signal-to-noise ratio as a weighting function for averaging antenna patterns and impedances over space and frequency. This method is also compared with the "antenna-system-efficiency" and "minimum level" methods.

The "minimum level" or "pattern-distribution function" [13] method[1] is based on the assumption that the effectiveness of a transmitting antenna is measured by the portion of the prescribed sector over which the signal amplitude (of prescribed polarization) is above a predetermined minimum level. This level is obtained from considerations of transmitter power and noise properties of the receiver. This method is frequently used for VHF and UHF

1 Reference to company reports is made where these are known and the material is not covered in the open literature.

$$\int p(\xi)\, d\xi = 1 .$$

Very extensive numerical work is required to compute the average information capacity for even the simplest case.

Moore has shown [7], [8] that for signal-to-noise ratios less than unity

$$\bar{C} \cong \log_2 [1 + (\frac{\bar{S}}{N})] \tag{1.5}$$

where

$$\frac{\bar{S}}{N} = \int p(\xi) \frac{S}{N}(\xi)\, d\xi = \text{average signal-to-noise ratio}$$

and that the radiation-pattern efficiency is closely related to the average signal-to-noise ratio. Moore reports calculations with radiation patterns of some HF antennas on a C-54 aircraft and shows that average difference between values calculated by Equations (1.5) and (1.4) is 8 percent. The noise N and function $p(\xi)$ were taken to be constant for these computations.

Blass [15] also suggests an evaluation method based on the time required to transcribe an amount of information without error.

1.2.3 Search for Improvements

Moore [8] sought an expression of relative ratings in terms of operationally significant parameters such as articulation scores. He proposed a "voice intelligibility index" obtained by averaging articulation scores over the useful solid angle sector Ω_u

For calculation purposes he linearized the curve of articulation score vs signal-to-noise ratio of Figure 1.5

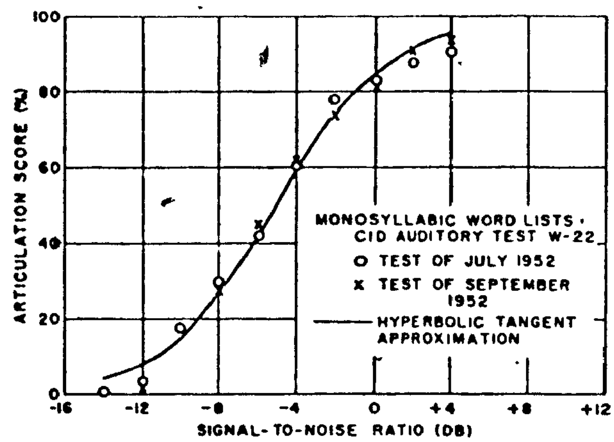

FIGURE 1.5. ARTICULATION SCORES AS A FUNCTION OF SIGNAL-TO-NOISE RATIO IN WHITE NOISE.

between the threshold value of gain and the value for an articulation score of 100%. Under these assumptions he derives a relationship for relative intelligibility indices and antenna system efficiencies as

$$I_2 - I_1 = \frac{100}{d} \left(10 \log_{10} \frac{\eta_{S_2}}{\eta_{S_1}} \right) \qquad (1.6)$$

where

I_1, I_2		are intelligibility indices
η_{S_2}, η_{S_1}		are system efficiencies, and
d	=	range in gain from 0 to 100% articulation score.

He concludes, however, that because of its simplicity, antenna system efficiency should continue to be used because interpretation in terms of articulation scores can easily be computed using Equation (1.6) when necessary.

Wong [16] sought a means of overcoming the lack of discrimination in the antenna-system efficiency criterion between antennas having different azimuth patterns. He proposed the incorporation of a deviation factor δ into the system calculation, δ being proportional to the deviation of a pattern from one which is omnidirectional in azimuth. This method is illustrated in Figure 1.6.

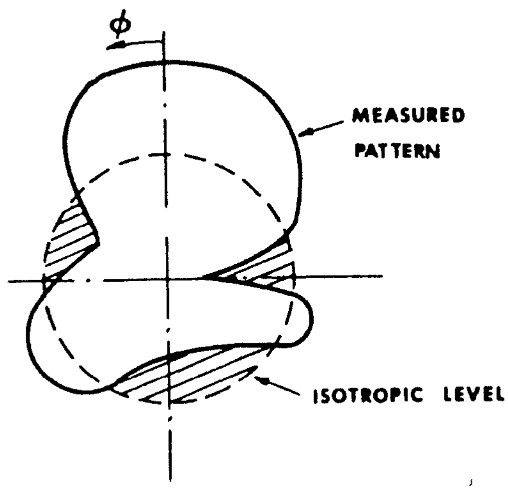

Granger:

$$\eta = \frac{\int_0^{2\pi}\int_{60^\circ}^{120^\circ} (E_\theta^2 + E_\phi^2)\,\sin\theta\,d\theta\,d\phi}{\int_0^{2\pi}\int_0^{180^\circ} (E_\theta^2 + E_\phi^2)\,\sin\theta\,d\theta\,d\phi}$$

Wong:

$$\zeta = \frac{\int_{60^\circ}^{120^\circ}\int_0^{2\pi} (E_\theta^2(1-\delta_\theta) + E_\theta^2(1-\delta_\phi))\,d\phi\,\sin\theta\,d\theta}{\int_0^{2\pi}\int_0^{180^\circ} (E_\theta^2 + E_\phi^2)\,\sin\theta\,d\theta\,d\phi}$$

$$\delta = \frac{\text{shaded area}}{\text{total pattern area}}$$

FIGURE 1.6. DEVIATION FACTOR AND WEIGHTING OF AZIMUTH PATTERNS.

The method is easy to apply since it involves only an additional area determination during pattern measurements and has been applied by Wong to the evaluation of antennas for ships.

Cline and Tanner [17] have attempted to overcome the lack of discrimination between antennas having different azimuth patterns while seeking a more operationally significant factor of merit. For ionospheric communication, they postulated a number of communications events for different path lengths, directions, geographic locations, times of occurrence and they calculate the signal-to-noise ratio at the receiver. They linearize Moore's articulation score curve, shown in Figure 1.5, and among a number of events having the same signal-to-noise ratio use the articulation score value to obtain the fraction of these events which they consider successful. They thus define the factor of merit as the ratio of the number of successful events to the total number of events postulated. Further it is suggested that curves of this factor versus transmitter power be used for antenna comparison. Values presented, however, are for a single antenna with assumptions of uniform power transfer efficiency over the frequency band.

Central to the application of all of the above evaluation methods is information on the radiation patterns and impedance of the antennas. Comparisons among antennas are very scarce in the literature because of the very extensive measurement and analytical work required in generating the data base and in making the comparative evaluation. Thus the need for more complete pattern and impedance information and the use of computer-aided analysis is evident.

1.2.4 Rotor Effects in Helicopters

Antenna location problems on helicopters were recognized some time ago [22]. The rotor modulation effect was measured by Adkar [18] for a HF wire antenna on the Sikorsky CHSS-2 helicopter and more extensively by Wong and Muilwyk [23] who showed a particularly large increase in pattern effect at frequencies close to a frequency of longitudinal resonance of the airframe. Andrews [24] measured the effect of rotor modulation on the behaviour of an automatic tuning unit for a HUS-1 helicopter HF antenna and showed the tendency for the unit to tune poorly or to hunt. Measurements on a VHF antenna installation to be carried on a Bell 47G-4A helicopter for field strength calibration purposes were reported by Pavlasek and Kubina [4] and some rotor modulation measurements at HF frequencies are reported in this work. Studies of problems such as this are also of significance for VTOL and STOL aircraft or high performance aircraft with variable geometry. On satellites and spacecraft a similar problem occurs due to deformation of antenna elements due to thermal or other physical factors.

1.3 Survey of Measurement Methods

The radiation characteristics of aircraft antennas must be obtained prior to the time the actual aircraft becomes available since decisions on structural details must be made before manufacturing begins. Even if the actual aircraft were available, testing on full-scale aircraft is very costly so that ground and flight tests are usually performed only as corroborative system tests. Measurements must therefore be carried out on equivalent electromagnetic models of these vehicles. Fortunately the technique of scale modelling is relatively well developed and a short survey is offered herein.

1.3.1 Radiation Pattern Measurement

The requirements for models on which measurements might be made on an absolute basis in terms of the full-scale system were reviewed by Sinclair [26] and discussed by Sinclair, Jordan and Vaughan [27] specifically in relation to measurement of aircraft antenna patterns. For the reader with a sustained interest in the subject these works also provide some earlier references and some interesting sidelights.[1] Sinclair shows that an electromagnetic system model M, obtained by dividing all dimensions of a full-scale system F by η, will have geometrically similar fields if the characteristic parameters of the media comprising the two systems are related by

$$\epsilon_M \mu_M f_M^2 = \eta^2 \epsilon_F \mu_F f_F^2 \qquad (1.7)$$

and

$$\sigma_M \mu_M f_M = \eta^2 \sigma_F \mu_F f_F \qquad (1.8)$$

---

1 For example, A. Alford first coined the word "balun" to replace "bazooka", the term for a balanced-to-unbalanced line transformer.

where

ϵ = dielectric constant

σ = conductivity

μ = permeability

f = frequency

η = arbitrary constant which determines model scale.

Antenna model measurements are done in air, so that $\epsilon_M = \epsilon_F$ and normally $\mu_M = \mu_F$. It follows then that

$$f_M = \eta f_F$$

and

$$\sigma_M = \eta \sigma_F \; .$$

It is pointed out that effects of inaccurate simulation of metals are most prominent with thin wires.

Measurements described are with models containing self-contained oscillators, modulated receivers and those with co-axial cables from the detector sufficiently masked by the model and located in regions of weak signal strength. Models described were constructed of hand-formed copper over pattern-maker's white pine and also pine models sprayed with metallic copper over a zinc base.

A more recent survey of measurements at radio frequencies was made by Cumming [28] who also discusses the use of high resistance leads to connect the detected audio signal in the model to a remote receiver. This technique was initially described by Peters [29]. Problems of model measurements on ground-based vehicles are discussed by Webster [30] and those on ships by Wong and Barnes [31]. Granger and Bolljahn's [1] classification of aircraft antennas is useful to recall in reading the review of Cumming with regard to difficulties with pattern ranges. The three divisions are: the low frequency range, the longitudinal resonance range and the transverse resonance or diffraction range. The distinction being in the relationship between the airframe dimensions and the wavelength. Bolljahn and Reese [32] show that in the low frequency range, from the electromagnetic point of view, the quasi-static approximations may be used and measurements carried out in electrostatic cages or electrolytic tanks.

Stembridge [33] reports that, in work done at Farnborough with copper and silver plated models of 1/4 or larger scale factor, experience over the years has shown agreement between model range and in-flight measurements to be of the order of ±3db, and with spacecraft for models 1/10 or 1/15 of full scale, estimates place agreement at ±1 or 2 db.

Tanner and Sharp [34] discuss the effect of poor modelling of wire diameters in HF array antennas. The modelling of the antenna element itself must be carefully considered and usually separate testing on reference ground planes is undertaken before its installation on the scale model of the vehicle itself.

1.3.2 Impedance Measurements on Models

Although impedances are best measured on full-scale aircraft, adequate model measurements can be made also. The instrumentation aspects are well covered in standard texts but a brief note on physical aspects is in order.

One method of impedance measurement with models consists of constructing a sufficiently large model of the aircraft to house the self-contained measuring equipment. The model is isolated from ground usually on a wooden tower and the measuring equipment is adjusted remotely. A representative arrangement is shown in Figure 1.7. This shows a 1/5 scale impedance model of a large transport aircraft on a 20 foot wooden supporting tower. Typical results obtained by this method are described by Granger [1], [35] and Figure 1.8 shows a comparison of impedance measured

FIGURE 1.7. IMPEDANCE MODEL AND SUPPORTING TOWER.

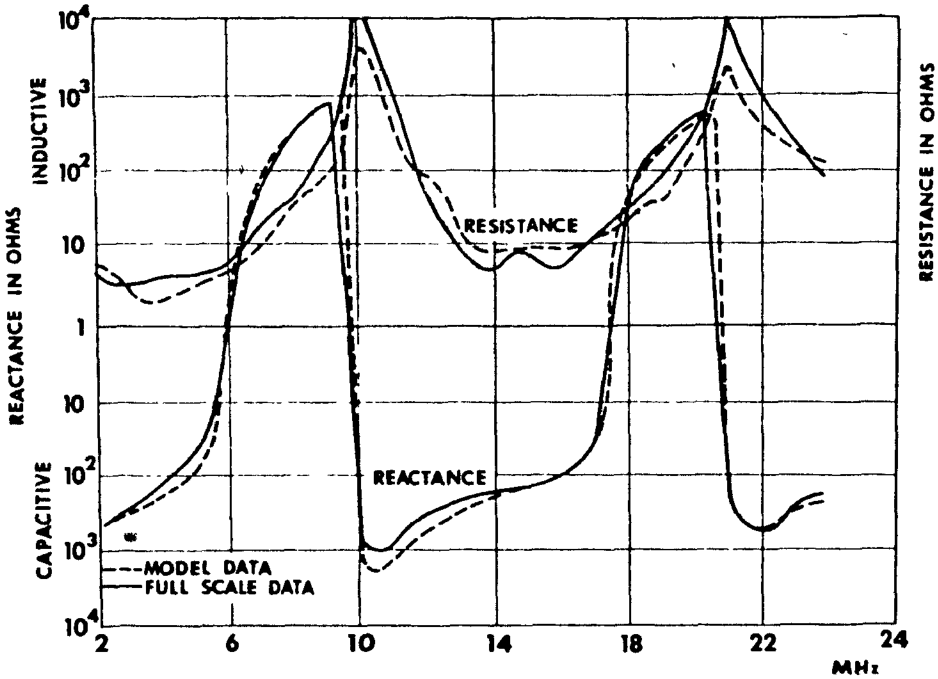

FIGURE 1.8. COMPARISON OF FULL-SCALE AND MODEL IMPEDANCE MEASUREMENT RESULTS.

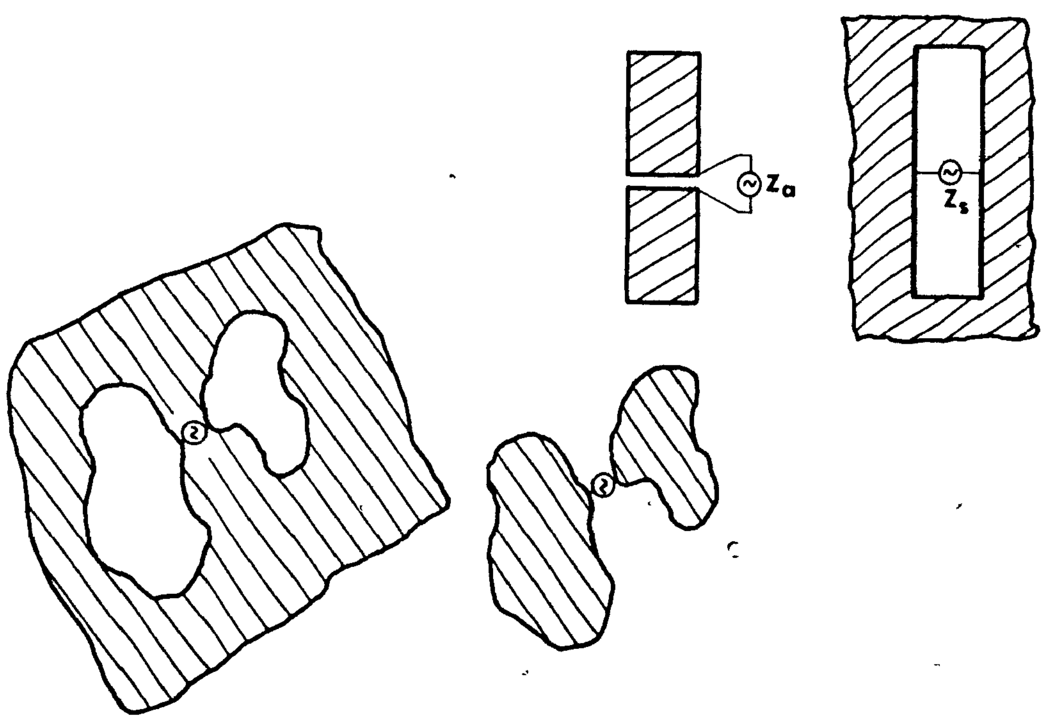

FIGURE 1.9. COMPLEMENTARY ANTENNAS.

on a full-scale aircraft and on a 1/5 scale model reported by Kubina [3]. For initial measurement, however, a less costly technique is preferred.

For some classes of antennas the complementary slot technique can be used. It is described by Bolljahn and Granger [36] and applied to aircraft antenna impedance measurements. The technique was suggested by Booker [37] who has shown that Babinet's principle, properly extended to electromagnetic fields, leads to a simple relation between the impedances of two planar complementary structures. This is illustrated in Figure 1.9.

The slot cut out from an infinitely large plane corresponds to the dipole. The impedances of the slot and dipole are shown to be related by

$$Z_a Z_s = \frac{\zeta^2}{4} \qquad (1.9)$$

where

Z_a = antenna impedance, in ohms

Z_s = slot impedance, in ohms

$\zeta = \sqrt{\mu_o/\epsilon_o} = 120\pi$ ohms.

Thus simplified aircraft models in planar form can be constructed using equivalent cross-sectioned shapes. In systems having image symmetry such as wing-cap antennas, measurements can be made on a half-slot and image plane. Several such measurements are reported by Bolljahn and Granger [36] and the method was used by Wong [38] for the investigation of isolated nose-cap antennas.

Although the radiation patterns and impedance data are necessary to establish the performance of antennas as considered in Chapter II, they are not sufficient for a full understanding of vehicle antenna behaviour. The determination of current distribution on the body helps to establish the characteristic radiation modes and should be considered also as a lodestone towards efficient wire-grid modelling of complex structures.

1.3.3 Measurement of Current Distributions

Computations of current distributions on linear antennas are frequently compared to the measurements of Morita [39] and Mack [60] and on coupled antennas and folded dipoles to the measurements of Morita and Faflick [40] and no other published measurements are available.

Current distributions on aircraft were published by Granger [41] for antennas[1] in the longitudinal resonance frequency range. More detailed current distributions were measured on aircraft models by Granger and Morita [42] for wire, wing-cap and tail cap antennas. A small external loop was used as a probe and the antenna on the aircraft was excited by a variable frequency RF source not contained within the model but reasonably well isolated from it. Still more comprehensive and sensitive measurements were carried out by Carswell [43] for wing-cap and tail-cap antennas. She improved on the technique of Granger and Morita by exciting the

---

[1] Results are from captured German documents showing results of full-scale measurements for a shunt excited wing antenna on a JU-52 aircraft.

external probe and connecting the detector to the antenna and taking out the detected audio signal through high resistance leads. These measurements were carried out to identify the airframe resonant current paths in an attempt to understand the impedance characteristics and patterns of these antennas.

It is rather important to note the observations of Granger and Morita that near the wing root and on the horizontal stabilizer, the quasi-static approximations of longitudinal lines of current flow do not apply and are nowhere applicable on the fuselage. Also there are substantial regions of the fuselage where the current measured is elliptically polarized. Near these regions, the authors point out, the assumption of "stationary lines of flow" implied in the usual applications of the integral-equation method of antenna analysis [44] is not adequate, and hence a guideline for efficient wire grid modelling based on such an assumption and exploited by Ghiorgis [45], cannot be used.

1.3.4 Full-Scale Measurements

The special techniques required in flight evaluations in order to obtain good correlation between model patterns and flight test data are discussed by Leopard [46] and Reed and Russel [47]. Although of direct applicability for frequencies above 50 MHz, nevertheless the precautions and statistical approach are also applicable to flight measurements at HF frequencies. Some other comparative results are presented by Kubina [3] and Stembridge [33]. Unfortunately the extensive measurements carried out during the HF antenna evaluation program at Stanford Research Institute are not available in the open literature.

Because of the special difficulties and cost in full-scale measurements the need for other methods continues and furthermore the ability to design the flight tests successfully is enhanced when complete predictions of performance are available.

1.4 Survey of Analytical Methods

Classical analytical methods have limited applicability to antennas mounted on complex structures such as aircraft, but a short resume is presented. An extensive survey is given by Wolde-Ghiorgis [45]. One of the methods, the integral equation formulation for linear antennas, forms the basis of the wire grid modelling technique being applied. Applications of the wire-grid technique to antennas on vehicles of complex geometry are reviewed as well as applications of the dual method, the surface element modelling technique.

1.4.1 Classical Methods

In practice, there is still no routine method of solving antenna problems. The general problem is to find a solution to Maxwell's equations for the boundary conditions of the radiator but the most convenient method is dependent on the geometric shape being considered and the most significant characteristics of the solution that are being sought. The three main methods are discussed fully by Aharoni [44] and Schelkunoff [59]. Schelkunoff's nomenclature for the three main antenna theories is related to the features of the solutions. The three are:

(1) Circuit theories

(2) Field Theories

(a) Resonator theories

(b) Mode theories

The first classification arises from the emphasis on currents in the various sections of the antenna using circuit-like techniques. Pocklington [61] was able to convert Maxwell's equations with various boundary conditions into integral equations and obtained the important sinusoidal approximation to the current on thin antennas. Later Hallén [62] reformulated the integral equations and discovered a method of deriving asymptotic solutions for thin antennas. This method allows the analysis of thin cylindrical antennas exemplified in Figure 1.10(a). Improved solutions are described in King's encyclopaedic book [63] and in his survey paper [64]. Although it is not possible to apply these solutions directly to vehicle antennas, King's approximation for the impedance of the asymmetrically excited dipole [65] serves as a good guide for the analysis of the impedance behaviour of isolated-cap antennas and has been used for this purpose by Granger [1], Adkar [61] and others.

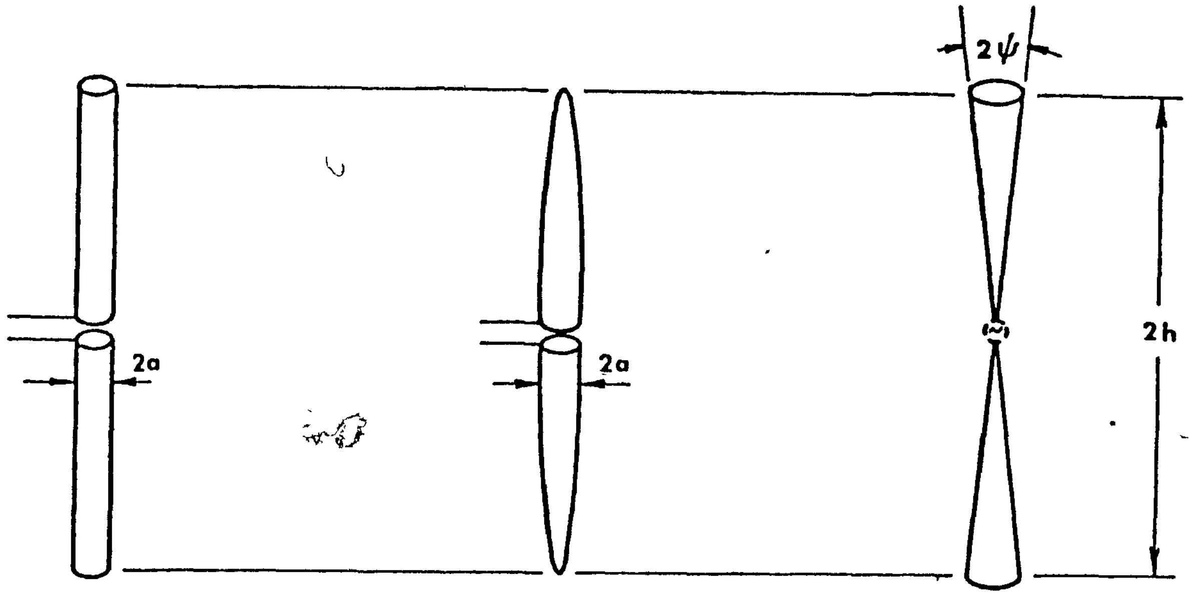

(a) Cylindrical

(b) Spheroidal

(c) Bi-conical

FIGURE 1.10. ELEMENTARY FORMS OF RADIATORS IN ANTENNA THEORIES.

The second classification arises from the solution of Maxwell's equations as a boundary-value problem in a prolate spheroidal system and an emphasis on fields. This is one of the few coordinate systems for which boundary conditions can be matched directly and the separation of variables carried out. This approach is usually associated with Stratton and Chu [67]. A general review is provided by Wait [68]. The applicable geometry is shown in Figure 1.10(b). The prolate spheroidal model maintains mathematical rigor and allows the consideration of end effects in a systematic manner. When the spheroid is elongated and the ratio $h/a \gg 1$, it approximates the thin cylindrical antenna. Schelkunoff labelled this the "resonator" theory of antennas because the individual terms of the solution represent certain modes of forced oscillation of the antenna as with resonators and thus exhibits an affinity between antennas and resonators. Myers

[69] has used this theory to determine the radiation patterns of unsymmetrically fed prolate spheroidal antennas and Wells [70] has obtained the current distribution and impedance for this condition.

The third theory was developed by Schelkunoff [71] by approximating the antenna as a wide-angled conical transmission line as indicated in Figure 1.10(c). It is called a "mode" theory because of its similarity to waveguides having many modes of propagation. If the cone angles 2ψ are allowed to decrease, the configuration approximates a cylindrical antenna. By applying Schwinger's variational method to biconical antennas, Tai [72] obtained more accurate impedance values. The impedance analysis of Tai was used by Adkar [66] to analyze the highlights of the impedance behaviour of the nose-cap antenna.

References to considerations of the excitation gap can be found in Schelkunoff's [59] and Kings's [64] monographs.

The above theories provide general understanding of the behaviour of vehicle antennas when these can be reduced to such simplified forms, but the theories are limited in the perturbations allowed to generate more complex shapes. Only the extension of the circuit theory to general shapes has been applied to the complex geometries considered in this thesis.

1.4.2 Numerical Techniques - Discretization of Integral Equations

A complex conducting surface may be assumed to be discretizable with a number of small surface current elements or with a grid of thin wire elements. Integral equations are then formulated in which the unknowns are either surface currents, in the case of the surface element method, or line currents in the wire-grid modelling method. By using point-matching techniques, for example, the integral equations can be transformed into a system of algebraic equations to be solved by matrix methods. As noted, a more general bibliography is found elsewhere [45] and the review here is restricted to applications involving more complex geometries. Other specific references are given in Chapter IV.

The surface element method has been formalized into a magnetic field integral equation by Poggio and Miller [73]. Although the method had been used for scattering studies [74] and antennas on bodies of elementary shapes [75], the first published study of the method for a monopole on a helicopter (CH-47) is reported by Knepp and Goldhirsh [76]. The study does not consider the rotor blades. The overall collective average deviation between measured and computed patterns is reported to be 2.5 db. The authors suggest a wire-grid modelling technique as the next step in their work.

The wire-grid modelling technique was first developed by Richmond [77] for the study of scattering by conducting surfaces. Tanner and Andreason [79] report its application to general wire antennas and to a fin-cap antenna on an RB-66 fixed-wing aircraft.

Miller and others [79] have applied the techniques to the analysis of homing system antennas on a helicopter (OH-6).

Results are given for a structure approximately 0.7λ long, with a total of 205 segments being used, with an average length of .047 λ . Maximum deviations from experimental patterns appear to be about 25% with generally good agreement in the lobe structure of the patterns. Thiele and his co-workers [80] have computed the radiation patterns of small loops on an F-4 pursuit aircraft. However no experimental data is provided.

Chao and Strait [81] claim a general program suitable for arbitrary configurations of wires and treat explicitly the problem of wire junctions, but do not treat structures of the complexity of those referenced above.

Tanner implies that as much accuracy as is desired might be obtained by increasing the complexity of the wire-grid model representing the structure. There is not enough evidence that this must necessarily follow and in fact the need for a more careful and systematic approach has already been corroborated by the work of Wolde-Ghiorgis [45] on a variety of structures, and is further reinforced by the results of this thesis. The problem of the numerical analysis techniques has been the one which has received most attention in the literature, however, the choice and arrangement of the wire-grid model finite elements has been based on a heuristic approach while the beginnings of a systematic attack have been considered only recently [45].

1.5 The Present Work

This work is devoted to three main areas of the aircraft antenna problem: evaluation, measurement and mathematical modelling. Its central theme is the use of computer-aided analysis in the comparative evaluation of antennas and for the prediction of radiation characteristics of vehicle antennas by the finite element technique of wire-grid modelling. An essential feature is the design, construction and use of a compact anechoic room facility to obtain measurements which at this stage remain a key guiding element for the further development of numerical techniques.

1.5.1 Evaluation of Antennas

Chapter II describes a comprehensive method for the evaluation of vehicle antenna performance in the HF frequency range. It is applied to the comparison of five similar antennas on a CHSS-2 helicopter and the results are compared to those obtained by other available methods. A fundamental feature of the method is that the evaluation is related directly to a commonly specified operational performance factor, namely range. The comparison shows that the method provides a better differentiation among similar antennas than can be achieved by other methods.

No claim is made for the originality of the individual elements of the method. However, the total ensemble of these elements to constitute a method of evaluation related directly to operational criteria as well as its comparative evaluation is believed to be new.

1.5.2 Experimental

Chapter III describes the construction of an anechoic test facility, its preliminary testing and the measurements carried out both at L-band and at S-band. The facility and the measurements carried out are an important part of the sequence of data acquisition necessary for the evaluation described above. Furthermore, measurements have been found crucial for the validation of the discrete finite element models. Measurements are presented for a folded dipole antenna with its supporting mast, a ground rod antenna and a monopole on a Bell 47G-4A helicopter. These measurements in turn indicate how wire-grid models can be used to overcome experimental problems in the scale-modelling of antennas.

The measurement methods used are well known. These have been systematically applied to testing the anechoic chamber, the design of the absorber configuration and the antenna measurements themselves. The test facility is considered to be an original engineering design, novel in its compact form and arrangement, and optimized for cost and performance factors.

1.5.3 Wire-Grid Modelling

The main objective of the research in wire grid modelling was to obtain the radiation patterns of antennas on helicopters with sufficient accuracy to be used in the evaluation methods described above and especially to show the rotor modulation effect. Previous work in computational techniques has been usually directed towards isolated antennas and the mathematical and numerical aspects of the techniques. At this time no systematic procedure for establishing wire-grid models of complex structures exists, although the beginnings of an initial systematic attempt to formulate definite methods has been made by Wolde-Ghiorgis [45] for certain antenna configurations emphasising the "stationary lines of flow" concept. The results of this latter work are applied and extended here to the case of the folded dipole and the ground rod antenna, but it is found that the concept of "stationary lines of flow" cannot be applied in a simple way to the complex and angular geometry of the helicopter. The specific objectives and results of the study are the following:

(a) To develop a wire grid model of a folded dipole and supporting mast. The achievement of this objective and the research leading to it have produced:

  (i) a guideline for the representation of a member with sizeable diameter in a directive antenna such as this.

  (ii) an appropriate model of the source at the driven element.

  (iii) the first wire-grid model for this configuration.

(b) To develop a wire grid model of a ground rod antenna used in the experimental measurements. The research work for this-objective has produced:

(i) the first wire-grid model for this configuration,

(ii) an appreciation of the effect of the feedpoint location on the lobe structure of the radiation pattern.

The above represent the first known use of the wire-grid modelling technique to support an experimental measurement and to resolve a discrepancy between two different measurements.

(c) To compute the radiation patterns of a monopole on a complete helicopter and to determine the effect of the rotor blades. Research work towards this goal has shown:

(i) that its attainment is not straight forward and routine,

(ii) that problems of this complexity require further research, both experimental and analytical, to define the modelling problems as to element location, diameter and length of element, basis function for best convergence and advantages of applying a junction constraint.

(iii) that some guidelines can be formulated both for the location of elements as well as the elimination of redundant elements.

(iv) that an acceptable wire grid model can be obtained, at this time with assurance, only when a reference measured pattern is available.

The basic equations and numerical techniques, together with their application are described in Chapter IV. No claim is made about the originality of these techniques. The wire-grid analysis method is applied first to a monopole for convergence testing and programming tests. It is then extended to the isolated antennas and finally to the monopole on a helicopter. A number of supporting graphical techniques are developed and used.

It is believed that this work represents the first comprehensive study of this type and the resulting guidelines and problem exposition have not been available heretofore.

The concluding Chapter V contains a summary and appraisal of the results. Recommendations are made for new promising avenues of investigation which are indicated as a consequence of this present work.

CHAPTER II

EVALUATION OF HELICOPTER HF WIRE ANTENNAS

2.1 System Requirements and Factors of Merit

The communications requirements for helicopters dictate a specialized approach to the determination of a factor of merit for antennas. Their range is much more limited than that of the transport aircraft for which most of the factors of merit were developed. Communication beyond line-of-sight is required but ranges of 100 miles are commonly specified for the frequency range 2-12 MHz. At these distances, ground wave propagation pertains and vertical polarization is used.

While antenna system efficiency is defined and calculated for both polarizations, it is common practice for antenna test facilities to calculate also the amount of power radiated in the vertical component

$$\%E_\theta = \frac{\int_0^{2\pi}\int_0^{\pi} E_\theta^2 \sin\theta \, d\theta \, d\phi}{\int_0^{2\pi}\int_0^{\pi} (E_\theta^2 + E_\phi^2) \sin\theta \, d\theta \, d\phi} \times 100 \qquad (2.1)$$

and the amount of power, in the E_θ component radiated in the useful sector, $60° \leqslant \theta \leqslant 120°$:

$$\%E_\theta \Big|_{\Omega_u} = \frac{\int_0^{2\pi} \int_{60^\circ}^{120^\circ} E_\theta^2 \sin\theta \, d\theta \, d\phi}{\int_0^{2\pi} \int_0^{\pi} (E_\theta^2 + E_\phi^2) \sin\theta \, d\theta \, d\phi} \times 100 \qquad (2.2)$$

These values can be used instead of antenna system efficiency in the evaluation of antennas for applications involving communication via the ground wave mode. The question of operational significance described in 1.2 and 1.2.3 is pertinent. The relationship of Equation (1.6), between relative intelligibility index and antenna system efficiency as proposed by Moore [8] could also be used here.

However, operational specifications for aircraft systems are not written by antenna designers familiar with the terms discussed here. Generally they are written in terms having direct operational significance such as communications to a given range over an operating frequency band. Furthermore, decisions on the selection and installation of antennas are not generally made by antenna engineers alone. It remains for the antenna engineer to propose the best antenna using the criteria discussed above and to substantiate the proposal by a range calculation for one or two representative operational conditions. While this procedure seems reasonable and straightforward, its effectiveness becomes marginal when two antennas seem equally satisfactory or when one with a poorer rating has some physical installation advantages. Under these conditions it is desirable to have a criterion directly related to the operational specifications so that any compromise or advantage would be evident in these terms.

It is believed that such a criterion is now possible using the method developed here. The method is based on a series of signal-to-noise ratio (SNR) calculations for all operationally significant conditions much in the manner suggested by Cline and Tanner [17]. Successful communication contact is assumed when an arbitrary but reasonable level of SNR is achieved. For each frequency a successful contact ratio (SCR) is computed versus range. Finally a value of SCR (0.9) is selected as a parameter and values of range versus frequency are computed and used as a criterion for the evaluation of the antennas being considered.

It is also shown that the critical conditions for communications can be clearly illustrated, making more visible than before, the complete performance of the antennas in operationally meaningful terms.

It was possible to apply the proposed method to a number of similar HF wire antennas installed on a Sikorsky CHSS-2 helicopter and make comparisons with some of the other factors of merit.

Since detailed pattern and impedance information about several similar antennas on the same aircraft is very rare, the access to such data constituted a unique opportunity to apply this method.

2.2 Description of Helicopter Antennas

Impedance and radiation pattern data was obtained[1] for five wire antennas which had been considered during the development of an HF antenna installation for the Sikorsky CHSS-2 helicopter. These antennas are shown in Figure 2.1. They vary in length, the location of the feedpoint, the height and the location of the stand-off insulators. The feedpoint for antenna A is different from all the others. Antennas B and C differ only by the height of the last two stand-off insulators. Antenna E differs from C in the location of the second and third stand-off insulators. The general form of Antenna D is essentially a mirror image of A, B, C and E.

2.2.1 Impedance and Coupler Efficiency

As an example of the range of resistance and reactance values which must be matched over the frequency range, the impedance of antenna A is shown in Figure 2.2. The impedance values of the other antennas are shown in Appendix I. The impedances had been measured on a full-scale helicopter on the ground. Based on these impedance values and information on the Q of the matching circuit[2] the coupler efficiency was calculated over the range 2-12 MHz. These values are shown in Table 2-1 and are used in the system calculations which follow.

---

[1] Courtesy of DND Directorate and Capt. (N) H.W. Isaac.

[2] NAVAER-16-35CU-351-502, Data on CU-351/AR Coupler used.

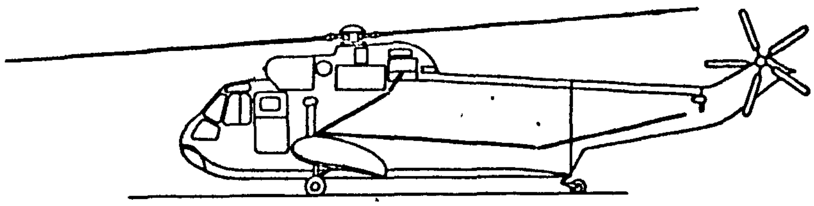

ANTENNA A

Total Length = 46 ft.

	STA	W.L.	Height
FP	343.2	192	---
ST1	310	163	10"
ST2	218	---	10"
ST3	435	---	10"
ST4	625	142	10"

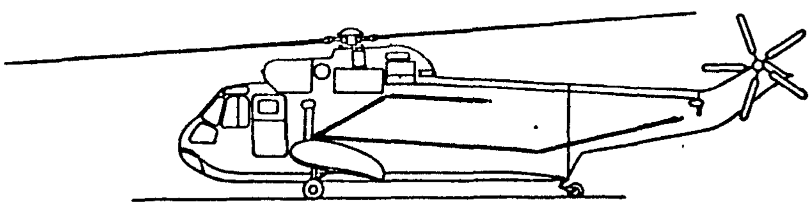

ANTENNAS B AND C

Total Length = 51 ft.

	STA	W.L.	Height	
			B	C
FP	405	162	---	---
ST1	310	163	10"	10"
ST2	218	163	10"	10"
ST3	435	113	10"	21/2'
ST4	625	142	10"	4'

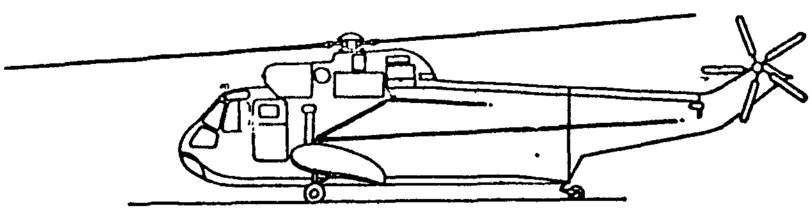

ANTENNA E

Total Length = 51 ft.

	STA	W.L.	Height
FP	405	162	---
ST1	310	163	10"
ST2	237	---	10"
ST3	435	130	21/2'
ST4	625	142	4'

Legend: FP = Feedpoint
ST1 = Stand-off #1 etc.
STA Aircraft coordinates:
W.L. Station, waterline, in inches

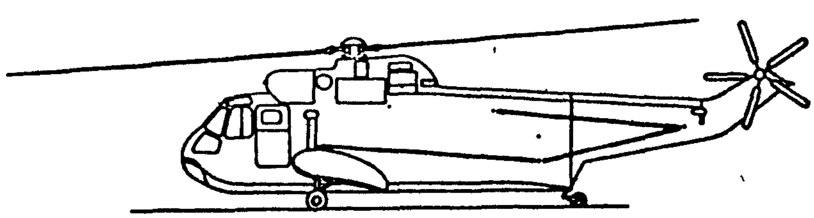

ANTENNA D

Total Length = 53 ft.

	STA	W.L.	Height
FP	405	162	---
ST1	625	142	4'
ST2	435	113	21/2'
ST3	218	---	10"

FIGURE 2.1. WIRE ANTENNAS ON SIKORSKY CHSS-2 HELICOPTER.

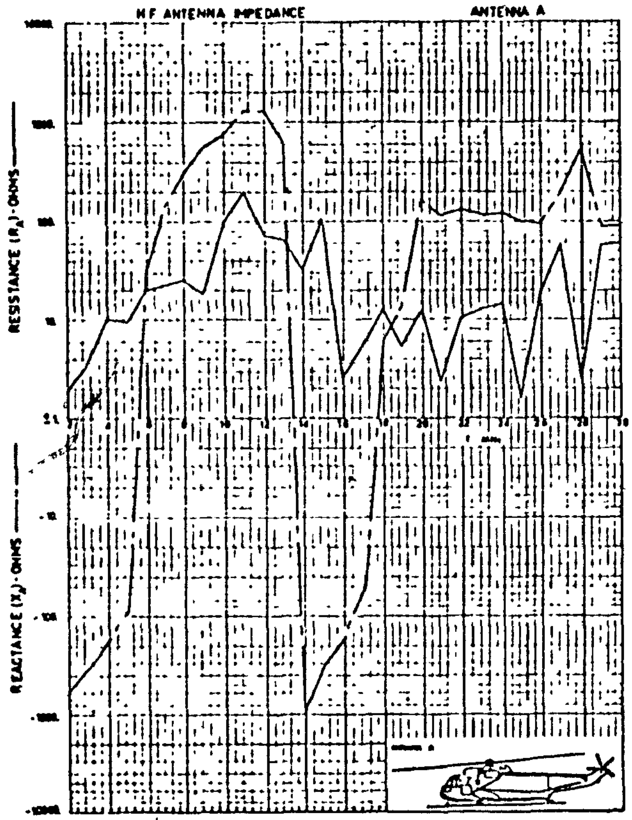

FIGURE 2.2. IMPEDANCE VS FREQUENCY-ANTENNA A

TABLE 2.1. MATCHING UNIT EFFICIENCY HF WIRE ANTENNAS.

f MHz \ ANTENNA	A	B	C	D	E
2.0	.306	.164	.264	.440	.264
3.25	---	----	----	----	.274
4.0	.700	.475	.507	.596	.507
6.0	.746	.716	.739	.733	.739
8.0	.732	.688	.704	.731	.704
10.0	.730	.663	.724	.679	.723
12.0	.662	.650	.678	.703	.673

Note: Values for antenna E were estimated to be the same as for C.

2.2.2 Radiation Patterns and Derived Values

The radiation patterns had been measured by Adkar [18] on a 1/24-scale model of the helicopter. A photograph of the model is shown in Figure 2.3. The patterns measured were the principal plane patterns and conical cuts at various values of θ as specified in MIL-A-9080 [6]. Representative principal plane patterns for E_θ are shown for antennas A and B in Figures 2.4 and 2.5 respectively for 2 and 4 MHz.

From the sets of radiation patterns, the pattern efficiency, % E_θ and % E_θ^* (in the Ω_v sector) were calculated for each frequency. These values are shown tabulated in Table 2.2.

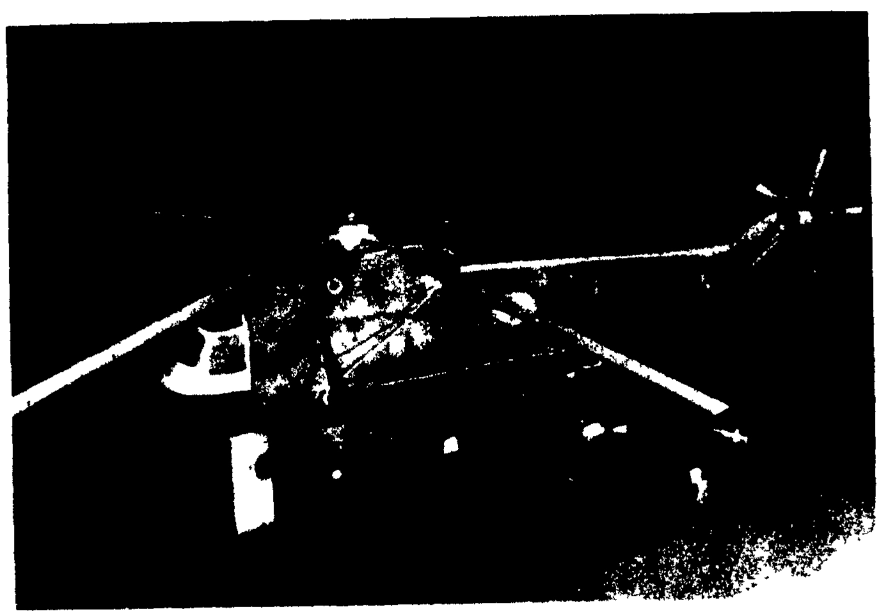

FIGURE 2.3. RADIATION PATTERN MODEL AND ANTENNA A.

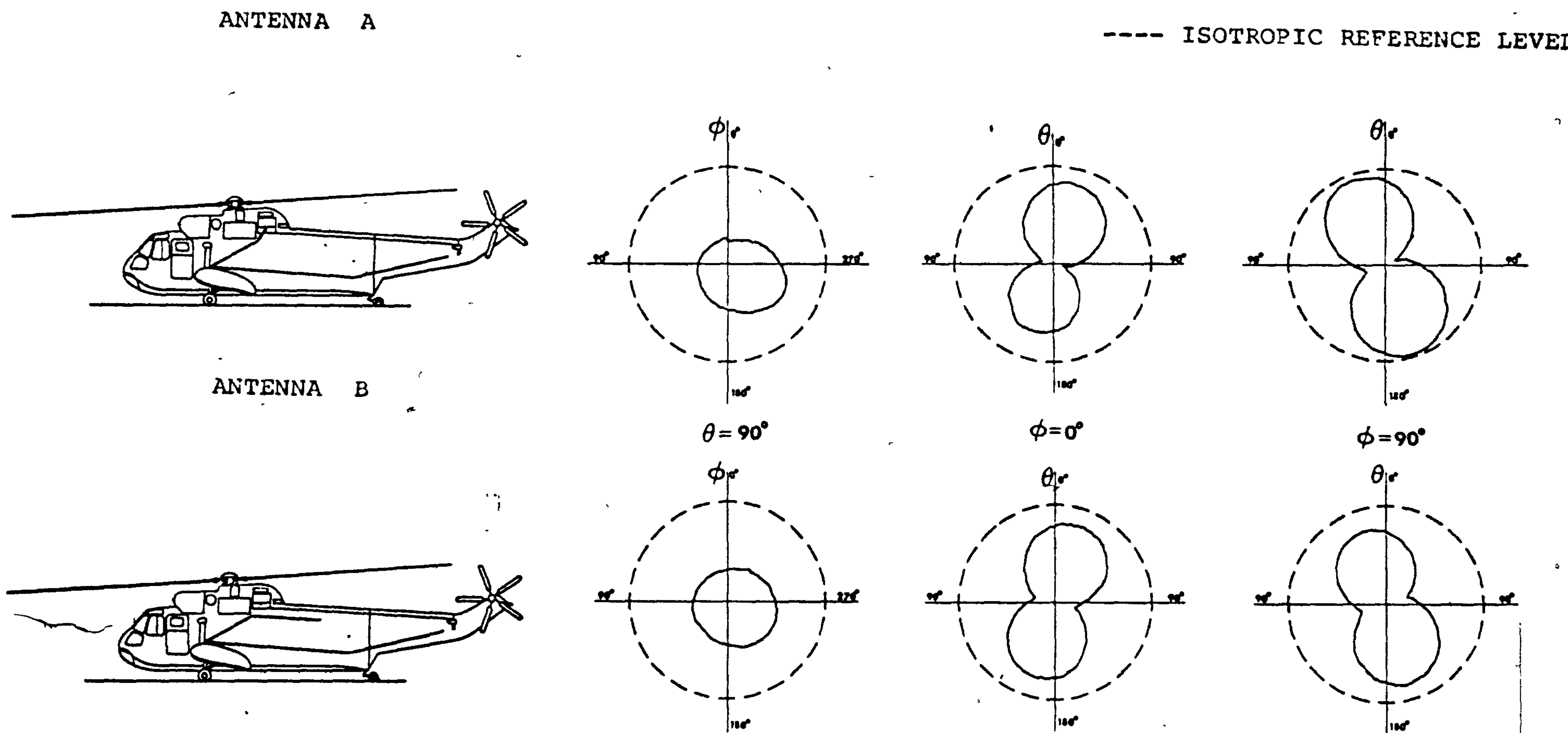

FIGURE 2.4. PRINCIPAL PLANE PATTERNS, ANTENNAS A AND B, f = 2 MHz, E_θ .

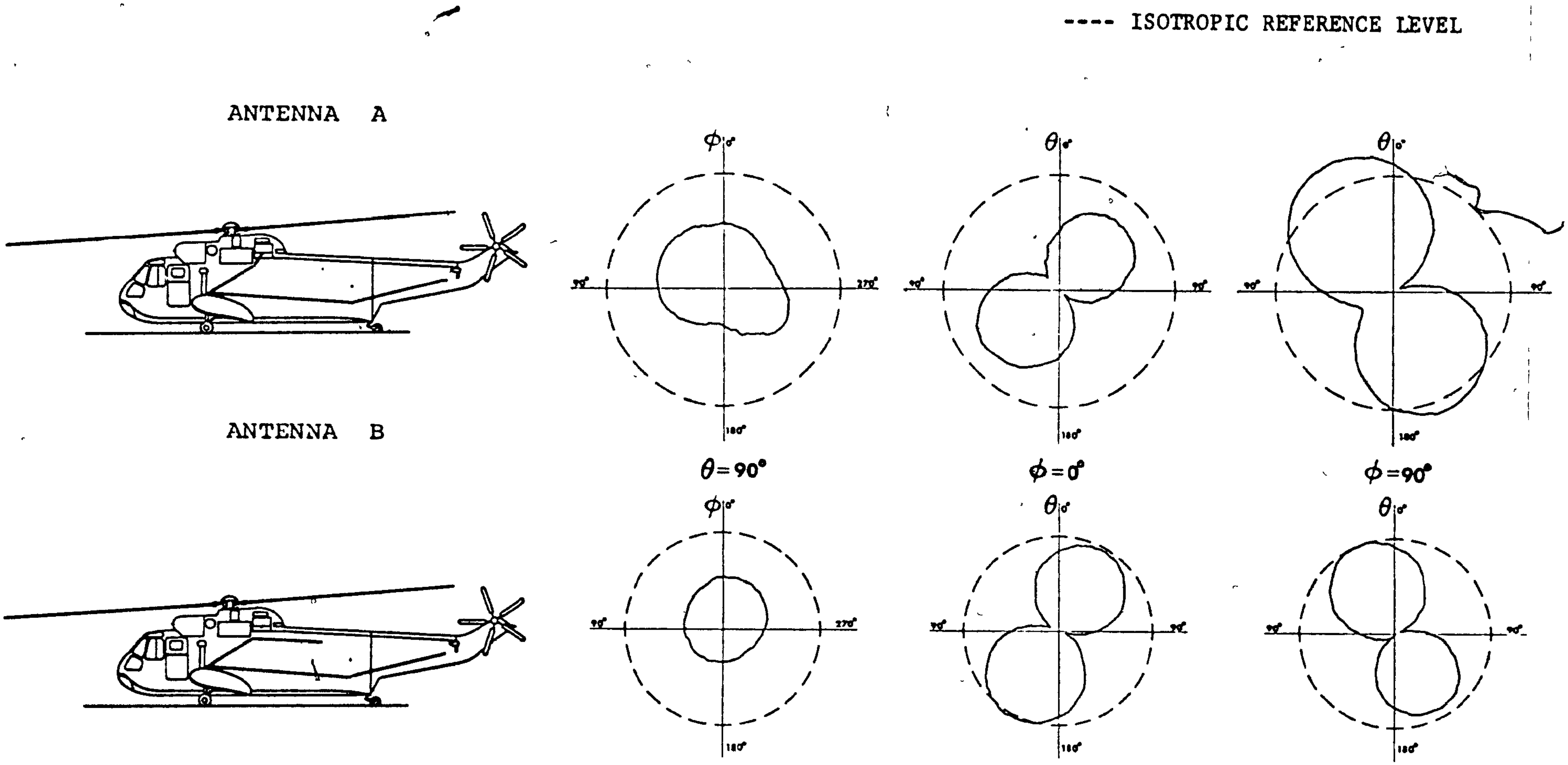

FIGURE 2.5. PRINCIPAL PLANE PATTERNS, ANTENNAS A AND B, f = 4 MHz, E_θ .

TABLE 2.2. η_p , % E_θ and % E^*_θ (Ω_u): HF WIRE ANTENNAS.

ANTENNA	A			B			C			D			E		
VALUE % / f MHz	η_p	$\%E_\theta$	$\%E^*_\theta$	η_p	$\%E_\theta$	$\%E^*_\theta$	η_p	$\%E_\theta$	$\%E^*_\theta$	η_p	$\%E_\theta$	$\%E^*_\theta$	η_p	$\%E_\theta$	$\%E^*_\theta$
2.0	44	37	12	43	35	10	42	32	8	40	33	7	40	33	8
3.25	--	--	--	--	--	--	--	--	--	--	--	--	41	32	6
4.0	43	41	16	42	38	12	42	39	13	43	27	5	43	26	6
6.0	42	32	7	43	42	14	44	41	14	44	23	4	44	28	6
8.0	51	43	21	46	38	14	51	55	28	52	49	25	50	42	20
10.0	50	48	18	46	44	17	50	59	29	50	51	25	53	61	34
12.0	45	25	4	50	15	2	48	21	3	47	25	4	48	25	7

$$\%E^*_\theta \equiv \frac{\text{power in } E_\theta \text{ component in sector } 60^\circ \leqslant \theta \leqslant 120^\circ \; (\Omega_u)}{\text{power radiated}}$$

From the radiation pattern efficiency column, it can be seen that it would be difficult to select an antenna by this factor alone. Nor is the difference between the antennas dramatically accentuated when the two other factors are examined. A clearer distinction could be made if a frequency weighting were established.

If now an antenna efficiency and a transmission line efficiency of unity are assumed, the antenna system efficiency can be computed. This is shown in Table 2.3 below.

TABLE 2.3. η_s AND η_s^*(E_θ ONLY): HF WIRE ANTENNAS.

ANTENNA	A		B		C		D		E	
VALUE / f MHz	η_s	η_s^*	η_s	η_s^*	η_s	η_s^*	η_s	η_s^*	η_s	η_s^*
2.0	13.5	3.7	7.1	1.64	11.1	2.1	17.6	3.1	10.6	2.1
3.25	----	----	----	----	----	----	----	----	----	----
4.0	30.1	11.2	19.9	5.7	21.3	6.6	25.6	3.0	21.8	3.0
6.0	31.3	5.2	30.8	10.0	32.5	10.3	32.3	2.9	32.5	4.4
8.0	37.3	15.4	31.6	9.6	35.9	19.7	38.0	18.3	35.2	14.1
10.0	36.5	13.1	30.5	11.3	36.2	21.0	32.9	17.0	38.3	24.6
12.0	29.8	2.6	32.5	1.3	32.5	2.0	33.0	2.8	32.5	4.7

$$\eta_s^* \equiv \begin{array}{c}\text{antenna system efficiency}\\ \text{for } E_\theta \text{ component alone}\end{array} = \frac{\text{power in } E_\theta \text{ component in sector } \Omega_u}{\text{total power available}}$$

It is surprising to find how little power there is in the vertical component in the sector useful to communications. The values of this table are shown plotted and compared to the proposed range versus frequency curves in ~~the~~ next section.

2.3 Proposed Analysis and Results

A successful communication contact is assumed to have taken place when the signal level at the receiving site is sufficient to overcome atmospheric noise or receiving set noise. A schematic of the communications geometry is shown in Figure 2.6, together with a listing of some of the factors entering into the communications equation.

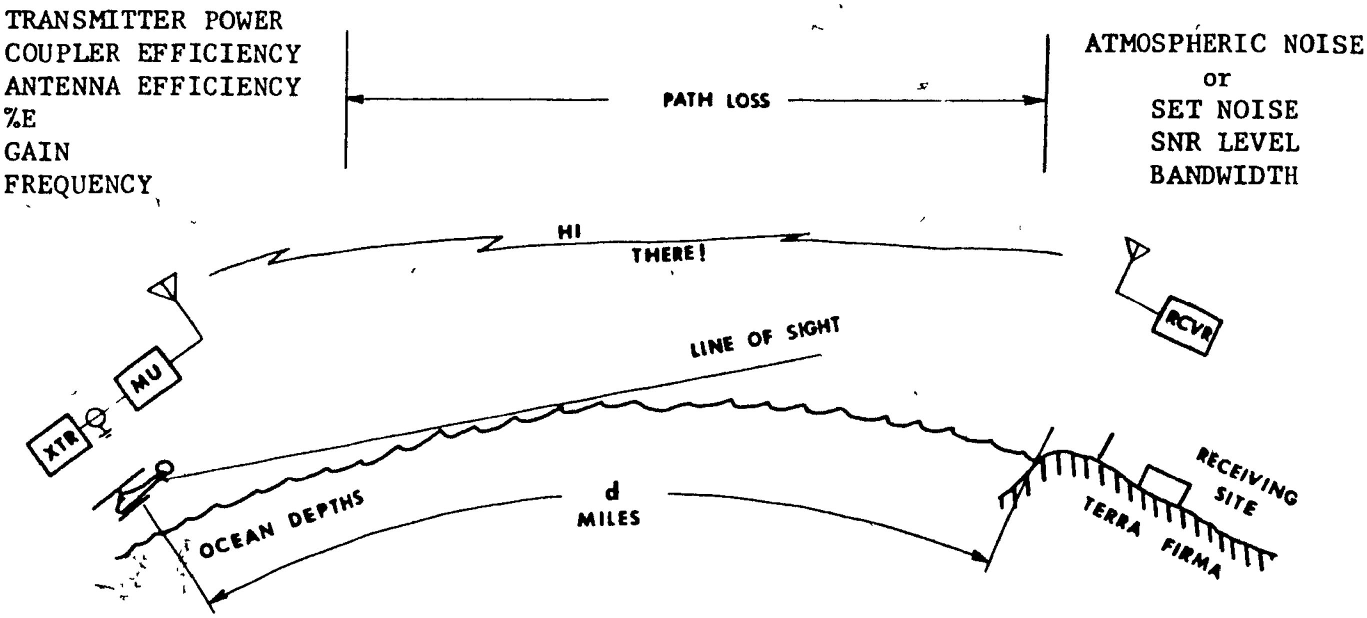

FIGURE 2.6. COMMUNICATIONS GEOMETRY AND RELATED PARAMETERS.

2.3.1 Signal Level at the Receiving Site

All azimuthal directions were considered equally probable for the helicopter. The great manoeuvrability of the helicopter results in attitude changes which make the sector, $60^\circ \leq \theta \leq 120^\circ$, a useful one even though the considerations of ionospheric propagation do not apply. Standard rate turns for example, can involve roll angles of 35°. To obtain representative values of antenna gain, therefore, increments of 10° in azimuth were selected and 6° in zenith angle were used because patterns for these increments were available. Thus a total of 396 antenna gain values, G_T were calculated at each frequency for each antenna.[1]

A transmitter power of 100 watts was assumed. Coupler efficiency values of Table 2.1 and $\%E_\theta$ values from Table 2.2 were used. No ohmic antenna losses were included and transmission line loss was neglected.

The path loss was determined for propagation over sea water because of operational reasons. For the sake of simplicity a series of seventeen range values from 10 to 250 miles was taken from published charts [19] for each frequency being considered. In more sophisticated versions of the digital computer program, the computations of Gerks [20] could be incorporated or for mixed paths, charts such as those of Wait and Walters [21] could be used.

The intensity at the receiving site can then be expressed as

$$S_R = P_T - L_C - T_P + G_T - P_L \qquad (2.3)$$

where

S_R = received signal intensity in db above 1 μV/meter.

P_T = transmitter power level, db above reference used.

L_C = coupler loss, db

T_P = transmission line loss, db

---

[1] Unfortunately the radiation pattern data were only available in analogue form. Hence data reduction of this type presents a formidable data reduction and computational task.

G_T = antenna gain with respect to reference antenna, db

P_L = intensity value at d for reference power, db > 1 μV/meter.

The values of minimum and maximum values are used separately for establishing signal limiting conditions as shown later in Figure 2.11.

2.3.2 Noise Levels at Receiving Site

The helicopter considered here is designed for all-weather day or night operation. Use is intended in the North Atlantic or Pacific regions. Atmospheric noise depends on latitude and varies with the time of day and season of the year. Figure 2.7 shows a representative noise distribution chart and one showing noise variations with frequency for selected hours of the day. A noise grade of 2.5 was selected mainly because of the availability of noise charts for this grade [25]. Charts for the summer, winter and equinox periods were used. Thus for each frequency 18 noise values were used for comparison with the received signal intensity.

Values of field intensity required to overcome set noise at the receiving site for a 15 ft. whip antenna where obtained from the equipment manufacturer.

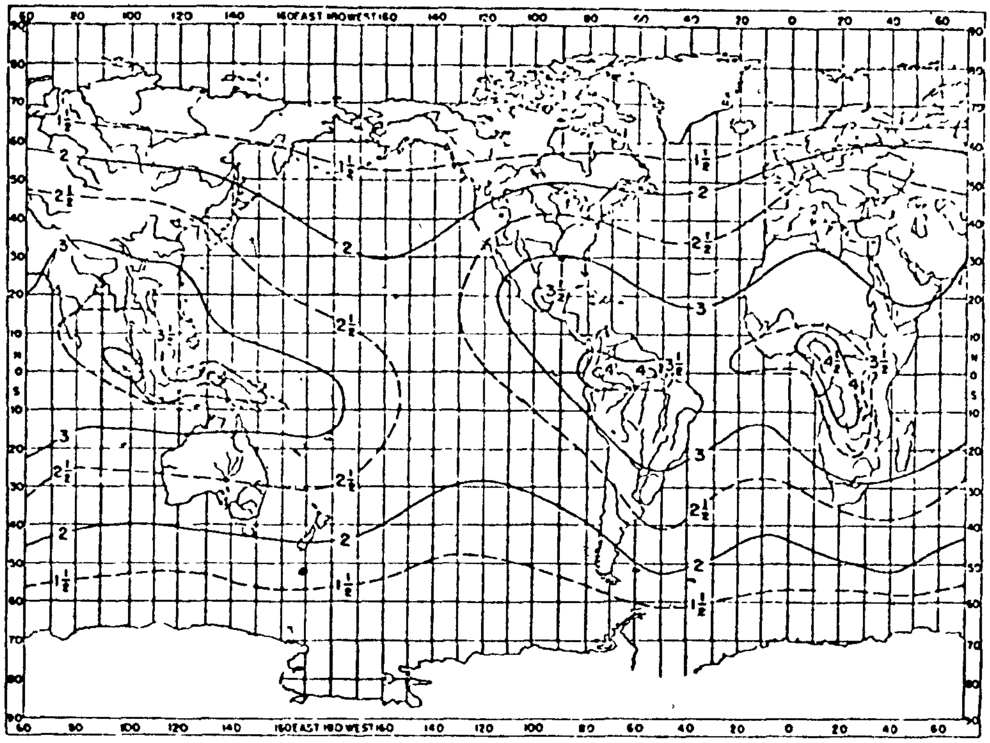

FIGURE 2.7(a). NOISE DISTRIBUTION CHART FOR MARCH, APRIL, AND MAY.

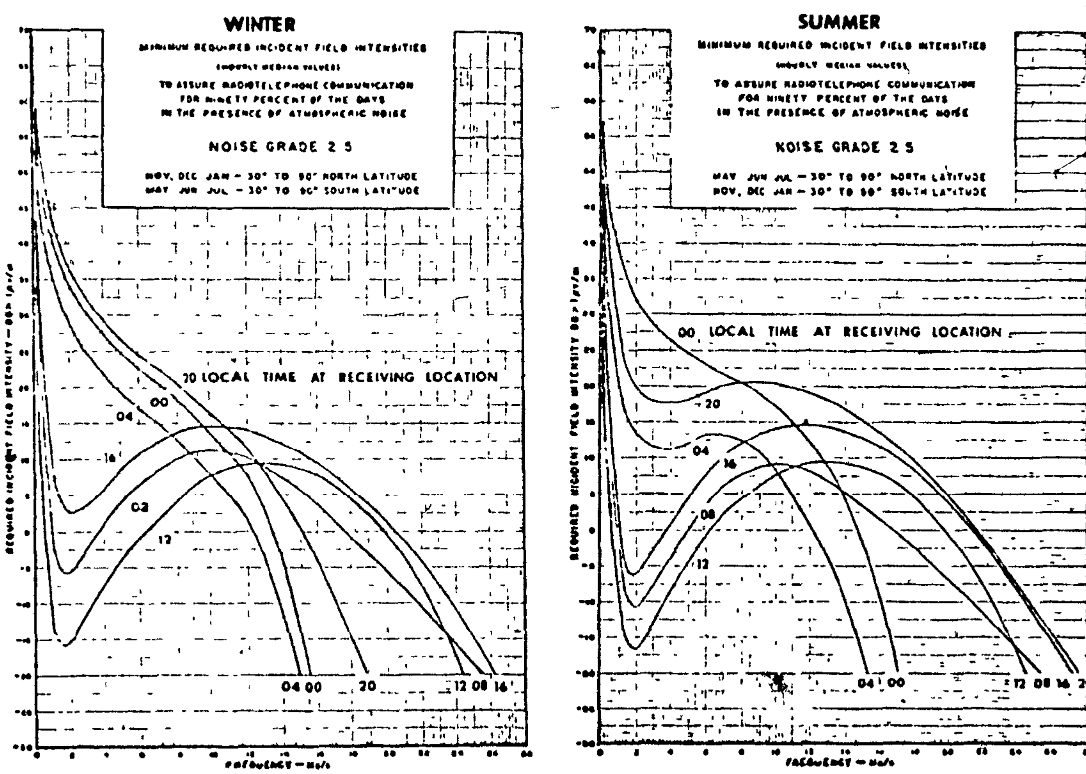

FIGURE 2.7(b). MINIMUM REQUIRED INCIDENT FIELD INTENSITIES, NOISE GRADE 2.5.

Thus a comparison could be made between the received signal intensity and atmospheric or set noise, S_R.

2.3.3 Successful Contact Ratio and Range Versus Frequency

A communications event was considered successful when the received field intensity was equal to or exceeded atmospheric or set noise. Thus at each frequency and range value all the signal values corresponding to the 396 values of antenna gain were compared to set noise and the 18 values of atmospheric noise. A total of 7128 events were used to determine the successful contact ratio, SCR, for each value of range at each frequency. Thus,

$$SCR = \frac{\text{no. of successful contacts}}{\text{total no. of contacts attempted}}$$

$$SCR = \sum_{N=1}^{6} \sum_{K=1}^{3} \sum_{L=1}^{11} \sum_{M=1}^{36} \delta_s /7128 \qquad \delta_s = \begin{cases} 1 \text{ if } S_R \geq S_N \\ 0 \text{ if } S_R < S_N \end{cases} \quad (2.4)$$

where,

K values correspond to seasons of the year and

N values correspond to hours of the day,

L values correspond to values of θ for antenna gain

M values correspond to values of ϕ for antenna gain.

Typical curves of SCR versus range are shown in Figure 2.8.

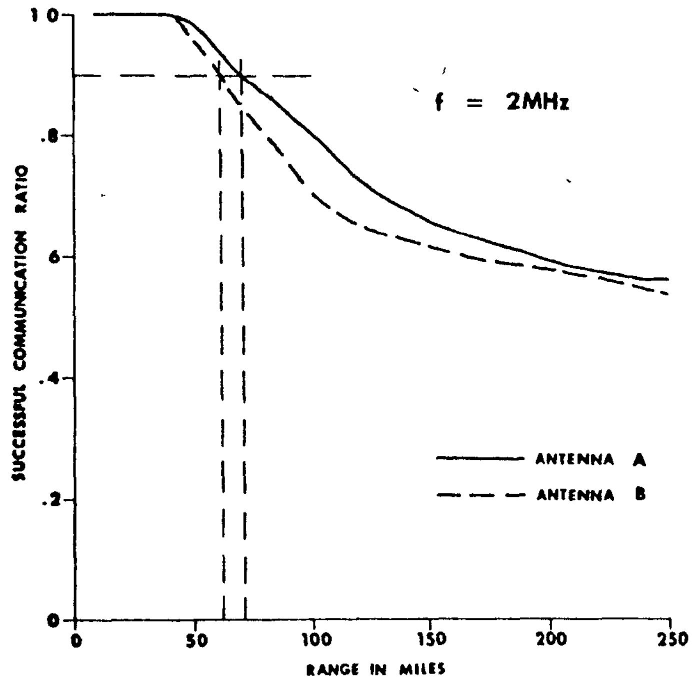

FIGURE 2.8. SCR VS R, ANTENNAS A AND B.

Although useful to the antenna evaluator per se, these do not give a quick view of antenna performance over the frequency range. If a parametric value of SCR is chosen, say 0.9 as indicated, then curves of effective range variation with frequency could be drawn for the antennas under evaluation.

From the set of SCR versus range values for the five HF wire antennas, curves of effective range with frequency were determined. These are shown plotted in Figure 2.9 and are compared with some of the other factors of merit.

2.4 Comparison of Evaluations

Examination of the curves of Figure 2.9 can be confusing unless separate features are examined in turn. The first set of curves (a) is for the antenna system efficiency factor as defined by Granger and in MIL-A-9080. It would generally be difficult to make a clear choice between the antennas, especially if there were serious installation factor[1] differences between them. It should be noted that antennas B and C are similar except for stand-off heights. Yet it is curious to note the substantial difference between their ASE rating at the middle frequencies. Antenna E is similar to C except for the location of the second and third stand-off insulator.

The curves in (b) showing the ASE term for the E_θ component, accentuate the differences between the antennas but the relative position of some antennas is changed at some frequencies. Note for instance that the relative ordering at 2 MHz is changed. The difference between the rating of antennas B and C at 8 and 10 MHz is particularly surprising.

The use of Moore's relative intelligibility index improves the discrimination at 2 MHz and de-emphasizes the large differences at 8 and 10 MHz. It should be remembered that these criteria still do not provide discrimination between antennas with different azimuth patterns.

---

[1] Such as location of coupler in high temperature zone, interference with other equipment or helicopter operations, etc....

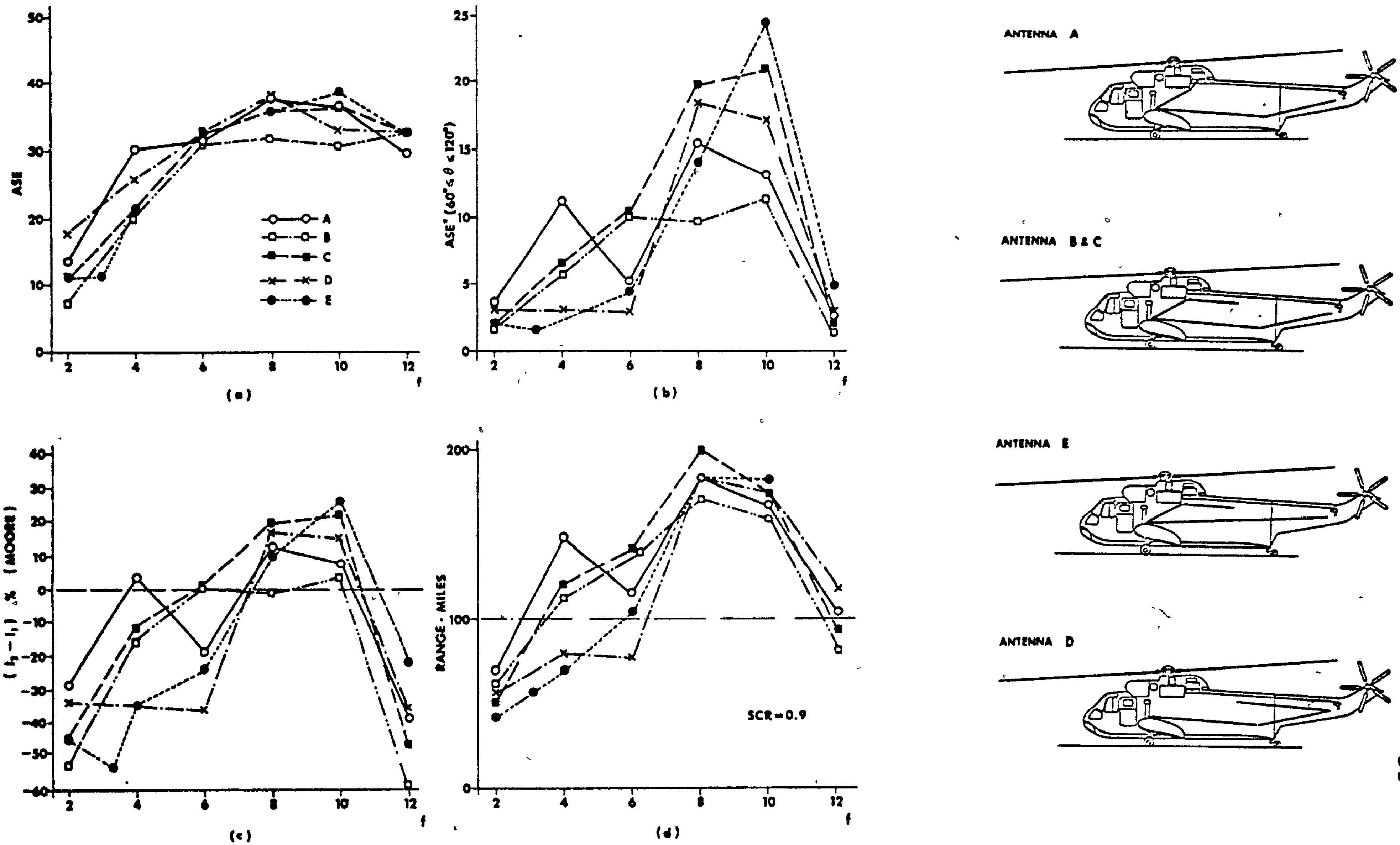

FIGURE 2.9. RANGE VS FREQUENCY AND OTHER FACTORS OF MERIT.

The computation of successful contact ratio and hence the range versus frequency curves of (d) provides a differentiation between antennas having different patterns in azimuth. Also direct account is taken of the variation in noise levels. It is interesting to note that the relative ordering of the antennas changes at 2 MHz and differences continue to be accentuated at the critical lower frequencies. In particular an operational reference is evident and the deficiencies of each antenna in this respect rather than relative comparisons can be observed. This is highlighted in Figure 2.10. The two extremes in performance at the

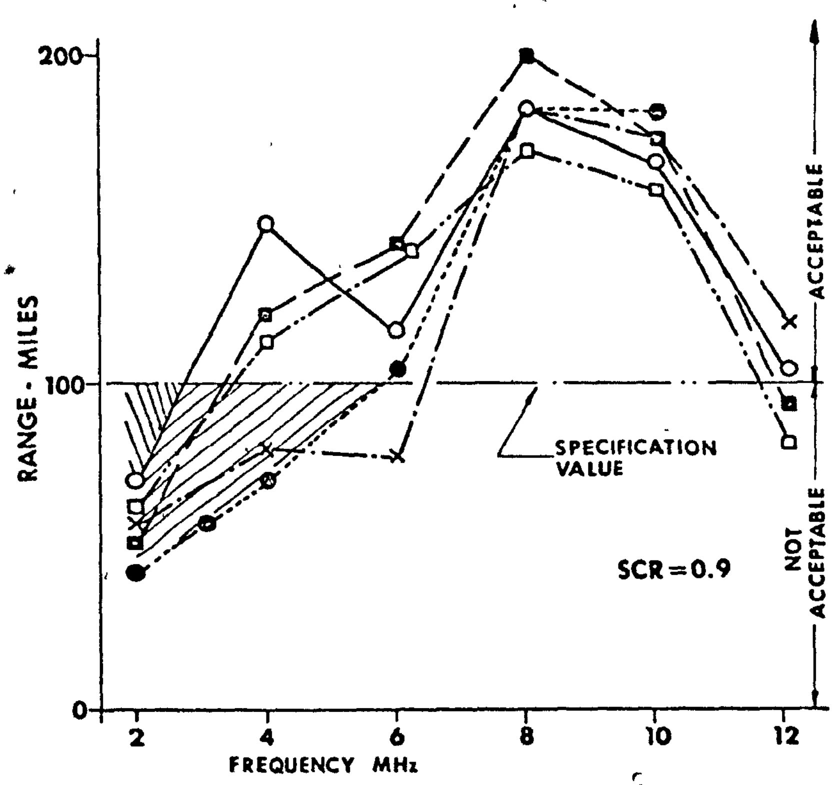

FIGURE 2.10. RANGE VS FREQUENCY AND OPERATIONAL DEFICIENCIES.

lower frequency are emphasized in this figure. Also apparent is the fact that the target range is easily achievable in the midfrequency range. In this respect, the apparent superiority of antenna E at 10 MHz is reduced, making it possible to emphasize the more critical frequencies. Perhaps the value of this operational reference in a factor of merit will be accentuated by the observation that an antenna similar to E was selected when at least one of the forms of B or C could have been considered, had such a reference been available early enough in the design evaluation.

In calculations of field intensity at the receiving site to determine the successful contact ratio, the minimum and maximum values can be identified easily. When superimposed on the curves of required field intensity to overcome noise, as shown in Figure 2.11, these provide an exceptionally good reference for radio

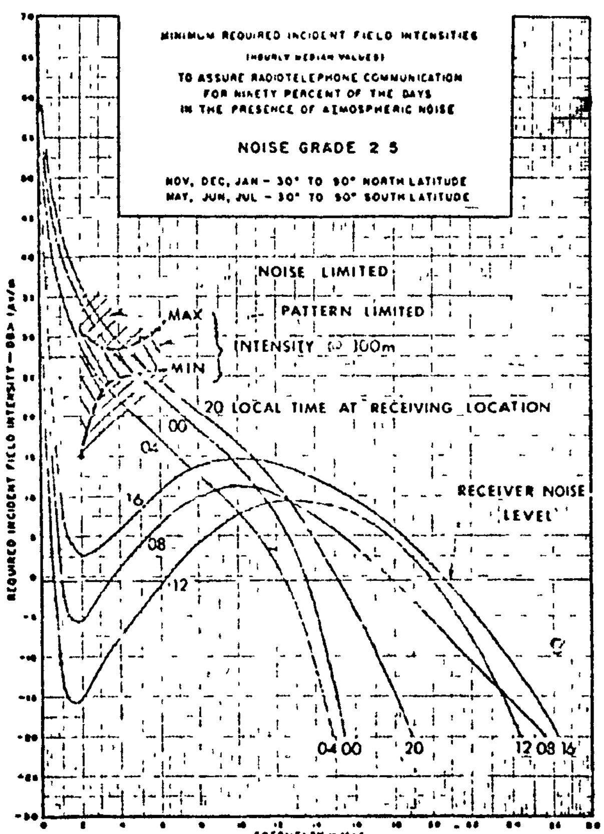

FIGURE 2.11. CRITICAL COMMUNICATION PERIODS.

operators who can now determine whether communications is likely to be gain or noise limited. When used with the data of Figure 2.10, a rather complete view of communications system performance is obtained. It is believed that such a complete evaluation has not been available heretofore and this new method should be useful for such a purpose.

2.5 Summary of Proposed Method

The major steps of the design and evaluation procedure are shown in the schematic of Figure 2.12. The core of the procedure is detailed in the flow chart of Figure 2.13. Impedance data is required to calculate matching unit and transmission line efficiency. The ohmic losses of the antenna need to be known to compute the antenna efficiency. Complete pattern data is required to determine the gain, $G_T(\theta,\phi)$, for desired values of θ and ϕ. A weighting factor can be introduced if a typical operational distribution of aircraft attitude is known. Ideally pattern data should be in digital form for direct computer processing. The cumbersome manual data reduction used in this work would have to be replaced by computer procedures in a practical operational application.

Path loss values can usually be taken from available curves. In full scale test programs these values should be recalculated for the specific test path being used.

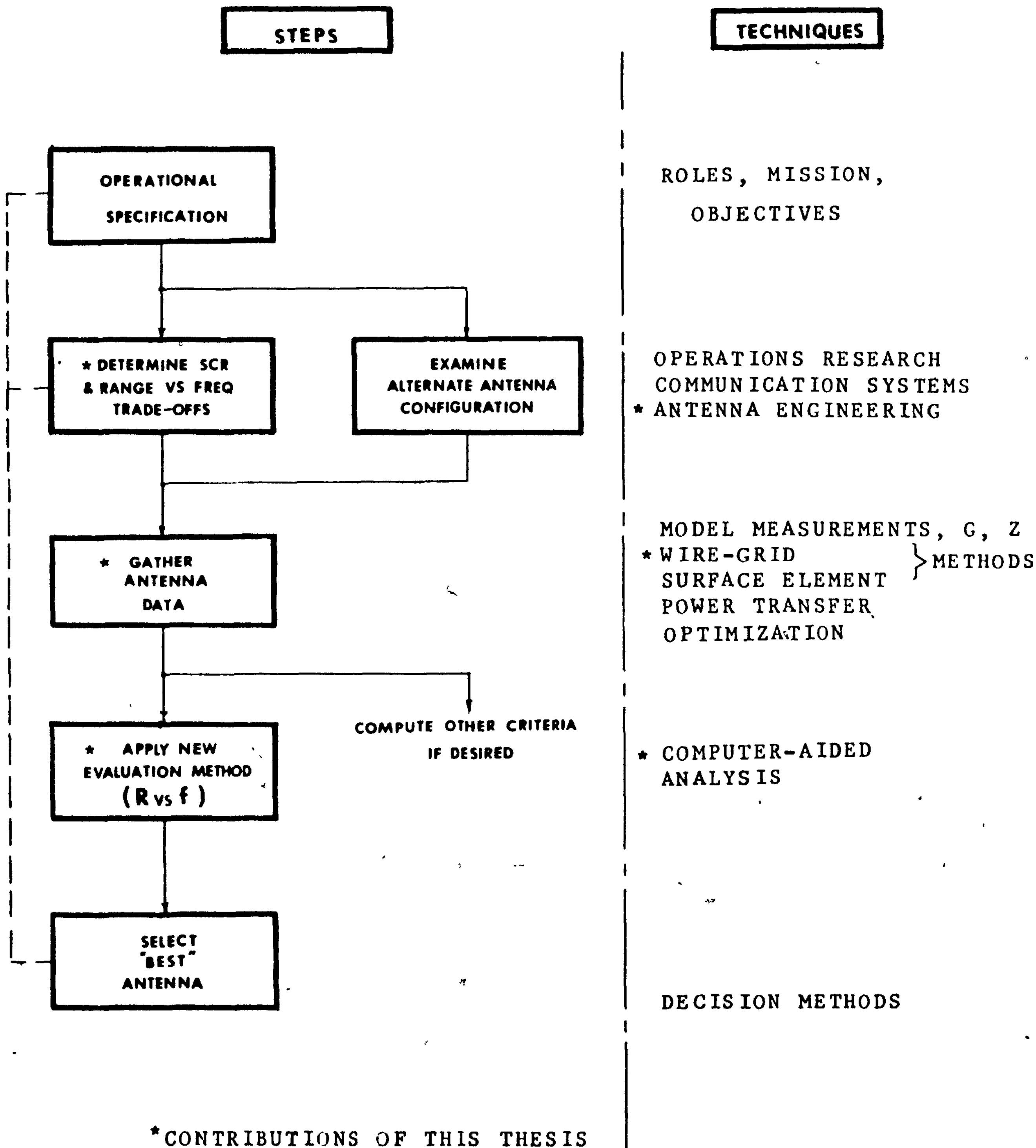

FIGURE 2.12. MAJOR STEPS IN DESIGN/EVALUATION PROCEDURE.

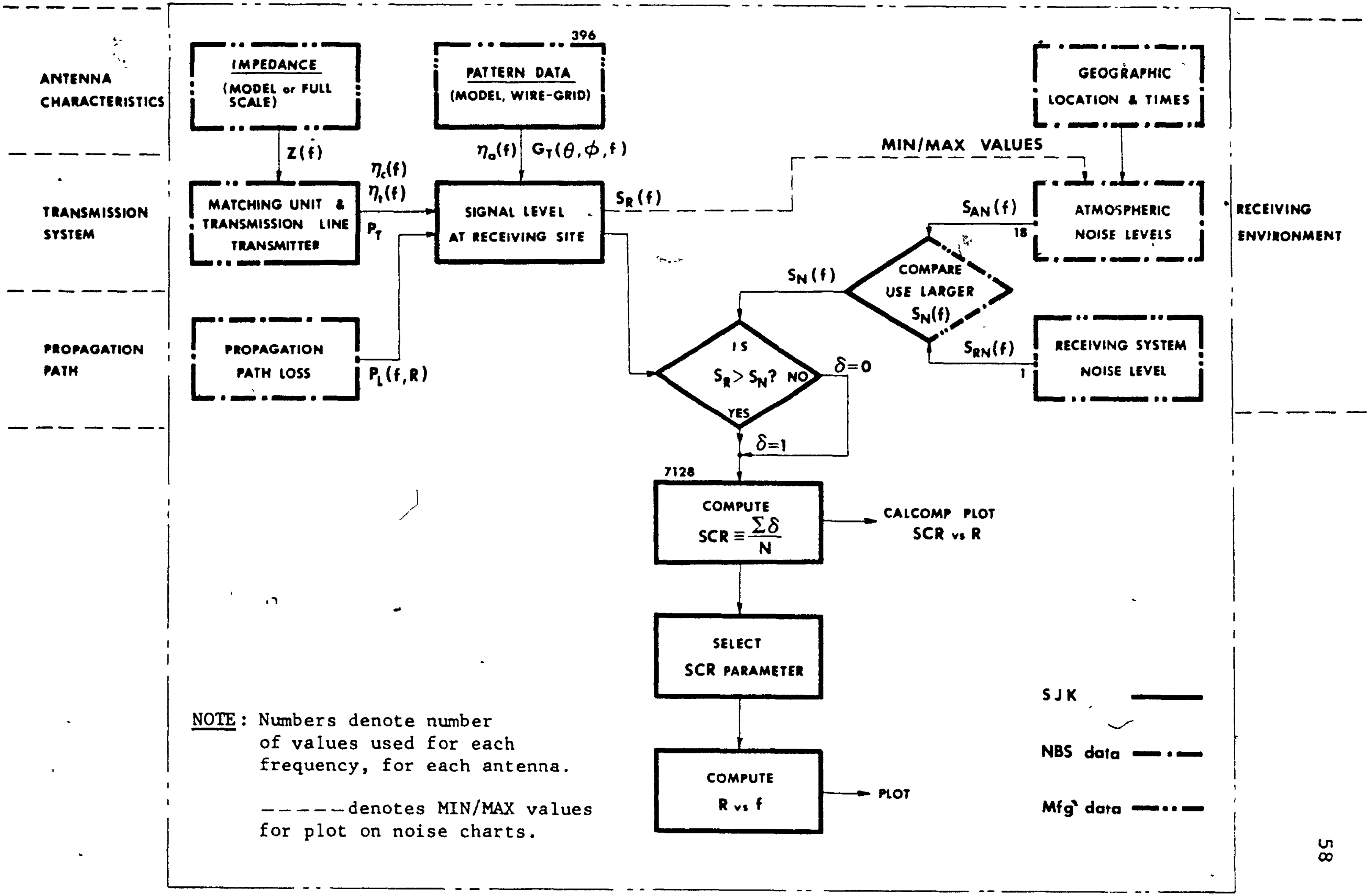

FIGURE 2.13. COMPUTER-AIDED ANTENNA ANALYSIS - FLOWCHART.

Noise at the receiving site must be measured sometimes because published atmospheric noise levels may not apply. This is especially the case for large modern ships or urban sites. These more stringent conditions emphasise the need for a more complete antenna evaluation.

The successful communications ratio, as shown in the flowchart and in Equation (2.4) has been chosen to be a δ-function because operational expectations are for a "GO/NO-GO" condition. When requirements so dictate, the function can be selected to be a continuous one based on articulation scores. The writer tends to favour use of a discontinuity at some threshold value based on operations research.

Similar considerations apply to the selection of a parametric value of SCR for the range versus frequency curves. Usually a representative value can be selected from an examination of the critical communications conditions (Figure 2.11). Furthermore, an entire family of values can be used to extend the understanding of the limitations of the communications system.

A program was written to carry out the computations indicated in Figure 2.13 and to plot (CALCOMP) the SCR versus frequency curves. The resulting graphs can be used manually or if an interpolation program is written the values of range can be determined to produce a completely automatic process.

It should be recalled that previously, range and SCR values were either not available or were obtained by rough estimates or by extrapolation beyond the validity limits of the basic data.

It can now be appreciated that the availability of a valid wire-grid model of the vehicle would make it possible to generate pattern data much more quickly and hence make the proposed analysis feasible for new antenna forms or locations.

2.6 Rotor Modulation

The additional problem peculiar to helicopters is the effect of the rotor on antenna characteristics at HF frequencies as illustrated in Figure 2.14, reproduced from measurements on the

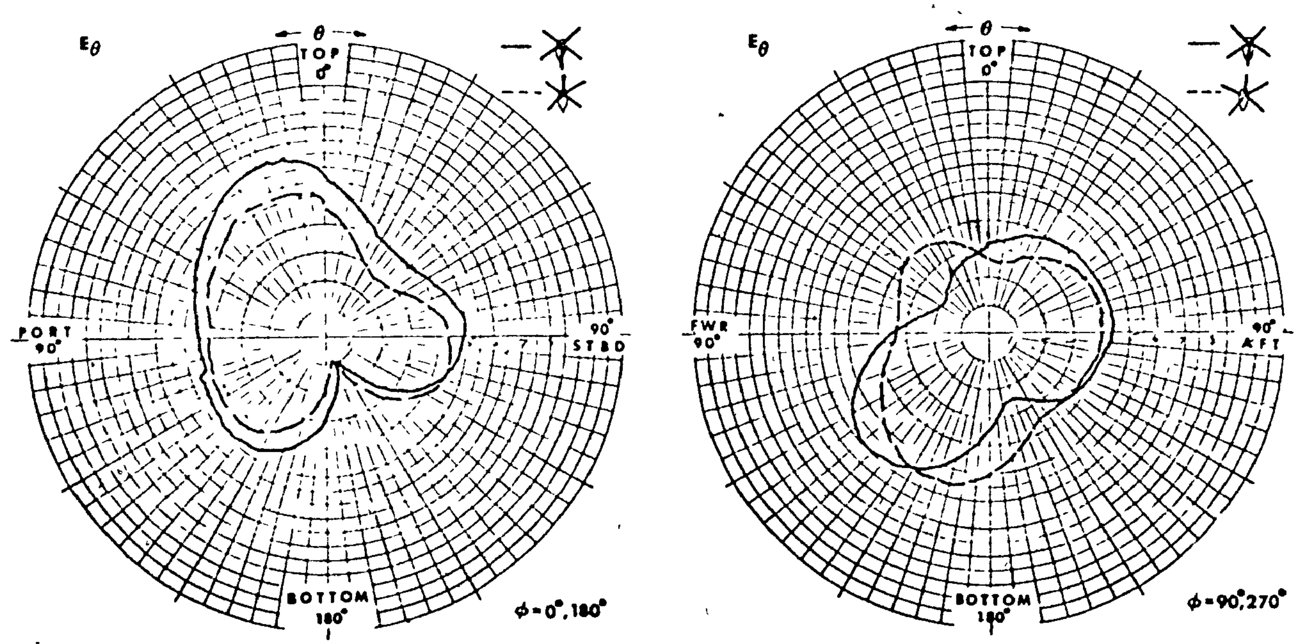

FIGURE 2.14. ROTOR MODULATION EFFECT - CHSS-2 HF ANTENNA.

CHSS-2 helicopter. A substantial test of the usefulness of any analytical or numerical technique would be the ability to predict the seriousness of this effect.

In the process of attempting to study this effect experimentally and to study wire-grid modelling techniques, it was essential to have an independent means of measuring radiation characteristics against which the results of numerical techniques could be compared.

CHAPTER III

ANTENNA TEST FACILITY AND MEASUREMENTS

3.0 Introduction

This chapter describes the design and construction of the test facility, the evaluation of its suitability for far-field measurements and the measurements of various model antennas including those mounted on a helicopter.

The measurements are typical of those necessary for antenna modelling, are representative of the type required for the pattern data used in Chapter II, and serve as a basis for the numerical analysis of Chapter IV. The facility in which they were made is unique for its compactness and cost performance optimization in the more practical engineering sense. Measurements with model antennas themselves and other standard types, were used for the design and test of the absorber layout in the anechoic chamber. These are supported by identical measurements made at a large industrial open air antenna pattern range.

In addition, brief results are presented from a developmental program, using this facility. These results indicate more clearly the effects of rotor modulation and the possibility of its control and demonstrate the usefulness of the experimental facility in resolving special problems which can only be solved by heuristic methods.

3.1 Preamble. Why a Test Facility?

Significantly investigators of numerical wire grid or surface element modelling techniques usually rely on measurements made by other experimental investigators.[1] Measurement facilities are costly and their setting up and operation is time consuming. By comparison, a quicker response is available from "software" trouble shooting than from the elimination of practical problems in an experimental facility. The scarcity of reliable experimental results poses a special problem to individual investigators who are in competition with larger groups whose results are nevertheless not generally available.

For the investigation of the class of antennas and phenomena of interest, an anechoic chamber for near and far field measurements was desired, usable down to UHF frequencies. Chambers of reasonable size for this frequency range can cost approximately $100,000.00. Their very size poses a problem of siting, funding, operation and maintenance. Curiously funds available for this project were almost in the same ratio to the above amount as was the scale factor for the model aircraft used. The material, the shape and form had to be chosen with great care to obtain the largest possible room for the funds available. Forms from igloos to geodesic domes were considered for essentially a near-field measurement facility. Fortunately a clear roof area of 56' x 34', surrounded by sheltering walls 14' and 18' in height, made it

---

[1] Note for example the frequent reference to the measurements of Morita, two decades ago and those used by Tanner for aircraft antenna modelling.

feasible to construct a roofless anechoic room protected by a removable plastic weather cover.
The corridor in an adjoining penthouse was converted into a control room. A description of this room and construction details are given elsewhere [52].

3.1 Design and Construction of Anechoic Chamber

Important factors involved in the design of an anechoic chamber are the type of microwave absorber and its cost, the form of the room and positioning of the absorber, location of antenna and its mount, location and positioning of probe and cables, and access to the chamber. The microwave absorber cost and performance are dominant factors. The placing of the absorber is also important and some aspects of this are described in 3.2.2.

3.1.1 Absorber Considerations

Low frequency microwave absorber is constructed in the form of wedges, pyramids or cones of homogeneous lossy material or thinner absorber sheets. The structure is similar to that used for acoustic absorbers, as discussed by Meyer [48]. The characteristics of this type of absorber are further discussed by Severin [49] and nominal curves of performance for various thicknesses together with room design considerations are presented by Galagan [50]. The thickness of the absorber determines its lowest useful frequency. The reflection level is relatively insensitive to incidence angle up to an angle of 45° and deteriorates thereafter.

Outdoor microwave absorber is expensive. For reasons of economy, therefore, an indoor type, McMillan BP-24 was selected. For walkways, the block-type BB-16 was used. The manufacturer defines the critical frequencies for low and high angles of incidence as shown in Figure 3.1 and the accompanying table. Emerson and Cumming Type CV-4 absorber was also used during specific measurements. From the manufacturer's data, the variation of reflectivity versus frequency is shown in Figure 3.2. The McMillan BP-24 and BB-16 absorber was protected from the weather by wrapping it with .006" black polyethylene film. According to the manufacturer this does not degrade the absorbent qualities of the material but may in fact further enhance them. With a dielectric constant of 2.3, it can be seen [51] that such a thin sheet would indeed have low reflectivity at moderate angles of incidences for the frequencies used here.

Anechoic chambers are normally rectangular in shape or tapered in a horn-like manner. These shapes arise from the requirements for testing highly directional antennas. The side walls are positioned so that a sufficiently large "quiet zone" is obtained at the aperture being tested. For rectangular rooms a low length-to-width ratio is preferred [50]. The anechoic chamber

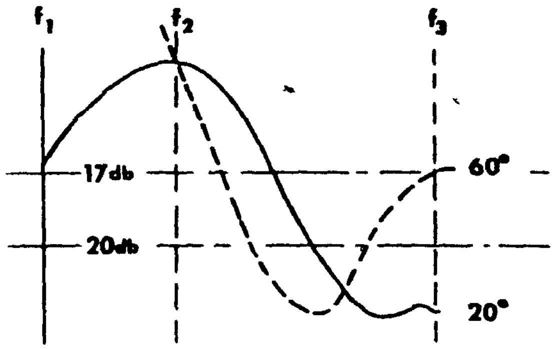

ABSORBER TYPE	f_3 - MHz	
	15°	60°
BP - 24	200	295
BP - 16	300	440

f_3 - low freq. cut-off freq. at 17 db level

FIGURE 3.1. ABSORBER CHARACTERISTICS.

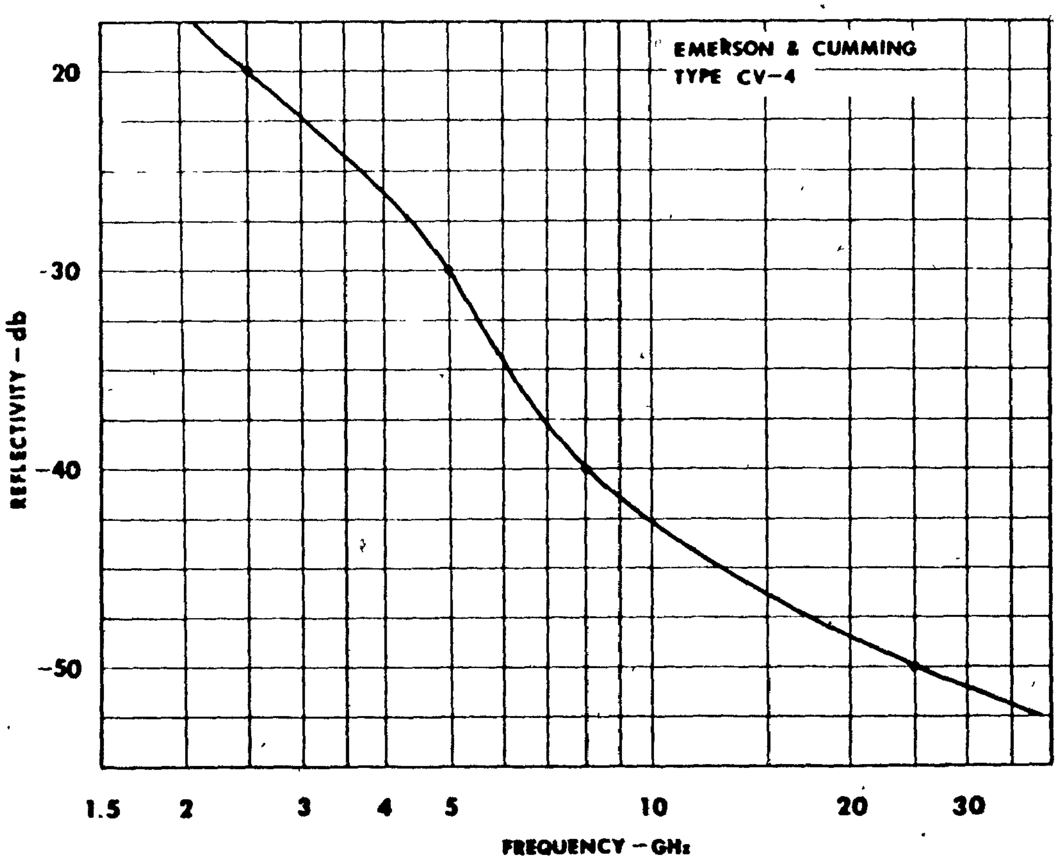

FIGURE 3.2. VARIATION OF REFLECTIVITY WITH FREQUENCY.

discussed here, however, was constructed primarily for near-field measurements around a centrally located antenna and for occasional far-field measurements of a limited type. A 14-sided polygonal shape was selected. For the test geometries used, the angles of incidence are small ensuring good absorption. The roofless design and the wall height (see below) have been arranged to provide an unobstructed view upwards.

3.1.2 Siting Considerations and Construction

The location of the anechoic chamber within a sheltered roof area is shown in Figure 3.3. The chamber sits on a 24 ft. square platform. Each section of the polygon consists of a supporting aluminum frame column to which is attached a 4' x 8' panel supporting the microwave absorber. Each section is bolted to the mounting platform except one which is mounted on casters and serves as a door to the chamber. The clear inside area is approximately 7'4" in radius centered on the antenna rotator shown. The elevation view of Figure 3.4 shows how the wall height and positioning is arranged with respect to the parapet walls and the penthouse roof. It can be seen that energy from a radiating model in a typical location should not irradiate sections of the wall or railing directly to produce an undesirable back scattered field into the chamber. A wooden beam serves to support the removable plastic cover.

The method of construction and assembly is illustrated in Figure 3.5 to 3.7, which show progress of construction from

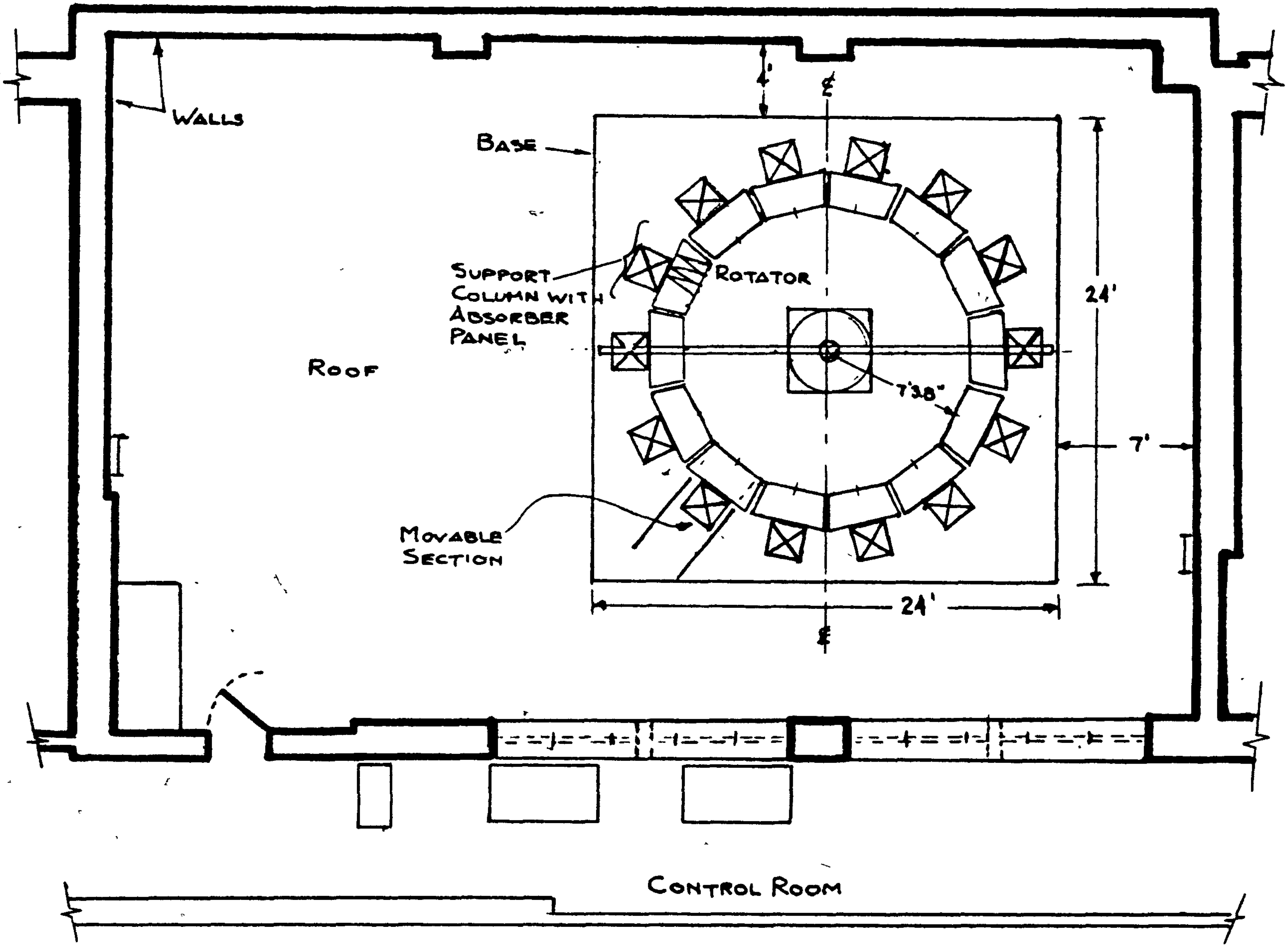

FIGURE 3.3. OUTDOOR ANECHOIC ROOM. - PLAN VIEW.

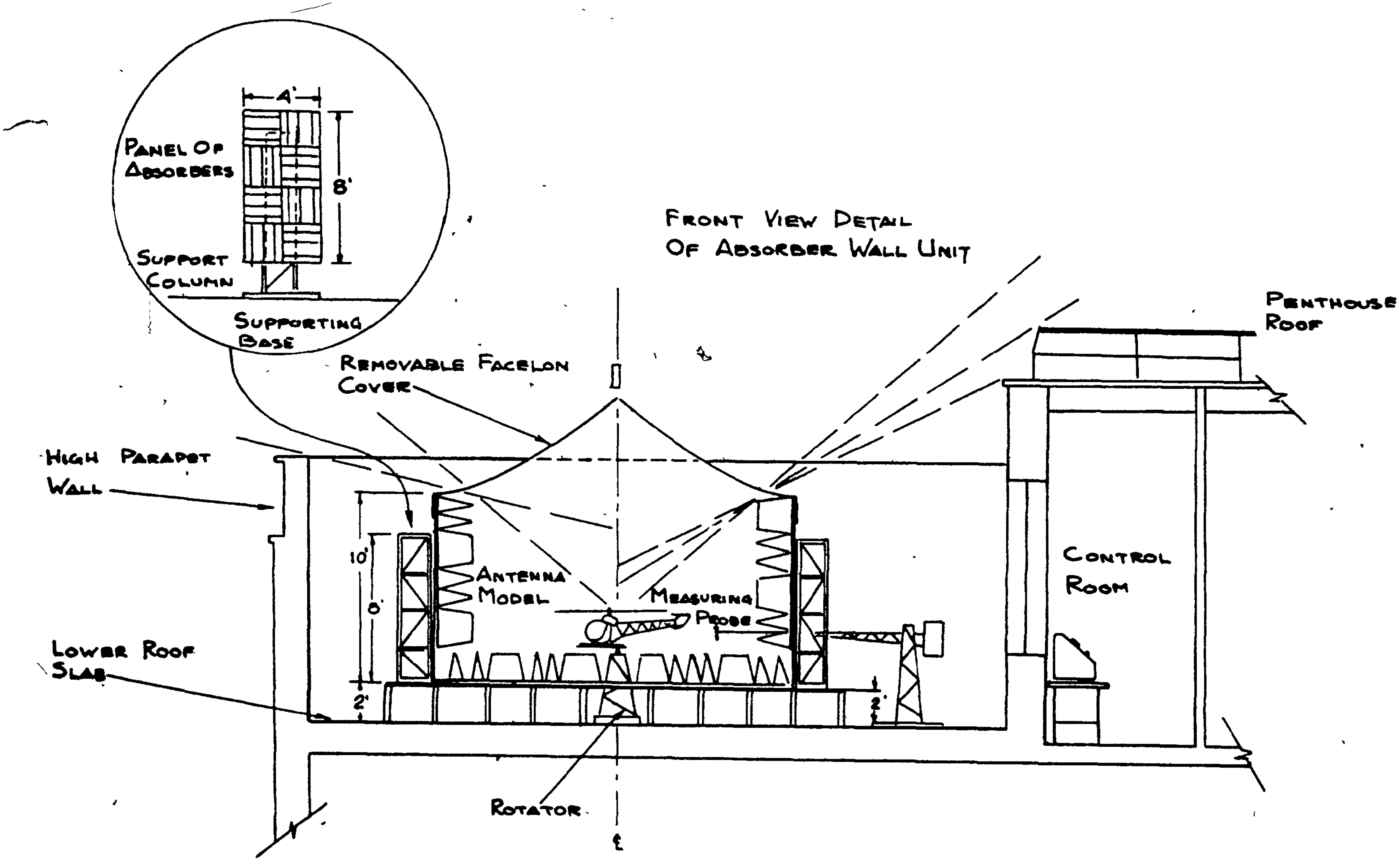

FIGURE 3.4. VERTICAL SECTION THROUGH ANECHOIC ROOM.

(a) Setting up Transit for Base Layout.

(b) Erecting Dexion Base

(c) Surfacing of Platform

FIGURE 3.5

(a) Mounting & Weather-proofing Absorber Panels.

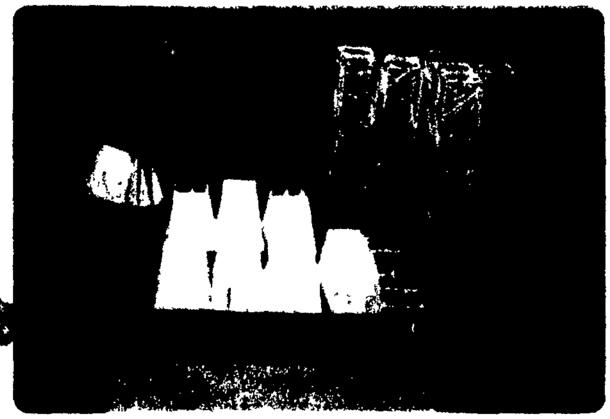

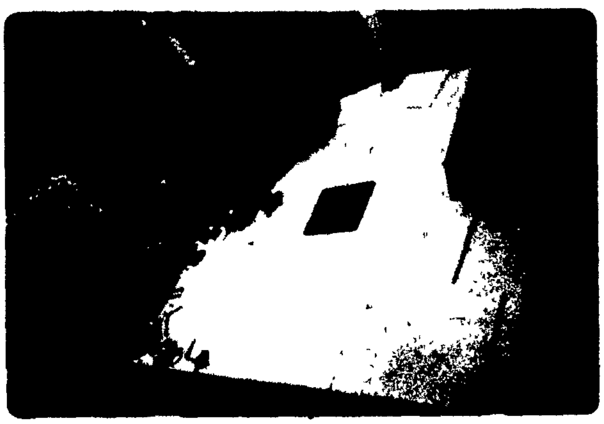

(b) Assembly of 14-sided Polygonal Wall.

(c) Fixed Walls with Access Section Removed.

FIGURE 3.6

(a) Walls Complete, Installation of Second Beam Support Column.

(b) Installation of Weather Cover, Access Section Open.

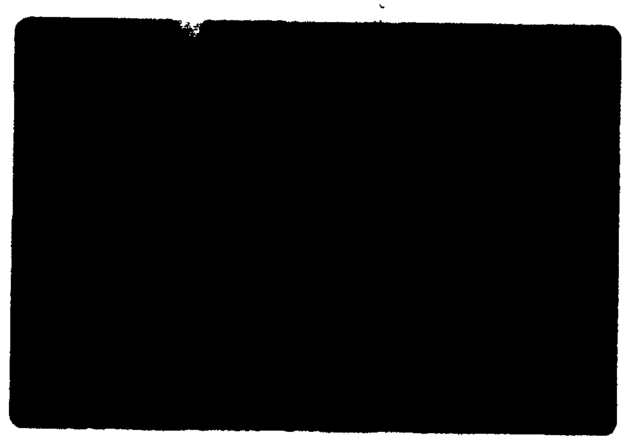

(c) Rooftop View with Mount Royal in Background.

FIGURE 3.7

surveying of the site to the attachment of the roof cover. Figure 3.8 shows the antenna rotator before installation. The arrangement of the floor absorber is described in a later section.

Most of the far-field ranges use three- or four-axis mounts for supporting the model antennas and allow complete θ, ϕ pattern measurements. With the larger distances used, the movement of the radiating source from a fixed position produces negligible variation in intensity. For near field measurements, however, the model must be at a fixed location and the probe position varied in three dimensions. An inner polystyrene and an outer plywood circular arch were constructed for probe mounting. These are shown in Figure 3.9. The outer arch is 7 ft. in radius, has a span of 40 degrees and angle markings every five degrees. The inner arch is 4 ft. in radius, has a span of 130° on both sides of the rotator axis and markings at one degree intervals. A movable probe carriage with a vernier scale is attached to the inner arch. The arrangement then accomodates the centrally located model which is rotatable in azimuth and allows the three dimensional positioning of the measuring probe. E_θ and E_ϕ components are measured by rotating the probe. In some cases, for linear antennas, to obtain E_θ vs θ and E_ϕ vs θ patterns, the model antenna was mounted at right angles to the vertical axis of the rotator. This positioning overcomes the span limitation of the arches and is described with the specific measurements which follow.

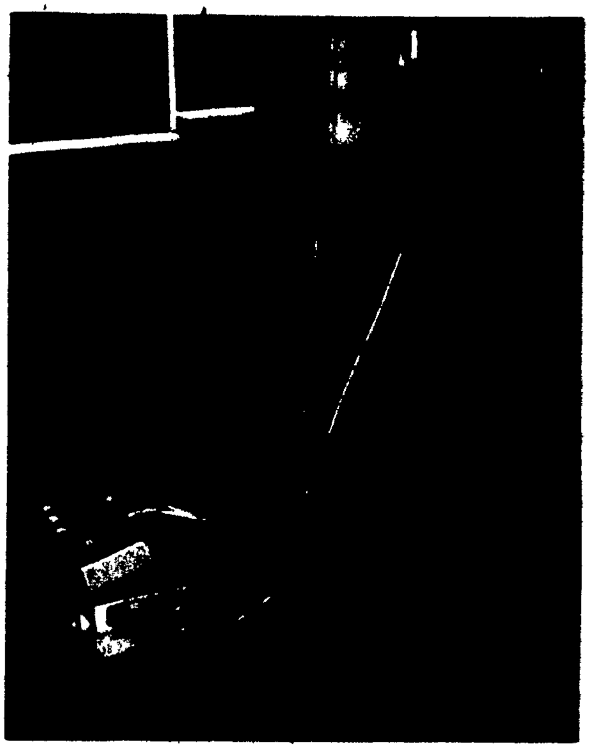

FIGURE 3.8. ANTENNA ROTATOR PRIOR TO INSTALLATION.

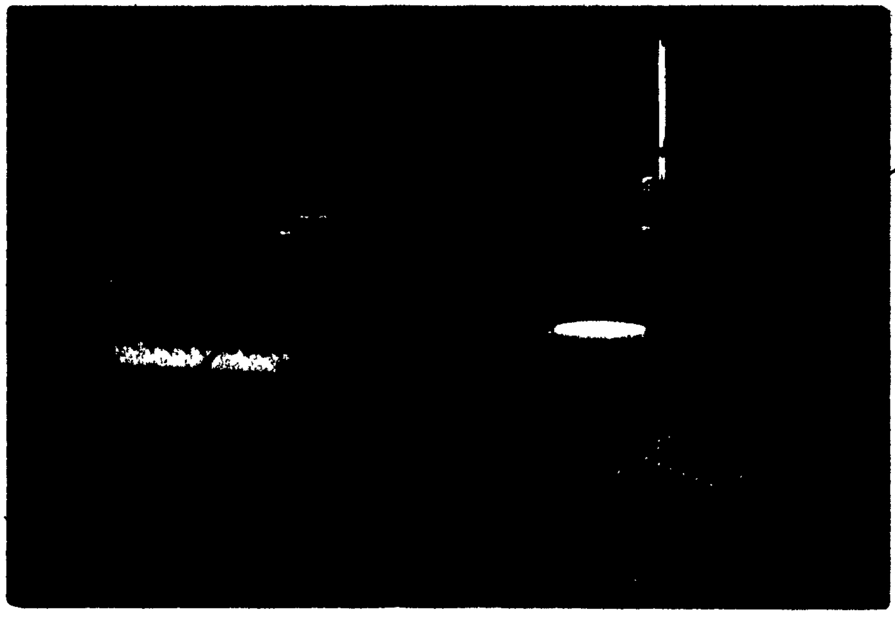

FIGURE 3.9. INNER AND OUTER ARCH.

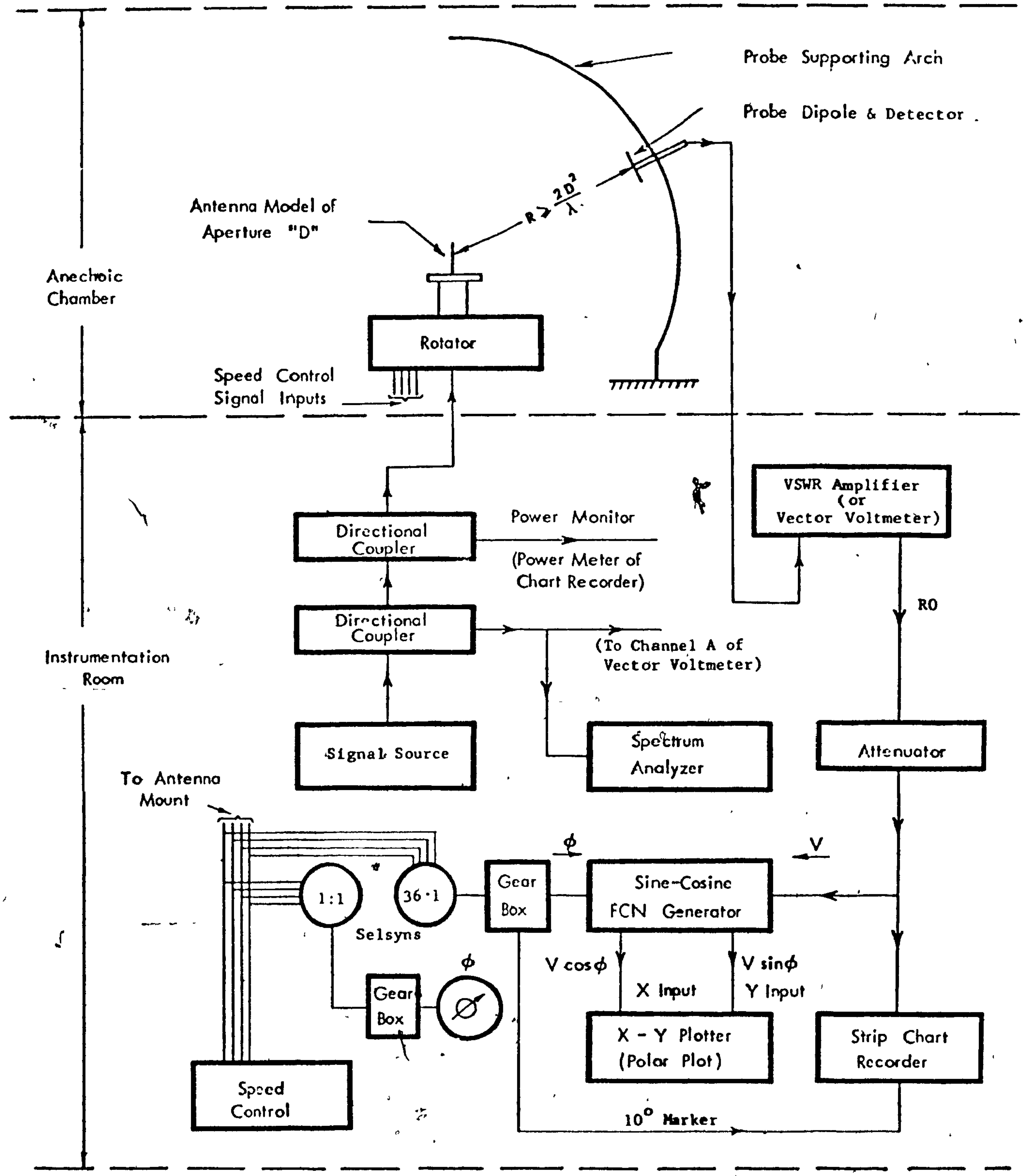

RO Recorder Output.

Ø Azimuth Position Indicator for Rotator.

FIGURE 3.10. SCHEMATIC OF INSTRUMENTATION.

3.1.2 Instrumentation

A complete schematic of the equipment is shown in Figure 3.10 and the physical arrangement in Figure 3.11.

The system consists of the following units:

1	AIL	125	Signal Source
1	Polarad	SSS	Signal Source
1	HP	8410A	Network Analyzer
1	HP	8405	Vector Voltmeter
1	HP	431B	Power Meter
2	HP	415E	VSWR Amplifier
1	Polarad	STU	Spectrum Analyzer
1	HP	7035B	X-Y Recorder
1	HP	7100B	Strip Chart Recorder
1	HP	393A	Variable Attenuator
1	Sierra	137A	Directional Coupler
1	Philco	640A	Directional Coupler
1	RL14	---	Sine-Cosine Potentiometer
1	HP	350A	Attenuator Set
1	EEL	---	Azimuth Rotator
1	S/A	24	Rotary Joint
1	HP	420A	Crystal Detector
1	OSM	20080	Crystal Detector
1	OSM	20750	Schottky Barrier Diode Detector
1	FXR	N210B	Bolometer Mount
1	HP	420A	Crystal Detector
1	McGill	Elec. Eng.	Rotator Speed Control

1	Beckman		Frequency Measuring Equipment
1	PRD	Co-ax.	Cavity Wavemeter

FIGURE 3.11.

The AIL 125C signal source was used in CW or AM modulation mode depending on the detection system used: Vector Voltmeter or HP 415 SWR amplifier. For frequencies above 3 GHz, the Polarad Model SSS signal source was used. The spectrum analyzer was used to check frequency and signal characteristics. At the start of measurements a PRD - co-axial cavity wavemeter was used to check frequency calibration of the spectrum analyzer at S-band frequencies and a Beckman transfer oscillator and digital counter at L-band. The output of the second directional coupler was terminated in an HP 420A crystal detector. The detected output was monitored on an HP 415B (or E) SWR amplifier for power monitoring purposes, as shown. The rectified output of the SWR amplifier was displayed on one channel of the HP 7100A strip chart recorder to allow power corrections to be made during data reduction. A type N to OSM adaptor (OSM 31010) was used in the upper part of the rotating joint to effect the transition to the miniature RG-174A/U cable connected to the antenna.

For tests at S-band, the receiving antennas were a flanged waveguide (HP S281A) or a standard gain horn. These were terminated in an FXR 213M co-axial bolometer detector mount. The detecting element was calibrated for square-law characteristics prior to the start of the measurements. The calibration curve is shown in Appendix II. In all cases and at all test frequencies, the transmitting signal was adjusted so that the received signal would be within the calibrated range of the detector for all signal levels measured. The flanged waveguide and detector are shown in Figure 3.12. In some cases a dipole probe with split-tube balun [53] was used (Figure 3.13).

For lower frequency measurements the probes shown in Figure 3.13 were constructed. They are constructed with 50-ohm

FIGURE 3.12. FLANGED WAVEGUIDE AND DETECTOR ON OUTER ARCH.

rigid .085" O.D. co-axial cable using Omnispectra OSM-207-1 connectors. The probe design was based on the work of Whiteside [54] and King and Whiteside [55].

FIGURE 3.13. $\lambda/2$ DIPOLE AND SMALL LOOP PROBES.

The probes were mounted on the inner or outer arch as necessary, and specific details about probe and test antenna mounting are given for the specific measurements described later.

The axis of the azimuth rotator was aligned carefully with the axis of the chamber and the arches in turn with this axis and with a center at the location of the test antenna. Two synchros geared 1:1 and 36:1 were connected to the drive shaft of the mount. Repeat synchros were used to drive a compass indicator, a sine-cosine potentiometer ~~and an~~ angular mark wheel used to actuate marker pens on the strip-chart recorder. The compass indicator allowed continuous knowledge of the direction of the antenna axis. The test antennas were supported by phenolic spacing tubes at the center of the test arch. The co-axial rotary joint was affixed to the bottom flange of this tube.

Both detectors used have an analog signal output for recording purposes. For most measurements, rectangular and polar plots were taken. The two channel strip chart recorder was used for more accurate data reduction purposes, since the power monitor output was recorded simultaneously with the received signal. The speed of rotation of the antenna mount was adjusted so that angle markings from the marker wheel would coincide with chart lines. The direction of rotation was marked on the face of the chart to remove doubt as to the angular values in later analysis. The polar plot was obtained using an X-Y plotter and a sine-cosine potentiometer driven by the repeat synchro. Thus an input signal V to the potentiometer generates V $\cos\phi$ and V $\sin\phi$ signals for the X and Y inputs of the plotter thus converting it to a polar plot recorder.[1] The polar plot was found to be invaluable in the quick comparison of patterns, especially when trouble shooting in the initial stages of any measurement.

---

1 This scheme was successfully developed as a student major project under the direction of Dr. T.J.F. Pavlasek.

3.2 Folded Dipole and Supporting Mast

The earliest utilization of the test facility was to develop and test antennas to be used in VHF airborne field strength and propagation measurements using a Bell 47G-4A helicopter[1]. Two antennas were involved, one a folded dipole for horizontal polarization and the second a sleeve monopole for vertical polarization. This section describes the work carried out on the folded dipole.

This antenna is an adaptation of a commercial (Sinclair 210-A) antenna for operation in the frequency range from 146-174 MHz. Radiation pattern measurements with a helicopter model were to be at 1/20-th scale near a full scale frequency of 150 MHz or at a scaled frequency of 3 GHz. The modelling and testing of this antenna followed conventional techniques, but in this program some special model validation problems were encountered to which new techniques were applied (Chapter IV) and the entire sequence of measurements represented the extension of the anechoic facility to S-band and its testing at these frequencies.

Since the commercial antenna is usually supplied for installation on a supporting mast, and radiation patterns are supplied by the manufacturer for this configuration, it was necessary to construct and test a 1/20-th scale model of the antenna and supporting mast for comparison with the reference patterns supplied by the manufacturer. In this 'antenna model validation phase' of radiation pattern measurements, some

---

[1] The basic principle of using the helicopter and the general type and method of use of antennas was conceived by Mr. Paul Robertson of Hydro Québec.

representative experimental problems were encountered and solved by a new combination of experimental and theoretical techniques.

3.2.1 Modelling of the Antenna

The antenna to be modelled is shown in Figure 3.14. with its normally supplied support mast. The insets of Figure 3.14 show details of the radio frequency feeding arrangement and dimensional data. Radiation patterns which are normally supplied are shown in Figure 3.15.

The folded dipole alone mounted on a special ground plane, was required for the helicopter and two were built and tested. These are shown in Figure 3.16.

In scaling the actual antenna, a number of physical constraints had to be considered. The folded dipole had to be constructed from miniature rigid co-axial cable with an outer diameter close to the scaled diameter of the antenna. The supporting mast diameter was also to conform to that used and provision needed to be made to install the co-axial feed cable within the mast in the manner of the actual antenna. The model was built as shown in the photograph and sketch of Figure 3.16. The small co-axial cable was brought inside the tube representing the mast and terminated in a miniature RF connector (OSM 207-1). The external surfaces were given a coat of conducting silver paint, in an attempt to approach the conductivity scaling requirements of Equation (1.8).

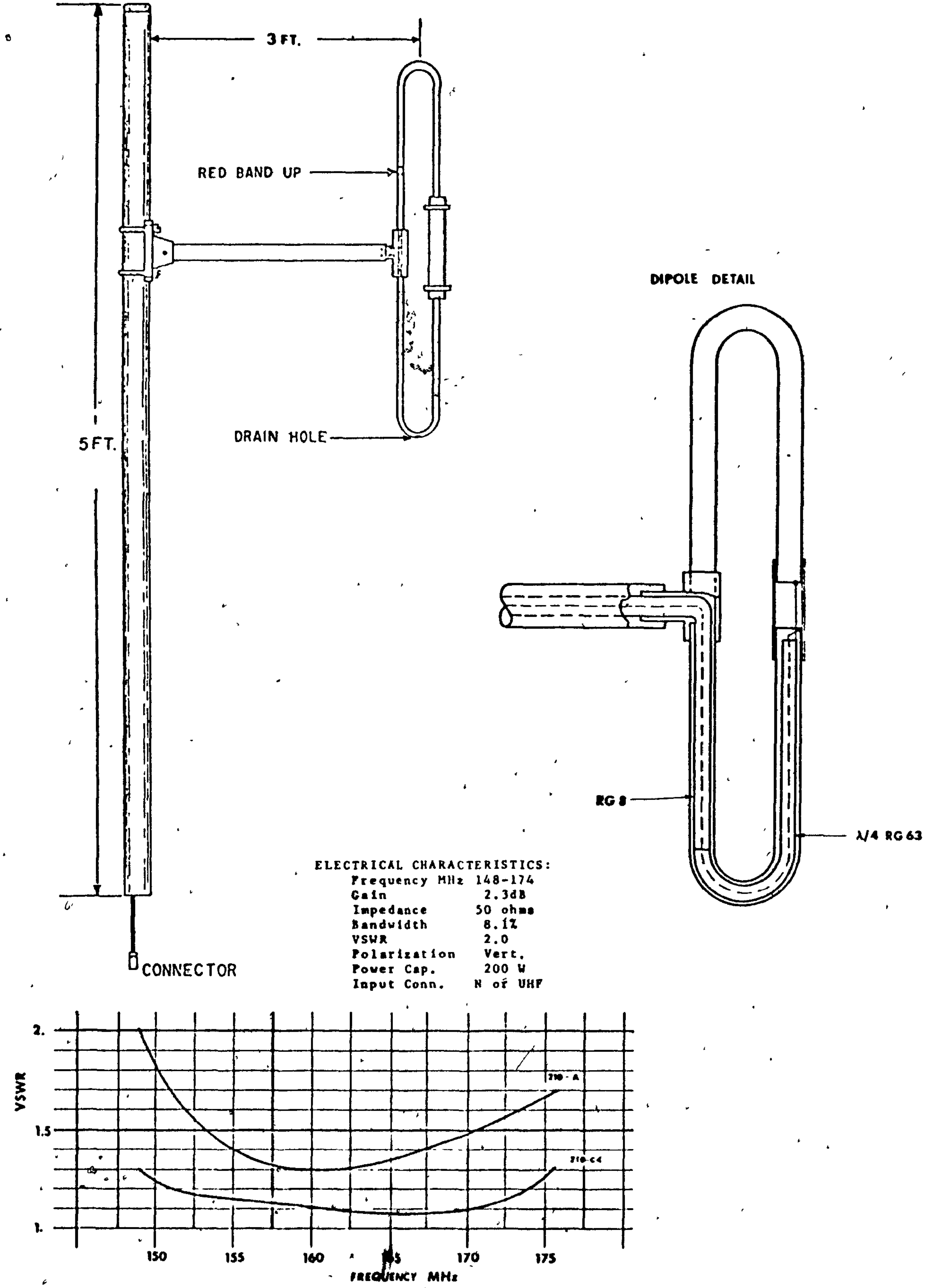

FIGURE 3.14. FOLDED DIPOLE AND SUPPORTING MAST.

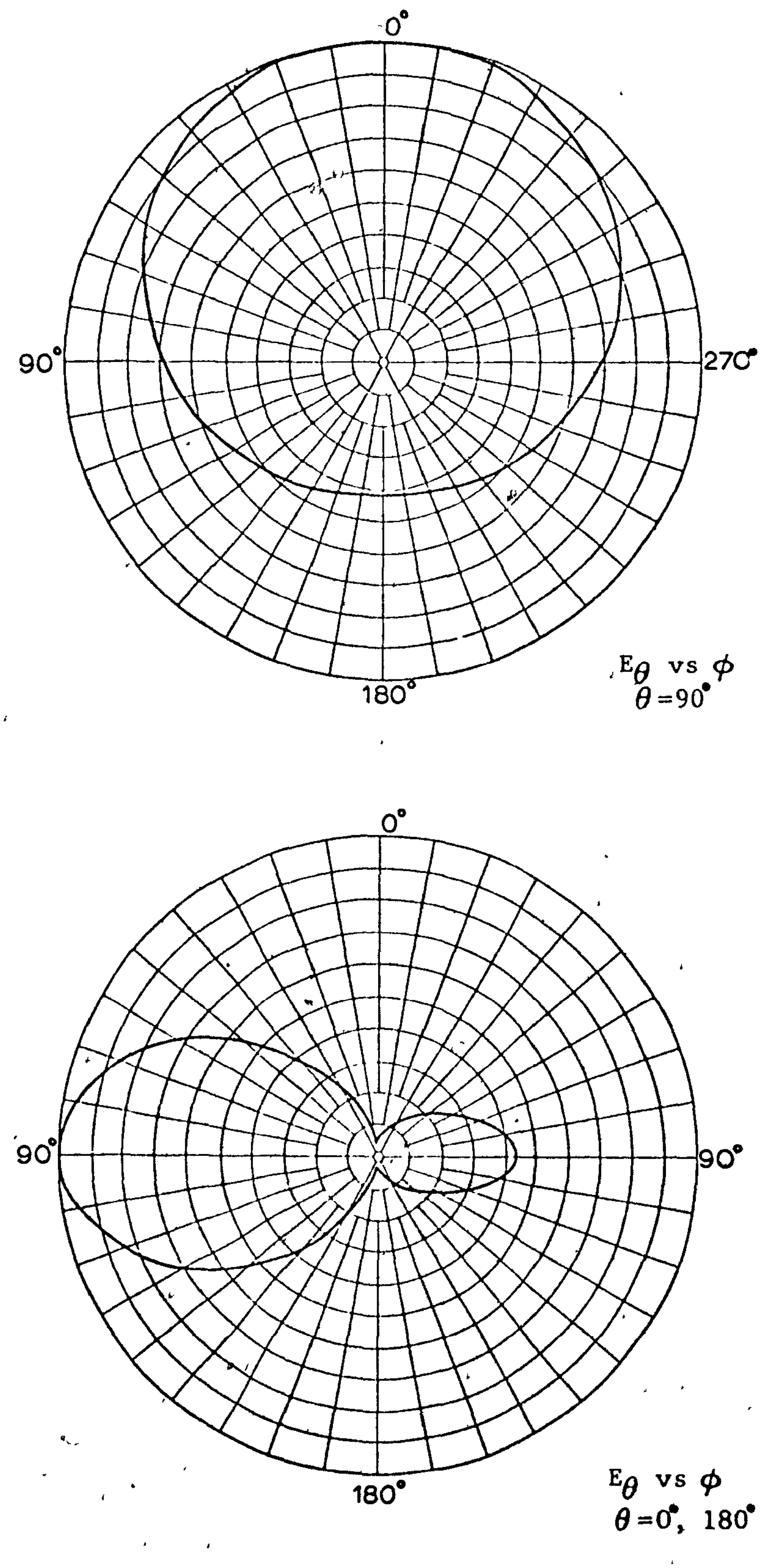

FIGURE 3.15. REFERENCE RADIATION PATTERNS OF FOLDED DIPOLE AND MAST.

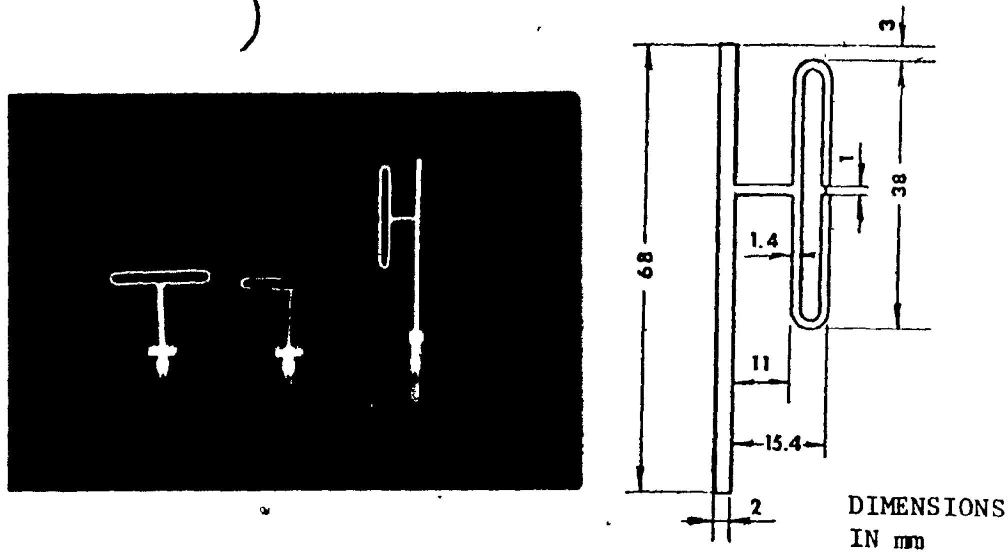

FIGURE 3.16. MODELS OF FOLDED DIPOLE ANTENNAS.

3.2.2 Design of Absorber Layout in Anechoic Chamber

In preparing the chamber for S-band measurements a number of major technical problems arose:

(a) The anechoic chamber was intended primarily for near field and quasi-near field measurements in geometrical arrangements where energy likely to cause perturbing reflections would impinge on the absorber at low angles of incidence which would result in good absorption. Inherently, the structure of the chamber assures this condition for the BP-24 absorber lining the walls. This desirable geometry does not apply to the floor absorber when test antenna and receiving probes are mounted close to the floor. The problem is only diminished for antennas mounted on large ground planes or for directional antennas where little energy is radiated towards the floor.

(b) The BP-24 microwave absorber is constructed of sizeable wedges, as shown in Figure 3.6. The absorption values of Figure 3.1 apply only to measurements where the reflection from the individual surfaces and the absorber can be considered to be diffuse rather than specular. This condition is assured for measurements close to the test antenna near the center of the room but not for antennas mounted near the outer walls.

(c) Anechoic chambers are commonly designed with the wall behind the test antenna lined with absorber of the highest absorption possible [50], since this is the region of illumination by the main lobe of the flooding antenna. Although the chamber here was intended generally for tests of less directional antennas and an optimum absorber had to be selected for the entire chamber subject to the limitation of funds available, additional improvements had to be made for the antennas tested at S-band, both for the region behind the test antenna and that behind the transmitting antenna.

(d) The problems discussed above are minimized when a small antenna of single polarization is being tested and its excursion around an axis is minimal as for example in Figure 3.17(a). However, to obtain the usual principal plane patterns, the antenna had to be mounted and rotated

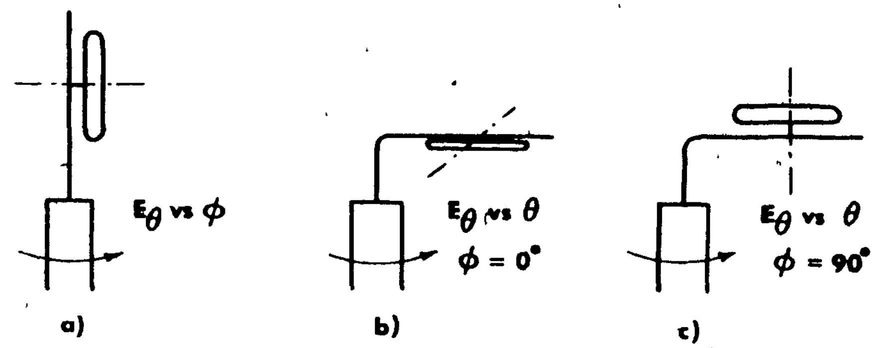

FIGURE 3.17. ANTENNA MOUNTING POSITIONS.

off-axis as shown in Figure 3.17(b) and (c). This tended to accentuate the problems discussed above, and tests had to be carried out and corrective measures applied for both polarizations.

The pace of the antenna development program did not permit extensive phase/amplitude probing of the antenna regions. Nor was appropriate instrumentation available at that time. Resort had to be made, rather, to a sequence of tests with antennas such as a disc-mounted monopole and folded dipole, having generally known and symmetrical patterns. When the measured patterns were suspect or were unsymmetrical, changes in absorber layout would be made until repeatable and symmetrical patterns were obtained.

A typical, rather haphazard initial absorber layout is shown in Figure 3.18. It should be observed that with the large blocks of absorber, freedom of layout design is limited and changes are awkward to make. Placing the probe antenna either on the inner or outer arch gave some ability to identify the effect of the floor absorber placement on the field being measured but isolation and control of different effects due to absorber positioning and orientation was still difficult to achieve.

Figure 3.18 shows some corrective measures tried. Note the absorber below the antenna on the rotator. This was initially necessary to prevent reflection and diffraction effects from an existing plywood fixture. Subsequently, for antennas of the type shown, a circular patch of absorber was used under the antenna and the phenolic support was encased in a cylinder of absorber to suppress any radiation from the feedline. Also shown is a strip of absorber backing for the dipole probe. This was found necessary for two reasons:

- first, to minimize the scattered field from the arch support and
- second, to overcome residual wall reflection problems discussed under (b) and (c) above.

With the flanged waveguide probe on the outer arch, this was not necessary because of its high front-to-back ratio.

After various and lengthy exploratory measurements, a more regular and successful arrangement was derived. This is shown in Figure 3.19. The absorber is placed in concentric rings and

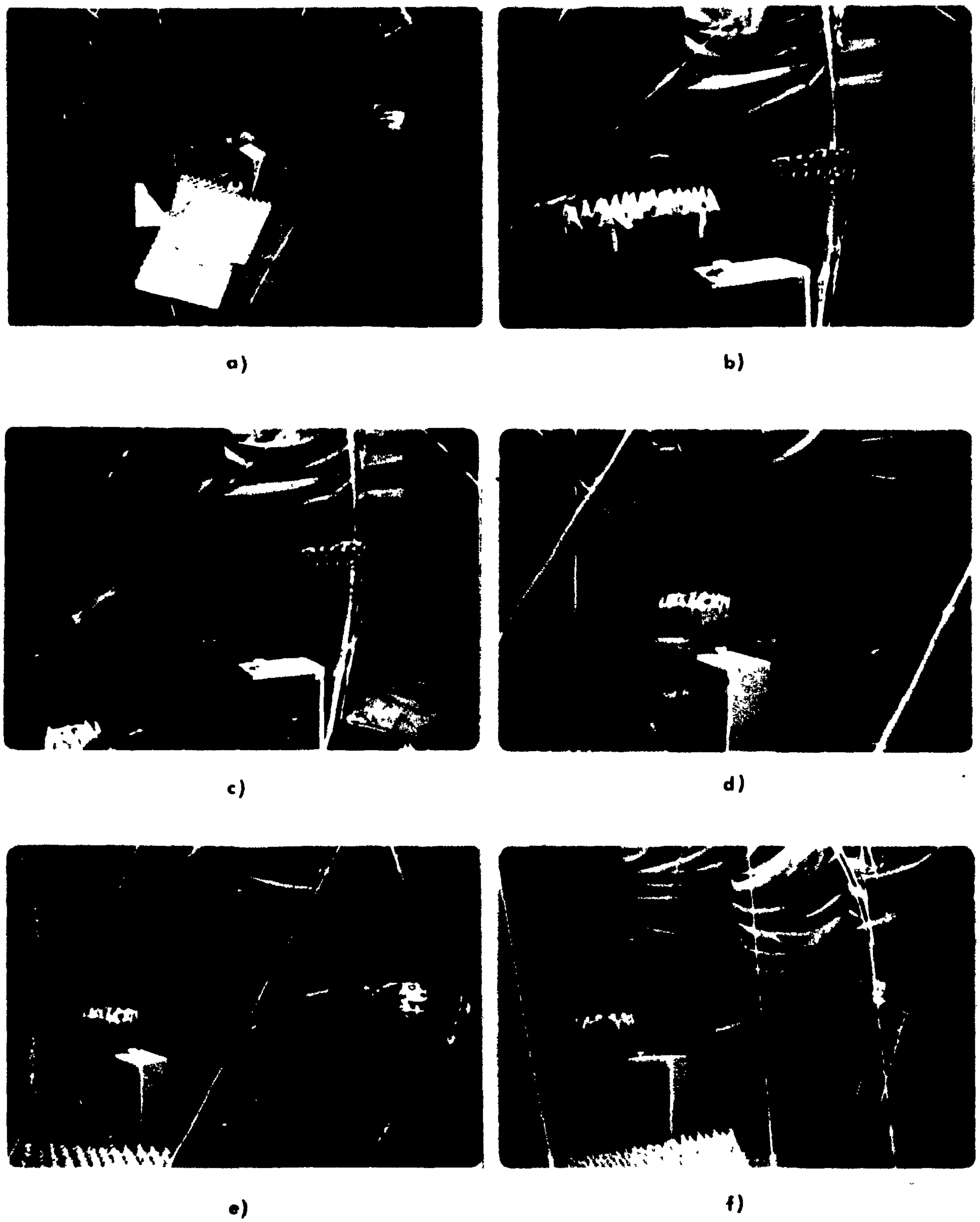

a) b) c) d) e) f)

FIGURE 3.18. INITIAL ARRANGEMENT OF ABSORBER AND TEST ANTENNAS.

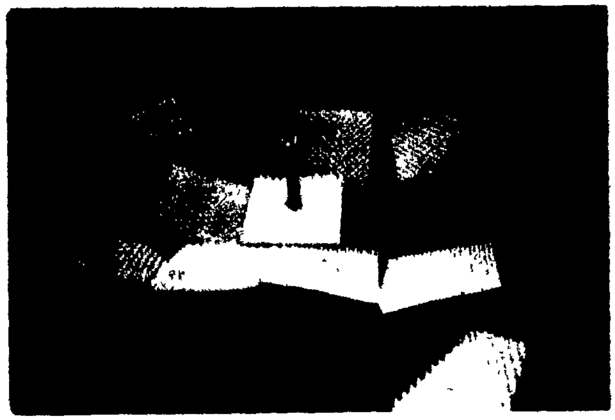

FIGURE 3.19. FINAL ABSORBER ARRANGEMENT ON FLOOR.

mounted at an angle to improve the angle of incidence. The high frequency CV-4 absorber covers all gaps and follows the profile established. In addition, along the line between the two antennas it is further elevated, but not so high as to cause diffraction problems from the absorber edge. It was also found necessary to place absorber on the wall facing the flanged probe. Thus in seeking a solution, essentially to problems discussed under (b) and (c) above, a natural dish-shaped configuration was derived and used for all the tests reported in this thesis. These are shown in the sections which follow. Results of a special comparative test, carried out on an outdoor range, are shown in Section 3.4 and these corroborate the reliability of the measurements in the chamber.

3.2.3 Method of Measurement and Results

In the case of antenna models (used as receivers), the attached detector can form a substantial part of the surface on which RF currents can flow and hence produce pattern distributions not representative of the current distribution on the actual antenna being modelled. In an attempt to minimize this problem, the antenna was used as a transmitter and the receiver was either a dipole plus detector mounted on the inner arch or a flanged waveguide and bolometer detector mounted on the outer arch. For these measurements the Hewlett Packard 415E SWR amplifier was used at a center frequency of 400 Hz. The Polarad Model SSS signal source was used instead of the AIL 125C because of its superior stability at 3 GHz. The remainder of the instrumentation was as shown in Figure 3.10 with the antenna mounting positions as illustrated in Figure 3.17.

Patterns of E_θ vs ϕ for $\theta = 90°$ and of E_θ vs θ for $\phi = 0°$ are shown in Figure 3.20. Shown also are the reference patterns provided by the manufacturer. There is excellent agreement in the E_θ vs ϕ patterns. The main lobe agreement in the E_θ vs θ pattern is good but agreement in the back lobe is poor. This was believed to be due to the lack of symmetry in the reflecting mast. Such an explanation, although plausible, does not remove all doubts about the validity of the model used. However, the construction of models with a symmetrical mast is rather awkward because of the difficulty in masking the feedline and detector. An opportunity thus arose to apply the wire-grid modelling process to this antenna in an attempt to substantiate the discrepancy. A successful

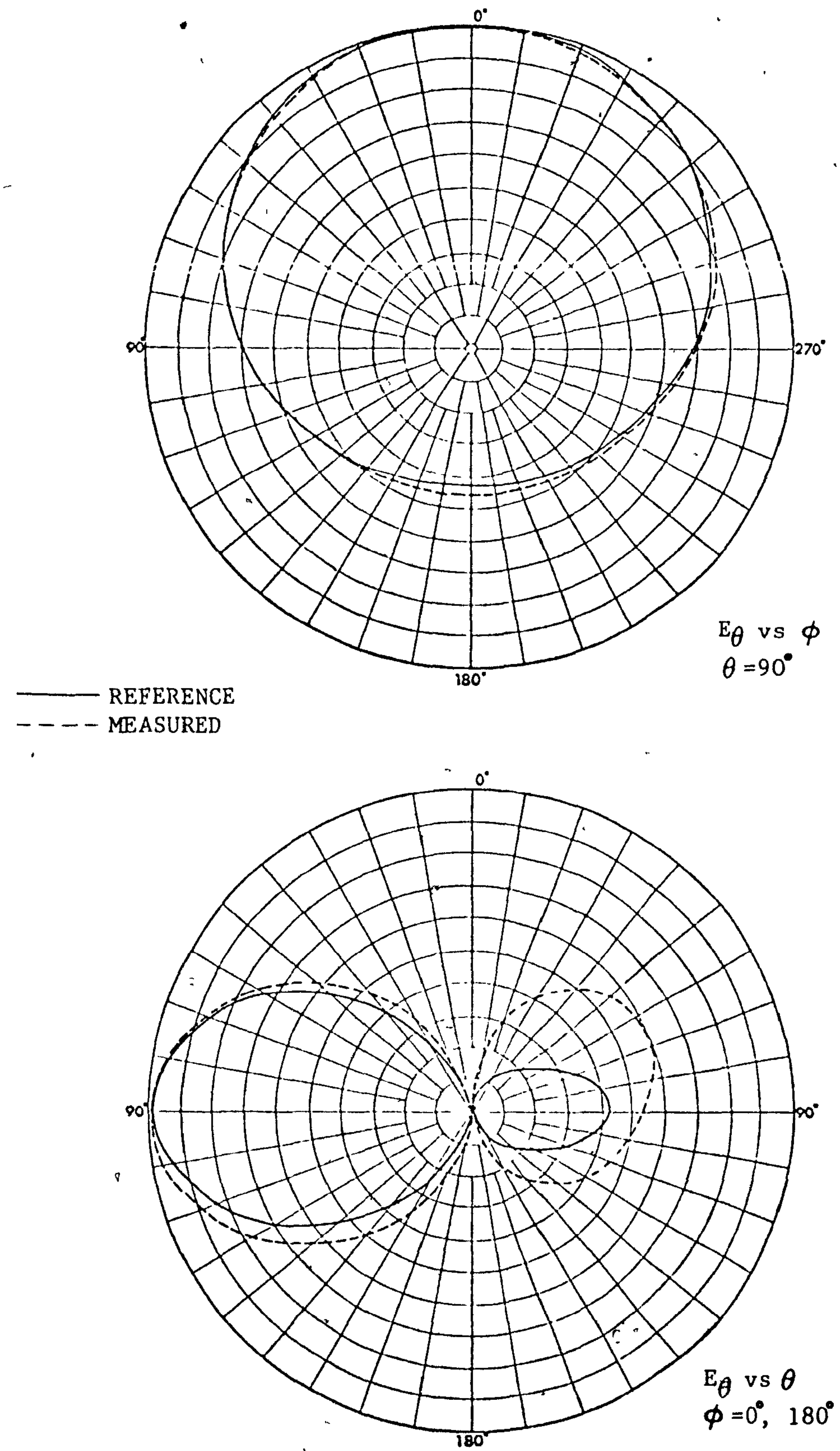

FIGURE 3.20. MEASURED AND REFERENCE PATTERNS FOLDED DIPOLE AND MAST.

substantiation was obtained and a few useful guidelines developed in the process. These remain to be presented in Chapter IV. It will be seen that this combined approach led to a reduced amount of time to achieve complete confidence in the antenna model.

3.3 Ground Rod Antenna

The second antenna developed for the airborne field measuring facility, as mentioned in Section 3.2 was a sleeve-monopole. The sleeve monopole chosen was a portion of a commercially available ground rod antenna, Sinclair Model 201. This antenna can be operated over the frequency range 146-174 MHz. As in the case of the folded dipole, a 1/20-th scale model of the antenna was constructed and tested. Another experimental problem was encountered, when it was found that the azimuth patterns were in agreement with reference data but the elevation plane patterns were not. Although in this case the disagreement was not fully resolved, once again the combination of experimental and numerical techniques has helped to establish that the measurement conditions for the reference and actual patterns are not directly comparable.

3.3.1 Modelling of the Antenna

The manufacturer's description of the antenna is shown in Figure 3.21. The antenna is normally mounted on a mast which

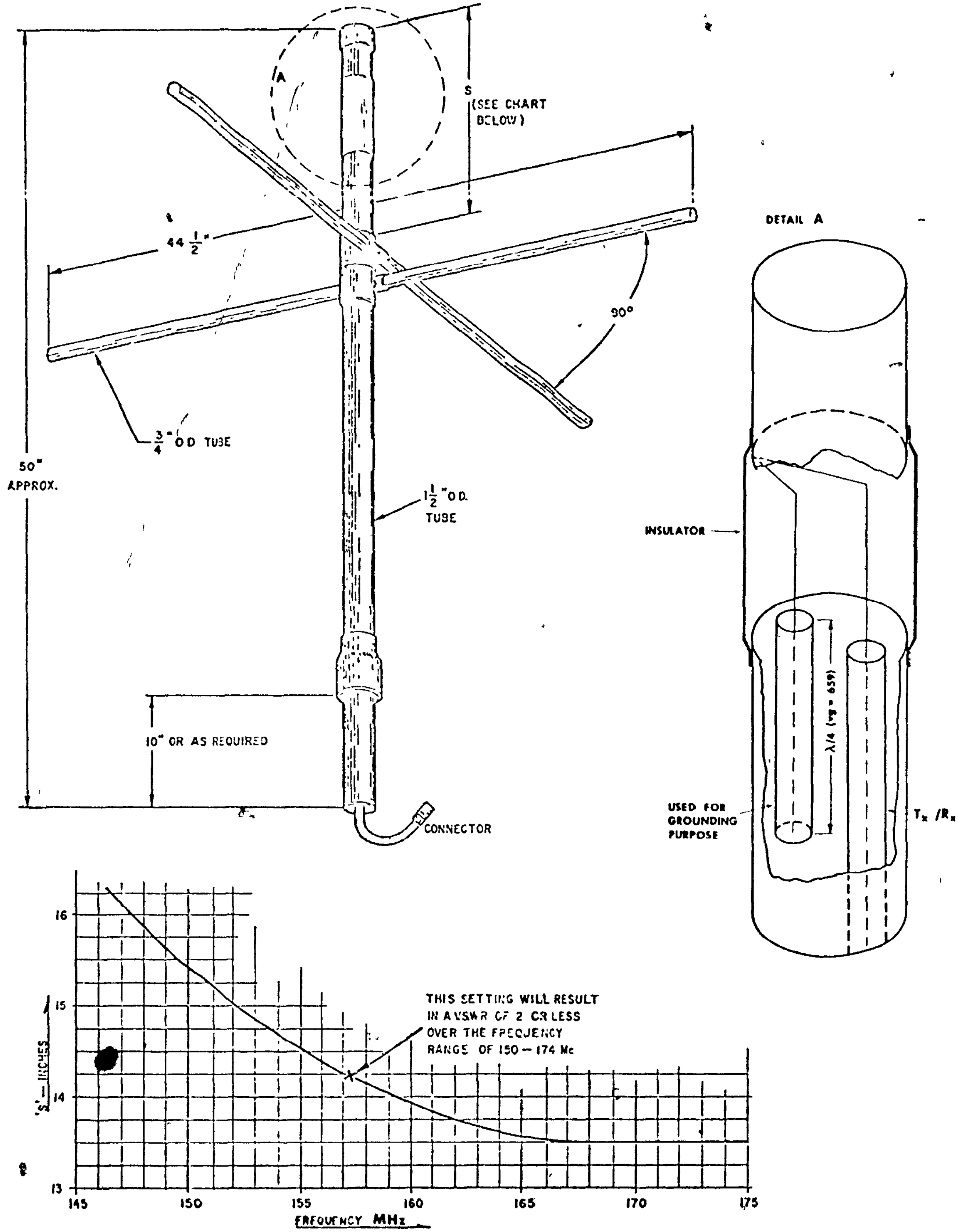

FIGURE 3.21. GROUND ROD ANTENNA.

fits into the coupling shown. The height of the monopole portion is adjusted to vary the VSWR as indicated in the inset. A schematic of the electrical connection is also shown. Advice on modelling was sought from the manufacturers, especially since the exact feed-point geometry was not specified and radiation patterns were not provided. For pattern information, reference was made to the paper of Tilston and Secord [56]. Representative vertical and horizontal plane patterns are shown in Figure 3.22.

The model antenna was constructed from .085" diameter rigid co-axial cable. The center conductor connected directly to the top section. All other dimensions were scaled from a full-scale model of the antenna as shown in Figure 3.23(a). Several

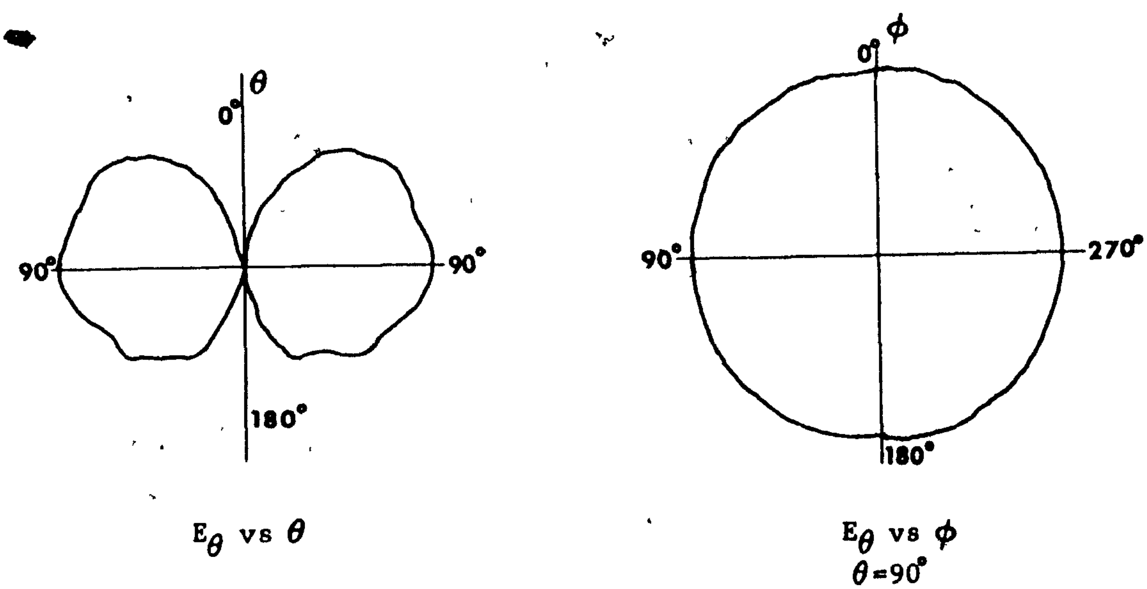

FIGURE 3.22. REFERENCE PATTERNS OF GROUND ROD ANTENNA.

(a)

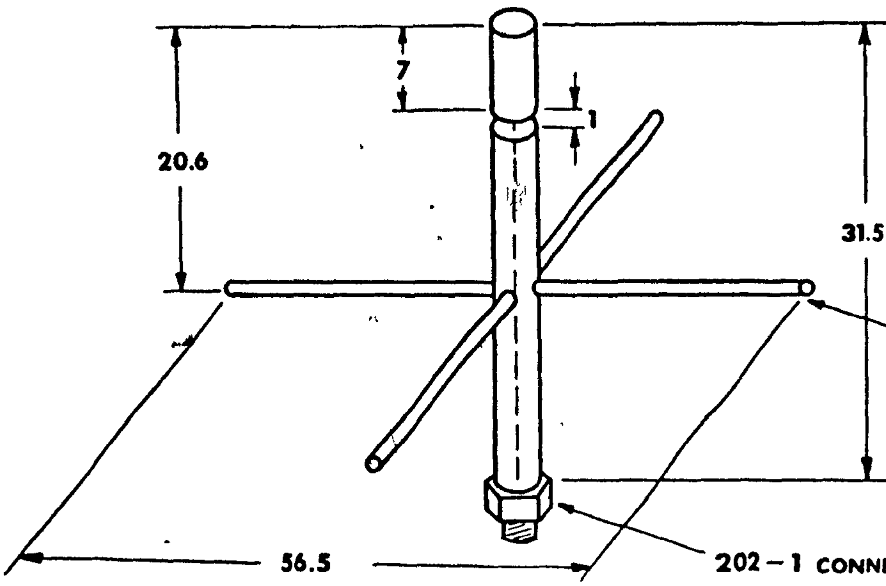

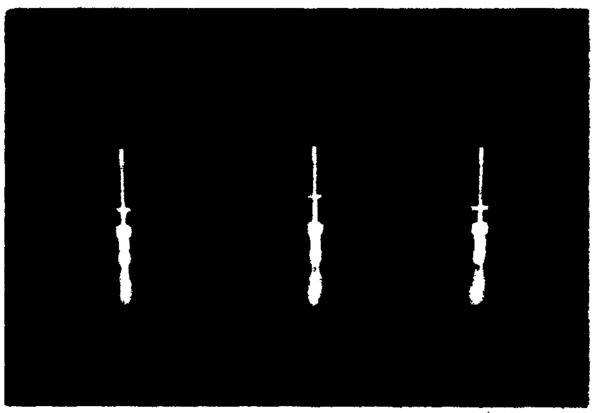

(b) Regular Antenna Models.

(c) Antenna with Choke and Feed at Rod Joint.

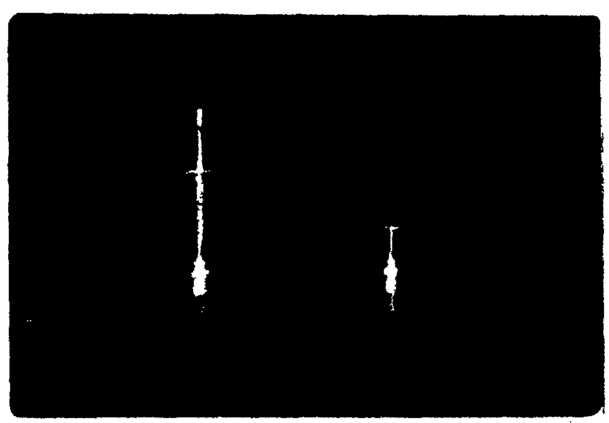

FIGURE 3.23 (a-b-c). MODEL GROUND ROD ANTENNAS.

other models were built with different monopole heights, ground rod lengths and overall dimensions. These are shown in the photographs of Figure 3.23. Although only the model of the monopole itself was required for the helicopter development program, the other models were made because of the difficulties encountered in the comparison of measured and reference patterns.

3.3.2 Method of Measurement and Results

The method of measurement was identical to that used for the folded dipole antenna. The antennas were mounted in the positions shown in Figure 3.24. Particular care was taken to cover the feed cable portions with absorber.

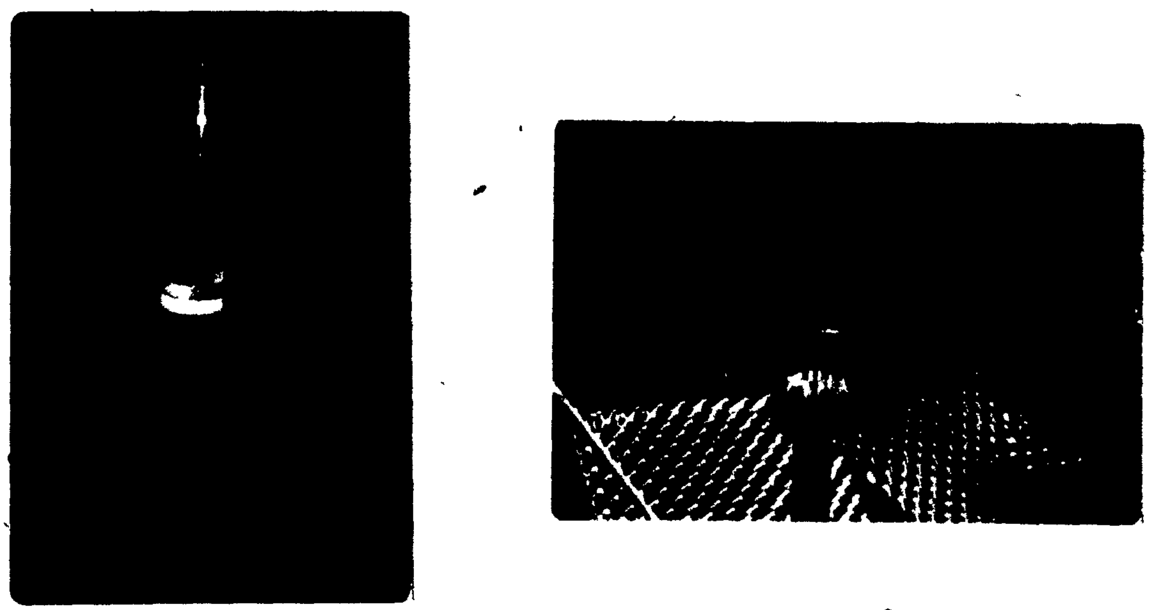

a. E_θ vs ϕ b. E_θ vs θ

FIGURE 3.24. GROUND ROD ANTENNA MOUNTING POSITIONS.

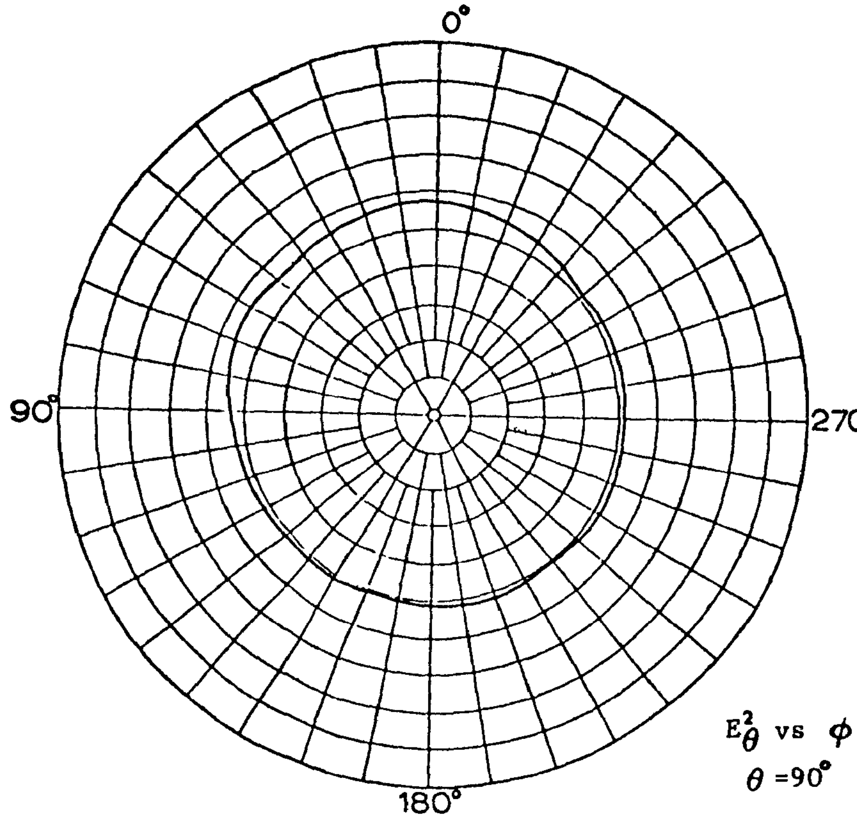

RELATIVE VALUES

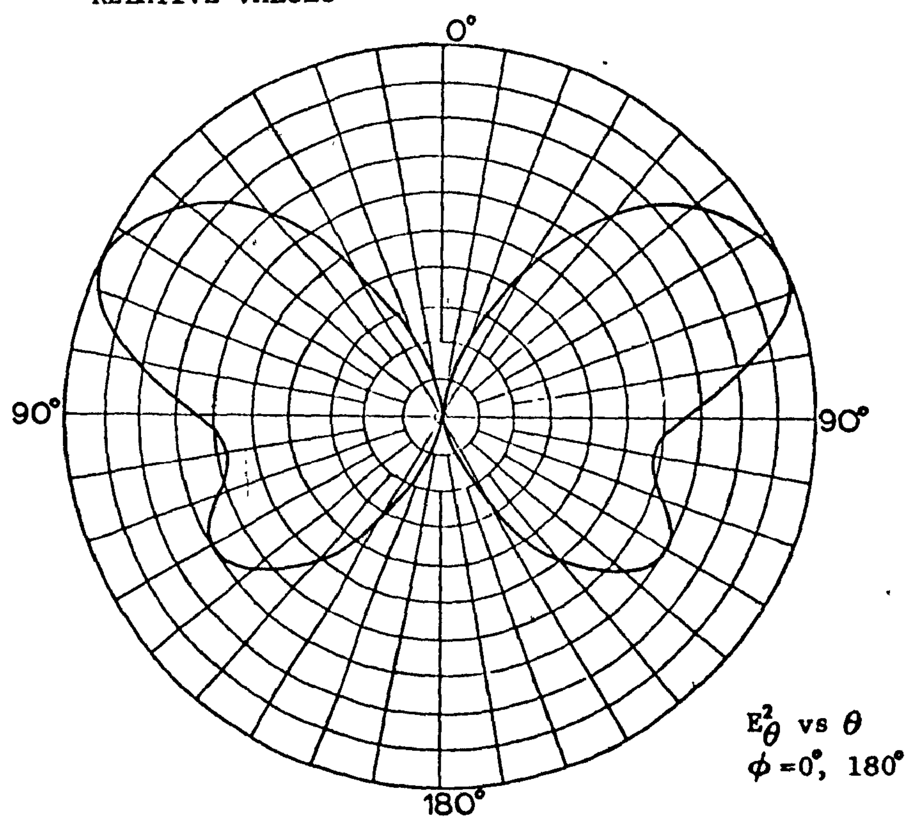

FIGURE 3.25. MEASURED RADIATION PATTERNS - GROUND ROD ANTENNAS.

Patterns of E_θ^2 vs ϕ and E_θ^2 vs θ are shown in Figure 3.25. The patterns of E_θ^2 vs θ for other azimuth angles are similar. The azimuth plane pattern is omnidirectional as expected. The vertical plane pattern, however, does not show the filling in on the horizontal axis of the "typical" reference pattern of Figure 3.22, although the width of the nulls and the areas of the lobes are similar. Also shown are patterns for an antenna fed at the ground plane level. The other antennas shown in Figure 3.23 were built in an attempt to investigate this discrepancy, but none of the other antennas tested, with longer and shorter rods and choke on the lower portion of the co-axial cable, showed the characteristics in the vertical plane at $\theta = 90°$ which were reported by Tilston and Secord.

This type of deviation was of little importance to the manufacturer. Its impact on the helicopter antenna developmental program was also of small significance since the sleeve monopole was to be mounted on a larger continuous ground plane. Also since the reference measurements were made five years previous, under unknown conditions and at a relatively difficult frequency for pattern measurements, it was difficult to establish how precise the reference patterns were.

Recourse was made once more to a wire grid modelling procedure. The results to be presented in Chapter IV, support the measurements carried out here, indicating that the reference measurements were made under different conditions. In the process of this analysis some additional useful guidelines for wire-grid modelling were generated.

3.4 Monopole on a Helicopter

The last two sections dealt with problems of modelling of antennas prior to their installation on models of vehicles. This section describes the measurements of the radiation pattern of a monopole antenna on a helicopter at a lower frequency, 675 MHz. The measurements were carried out for various rotor positions, so that the effect of rotor modulation could be determined.

During the feasibility study phase for the development of a helicopter field strength measuring system, exploratory measurements were made by Pavlasek, Kubina and Wolde-Ghiorgis [57] at frequencies in the 675-700 MHz range on a 1/20-th scale model of the tail section of a Bell 47G-2A helicopter. Subsequently the frequency of operation and the helicopter model were altered. The development of the antenna system for the higher frequency is described elsewhere [4] and the modelling problems for the individual antennas have been discussed. In operation the two antennas are positioned sequentialy in time over a mesh screen as shown in Figure 3.26. During this experimental program, measurements were made at 675 MHz with the monopole, specifically to have some data for comparison with planned wire-grid modelling calculations.

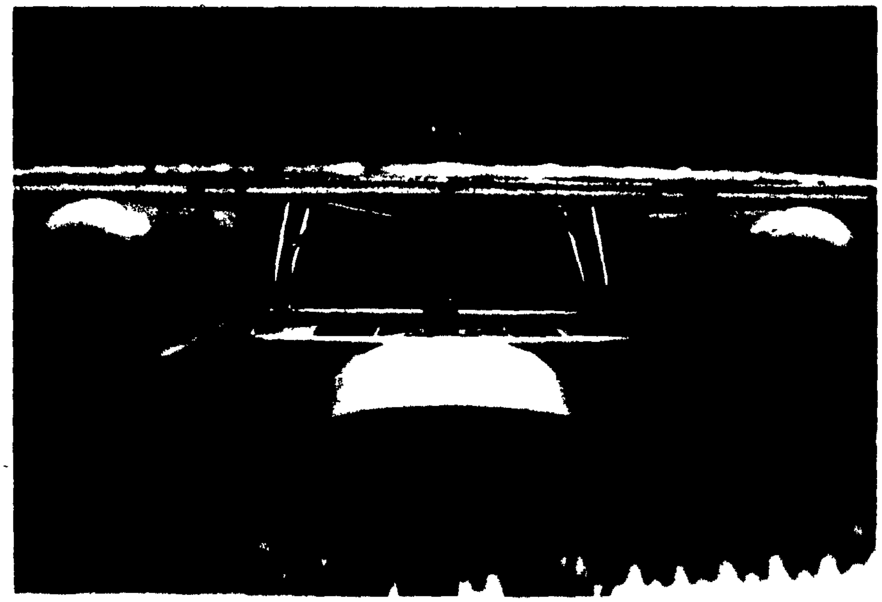

FIGURE 3.26. TEST ANTENNAS AND SCREEN ON BELL 47G-4A HELICOPTER.

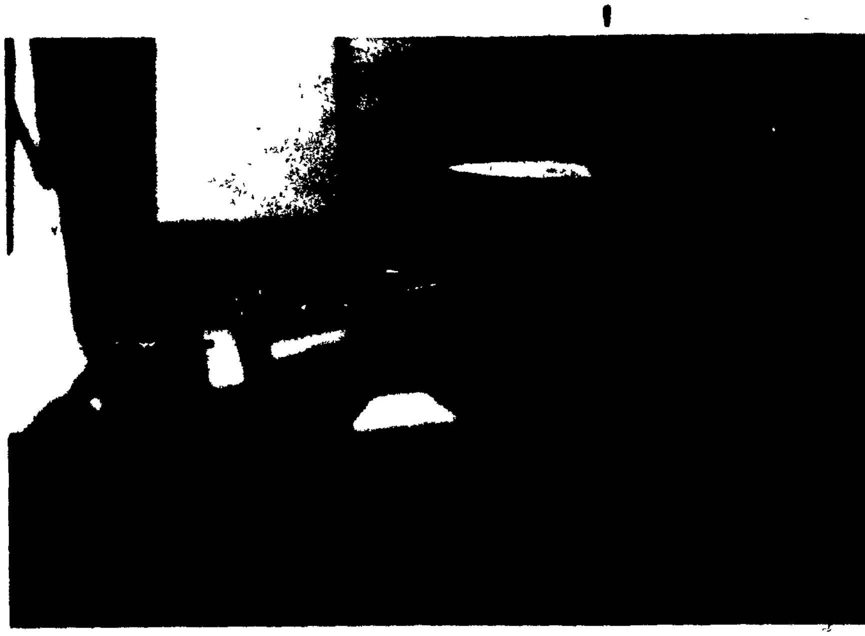

FIGURE 3.27. TEST MODEL, GROUND SCREEN AND MONOPOLE.

3.4.1 Description of the Model

The 1/20-th scale model of the Bell 47G-4A helicopter was built at Canadair Ltd. of brass rods and copper and brass sheet and was painted with two coats of conducting silver paint. The model was mounted in an inverted position as shown in Figure 3.27. The figure also shows the ground screen for the 3 GHz measurements. For the measurements at 675 MHz, the ground screen was removed and the monopole length extended to .268 λ . The pneumatic, rubber landing pads of the actual aircraft were modelled in mahogany. The screen shown is designed to be tightened against the pads by spring tension.

Attention is also directed to the gold-coloured crystal detector and the black resistance cable leading into the support tube. In an open structure of this type, the location of the detector and the RF lead tends to influence the patterns measured.

3.4.2 Method of Measurement and Results

At this frequency, the AIL 125 Signal Source and a dipole were used to irradiate the model. The antenna on the helicopter was used in the receiving mode. A crystal detector was connected to an HP 415E VSWR amplifier through a suitably matched high resistance cable and co-axial rotary joint at the base of the support tube. Figure 3.27 shows some of this detail and the remainder of the equipment was as shown in Figure 3.10.

The helicopter was mounted so that the monopole antenna axis was in line with the rotator axis to minimize the displacement effect of the model. The horizontal axis of the helicopter was aligned visually with the transmitting antenna. The rotor blades were locked in the following positions: in line with the fuselage, at right angles and at 45°, while the conical pattern cuts were made. The angles used were 70° and 80° since at the time of measurement these were the angles of practical interest for the field strength measuring system mentioned above.

The patterns are shown in Figures 3.28 and 3.29. Major lobes occur in those directions where substantial portions of the helicopter provide a counterpoise. The rotor is seen to produce a slight shift as well as change in the amplitude of the lobes. Thus some change in the current distribution is to be anticipated in the numerical analysis.

These measurements were taken with a shorter RF lead to the detector than shown in Figure 3.27 since the location of the detector in the open helicopter frame structure was found to have an effect on the radiation pattern especially at $\theta = 70°$. The patterns shown in Figures 3.28 and 3.29 represent the patterns of the helicopter but with some residual influence due to the detector.

Other wire-grid modelling results [45] on a portion of a Bell 47G-2A tail structure had shown the presence of four lobes in the E_θ pattern at this frequency. It is seen that in Figure 3.28 the front lobe is suppressed. In order to further isolate the effect of the detector inside the model, the helicopter antenna was

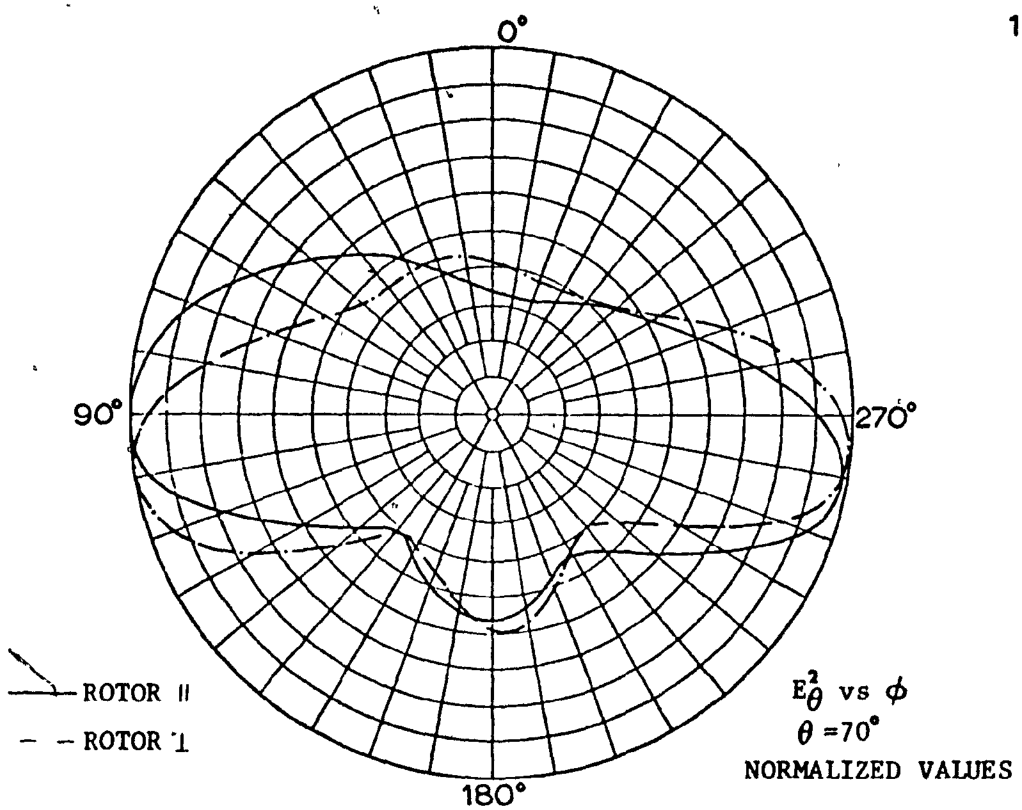

FIGURE 3.28

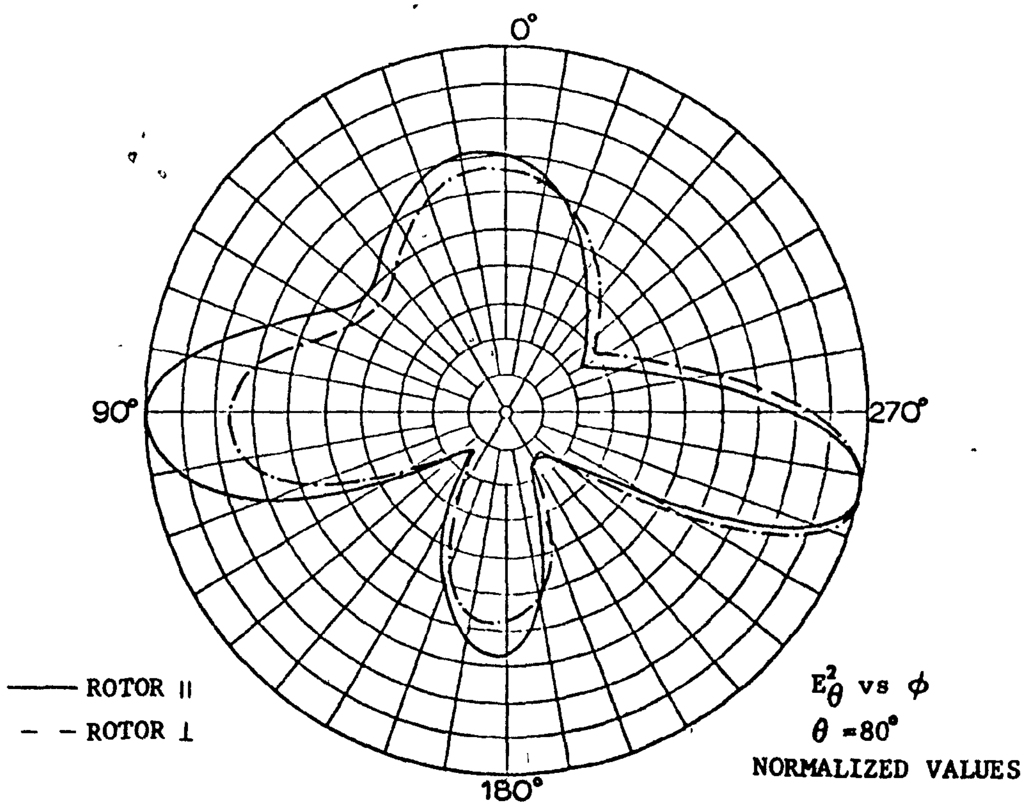

FIGURE 3.29

used as a transmitter and microwave absorber was used around the support tube. Figure 3.30 a,b,c shows some of the results with and without the absorber and with a dummy detector (unconnected) within the helicopter. It can be seen that the absorber is required and that an active detector produces differences in the front and back lobe. The pattern with the detector removed is shown in Figure 3.30. The four lobes are distinctly shown.

The above results are an indication of two problems: a measurements difficulty per se, in the case of open structures which do not provide RF shielding, and a problem in obtaining reliable data for wire grid modelling verification for these structures. However, once an acceptable wire grid model is approached, it aids in the critical analysis of experimental results and dictates a comparison of alternate measurement methods as indicated. Full advantage of this interaction was not obtained in this work because the measurements had to be terminated prior to the completion of the modelling but the results clearly show the value of this interaction.

Permission was obtained to try to repeat these measurements on Canadair's outdoor range. Unfortunately, the only day available turned out to be extremely windy. Although the patterns taken seemed to indicate the presence of four major lobes with less sharp nulls, the patterns were too noisy for detailed conclusion to be made. Thus corroboration at the low frequency is not as good as at high frequencies.

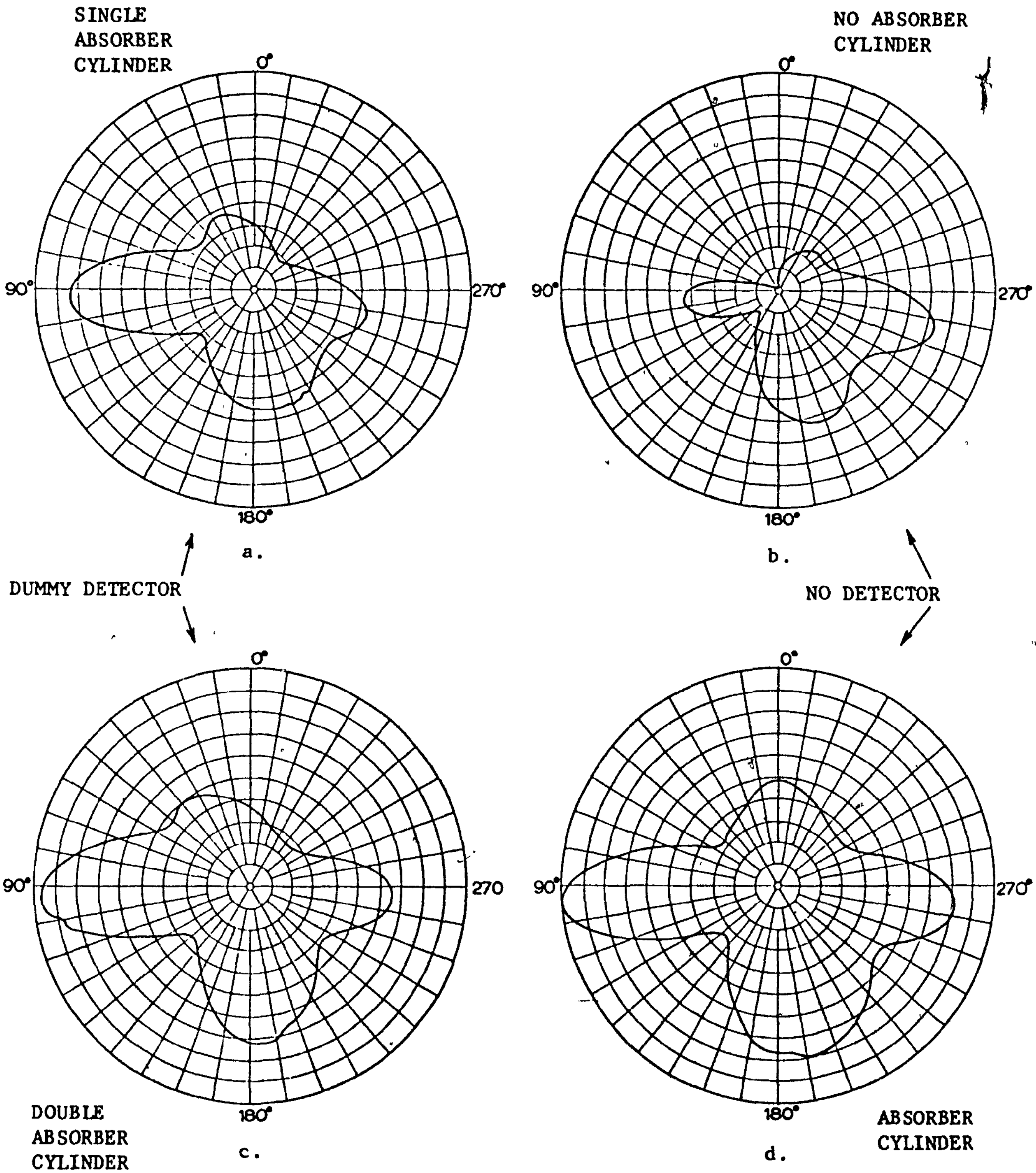

FIGURE 3.30. MEASUREMENTS WITH ANTENNA AS TRANSMITTER

(E_θ^2 vs ϕ , $\theta = 70^\circ$).

3.5 Other Measurements

Amplitude and phase probing of the anechoic chamber remain to be completed. However, results of comparative pattern and "free-space VSWR" measurements carried out at L and S-band are presented in this section as well as additional rotor modulation data.

3.5.1 Pattern Comparison and Free-Space VSWR

Successful measurements at 3 GHz with this facility have already been reported by Wolde-Ghiorgis [45] for a variety of antennas. It was also possible to make a direct comparison with helicopter measurements made at Canadair. During the development of the VHF antenna system for the helicopter [4] many patterns were measured at S-band for various ground screen configurations at several elevation angles. Since the complete three-dimensional patterns required for the determination of isotropic reference level could not be made, these were carried out at Canadair where a 600 ft. outdoor range with four-axis mount and instrumentation is available. Comparable patterns are shown in Figure 3.31 and an illustration of the model on the support tower in Figure 3.32. The agreement in detail can be seen to be very close. This corroboration was found to be quite useful during the initial comparison with results from numerical wire-grid modelling.

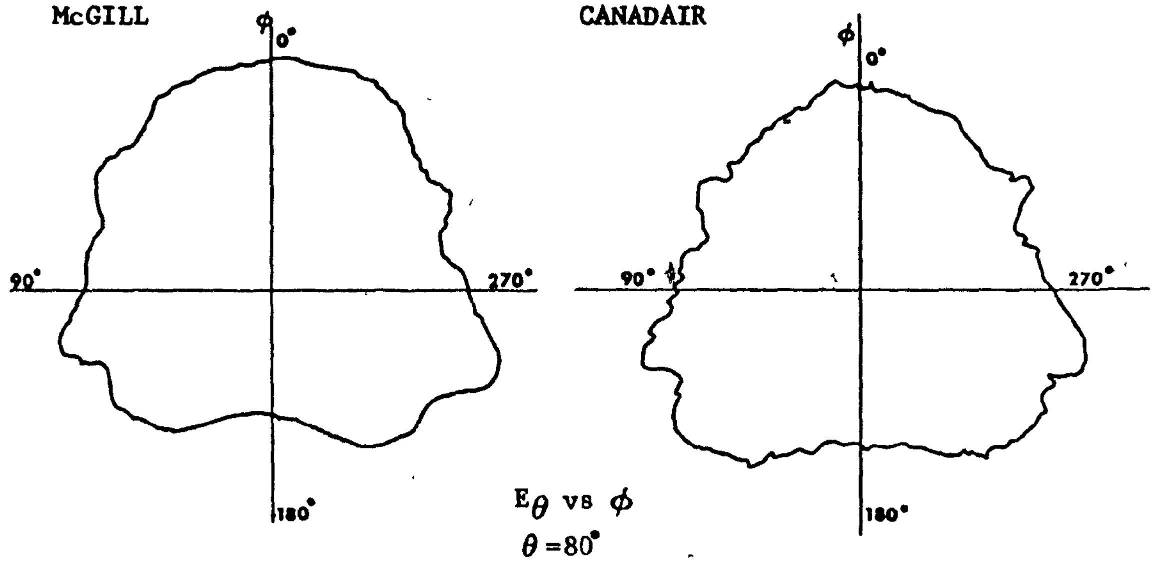

FIGURE 3.31.

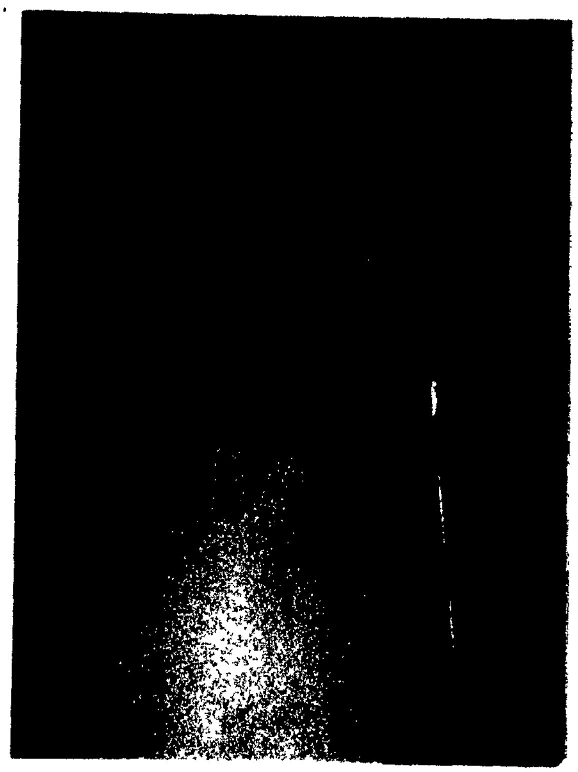

FIGURE 3.32.

An initial room VSWR measurement was carried out at 900 MHz with a disc-mounted monopole in the center of the room. A probe was supported on a low-density styrofoam frame which could slide on fine nylon string guide lines. Figure 3.33 shows the probe arrangement and the results of a typical scan. It can be seen that there is no evidence of a standing wave pattern in this region. These "pattern comparison" and "free-space VSWR" evaluation techniques parallel the evaluation of M.I.T.'s anechoic chamber described by Frediani [58].

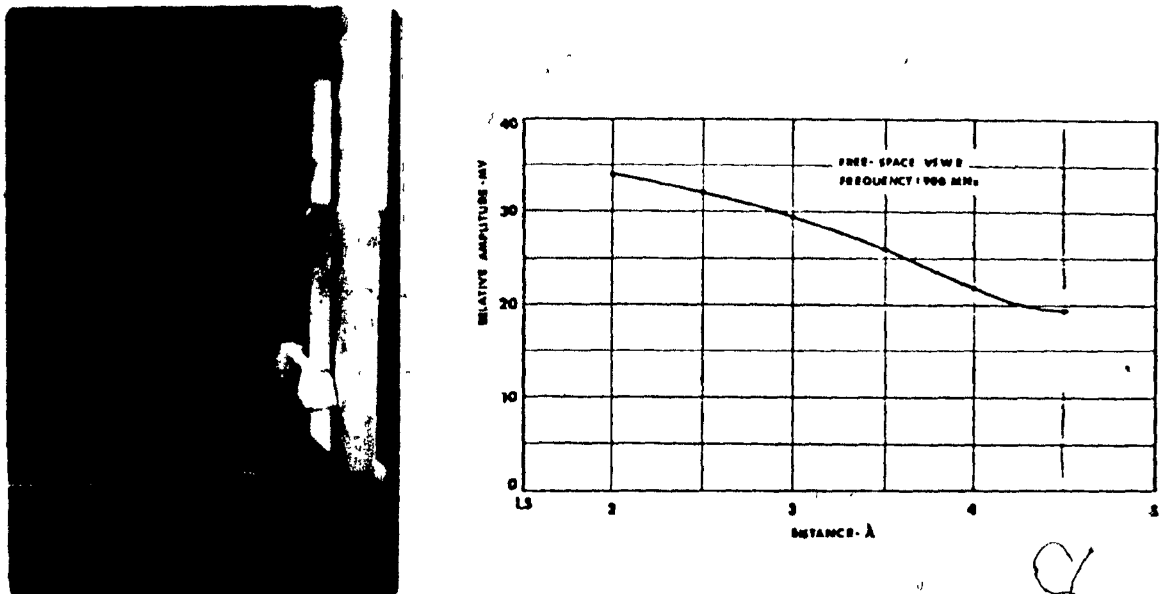

FIGURE 3.33. FREE-SPACE VSWR MEASUREMENT, 900 MHz.

3.5.2 Rotor Modulation Measurements

One of the productive experimental rotor modulation studies carried out at the facility was one which resulted in the airborne VHF field strength measuring system shown in Figure 3.26. Some highlights are presented here.

During an exploratory measurement program on a tail section of a similar helicopter type, a Bell 47G-2A, means of rotor modulation control were studied at 600-700 MHz. Measurements were made at several frequencies, with and without the rotor blades and with screening discs of several diameters. In some of these measurements the rotor blades were rotated at a relatively faster speed (about 12 r.p.m.) while the helicopter was rotated more slowly (0.8 r.p.m.). The representative measurements shown in Figure 3.34 demonstrate the usefulness of this type of data presentation when the model can be built to allow driving the blades. This program demonstrated that in this frequency range

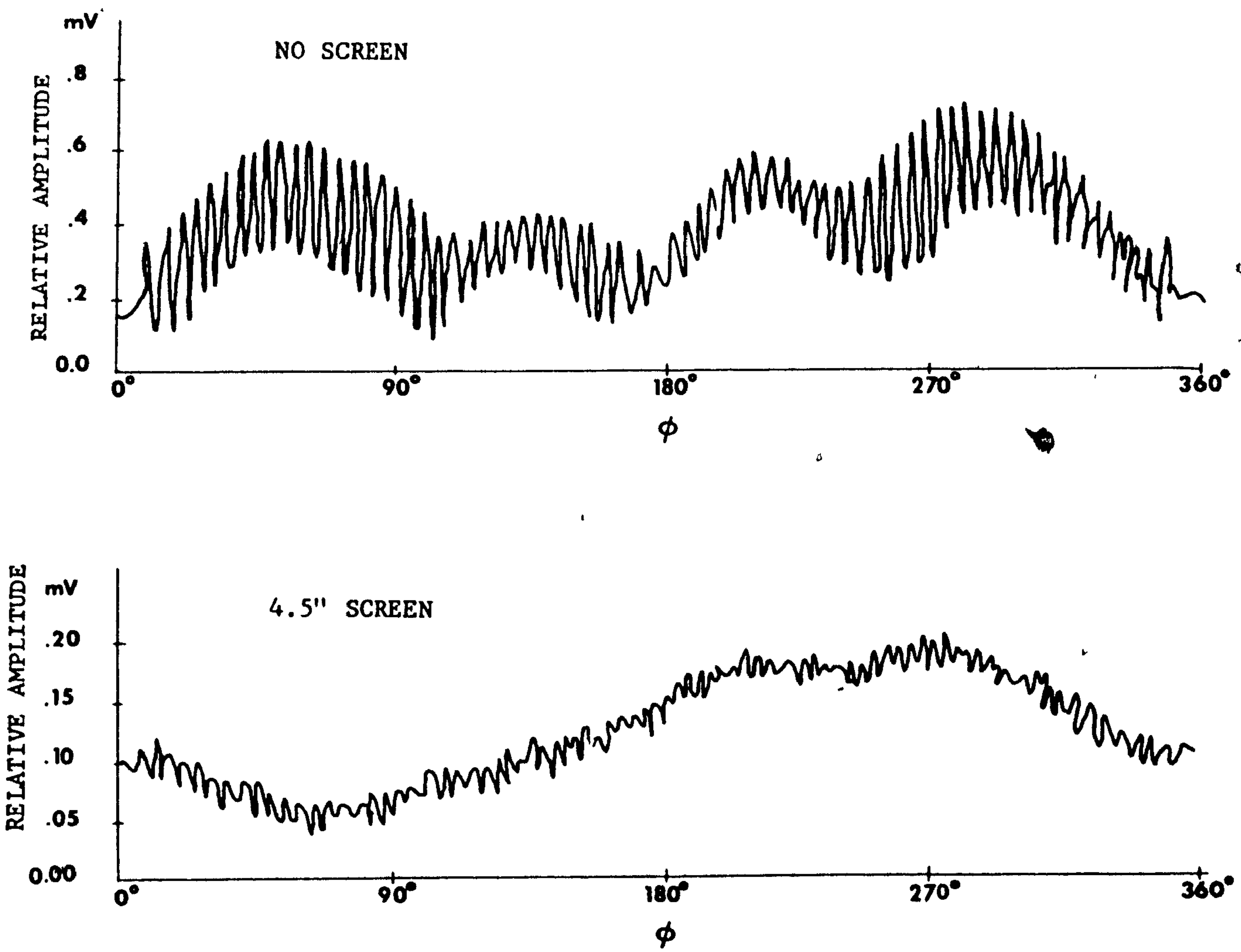

FIGURE 3.34. ROTOR MODULATION, TAIL SECTION, E_ϕ, $f = 675$ MHz, $\theta = 45^\circ$

within which the airframe can exhibit longitudinal resonance, two factors offer the possibility of some control:

(i) The frequency dependence of the effect, especially a minimization at antiresonant frequencies for the effective length of the helicopter/antenna paths.

(ii) The shielding effect of screens of substantial size which at the same time produce a more uniform pattern distribution.

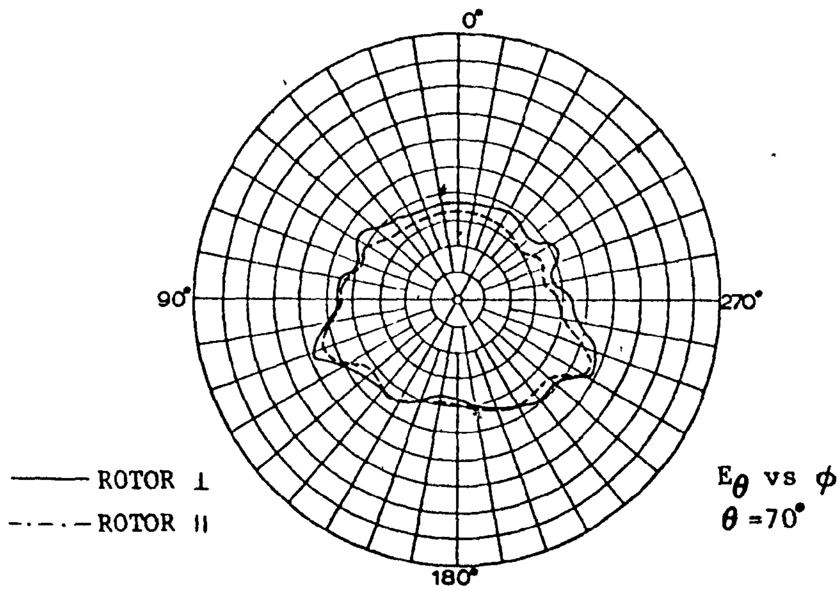

FIGURE 3.35. ROTOR MODULATION WITH MONOPOLE AND LARGE SCREEN, f = 3 GHz.

The second effect was exploited in the development of the airborne VHF field strength measuring system to produce an acceptable level of pattern uniformity and rotor modulation control. Typical results, in Figure 3.35 show a pattern relatively uniform, especially near $\phi = 90°$ and $270°$ which are operationally useful angles, and with small perturbations due to rotor modulation.

The next chapter is devoted to the numerical techniques which might be used to predict these effects and the guidelines for their application and future development.

CHAPTER IV

APPLICATION OF NUMERICAL TECHNIQUES

4.0 Introduction

The measurements of Chapter III leave unresolved the discrepancy between measured and reference patterns for the folded dipole and ground rod antenna. This problem and the measurements on the helicopter-mounted monopole invite the application of the wire-grid modelling technique. A cursory examination of the literature might suggest that these applications are a straight forward extension of the technique; but it will be evident that the number of unknowns in the state of the art increases with the complexity of the application.

The theory is summarized here in a manner similar to that used by Wolde-Ghiorgis [45] and Thiele [80]. The essential elements and their inter-relations are shown in the chart of Figure 4.1, previously used by Kubina, Pavlasek and Wolde-Ghiorgis [82]. The central, numerical analysis portion is discussed extensively in the literature and some pertinent results are noted later. The right hand portion indicates the assumptions usually made for the source and the current distribution on the individual segments. In this work both a delta-gap generator and a magnetic frill source have been used equally well. The pulse current distribution has been used except for the initial work on the monopole. Emphasis has been placed on the left hand portion

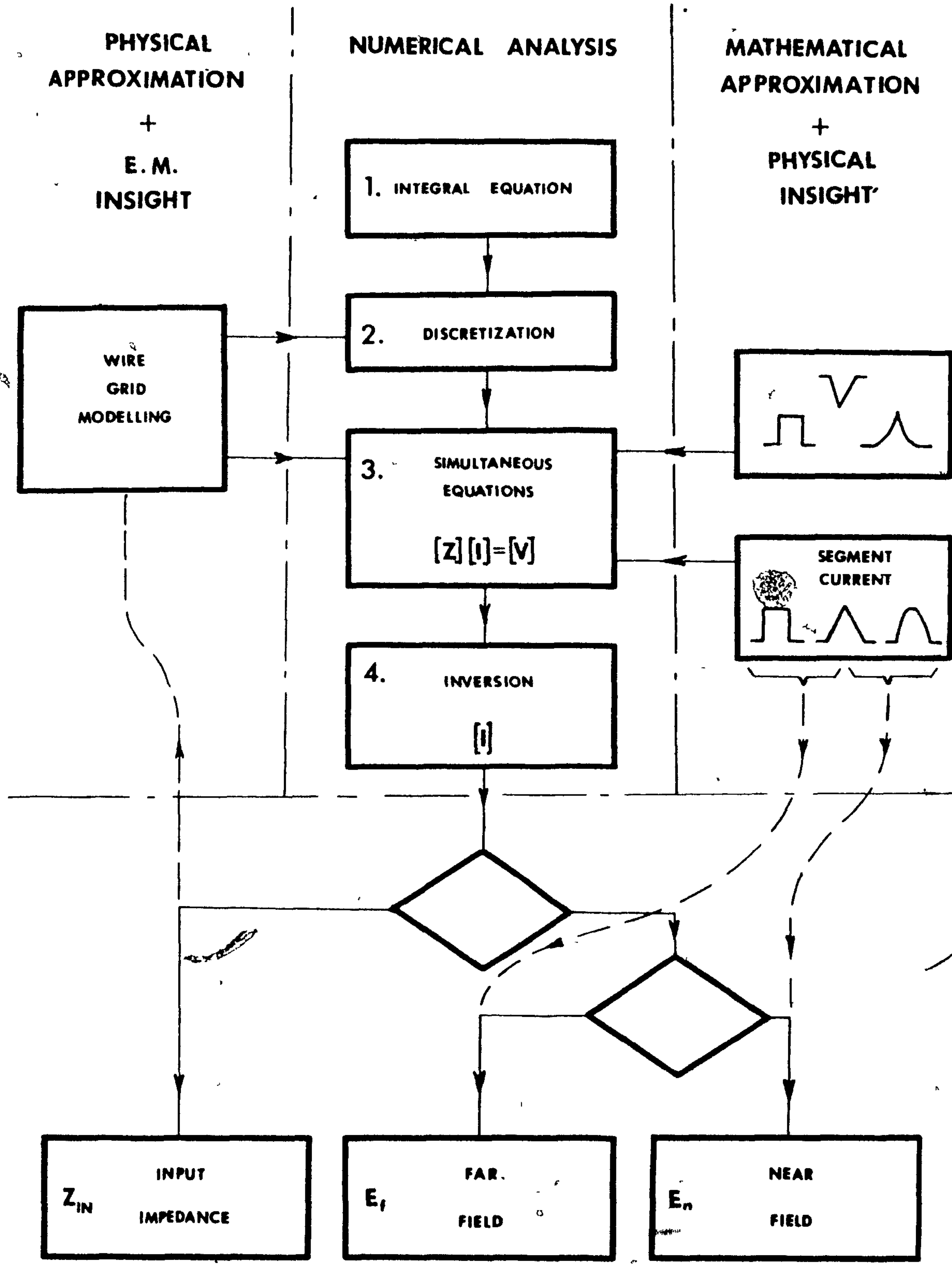

FIGURE 4.1. ELEMENTS OF WIRE GRID MODELLING TECHNIQUE.

designating the structuring of the wire-grid model and especially on factors such as the location and radius of the elements of the wire grid. This emphasis and the consequent results can be related qualitatively to the error analysis curve of Figure 4.2. This suggests that the error analysis curve is multi-dimensional. A convergence of the wire grid process must be related not only to the numerical techniques used and the length of the element but also the location, presence or absence and radius of the elements.

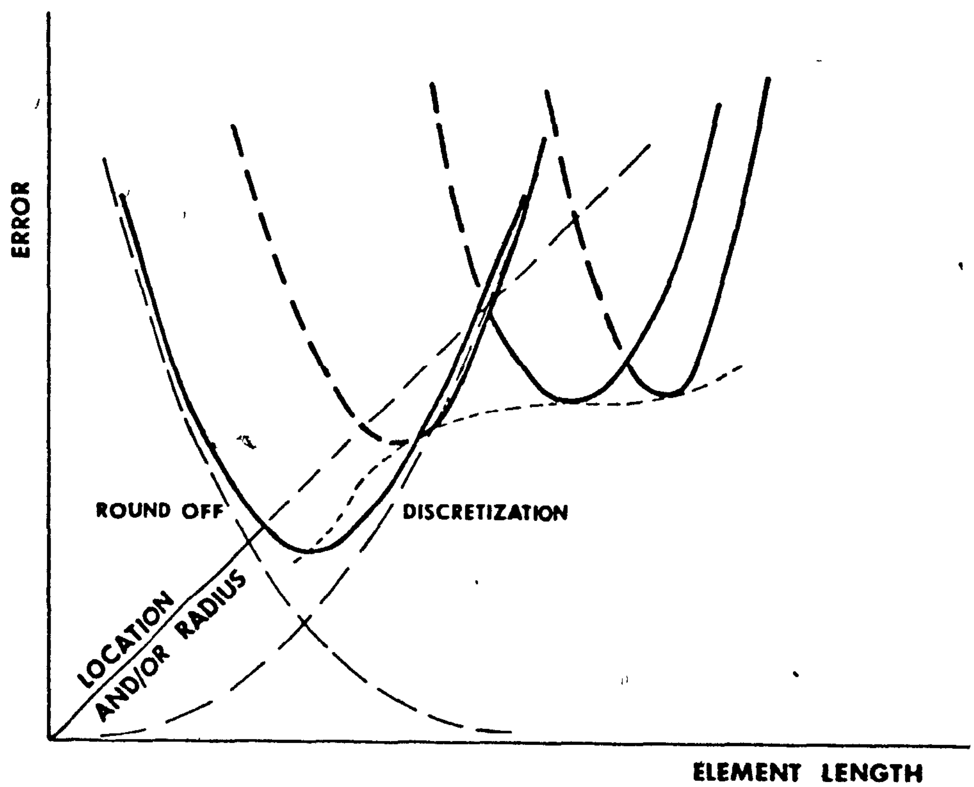

FIGURE 4.2. CONVERGENCE FACTORS.

4.1 Theory and Method

In this section, the basic equations necessary for the wire grid modelling technique are presented and the basic programming structure is outlined. Thus a summary is given of one form of the "circuit theory" of antennas based on Pocklington's integral equation. The transformation of this integral equation into a system of algebraic equations resembling network equations, was formulated by Aharoni [44] and Schelkunoff [59]. The formalism of the generalized method of moments as described by Harrington [108] is used for convenience to describe the techniques which were applied in this work.

4.1.1 Transformation of Integral Equations - Method of Moments

The equation to be formulated and solved is for the scattered and incident field on a perfectly conducting body. The total tangential electric field will be zero everywhere on the surface as shown in Figure 4.3. $\bar{J}$ is the current density. Thus,

$$\bar{E}^s_{tan} + \bar{E}^i_{tan} = 0 \tag{4.1}$$

where,

$\bar{E}^i_{tan}$ = incident electric field due to an external or local source.

$\bar{E}^s_{tan}$ = scattered electric field radiated by the current density $\bar{J}$.

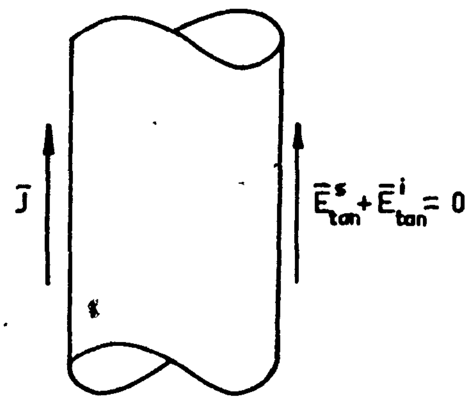

FIGURE 4.3.

Dropping the subscript, Equation (4.1) can be re-written,

$$- \bar{E}^s = \bar{E}^i \tag{4.2}$$

where $\bar{E}^s$ will be the integral expression involving the unknown current density $\bar{J}$. In the terminology of the method of moments and the concept of linear vector spaces and operators, a linear operator L is defined such that

$$L(\bar{J}) = -(\bar{E}^s) \tag{4.3}$$

Hence from Equation (4.2) an operator equation can be written

$$L(\bar{J}) = (\bar{E}^i) \quad (4.3)$$

where

L = the linear integro-differential operator of the problem.

E^i = the known source function or excitation.

$\bar{J}$ = unknown response function or current[1] to be determined.

The operator maps a subset containing (J) to one containing (E^i) and for a unique solution, the mapping is one to one. The solution to this equation by the method of moments or "weighted residuals" can be divided into four steps.

(1) The unknown function, say the current J, is represented by a series of basis (trial, expansion) functions spanning the domain of the operator L such as,

$$\bar{J} \approx \sum_{n=1}^{N} I_n \bar{J}_n \tag{4.4}$$

where

$\bar{J}_n$ are the independent basis functions, and

I_n are the complex unknown current coefficients which must be determined.

Substituting in Equation (4.3) and noting that the operator is linear, the equation becomes,

---

[1] J is used to designate current in the remainder of the text in order to have a symbol having some identification with current, in the moment method outline.

$$\sum_{n=1}^{N} I_n \, L(\bar{J}_n) \approx (\bar{E}^i) \qquad (4.5)$$

Now a residual error $\bar{\epsilon}$ can be defined by

$$\bar{\epsilon} = \sum_{n=1}^{N} I_n \, L(\bar{J}_n) - (\bar{E}^i) \qquad (4.6)$$

Since the summation is finite, the residual error will not be zero. The types of functions ($\bar{J}_n$) used are tabulated in Table 4.1.

(2) A set of M weighting or testing functions $\left\{ \bar{\omega}_m \right\}$ in the range of the operator L is introduced and an inner product [109] defined and taken for each side of Equation (4.5).

$$<\bar{\omega}_m , \epsilon> = \sum_{n=1}^{N} I_n <\bar{\omega}_m , L(\bar{J}_n)> - <\bar{\omega}_m , \bar{E}^i> \qquad (4.7)$$

$$m = 1,2, \ldots M$$

Thus the residual error is weighted by the set of functions $\left\{ \bar{\omega}_m \right\}$ and by constraining the residual error to be orthogonal to each of them the required matrix representation is obtained.

$$<\omega_m , \epsilon> = \left[Z'_{mn} \right] \left[I_n \right] - \left[E_m \right] = 0 \qquad (4.8)$$

where,

$$Z'_{mn} = <\bar{\omega}_m , L(\bar{J}_n)> = \int \bar{\omega}_m(z) \, L \, \bar{J}_n(z) \, dz \qquad (4.9)$$

and

$$E_m = \langle \bar{\omega}_m , \bar{E}^i \rangle = \int \bar{\omega}_m \bar{E}^i(z)\, dz \tag{4.10}$$

(3) The inner products given in (4.9) and (4.10) are calculated for m = 1, 2, ... N to give the N x N matrix equation.

$$\begin{bmatrix} \langle \bar{\omega}_1, L(\bar{J}_1)\rangle & \langle \bar{\omega}_1, L(\bar{J}_2)\rangle & --- & \langle \bar{\omega}_1, L(\bar{J}_n)\rangle \\ \langle \bar{\omega}_2, L(\bar{J}_1)\rangle & \langle \bar{\omega}_2, L(\bar{J}_2)\rangle & --- & \langle \bar{\omega}_2, L(\bar{J}_n)\rangle \\ - & - & --- & - \\ \langle \bar{\omega}_n, L(\bar{J}_1)\rangle & \langle \bar{\omega}_n, L(\bar{J}_2)\rangle & --- & \langle \bar{\omega}_n, L(\bar{J}_n)\rangle \end{bmatrix} \begin{bmatrix} I_1 \\ I_2 \\ - \\ I_n \end{bmatrix} = \begin{bmatrix} \langle \bar{\omega}_1, \bar{E}^i \rangle \\ \langle \bar{\omega}_2, \bar{E}^i \rangle \\ - \\ \langle \bar{\omega}_n, \bar{E}^i \rangle \end{bmatrix} \tag{4.11}$$

or

$$\left[Z'_{mn}\right] \left[I_n\right] = \left[E_m\right] \tag{4.12}$$

Hence the original integral equation has been reduced to a linear system of N equations. The amount of computation necessary for each of the terms is dependent on the type of basis and weight functions used. This is indicated in Table 4.1.

(4) Provided [Z'] has an inverse, then a solution for the column vector [I] can be obtained,

$$\left[I\right] = \left[Z'\right]^{-1} \left[E\right] \tag{4.13}$$

Therefore an approximate solution for the function $\bar{J}$ is obtained as indicated by Equation (4.4).

The basis functions $\bar{J}_n$ and the weighting functions $\bar{\omega}_m$ are chosen to minimize computation cost while maintaining solution accuracy. Table 4.1, adapted from Fenlon [110], lists the common functions used and consequently the nomenclature for the method.

TABLE 4.1. MOMENT METHODS AND COEFFICIENTS.

METHOD	FUNCTIONS		Z'_{mn}	E_m
	TRIAL	WEIGHT		
1. Galerkin	$J_n(z)$	$J_m(z)$	$\int J_m(z)\left[L\ J_n(z)\right] dz$	$\int J_m(z)\ E^i(z)\ dz$
2. Least Squares	$J_n(z)$	$Q(z)\ \dfrac{\partial\epsilon(z)}{\partial I_m}$	$\int Q(z)\ \dfrac{\partial\epsilon(z)}{\partial I_m}\left[L\ J_n(z)\right] dz$	$\int Q(z)\ \dfrac{\partial\epsilon(z)}{\partial I_m}\ E^i(z)\ dz$
3. General Collocation	$J_n(z)$	$\delta(z - z_m)$	$\int \delta(z - z_m)\left[L\ J_n(z)\right] dz$	$\int \delta(z - z_m)\ E^i(z)\ dz$
4. Subsectional Collocation	$J_n(z)\ \delta(z - z_n)$	$\delta(z - z_m)$	$\sum_N \int \delta(z - z_m)\left[L\ \{J_n(z)\ \delta(z - z_n)\}\right] dz$	$\int \delta(z - z_m)\ E^i(z)\ dz$
5. Point Matching	$\delta(z - z_n)$	$\delta(z - z_m)$	$\int \delta(z - z_m)\left[L\ \{J_n(z)\ \delta(z - z_n)\}\right] dz$	$\int \delta(z - z_m)\ E^i(z)\ dz$
$Q(z)$ is an arbitrary positive definite function; $\delta(z)$ is the Dirac delta function[1]				

Only the third and fifth methods were used in this work. Details on the first, fourth and fifth methods are discussed by Harrington [109] and reference is made to Ames [111] and Becker

[1] Some authors point out that since the δ-function is not part of Hilbert space, the inner product is not defined and hence the method should not be classed with the others.

[112] for the third and second respectively. The required expressions for the operator L remain to be specified.

4.1.2 Fields of Current Elements

Evaluation of the Z'_{mn} terms of Equation (4.12) requires the expression for the scattered field of one or more elements. Detailed derivations are given by Richmond [113] and Wolde-Ghiorgis [45] and a synopsis is given below.

Figure 4.4 shows a thin finite element of length s^1 in free space. It is assumed to support a current $I(z')$ exp $(j\omega t)$ uniformly distributed around its periphery. Since the current is uniform around its periphery, the electric field at an observation point $P(\rho, \phi, z)$

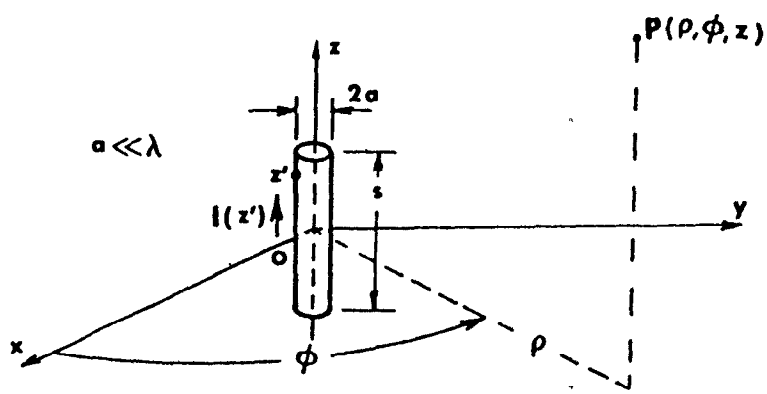

FIGURE 4.4

[1] The superscript 's' denotes the scattered field and should not be confused with element lengths which are usually subscripted later in the text: s_m etc...

will be independent of ϕ. Hence the observation point can be taken in the y-z plane. The time exponential is suppressed in the expressions which follow. The scalar potential and the z-component of the vector potential A can be written,

$$\phi(\rho, \pi/2, z) = \frac{1}{4\pi\epsilon_0} \int_{-S/2}^{S/2} q(z')\, G(z,z')\, dz' \tag{4.14}$$

and

$$A_z(\rho, \pi/2, z) = \frac{\mu_0}{4\pi} \int_{-S/2}^{S/2} I(z')\, G(z,z')\, dz' \tag{4.15}$$

where q(z') is the charge per unit length. The Green's function G(z, z') is given by

$$G(z,z') = \frac{1}{2\pi} \int_0^{2\pi} \frac{e^{-jkR}}{R}\, d\phi' \tag{4.16}$$

where

$$R = \left[(z - z')^2 + \rho^2 + a^2 - 2\, a\, \rho \cos\phi'\right]^{1/2}$$

and $j = \sqrt{-1}$ and $k = \omega\sqrt{\mu_o \epsilon_o}$, is the wave number. The cylindrical coordinates for the source point on the element surface are (a, ρ', z').

The scattered electric field $\bar{E}^s$ due to the current and charge on the element can be expressed as

$$\bar{E}^s = -j\,\omega\,\bar{A} - \nabla\Phi \qquad (4.17)$$

From ~~the~~ condition

$$\nabla \cdot \bar{A} + j\,\omega\,\mu_o\,\epsilon_o\,\Phi = 0 ,$$

and the continuity relation

$$\frac{dI(z')}{dz'} + j\,\omega\,\epsilon_o\,q(z') = 0$$

it can be shown that

$$\bar{E}^s = -\frac{j\omega}{k^2}\left[\nabla(\nabla \cdot \bar{A}) + k^2\,\bar{A}\right] \qquad (4.18)$$

Since the field has ϕ-symmetry,

$$\bar{E}^s = \bar{i}_z\,E_z^s + \bar{i}_\rho\,E_\rho^s \qquad (4.19)$$

and thus,

$$E_z^s = \frac{-j}{4\pi\omega\epsilon_o} \int_{-S/2}^{S/2} I(z') \left[\frac{\partial^2 G(z,z')}{\partial z^2} + k^2 G(z,z') \right] dz' \qquad (4.20)$$

and

$$E_\rho^s = \frac{-j}{4\pi\omega\epsilon_o} \int_{-S/2}^{S/2} I(z') \frac{\partial^2 G(z,z')}{\partial z \quad \partial\rho} dz' \qquad (4.21)$$

When an impressed field E_z^i is applied parallel to the axis of the element and is also uniformly distributed around the periphery, then because of Equation (4.1)

$$E_z^s = - E_z^i$$

and thus Pocklington's integral equation is obtained:

$$\frac{-j}{4\pi\omega\epsilon_o} \int_{-S/2}^{S/2} I(z') \left[\frac{\partial^2 G(z,z')}{\partial z^2} + k^2 G(z,z') \right] dz' = - E_z^i \qquad (4.22)$$

The Green's function G(z, z') is usually approximated by

$$G(z,z') = \frac{e^{-jkr}}{r} \qquad (4.23)$$

where,

$$r = \left[(z - z')^2 + \rho^2 + a^2 \right]^{1/2} \qquad (4.24)$$

With this approximation, and for an observation point on the axis of the wire [113], from Equation (4.20) and (4.21),

$$E_z^s = \frac{-j}{4\pi\omega\epsilon_o} \int_{-S/2}^{S/2} I(z') \Big[2r^2 (1 + jkr) - (\rho^2 + a^2)(3 + 3jkr - k^2r^2) \Big] \frac{e^{-jkr}}{r^5} \, dz' \tag{4.25}$$

and

$$E_\rho^s = \frac{-j}{4\pi\omega\epsilon_o} \int_{-S/2}^{S/2} I(z') \Big[(z - z')(3 + 3jkr - k^2r^2) \Big] \frac{e^{-jkr}}{r^5} \, dz' \tag{4.26}$$

These are the basic expressions used by Richmond [113] for the wire-grid analysis method.

Both z and ρ components are needed to compute the total scattered field at any element due to contributions of its own scattered field and that caused by all other elements in a wire-grid. Thus for the four interacting elements shown in Figure 4.5, the field at an observation point Q(x, y, z) at the centre of the fourth element would be given by

$$E_\xi^s = (E_4^s)_4 + \sum_{n=1}^{3} (E_n^s)_4 \tag{4.27}$$

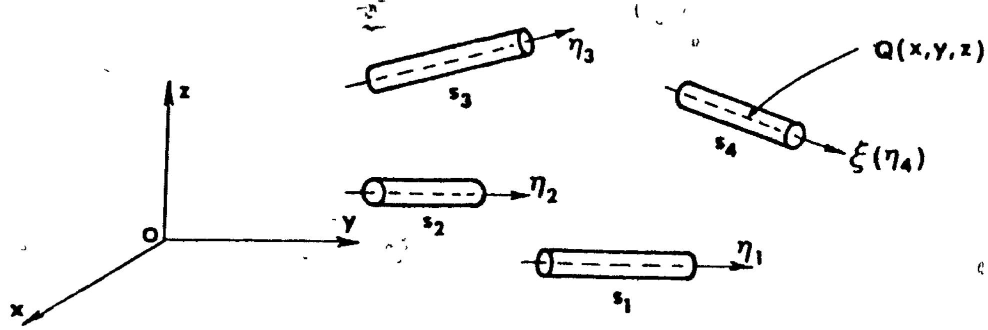

FIGURE 4.5. ARBITRARILY ORIENTED CURRENT ELEMENTS.

where $(E_4^s)_4$ is the self-generated field and $(E_n^s)_4$ represents the contribution from each of the neighbouring elements at element s_4. Thus the internal subscript denotes the source current and the external subscript refers to the point of observation. Thus for N elements, the field along the axis of the mth element can be written

$$E_\xi^s = (E_m^s)_m + \sum_{\substack{n=1 \\ n \neq M}}^{N-1} (E_n^s)_m \qquad (4.28)$$

The point of observation is the match point at the center of each element shown as Q in Figure 4.5. The axial and radial component of the field of each element obtained from Equation (4.25) and (4.26) must be transformed to compute the E_ξ field at Q. Richmond [77] was the first one to simplify this coordinate transformation in the wire-grid technique and a detailed derivation is given by Wolde-Ghiorgis [45]. Each element is specified by its length s_m, centre coordinates (x_m, y_m, z_m) an angle 'α', below a plane parallel to the x-y plane and the angle 'β' its projection makes with the x-axis as shown in Figure 4.6.

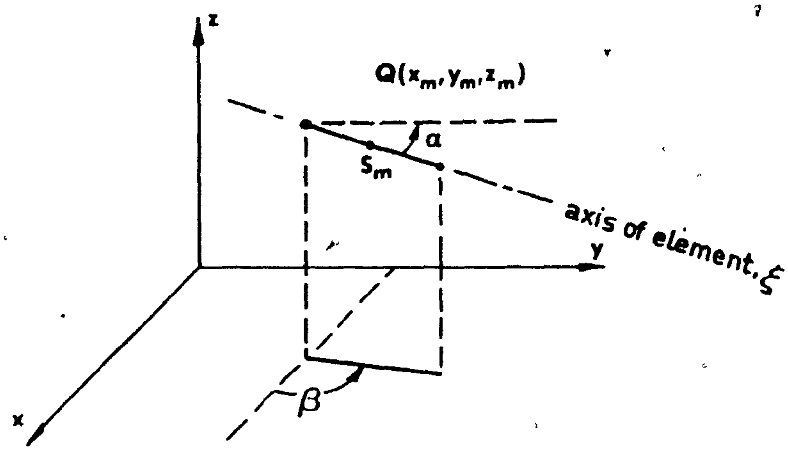

FIGURE 4.6. ELEMENT DESCRIPTION.

Using Richmond's notation, by defining

$$E'_z = E^s_{z'_m} / I_n$$

$$E'_\rho = E^s_{\rho'_m} / I_n$$

where the subscripts z'_m and ρ'_m refer to the axial and radial components of the electric field due to current element s_n at these coordinates of Q which are defined with respect to the coordinate system centered at (x_n, y_n, z_n). Explicitly, from Equations (4.20) and (4.21),

$$E_z' = \frac{-j}{4\pi\omega\epsilon_o} \int_{-S_n/2}^{S_n/2} \left[\left. \frac{\partial^2 G(z,t)}{\partial z^2} \right|_{z = z_m'} + k^2 G(z_m',t) \right] dt \qquad (4.29)$$

and

$$E_\rho' = \frac{-j}{4\pi\omega\epsilon_o} \int_{-S_n/2}^{S_n/2} \left. \frac{\partial^2 G(z,t)}{\partial z \; \partial t} \right|_{\substack{z = z_m' \\ \rho = \rho_m'}} dt \qquad (4.30)$$

Applying the coordinate transformation to obtain the tangential component at s_m will yield the Z_{mn}' terms for a piece-wise uniform, $\delta(z - z_m)$ current expansion. These terms are direct measures of the field interaction between elements s_m and s_n. The expression can be shown to be

$$\begin{aligned} Z_{mn}' = {} & (E_z' - z_m' E_{\rho'} / \rho_m')(\cos\alpha_m \cos\beta_m \cos\alpha_n \cos\beta_n + \\ & + \cos\alpha_m \sin\beta_m \cos\alpha_n \sin\beta_n + \sin\alpha_m \sin\alpha_n) + \\ & + E_{\rho'} (x_{mn} \cos\alpha_m \cos\beta_m + y_{mn} \cos\alpha_m \sin\beta_m - \\ & - z_{mn} \sin\alpha_m) / \rho_m' \end{aligned} \qquad (4.31)$$

where

$$x_{mn} = x_m - x_n \, , \quad y_{mn} = y_m - y_n \, , \quad z_{mn} = z_m - z_n$$

$$\bar{r}' = \bar{i}_x x_{mn} + \bar{i}_y y_{mn} + \bar{i}_z z_{mn}$$

$$z'_m = x_{mn} \cos \alpha_n \cos \beta_n + y_{mn} \cos \alpha_n \sin \beta_n - z_{mn} \sin \alpha_n$$

$$\rho'_m = (|r'|^2 - z'^2_m)^{1/2}$$

and

i_x, i_y, i_z are unit vectors.

The E_m terms on the right hand side of Equation (4.12) remain to be specified.

4.1.3 Representation of the Source

The computational representation of two sources, the delta-gap generator and the magnetic current frill are summarized below. The former arises directly from consideration of a dipole fed from a balanced transmission line, while the latter arises from an attempt to more faithfully represent the source region of a monopole fed from a co-axial line. A good general review of these representations and their development is to be found in Wolde-Ghiorgis' [45] work.

In the case of the dipole, the source is easily visualized to exist between the arms of the antenna as shown in Figure 4.7. In the finite element model, the voltage V is placed across the finite source element, Δz as shown. This condition can be expressed as

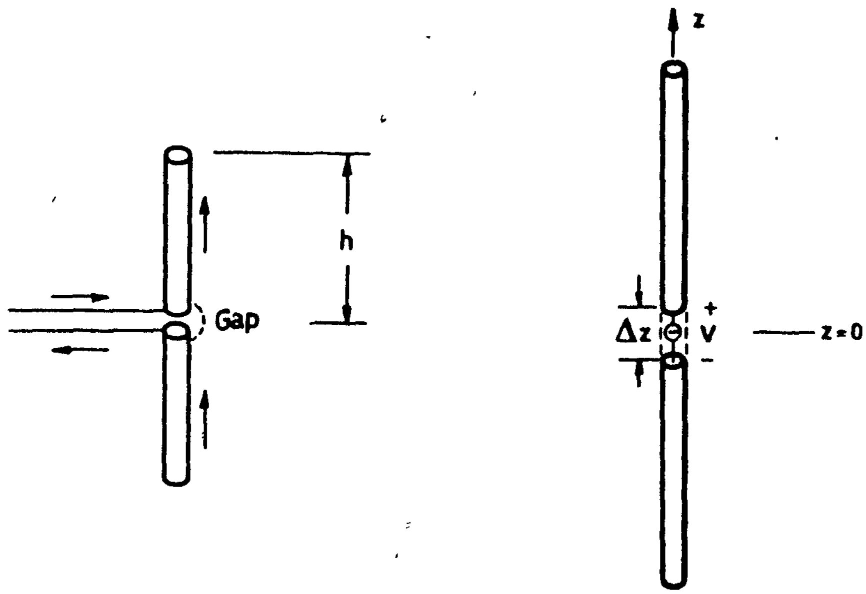

FIGURE 4.7. DIPOLE REPRESENTATION.

$$E_z^i = \frac{-V}{\Delta z}, \quad |z| < \Delta z/2 \qquad (4.32)$$

$$= 0, \quad |z| > \Delta z/2$$

This gap element is considered to be a typical current element over which current flows and at the center of whith the constraint of Equation (4.2) is to be satisfied. If Equation (4.12) is rewritten with the mth element multiplied by $-s_m$, then

$$\sum_{n=1}^{N} Z_{mn} I_n = V_m^i \qquad (4.33)$$

where

$$Z_{mn} = (-\ S_m)\ Z'_{mn}$$
$$V_m = (-\ S_m)\ E^i_m$$

Thus with the source gap at the Ith element, the matrix expression is

$$\left[Z_{mn}\right]\left[I_n\right] = \left[V^i_m\right] \tag{4.34}$$

and

$$V^i_m = \begin{bmatrix} 0 \\ \vdots \\ 1 \\ \vdots \\ 0 \end{bmatrix} \longleftarrow \text{I-th row} \tag{4.35}$$

Where the excitation voltage has been normalized to 1 volt and is zero at all other elements. This specific representation was first used by Harrington for straight wires [108] and by Wolde-Ghiorgis [45] for three-dimensional structures.

It is more difficult to visualize and accept a delta-gap representation for a co-axially fed antenna unless the source region is assumed to be a small spherical boundary acting as a source of TEM waves as considered by Schelkunoff [59]. Then the axial gap might be considered to be a first approximation of such a source region. However, Albert and Synge [114] proposed that the magnetic frill source shown in Figure 4.8 could represent the co-axial feed more directly. The excitation source is

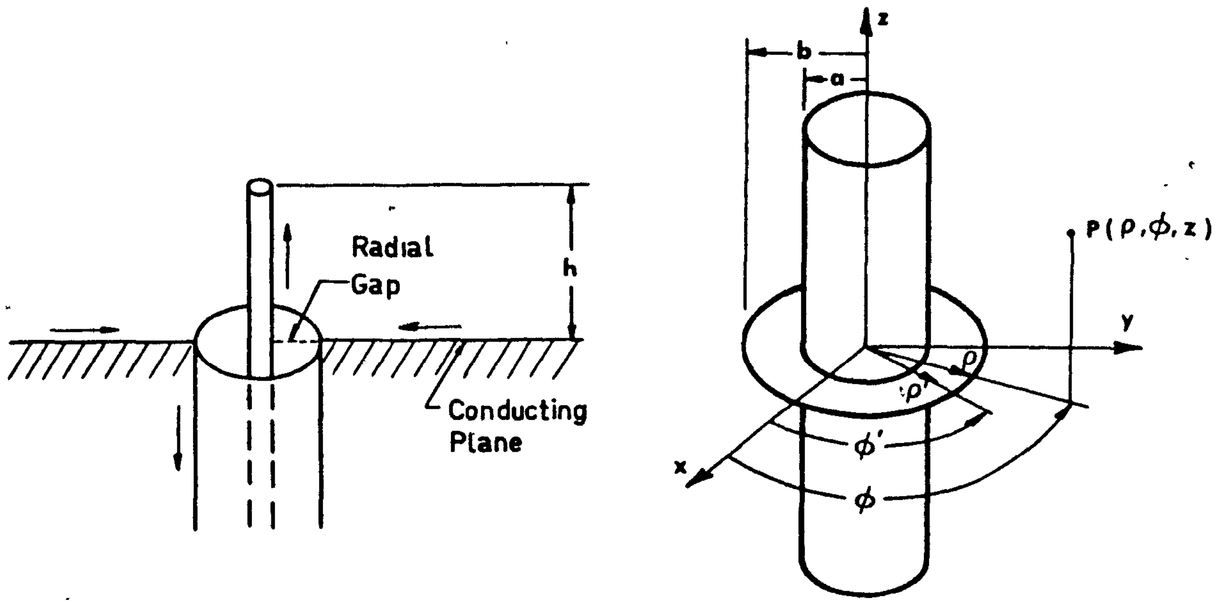

FIGURE 4.8. REPRESENTATION OF CO-AXIAL FEEDPOINT.

a radial field

$$E^{i}_{\rho} = \frac{V}{\rho' \ln(\frac{b}{a})} \quad , \qquad a < \rho' < b$$
$$= 0 \quad , \qquad \rho' > b \tag{4.36}$$

Where V is the voltage amplitude and a, b and ρ' are defined in Figure 4.8. From the relationship [115]

$$\overline{M} = \vec{E} \times \overline{n} \tag{4.37}$$

where

$\overline{M}$ = magnetic surface current density

$\overline{n}$ = unit vector normal to the plane of the frill,

the source can be expressed as

$$M^{i}_{\phi'} = \frac{-V}{\rho' \ln(\frac{b}{a})} \quad , \quad a < \rho' < b$$
$$= 0 \quad , \quad \rho' > b \tag{4.38}$$

and the field at any point P can be derived from the electric vector potential, $\overline{F}$.

The electric vector potential, $\overline{F}$ can be written [115]

$$\overline{F} = \frac{\epsilon_o}{4\pi} \iint_{\substack{\text{Frill} \\ \text{Surface}}} \frac{\overline{M}\, e^{-jkr_o}}{r_o} \, dS' \tag{4.39}$$

where

$$r_o = \left[z^2 + \rho^2 + \rho'^2 - 2\rho\rho' \cos(\phi - \phi')\right]^{1/2} \tag{4.40}$$

Note the source coordinates are indicated by primes. $\overline{F}$ has only one component F_ϕ since only M_ϕ exists and because of axial symmetry, it will be independent of ϕ. Hence the observation point can be taken in the x-z plane and thus from Equation (4.38),

$$F_\phi = \frac{\epsilon_o}{4\pi} \int_a^b \int_0^{2\pi} \frac{-V}{\ln(\frac{b}{a})} \frac{e^{-jkr_o}}{r_o} \cos\phi' d\phi' d\rho' \qquad (4.41)$$

and since

$$\bar{E} = \frac{1}{\epsilon_o} \nabla \times \bar{F}$$

then

$$\bar{E}^i = \bar{i}_z E_z^i + \bar{i}_\rho E_\rho^i \qquad (4.42)$$

where

$$E_z^i = -\frac{1}{\epsilon_o} \frac{1}{\rho} \frac{\partial}{\partial \rho}(\rho F_\phi) \qquad (4.43)$$

and

$$E_\rho^i = \frac{1}{\epsilon_o} \frac{\partial}{\partial z} (F_\phi) \qquad (4.44)$$

Thus the excitation values for Equation (4.12) can be computed from

$$E_m^i = \bar{i}_\xi \cdot \bar{E}^i \qquad (4.45)$$

where again i_ξ is the unit vector parallel to the axis of element s_m and the field components given by Equation (4.43) and (4.44) are evaluated at the center of s_m. Tsai [116] and Thiele [80] have shown that the integration in Equation (4.41) with respect to ϕ' involves Bessel functions of zero, first and second order and with respect to ρ', complete elliptical integrals of the first kind and that the expression can readily be evaluated numerically.

Both of the two source representations have been used in the computations reported in this work. Once a satisfactory equivalence had been established, the delta-gap generator was used more frequently because of its inherent computational simplicity. With all elements of the matrix equation computed, it can then be solved for the unknown current values from which the radiation fields can be determined.

4.1.4 Computation of Radiated Field

When the current distribution on the system of N elements is found, the far field can be calculated by superimposing the field from each element. The geometry of this calculation is shown in Figure 4.9 for an element s_m with center coordinates x_m, y_m, z_m, and angles of orientation α_m and β_m. If the element supports a constant current I_m and i_ξ is the unit vector in the direction of current flow as defined by Equation (4.45) then the vector potential at observation point P is,

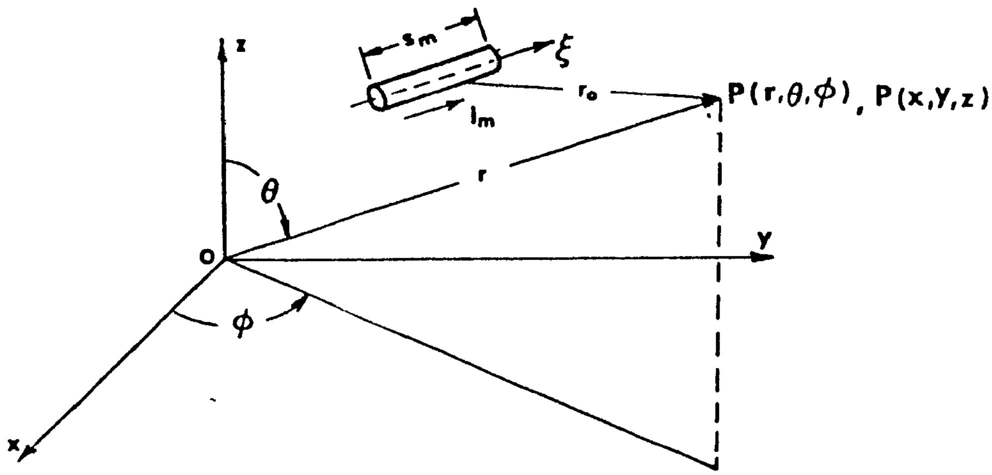

FIGURE 4.9. GEOMETRY OF RADIATION FIELD CALCULATION,

$$\bar{A}_m = \bar{i}_\xi A_m$$

$$= \bar{i}_\xi \frac{\mu_o I_m s_m}{4 \pi r_o'} e^{-jkr_o'} \tag{4.46}$$

where

$$r_o' = \left[(x - x_m)^2 + (y - y_m)^2 + (z - z_m)^2 \right]^{1/2} \tag{4.47}$$

or in spherical coordinates,

$$r_o' = r \left[1 - \frac{2}{r} (x_m \sin\theta \cos\phi + y_m \sin\theta \sin\phi + z_m \cos\theta) \right]^{1/2} \tag{4.48}$$

$$\simeq r - (x_m \sin\theta \cos\phi + y_m \sin\theta \sin\phi + z_m \cos\theta) \tag{4.49}$$

With the far field approximation $r' = r$ in the denominator of (4.46)

$$\bar{A}_m = \bar{i}_\xi \, \mu_o \, \frac{I_m \, s_m}{4\pi r} \, e^{-jkr} \, e^{jk\left[(x_m \sin\theta \cos\phi \; + \; y_m \sin\theta \sin\phi \; + \; z_m \cos\theta\,)\right]} \tag{4.50}$$

The electric field had been expressed in Equation (4.18) in terms of the vector potential:

$$\bar{E}^s = - \frac{j\omega}{k^2} \left[\nabla(\nabla \cdot \bar{A}) + k^2 \, \bar{A} \right]$$

The first term can be neglected because of its $1/r^2$ dependence, and thus

$$\bar{E}_m = - \, j \, \omega \, \bar{A}_m \tag{4.51}$$

This can be expressed in terms of its two polarization components,

$$\bar{E}_m = \bar{i}_\theta \, E_{\theta_m} + \bar{i}_\phi \, E_{\phi_m} \tag{4.52}$$

where $\bar{i}_\theta$, $\bar{i}_\phi$ are the spherical unit vectors,

$$\bar{i}_\theta = \bar{i}_x \cos\theta \cos\phi \; + \bar{i}_y \cos\theta \sin\phi \; - \bar{i}_z \sin\theta$$

$$\bar{i}_\phi = - \, \bar{i}_x \sin\phi + \bar{i}_y \cos\phi$$

and

$$E_{\theta_m} = \bar{i}_\theta \cdot \bar{i}_\xi \, (- \, j\omega A_m)$$

$$E_{\phi_m} = \bar{i}_\phi \cdot \bar{i}_\xi \, (-j\omega A_m)$$

Hence the total field can be expressed in terms of its E_ϕ and E_θ components as,

$$E_\theta = -j\omega \sum_{n=1}^{N} (\cos\theta \cos\phi \cos a_m \cos\beta_m + \cos\theta \sin\phi \cos a_m \sin\beta_m + \sin\theta \sin a_m) A_m \tag{4.53}$$

and

$$E_\phi = -j\omega \sum_{n=1}^{N} (\sin\phi \cos a_m \cos\beta_m - \cos\phi \cos a_m \sin\beta_m) A_m \tag{4.54}$$

These two expressions form the latter part of the computer program described in the next section.

4.1.5 Computation Program

The flow chart of Figure 4.10 depicts the organization of the basic program used for the complex body computations. It represents the evolution of a program adapted by stages from Thiele's work [80] and that of Wolde-Ghiorgis [45]. The refinements made involved the segmentation subprogram, the testing of integration and matrix reduction schemes and the output subroutines. The current plotting programs used to generate the graphs of Figures 4.11 and 4.13 and the three-dimensional wire grid plotting programs used for the figures of Section 4.5 are not described. These involve the use of CALCOMP plotting routines with short FORTRAN main programs and axis rotation routines for the three-dimensional displays.

For the monopole tests, the segmentation was incorporated in the main program. For the dipole and ground rod antennas, coordinates were defined within the segmentation subprogram and for the helicopter, the segmentation was generated from end point coordinates read in from a data card for each member. All dimensions are normalized with respect to λ and center coordinates and orientation angles α, β are computed in the subroutine.

An initial data card contains a parameter which mid-way in the program governs the selection of a source model and then evaluation of either Z'_{mn} of (4.9) or Z_{mn} of (4.31). Excitation voltage is set at one volt.

Radiation pattern computation is done in the main program. An initial data card parameter governs the choice of either principal plane patterns or selected conical cuts. The printer plot subroutine is always called but the CALCOMP polar pattern plot subroutine is optional. Data card output of pattern values is optional and this can be stored for later plotting.

For testing of basic programming, development of subroutines and general familiarization with numerical technique differences, extensive tests were done on dipoles using sinusoidal and pulse basis functions and point-matching. The point-matching method was then used exclusively for the more complex antennas and the monopole on a helicopter.

4.2 Familiarization and Convergence Tests

Much of wire-grid modelling must be considered as computer experimentation. In this mode it is essential to have a means of removing programming errors, to test relative merits of different numerical techniques, to develop an insight into convergence problems and to obtain a general familiarity with this experimentation mode. Tests with dipoles and monopoles serve this purpose very well and are to be recommended because of the volume of available published information. In this work pulse and entire-basis functions were used in programs incorporating three types of integration schemes in the evaluation of the Z_{mn} elements, double and single precision, and two methods of matrix reduction and both the delta-gap and magnetic frill current source excitation. Some of the results are described below to illustrate the type of parametric study which has been found useful.

4.2.1 Collocation Method : Entire-Domain Basis Function

The finite Fourier Series

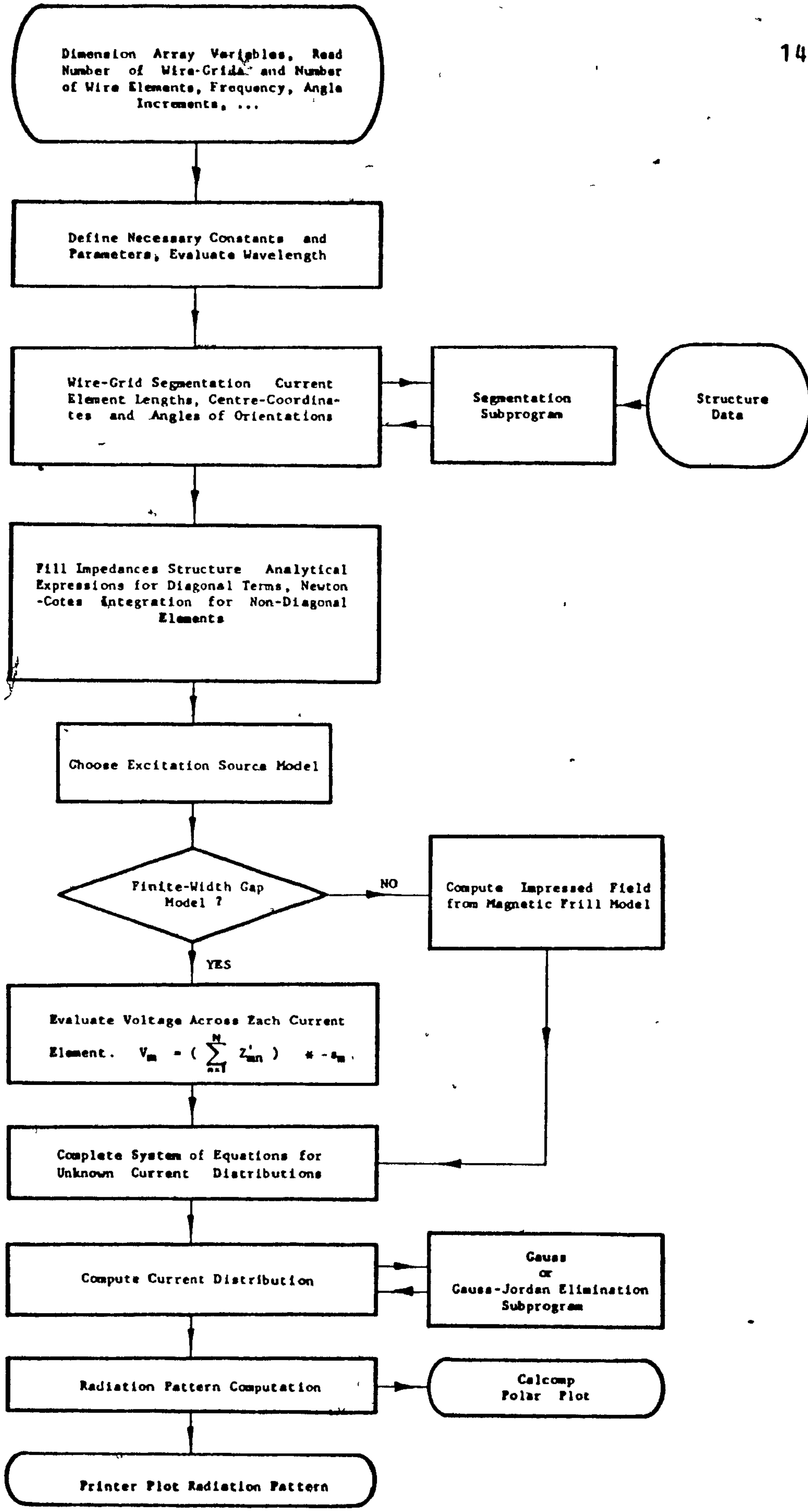

FIGURE 4.10. FLOW CHART FOR CURRENT AND FIELD COMPUTATION PROGRAM.

$$J(z) = \sum_{n=1}^{N} I_n \cos(2n - 1) \frac{\pi z}{L} \qquad - L/2 \leqslant z \leqslant L/2 \qquad (4.55)$$

was used as the basis function, chosen so that the current goes to zero at the ends of the antenna. The Z'_{mn} terms then become

$$Z'_{mn} = \frac{\lambda \sqrt{\mu/\epsilon}}{8 \pi^2 j} \int_{L/2}^{L/2} G(r_m, r') \cos(2n - 1) \frac{\pi z'}{L} dz' \qquad (4.56)$$

which must be integrated over the antenna length, L. The integration was carried out numerically using trapezoidal rule, Newton-Coates and Romberg integration schemes. The kernel transformation scheme used by Richmond [77] which provides non-uniform sampling was also tried. Both a Univac 1108 and an IBM 360/75 were used with the Univac 1108 showing faster convergence because of its longer word length (i.e. an extra digit). Crout-reduction [83] and a standard computer routine based on Gauss-Jordan elimination with columnal pivoting were used interchangeably.

Results were compared to the values reported by Thiele [80]. Typical current distribution plots are shown in Figure 4.11. The convergence with number of terms is clearly evident. However, it can also be seen that if current values from such a basis function are used for near field calculations, small perturbations might be obtained.

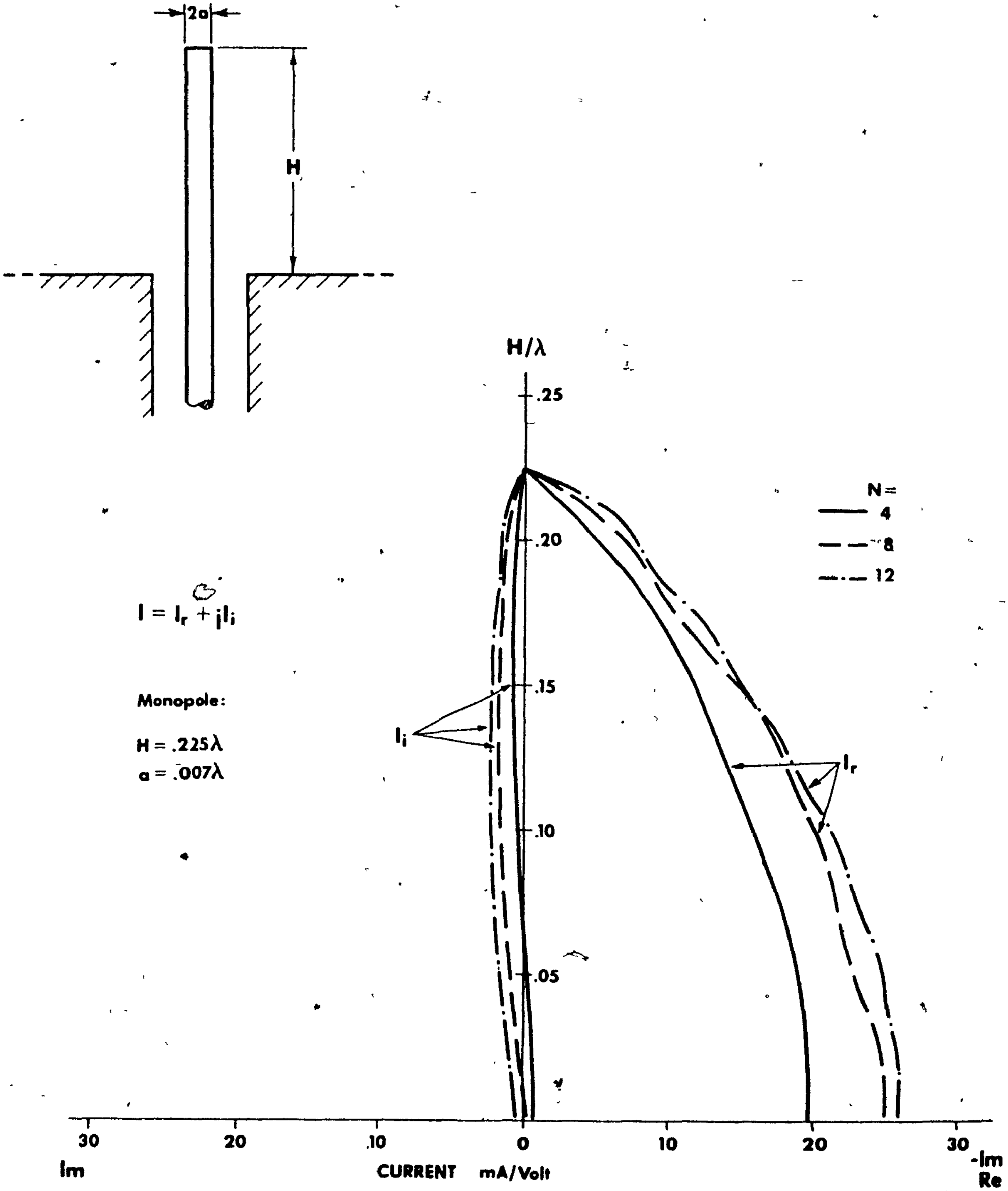

FIGURE 4.11. CURRENT DISTRIBUTION - MONOPOLE ANTENNA.

4.2.2 Point Matching: Piece-Wise Continuous Basis Function

The pulse-basis function with point matching involves integration only over the element lengths, but requires a greater number of segments for the same accuracy. In these tests the Newton-Coates 5th and 9th order integration formulae and the Univac 1108 library routine for matrix reduction were used. Computation of the Z_{mn} elements was carried out in double precision.

Here again the published impedance convergence data [80] was matched, as shown in Figure 4.12, for 40, 80 and 120 elements. The convergence is still more clearly evident in the current plots of Figure 4.13.

The above tests are near the sensitive reactance cross-over point of the monopole impedance characteristics. Invaluable for program verification, they offer the opportunity for the gradual introduction of computer graphics which will be found vital for the helicopter analysis.

Interesting comparisons of the use of other basis functions in Hallen's and Pocklington's equations are found in Thiele's survey [80].

4.3 Folded Dipole and Supporting Mast

The departure from symmetry in the measured E_θ vs θ pattern (Figure 3.20), although attributable to the

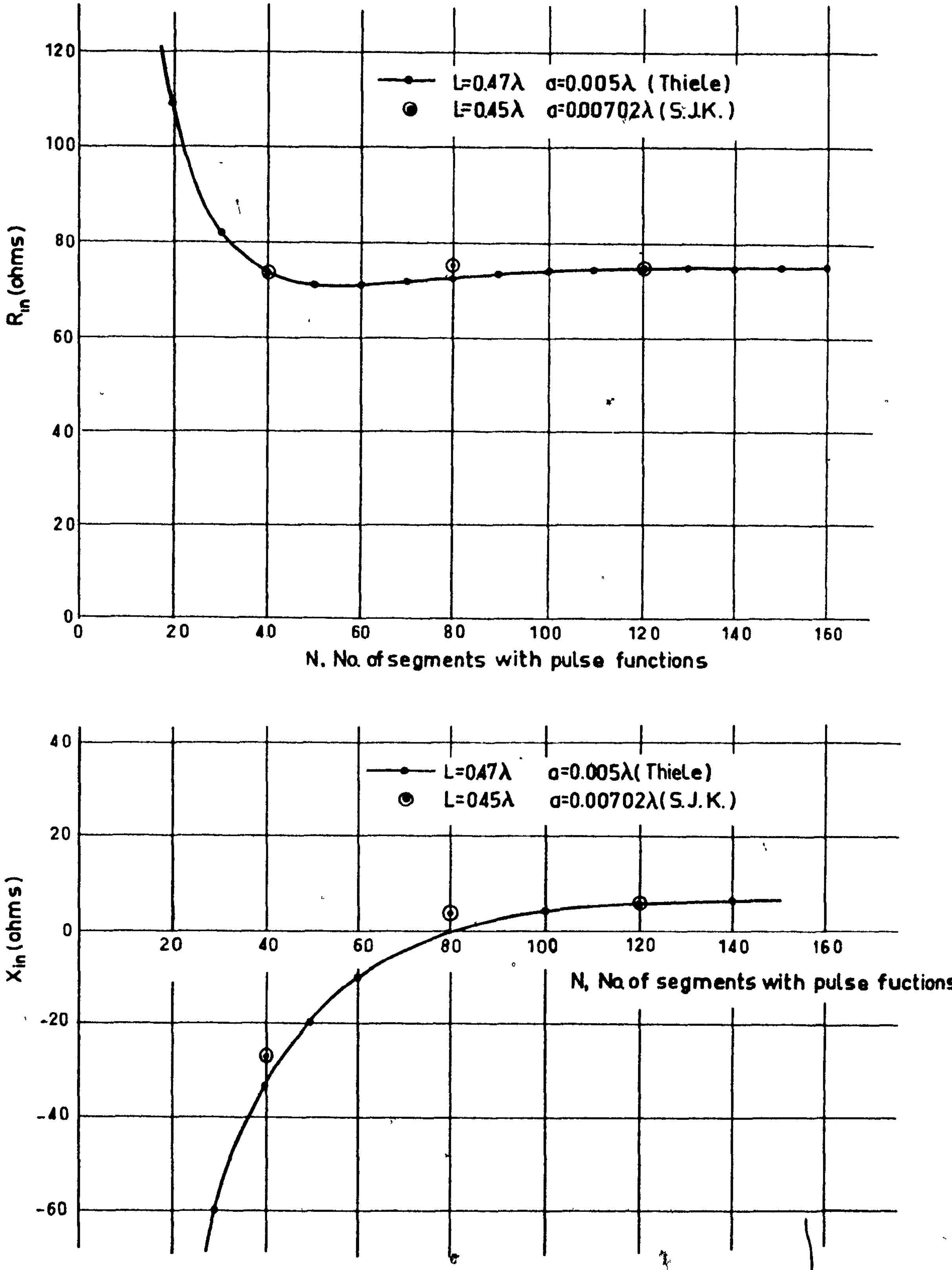

FIGURE 4.12. CURVE SHOWING CONVERGENCE OF INPUT REACTANCE AS THE NUMBER OF PULSE FUNCTIONS IS INCREASED.

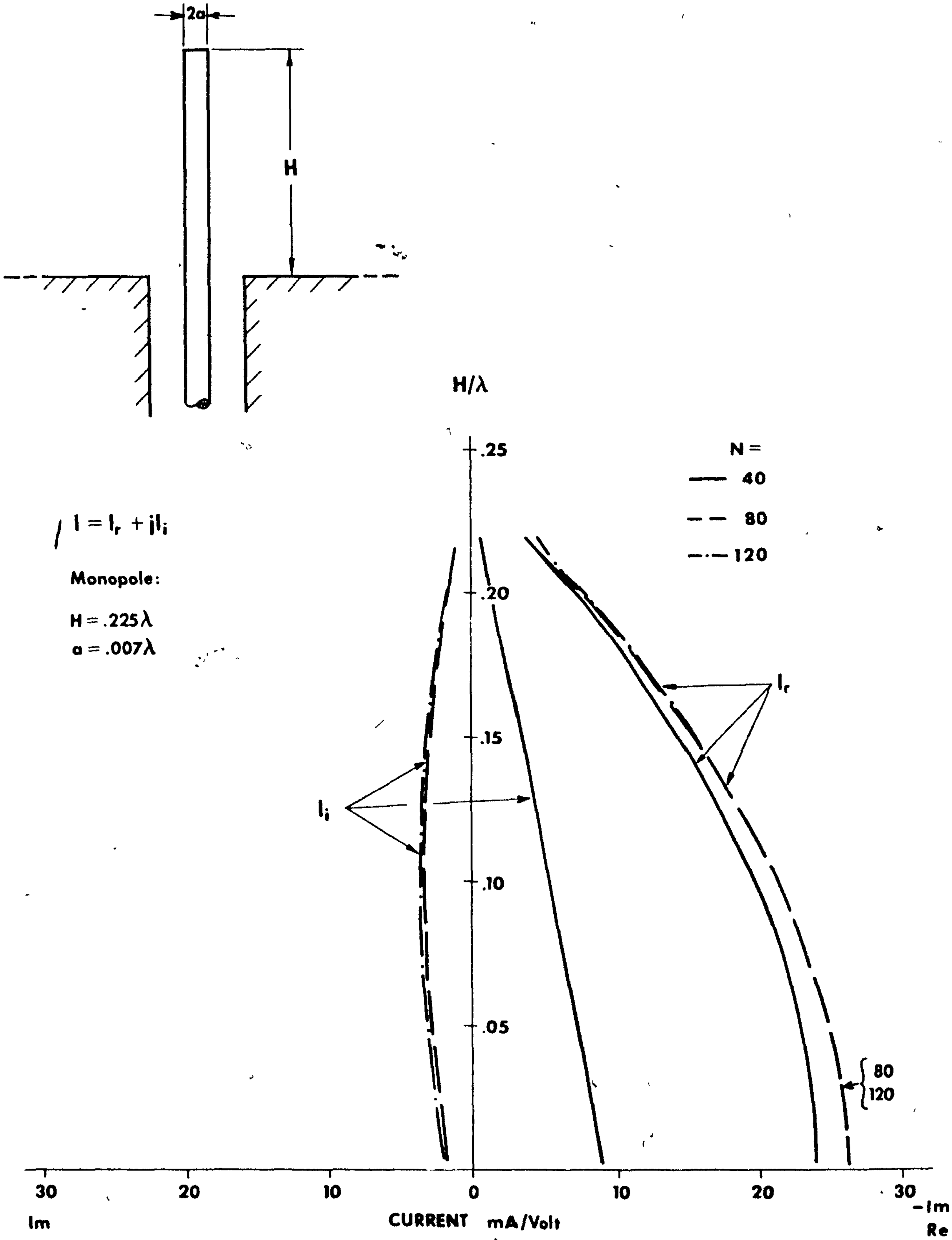

FIGURE 4.13. CONVERGENCE OF CURRENT DISTRIBUTION WITH N.

longer lower portion of the reflecting mast, could not be verified by additional data from the manufacturer. However, it was argued, that if wire grid modelling of the structure could show such a departure from symmetry, then this would corroborate the scale modelling of the antenna while at the same time representing a new application of the technique itself. Pulse basis functions and point matching were used.

4.3.1 Modelling of the Structure

While the modelling of the dipole involved the choice of a suitable number of segments necessary for convergence and the use of either a delta-gap or a magnetic frill source, the folded dipole and supporting mast involves the further consideration of appropriate representation of the folded dipole radiating element and the relatively thick reflecting mast.

Transmission line theory aside, the simplest model which can be considered, would represent the mast as a single rod and one arm of the folded dipole as a parasitic element in the manner shown in Figure 4.14. This representation suggests itself for trial since it is considered a close representation as to type by King [63]. The literature does not show an analysis of this antenna by numerical techniques except by Chao and Strait [81]. Although they examine a number of antennas by numerical techniques and show current distributions and radiation patterns for them, only the computed current distribution is shown for the folded dipole.

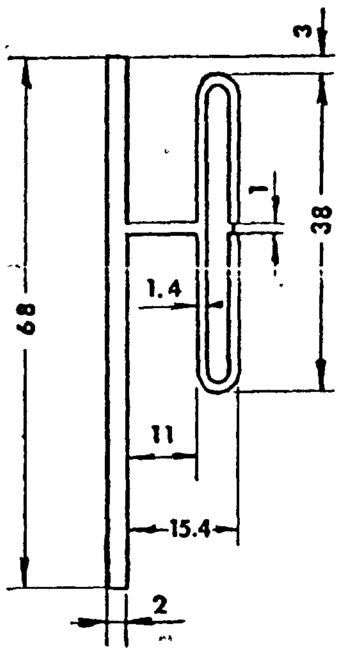

1/20th SCALE MODEL
DIMENSIONS IN mm

WIRE GRID
MODEL

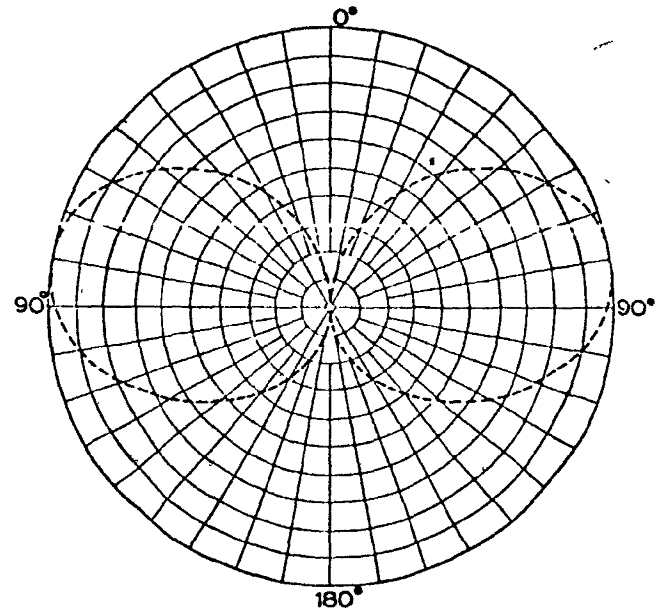

E_θ vs θ, (Normalized)

$\phi = 90°, 270°$

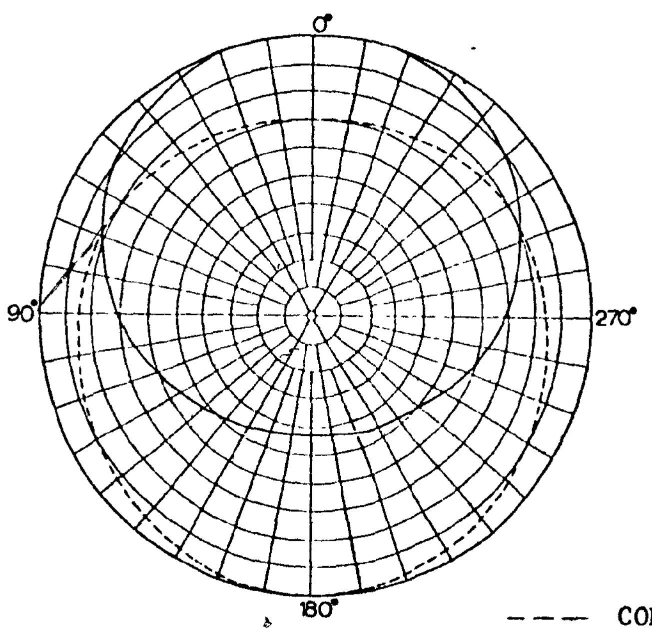

E_θ vs ϕ

$\theta = 90°$

--- COMPUTED

—— EXPERIMENTAL

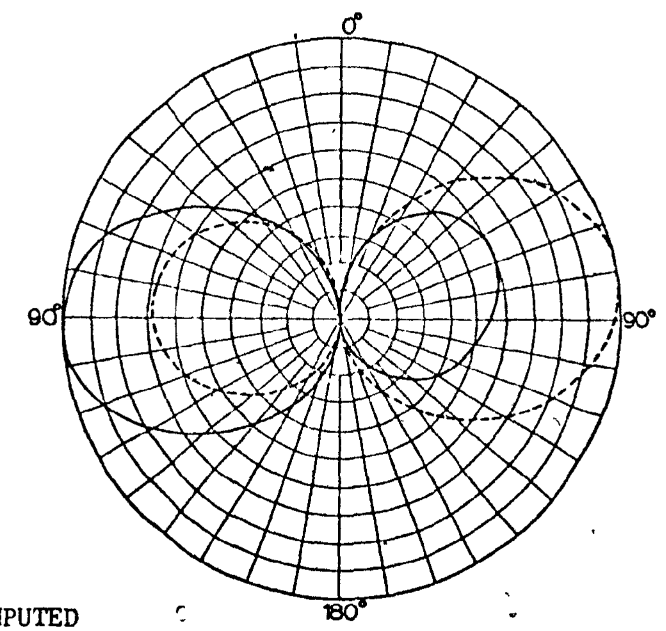

E_θ vs θ

$\phi = 0°, 180°$

FIGURE 4.14. FOLDED DIPOLE & MAST - INITIAL MODEL

- PRINCIPAL PLANE PATTERNS, f = 3020 MHz.

In their work the folded dipole is represented by a single source and conductors overlapping at the ends. The calculated results shown in Figure 4.14 show that such an arbitrary but simple model provides useless results. Hence a closer examination of the basic radiation model is required if better modelling is to be obtained.

4.3.1.1 Modelling of the Folded Dipole

Folded dipoles are discussed in most standard textbooks on antennas [85, 86, 87] but more exhaustive analysis is to be found in the articles of Carter [88], Roberts [89], Guertler [90] and the more recent articles of Harrison and King [91], Germain and Brooks [92] as well as King's classic book [63] on linear antennas. Roberts [89] and Wing, King and Mimno [93] suggested at about the same time that the folded dipole be considered to support symmetric and antisymmetric transmission line modes as represented in Figure 4.15.

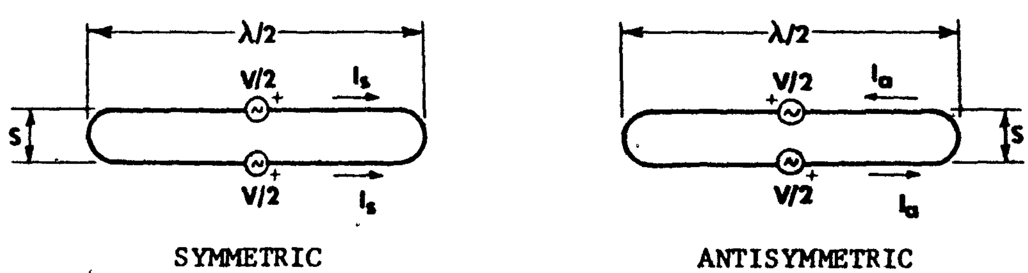

FIGURE 4.15. EXCITATION MODES - FOLDED DIPOLE.

In the antisymmetric case, the radiation is small since the currents are equal and opposite and closely spaced. For radiation calculations, therefore, the representation shown for the symmetric excitation mode seemed appropriate for use in the wire grid model.

Results of calculations with such a model are shown in Figure 4.16. Considerable improvement is evident. The pattern of E_θ vs θ shows remarkably good agreement. However the E_θ vs ϕ pattern does not agree as well as the measured and reference patterns. In the application of the antenna, more weight was placed on agreement of the E_θ vs ϕ pattern. Hence to improve the model a better representation for the parasitic supporting mast was sought.

4.3.1.2 Modelling of the Mast

A number of investigators have examined antennas around cylinders. An extensive bibliography is to be found in the work of Wolde-Ghiorgis [45]. Reference can be made also to the work of Carter [94], Lucke [95], Wait [96] and Sinclair [97]. Although these do not provide guidance towards improved modelling of the mast, they provide a background of detail for understanding the effect of spacing parameters on the radiation characteristics. The problem centers around the mast radius used, $a/\lambda = .2$ which is beyond the approximation condition ($a/\lambda \ll 1$) used to derive the approximate "thin wire" kernel. An examination of the pattern differences in Figure 4.16 and work on other structures reported by

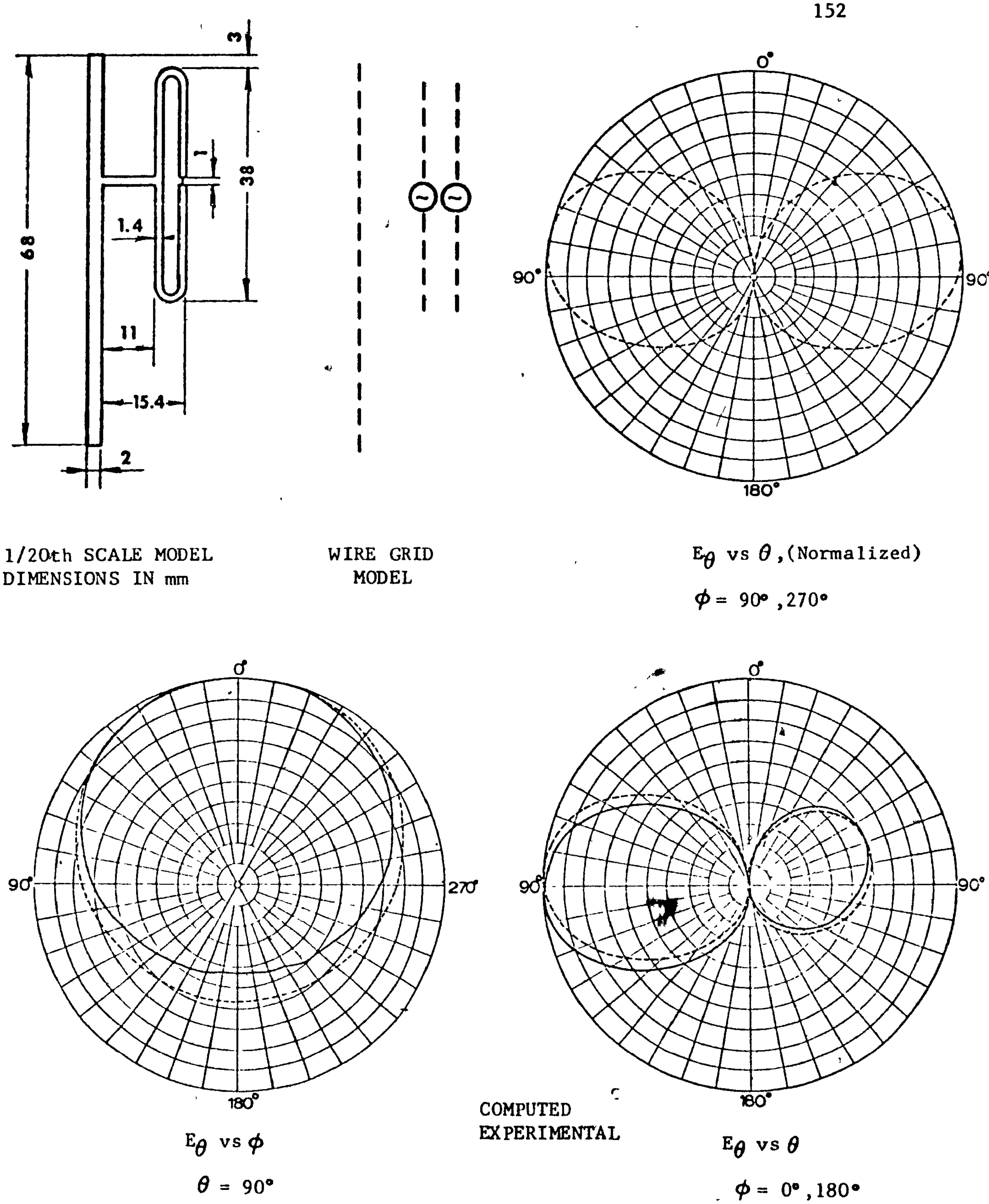

FIGURE 4.16 FOLDED DIPOLE & MAST - SECOND MODEL

- PRINCIPAL PLANE PATTERNS @ 3020 MHz.

Wolde-Ghiorgis [45] led to the modelling of the mast by two thin elements on diametrically opposite axial points as shown in Figure 4.17. This pre-supposes an edge-like current concentration on the diametric points on the axis of the elements and is further discussed in Chapter V.

Results here show that this model produces good agreement in both azimuth and elevation planes. The degree of this agreement was considered sufficient to establish that the characteristics of the scaled models were predictable and satisfactory for further measurements with the dipole alone, mounted on a helicopter. No further refinement in modelling was pursued. It is interesting nevertheless to make a comparison of the modelling steps and in particular of the current distribution.

4.3.2 Comparison of Current Distributions

The unknowns in the simultaneous equations obtained by the discretization of Pocklington's equation and point matching, are the currents on the individual wire segments. The program has also been arranged so that principal plane patterns or conical cuts can be produced at will. In Figure 4.18 the current distributions are shown for the 2nd model used. The current distribution on the elements of the 3rd and final model has been plotted separately in Figure 4.19. It is most evident here that the assymmetry in the E_θ vs θ pattern is due to the current shown on the longer bottom portion of the reflecting mast. It is to be observed that the

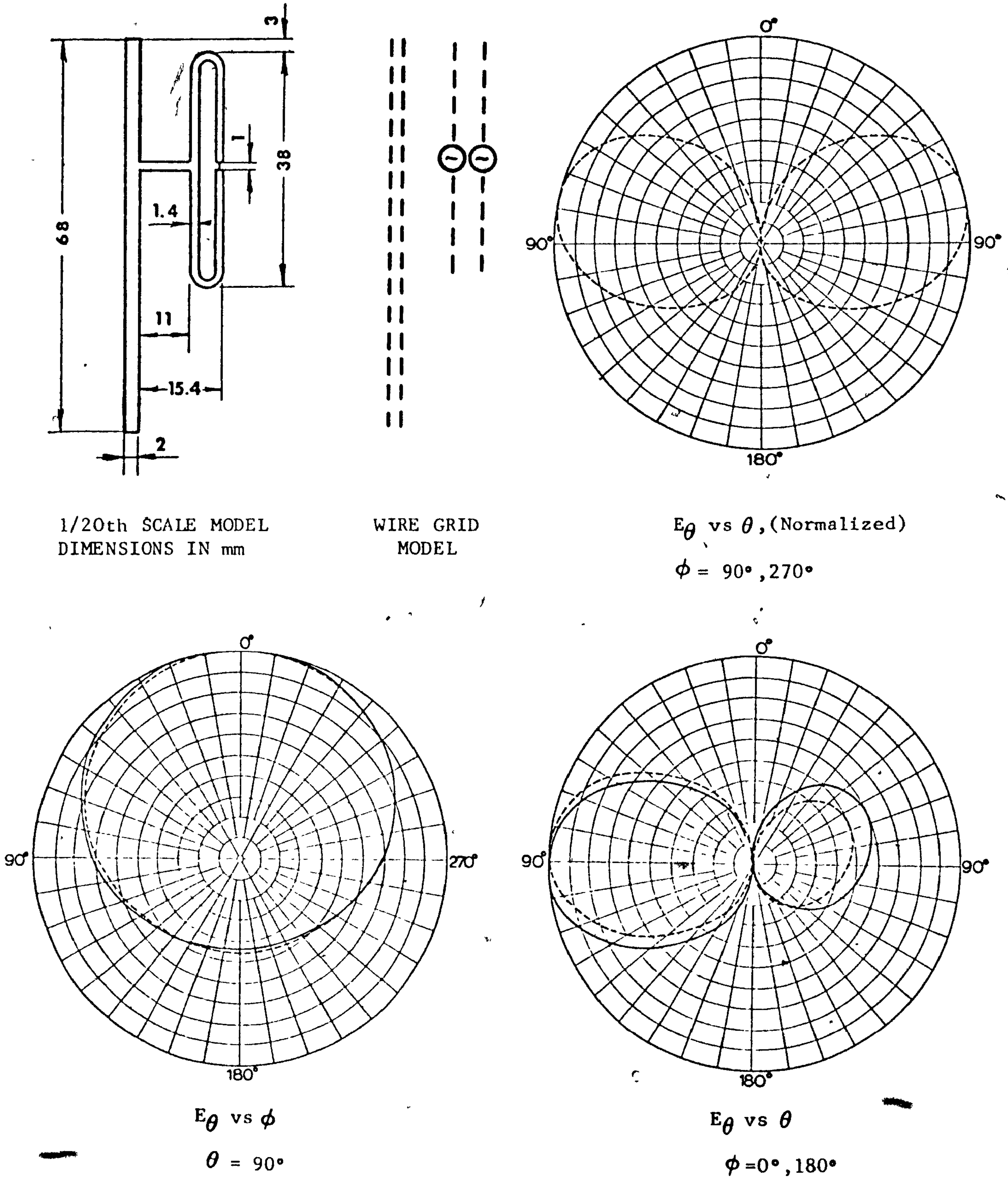

FIGURE 4.17 FOLDED DIPOLE - FINAL MODEL

- PRINCIPAL PLANE PATTERNS @ 3020 MHz.

relative amplitudes and phases of the currents on the two models are not vastly different. But it can be appreciated that when close agreement is sought, a general knowledge of the effect of spacing and length on the current values and hence pattern effects is very useful.

However, the appreciation of the physical possibility of having current concentrations at certain points and the insight into the effect of small current changes on the radiation patterns plays an important part in an iterative approach to modelling and especially in the modelling of more complex bodies.

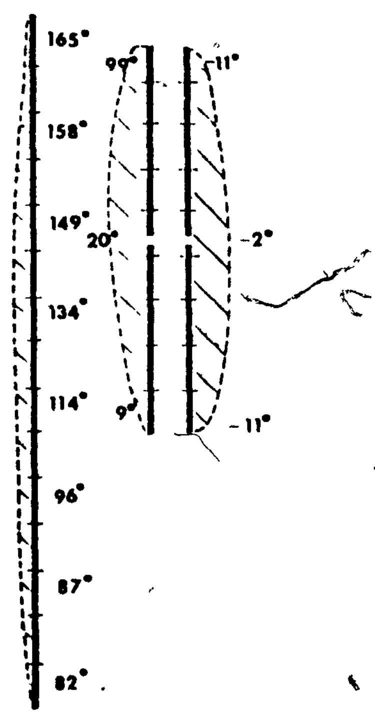

FIGURE 4.18 CURRENT DISTRIBUTION - SECOND MODEL

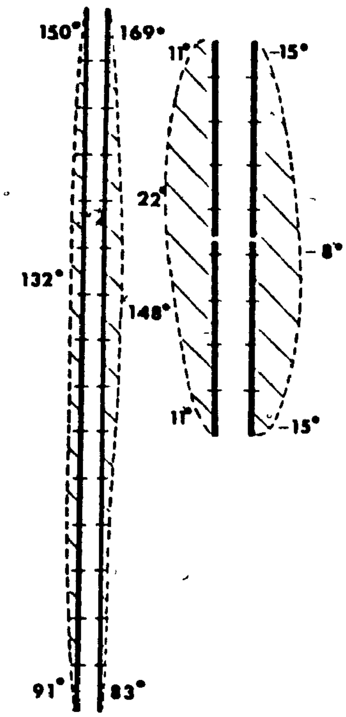

FIGURE 4.19. CURRENT DISTRIBUTION ON WIRE GRID SEGMENTS - FINAL MODEL.

4.3.3 Essential Factors in Modelling of Folded Dipole and Mast

The prime factors which were responsible for the development of an adequate wire grid model are as follows:

(a) The segment length used was from 0.042λ to 0.045λ. This segmentation is also consistent with that used by others [45,84] for radiation pattern and scattering computations. The substantial differences in the results for the models suggest that the use of other than pulse expansion functions would have been of secondary importance, while factors associated with the fundamental representation of the structure predominate.

(b) The identification of the characteristic modes of the radiator and their proper representation seems crucial. This might appear to be a truism after its substantiation, yet it has not been noted by other investigators or sufficiently tested since most of the work reported is with loops and simple dipole or monopole feeds [98]. Although a fundamental understanding of the radiation modes is essential, when experimental results are available an iterative procedure by analysis of results such as those in Figures 4.18 and 4.19 and helps in the development of a working model and perhaps in some cases the identification of the natural modes themselves.

(c) Thick elements, where the effect of non-uniform surface current distribution must be anticipated, are best represented by thin wire elements at the peripheral points where current concentrations are likely. In the case reported here, the two axial points were sufficient. For other radiators and thicker structures, Wolde-Ghiorgis [45] has examined the effect of the number of elements around the periphery.

These concepts are further tested and corroborated in the ground rod and the helicopter antenna models. Should computation of impedance or near fields be required, the tests of Section 4.2 and other work [84] clearly indicate that a greater number of segments would be required. For this purpose, on this type of linear structure, the sinusoidal basis functions should prove superior.

4.3.4 Versatility of Model: Bandwidth, Dimensional Variation

Once a working wire-grid model is obtained, its usefulness is similar to that of an analogue computer simulation of

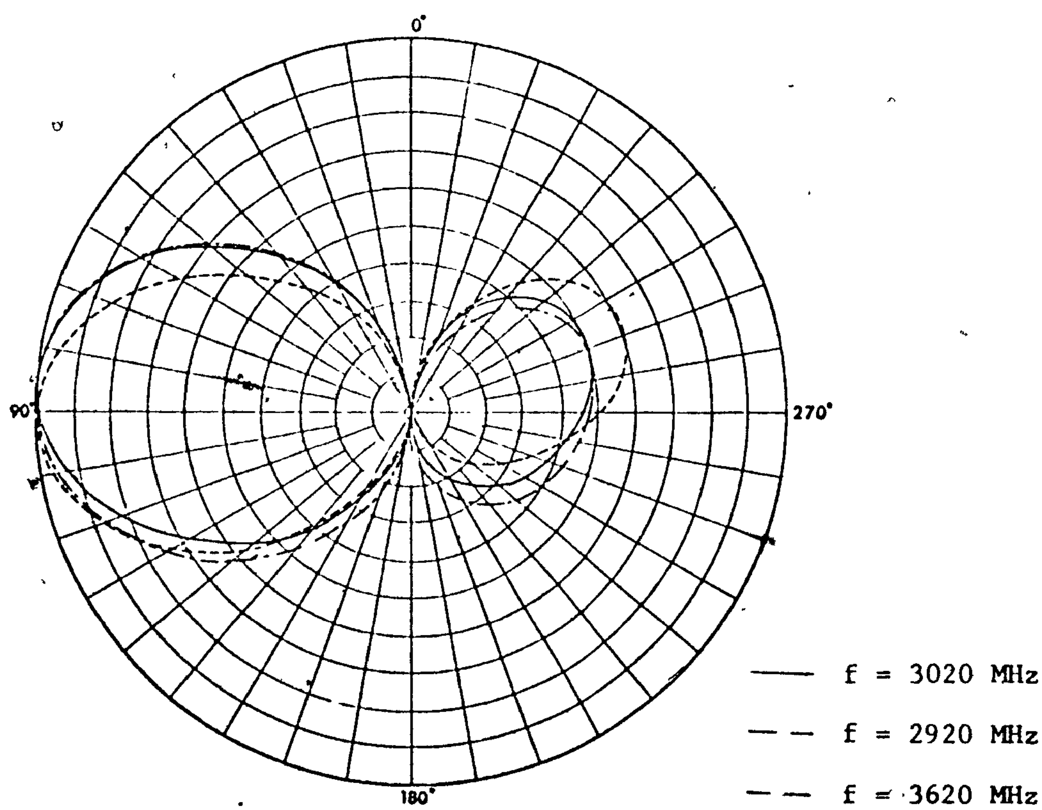

FIGURE 4.20 BANDWIDTH STUDY

a physical system. For example, the variation of the radiation pattern over the bandwidth of the antenna can be determined by merely changing the frequency parameter in the computer program. Figure 4.20 shows the radiation patterns at 2920, 3020 and 3620 MHz. It can be seen that the pattern variation is small.

With similar ease, dimensional changes can be studied. Figure 4.21 shows results with the second model using a symmetrical mast. The E_θ vs θ pattern is now seen to be symmetrical as expected.

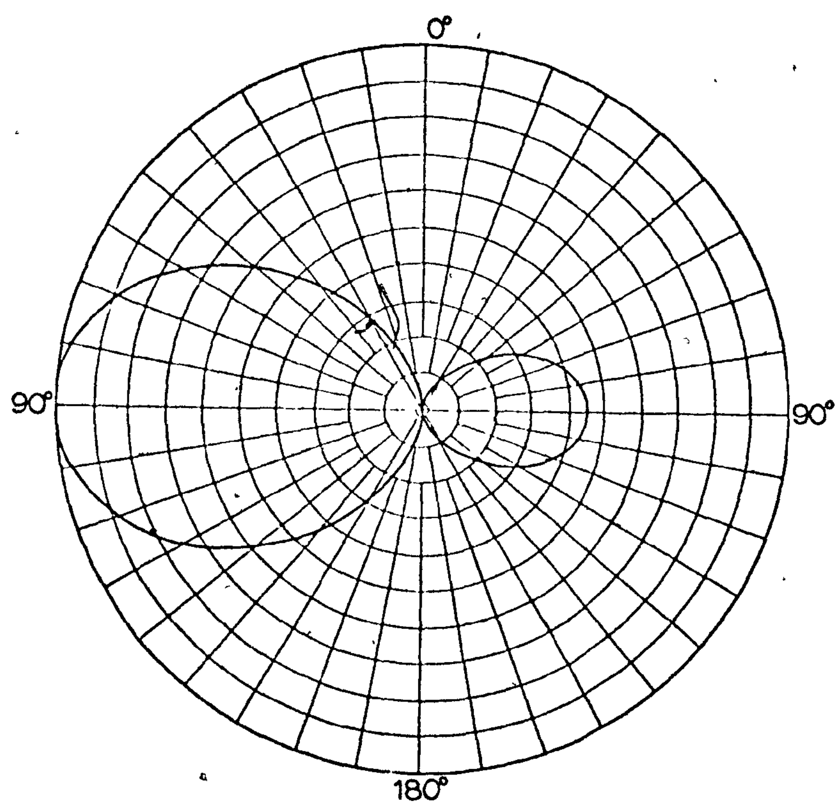

FIGURE 4.21 COMPUTED PATTERN WITH SYMMETRICAL MAST

4.4 Ground Rod Antenna

As noted in Chapter II, the sleeve monopole portion of the Sinclair 201 ground rod antenna was chosen as the vertical radiator for the field strength measuring system for the Bell 47G-4A helicopter. The various models built (Figure 3.23) did not exhibit the radiation characteristics reported by Tilston and Secord [56] near the $\theta = 90°$ plane. Since additional and more precise information on the measurement conditions was not available, a wire-grid modelling was undertaken to explain the measured results. Here again pulse basis functions and point-matching were used.

4.4.1 Modelling of the Antenna

A wire-grid model of this antenna type has not yet been reported in the literature. The structures closest in geometry are the quadrafin whose scattering properties were analyzed by Miller, Burke and Selden [84] and the monopole and ground plane studied by Wolde-Ghiorgis [45]. After repeated attempts, the modelling was almost abandoned because of the difficulty, for example, in establishing how much of the experimental model should be considered as radiating. Note that in Figure 3.23 the miniature connector dominates the model. One could argue that an impedance discontinuity exists at its upper end and hence the surface of the connector can be ignored. This turned out to be misleading and incorrect.

The ground rod antenna was developed by Brown [99]. Impedance characteristics were computed by Bouwkamp [100] and King [63]. The latter considers it as a generalized 90° V-antenna as shown in Figure 4.22.

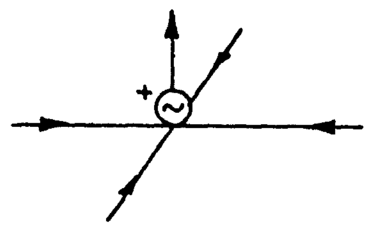

FIGURE 4.22. CURRENTS AND SOURCE, GROUND ROD ANTENNA.

Following this representation, a single source is used in the wire-grid model at the location of the feedpoint. Actual wire radii are used for the elements except for the connector portion. This portion is represented by two thin peripheral elements. The segmentation is shown in Figure 4.24.

4.4.2 Results

The computed E_θ vs θ patterns is shown in Figure 4.23 together with the measured results. The E_θ vs ϕ pattern is a circle as expected. The agreement in the pattern shape is acceptable.

Figure 4.24 shows the computed current distribution on the antenna sections. Also shown are the computed current distributions for other source locations. Changing the feedpoint changes the input impedance but is claimed not to alter the current distributions [56]. Here the element current plots of Figure 4.24 clearly show an impedance variation but also a current distribution change. This change affects the amplitude of the lower lobe. The variation is shown in Figure 4.25. Also shown is the radiation pattern of the antenna with feedpoint at the level of the ground rods (see Figure 3.23 (c)). This pattern also has the higher lobe predicted by the wire grid model.

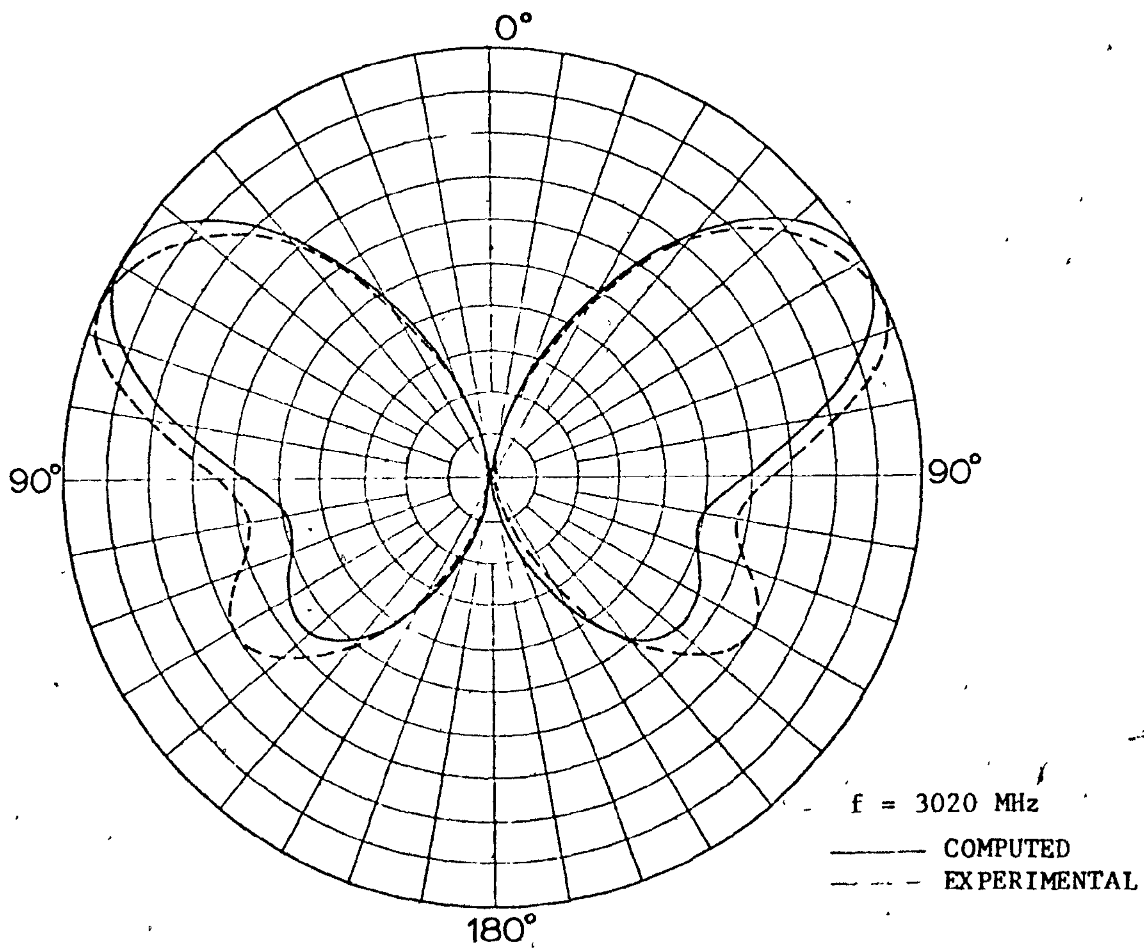

FIGURE 4.23 GROUND ROD ANTENNA - COMPUTED & MEASURED PATTERNS

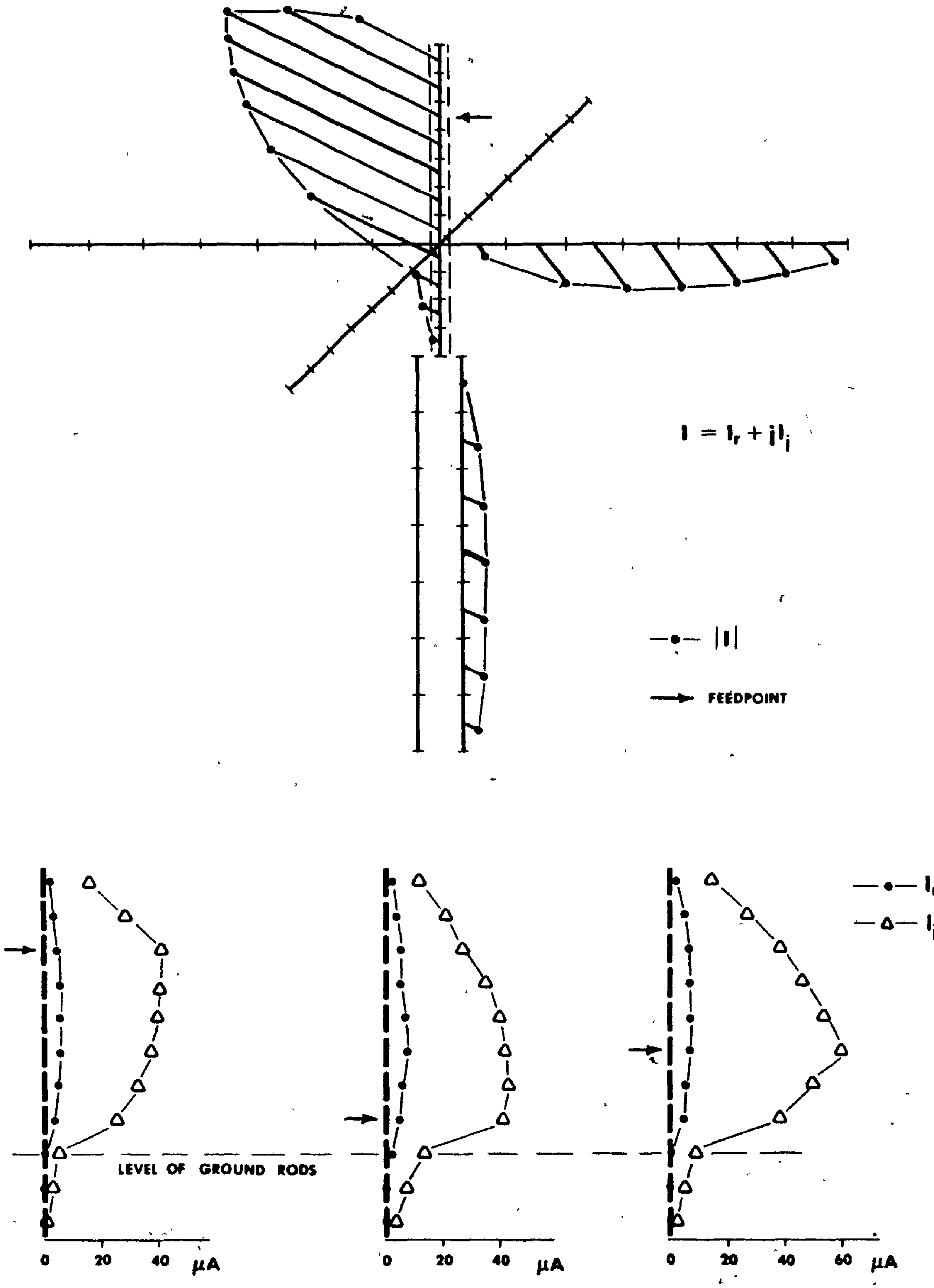

FIGURE 4.24 CURRENT DISTRIBUTION & VARIATION WITH FEEDPOINT

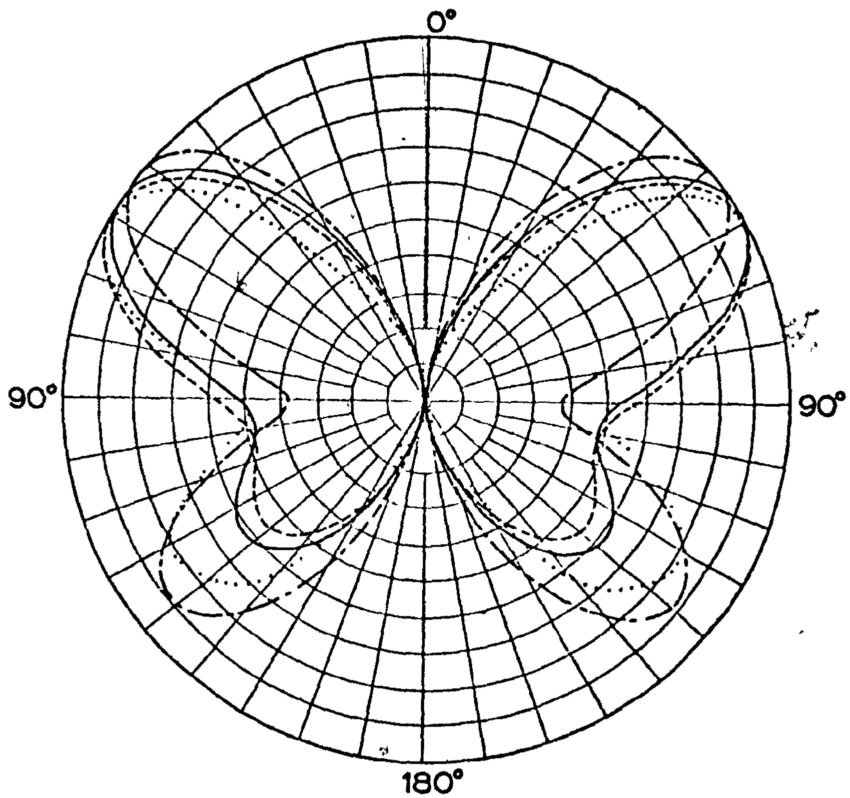

· EXPERIMENTAL, FEEDPOINT AT GROUND ROD LEVEL

— — — COMPUTED, FEEDPOINT AT GROUND ROD LEVEL

——— COMPUTED, FEEDPOINT MIDWAY (ACTUAL)

- - - - COMPUTED, FEEDPOINT AT TOP ELEMENT

FIGURE 4.25.

4.4.3 Factors in Modelling of Ground Rod Antenna

The development of an adequate wire-grid model involved the following factors and considerations:

(a) The segment length used was .029λ to .055λ, comparable to that used in the case of the folded dipole. With the smaller value used on the vertical element.

(b) It was essential that all the elements, which could support RF currents in the experimental model, be represented. Because of the thickness of the connector ($a/\lambda = .0176$) a minimum of two peripheral elements were required as with the folded dipole mast.

(c) In this assymmetrically fed antenna, the location of the source affected the current distribution which in turn indicated a driving point impedance change and produced a small but significant change in radiation patterns.

4.4.4 Other Uses of Wire-Grid Model

As with the folded dipole, the working model can be used for the study of dimensional changes, frequency variation and as seen above, for feedpoint location studies. The nature of the current plots suggests that these distributions could also be used in optimization studies to select the most efficient basis functions. This could be regarded as the experimental equivalent of the basis transformation technique used by Turpin [101].

4.5 Monopole on Bell 47G-4A Helicopter

An experimental model, Bell 47G-4A helicopter, is shown in Figure 4.26 and it may be noted that part of its tail structure is a truss resembling closely a wire grid structure.

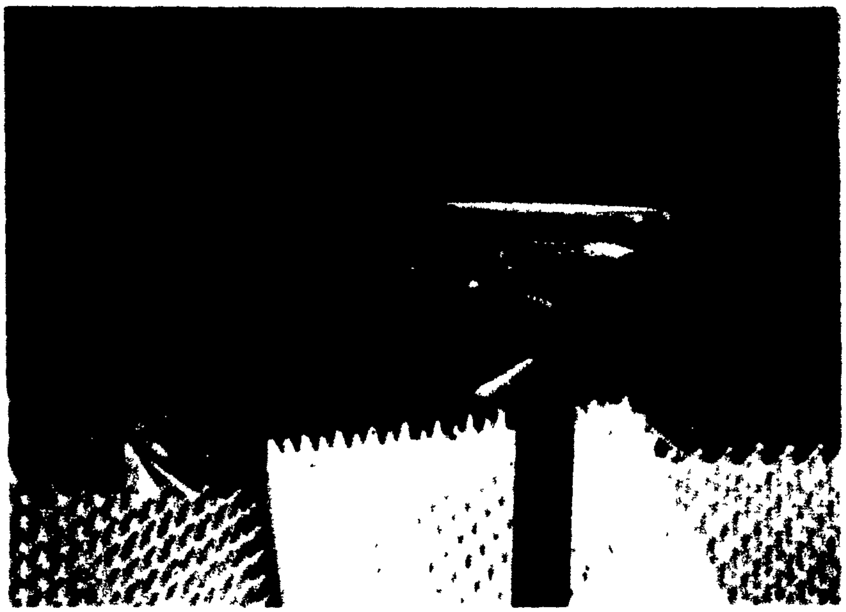

FIGURE 4.26. BELL 47G-4A HELICOPTER MODEL.

This structural form eliminates doubt as to where elements should be placed to represent this section. Surface areas, however, occur in the tail section, the cockpit, fuel tanks and the rotor blades themselves. At the frequency considered (675 MHz), the structure is approximately 1 and 1/2 λ long. The radiating monopole was mounted below the helicopter in line with the rotor axis as shown.

Modelling of the previous antenna forms involved linear antenna elements. Problems centered on the radius of the elements, source representation and location, inclusion of all radiating members and placement of elements on thick members. However, the antennas were of regular shape. Hence the regular or "canonic" forms proposed by Wolde-Ghiorgis [45] apply since there is not much doubt about the location of the stationary current flow lines. The number of elements necessary for the determination of radiation patterns is relatively modest (53-64), therefore computation cost is not a large factor in parametric experimentation. With the helicopter, problems on a different scale and of several types occur. The physical representation of the shape is several orders of magnitude greater in complexity, directly magnifying the possibility of error. Computer memory size limits the number of elements which can be used and computation category[1] and cost restrict parametric experimentation and increase "turn-around" time. Only limited guidance can be obtained from the concept of "stationary lines of flow" in regular shapes. It would be appropriate to say that Schelkunoff's comment [71],

> "-----Problem B presents many difficulties and it is the engineer's hard luck that he happens to be interested in just this problem",

applies equally well here. A realistic presentation is made of the steps which have been found to be important. The problem of the physical representation is similar to that faced in the construction of aircraft where special technical "master line"

---

[1] For example job class "G" (IBM 360/75) assures good 'turn around' but the 300 K memory limit allows only 176 segments while class "H" with 400 K memory allows 210 elements but requires a one-day turn around.

groups are responsible for accurate lofting data to be used for fabrication of master assembly jigs. There are no technical problems in this step but rather the difficulty of having correct information and using it without error. This difficulty has not been underestimated by others [75], [76], and is emphasized by the fact that close to 50% of the computation effort was expended either to remove errors or carried out with undetected errors. Although a chronological presentation would be most effective in demonstrating the various errors encountered, it is used with restraint in the material which follows.

Once again pulse basis functions and point matching were used, with both a magnetic frill source and a delta-gap generator.

4.5.1 Modelling of the Helicopter

Where should the finite elements be placed? How many are needed? What are the co-ordinates of the end points? What radius should be used? These are the questions which need to be answered in the development of a suitable model. The objective is to obtain data cards with co-ordinates of the end points for each finite element and to use these as input for the segmentation subroutine of the program.

The best primary source information is of course the "master lines" data used in aircraft design, usually available as a series of co-ordinate values together with precise contour drawings. These were not available for this helicopter. The source information was a set of detail drawings used for the construction of the 1/20-th scale model. From these drawings and a set of large photographs of the model, three-view drawings of the structure were prepared to scale using element lines only. Element length was generally kept under .1λ. Each element and junction was numbered and tables were prepared listing each element, its end co-ordinates and the junction numbers. These lists were scanned element by element for accuracy of co-ordinates and end points. A total of 274 elements was tabulated and data cards prepared.

A WATFOR program was used to produce listings of these points together with their co-ordinates, their lengths and the α and β angles defined in Section 4.1. The length values were scanned for errors and closeness to the .1λ value set, and the α and β angles were examined closely for agreement in segments judged to be in the same direction on the drawigns. In this manner several errors were detected and removed prior to the final computer runs. In spite of these precautions other errors remained undetected at this time.

During later phases of the modelling development, a CALCOMP three-dimensional program was completed which permitted the plotting of the three-dimensional figure from the data cards. The model could be rotated to any angle of viewing, the elements numbered alongside their center and individual sections of the structure expanded for closer examination. The large scale 3-wiew drawings and large CALCOMP plots are not included in this work, but a replica of three presentations is shown in Figures 4.27, 4.28 and

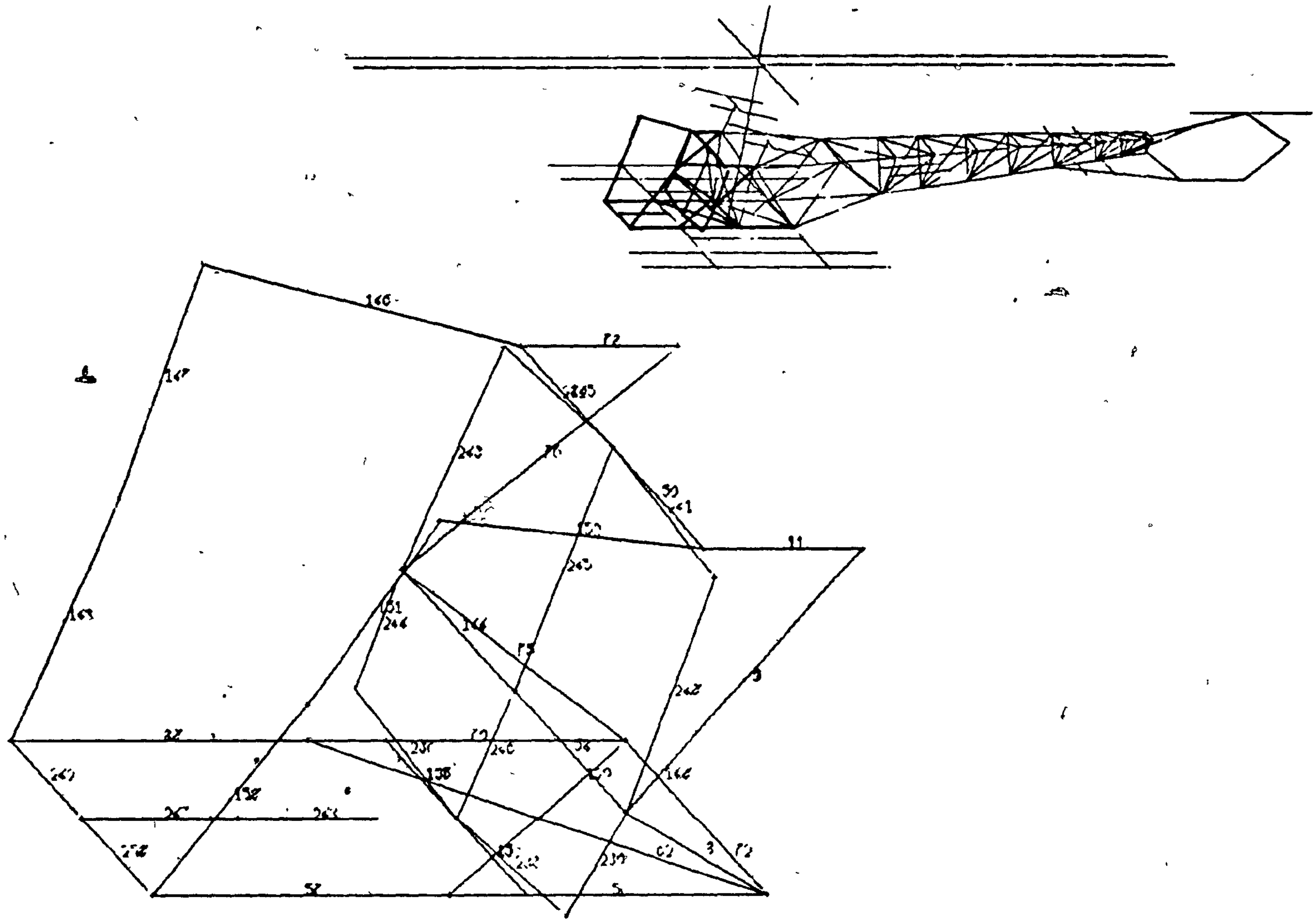

FIGURE 4.27 WIRE GRID MODEL OF HELICOPTER & COCKPIT SECTION.

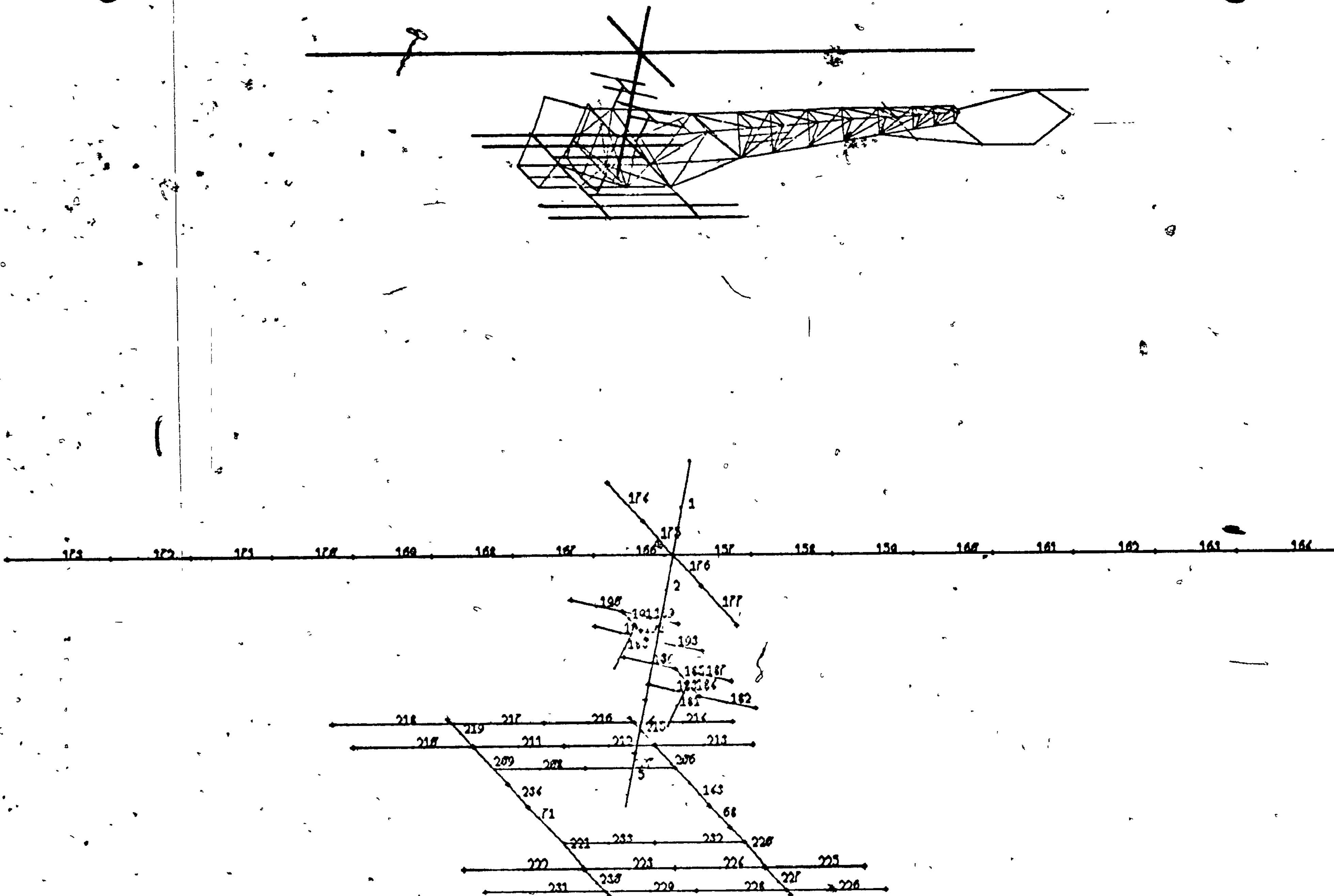

FIGURE 4.28 WIRE GRID MODEL OF HELICOPTER & LANDING GEAR, FUEL TANKS, ROTOR.

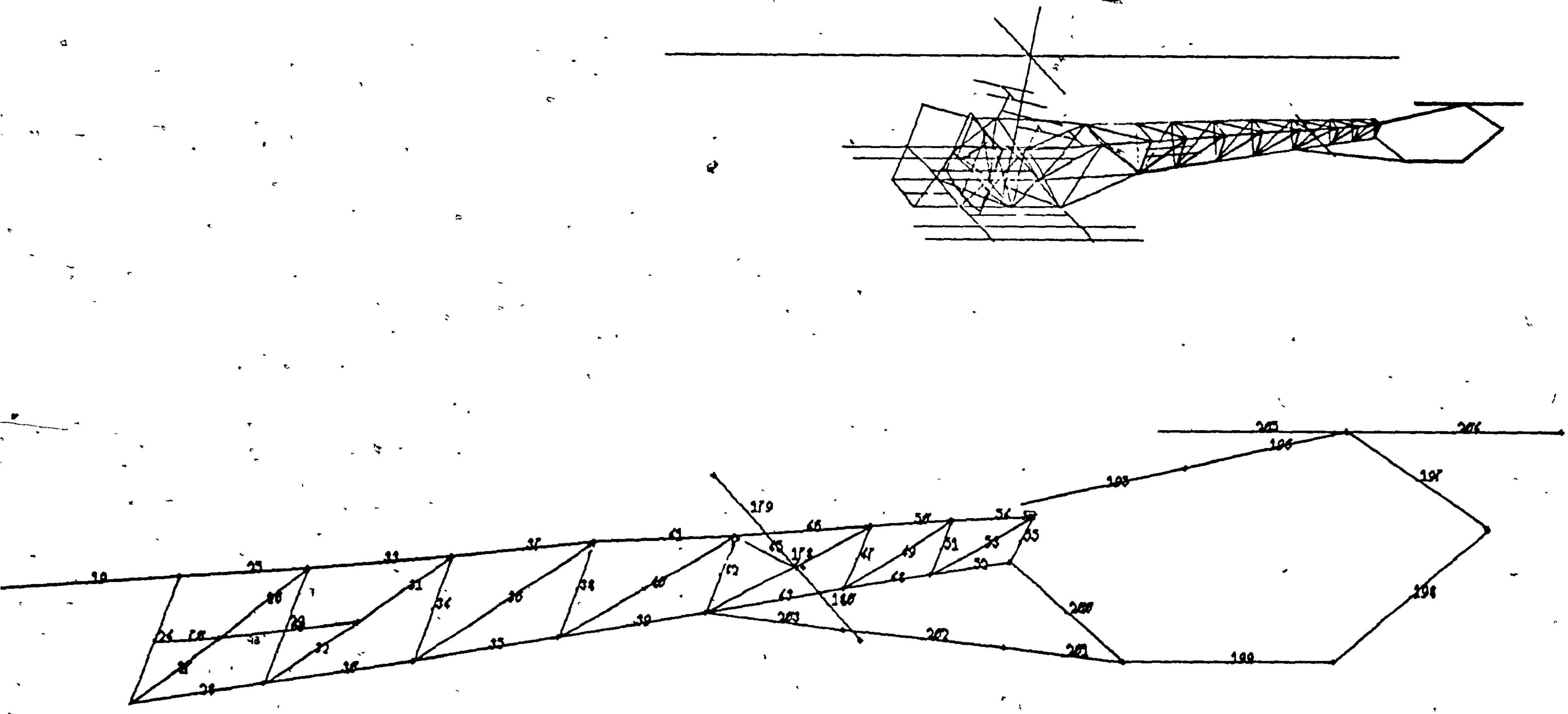

FIGURE 4.29 WIRE GRID MODEL OF HELICOPTER & PORT TAIL SECTION.

4.29. These show sections of the cockpit, fuel tanks and landing gear, and the tail section, expanded and numbered. Clearly such a presentation is most useful in the spotting of errors and one major one would have gone undiscovered were it not for the unambiguity of this presentation. The program might also be used for the plotting of computed currents.

The illustrations also show some of the approximations used in the modelling.

(a) The rotor and horizontal stabilizer were represented by one line of finite elements initially. Later, elements on the leading and trailing edges were used as shown in the frontispiece.

(b) The rudder section in the tail was represented by peripheral elements initially. Later vertical elements, extensions of the vertical tail section elements were tried as well as some diagonal elements

(c) The fuel tanks were represented by the peripheral elements shown, although for the runs with minimum elements, only the outer members were used.

(d) The bottom of the cockpit was assumed to be at the same level as the landing pad. Peripheral and central elements in the door area and finer segmentation at the base were tried.

(e) Initially the mesh section on the landing pad (see Figure 3.26) was represented by the peripheral elements shown and later by semi-diagonal and parallel elements in turn.

(f) Other elements were placed along the tubular members of the structure as shown.

The general guideline used in the modelling was to place elements along all edges and continuously along all peripheral lines which could govern longitudinal or lateral resonance of the structure.

The actual diameters of tubular members and thicknesses of sheet metal parts were used for the assumed diameters of the wire grid elements. The actual monopole diameter was used in its representation and it was divided into 5 elements. The monopole was .268λ long at 675 mhz.. The final segmentation produced elements ranging in length from .03 to .16λ.

Having obtained a reasonable representation with some 270 elements, the program could not be executed since only 176 elements could be used with the 300 k bytes of memory and 210 elements with the 400 k bytes of memory available on the computer. It remained to apply some intuitive reasoning or guidelines for the elimination of 30% of the elements.

4.5.2 Computations, Variants & Results

The computations and results are summarized in major groups or steps, generally in the sequence of their execution.

The minimum number of elements was sought using the following considerations.

(a) Keeping all elements in the immediate vicinity of the radiator: landing gear and bottom of seat.

(b) Keeping all edge elements along the periphery.

(c) Deleting inner elements of fuel tanks.

(d) Deleting elements in the tail structure which might be in areas of assumed weak current concentration or orthogonal to the current flow lines. Here an intuitive reasoning based on detailed examination of the measurements of Carswell [43] was used.

(e) Using single elements for rotor and horizontal stabilizer.

(1) Figure 4.30 shows the major elements deleted to obtain 176 elements and the results obtained at $\theta = 70^\circ$ and 80° with rotor parallel. These results are compared to the normalized measured values of Figure 3.28 and 3.29. The

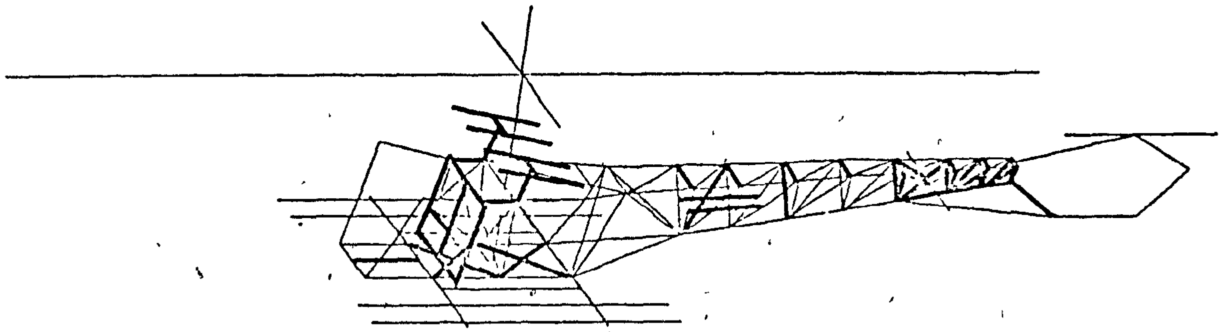

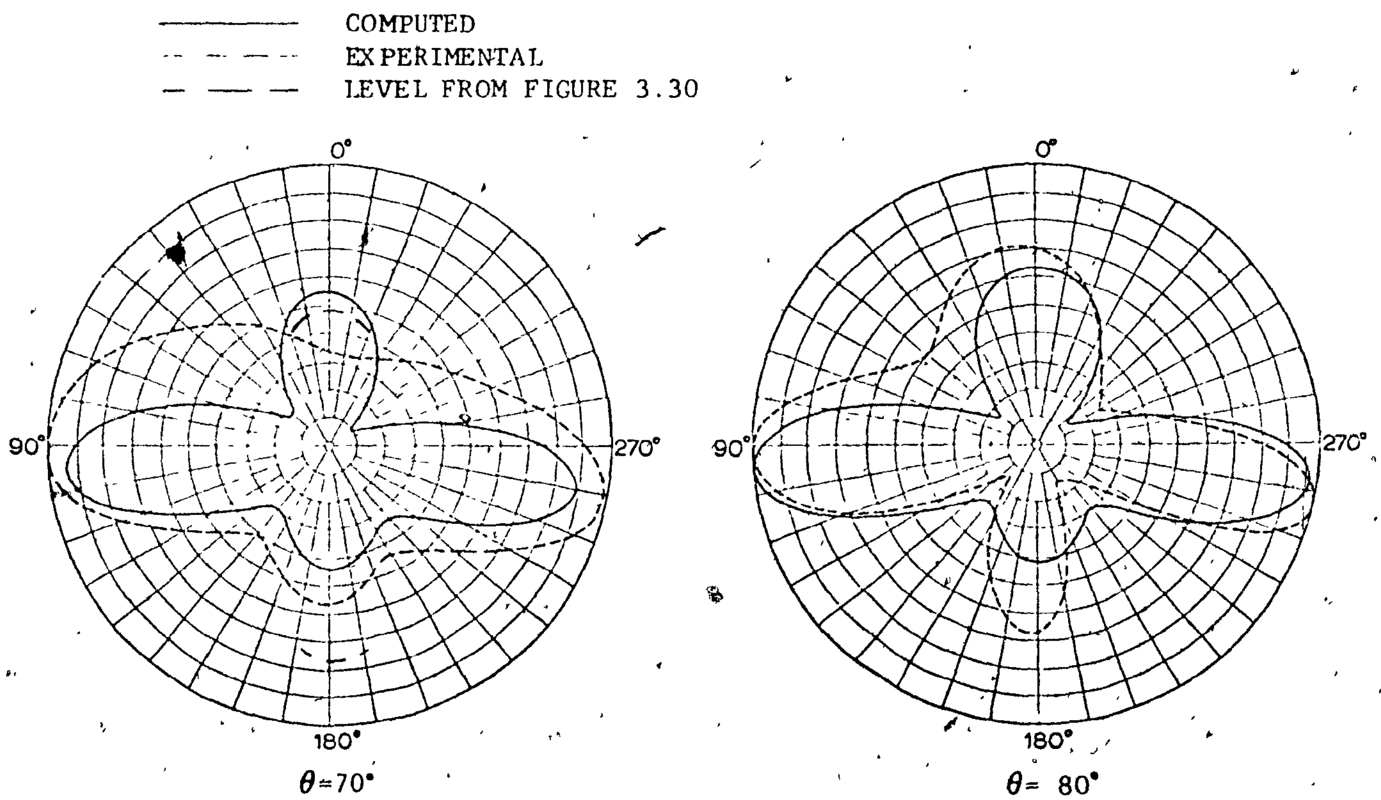

FIGURE 4.30 COMPUTED RADIATION PATTERNS - 176 ELEMENTS, E_θ^2 vs ϕ , f = 675MH

suppression of the front lobe in the $\theta = 70^\circ$ pattern is recognized by outlining its probable level based on the results of Figure 3.30. The results show surprisingly good agreement in view of the drastic reduction in the number of elements. Since the plot is on a linear power scale, the results are in fact comparable to those reported in the literature [76] for similar structures. The computer time involved was about 3 and 1/2 minutes representing a commercial cost of about $50.00.

(2) Further testing showed some small discrepancies in α-angle values which were corrected and additional elements were added while trying to maintain element symmetry on the model. With 203 elements, slightly better results were obtained. These are shown in Figure 4.31. An improvement in the E_ϕ pattern also occurred but this is not being considered in detail since the measured E_ϕ level was 10 db below the E_θ level.

(3) Changes were made to the program to improve the linkage with subroutines and to improve the graphical output. At this point further errors (max. 20%) in length of two segments were discovered and corrected and three elements were added. The results are shown in Figure 4.32. Clearly they bear negligibly small resemblance to the measured values and were not anticipated! Execution time on an IBM 360/75 was about

4 and 1/2 minutes representing a commercial cost of approx. $60.00. Because of the limitation on the number of elements used and the substantial cost of each run, the range of possible experimentation was now limited. One conclusion which suggests itself is that seemingly correct results may be obtained fortuitiously possibly, as a result of errors in modelling detail because some elements play an especially critical role. After another complete test for errors, it was decided to concentrate on changes in the cabin and landing gear area rather than further attempt to isolate details of this phenomenon at this stage.

(4) A diagonal element was added to the representation of the cabin in the door area. The rationale for this otherwise intuitive choice was an effort to improve representation of the cabin surface. The results, shown in Figure 4.33, once more show the desired main lobe structure. This result represented the limit of experimentation which could be undertaken without undertaking massive re-programming using partitioned matrices or matrix manipulative languages (MATLAN). In June of 1972, however, 1 million bytes of core memory became available on an IBM 360/65 and arrangements were made[1] for its use. Increasing the matrix size to permit 214 elements allowed the representation of the meshed portion of the landing gear by semi-diagonal and parallel elements. Results for both schemes are shown in Figure 4.34. There is better agreement now with measured values than that shown in Figure 4.33, mainly in the reduction of

[1]Courtesy of Loyola with Computel, Ottawa.

the front lobe and a slight change in direction of the side lobes. The difference in representing the mesh by parallel or semi-diagonal elements is not large enough for firm conclusions to be made. The E_ϕ patterns were also similar in level and lobe structure.

(5) With agreement between experimental and computed values now at a reasonable level it was logical to seek and expect better agreement if additional elements were included. The execution times on the IBM 360/65 for the last runs were approximately 7 minutes and costs exceeded $100.00 per run. With 600 k bytes of core, 254 elements could be used. Execution time was above 10 minutes and costs proportionately higher. The elements added and the results obtained are shown in Figure 4.35. The graphs are surprising and interesting. Their significance is not readily apparent. By implication they reflect on the success of the intuitive insight and heuristic approach built up by progressive testing and evaluation and the fallacy of assuming that more arbitrary elements will assure convergence. However, this was difficult to quantify methodically in view of the problem complexity and cost. A simultaneous examination of the current distribution was found to be helpful in trying to establish differences between runs, where changes should be contemplated, and

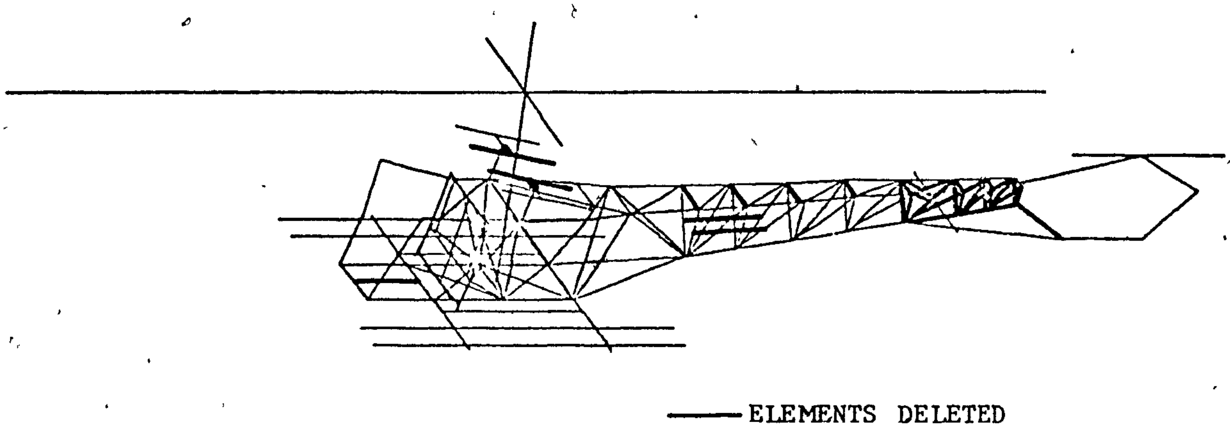

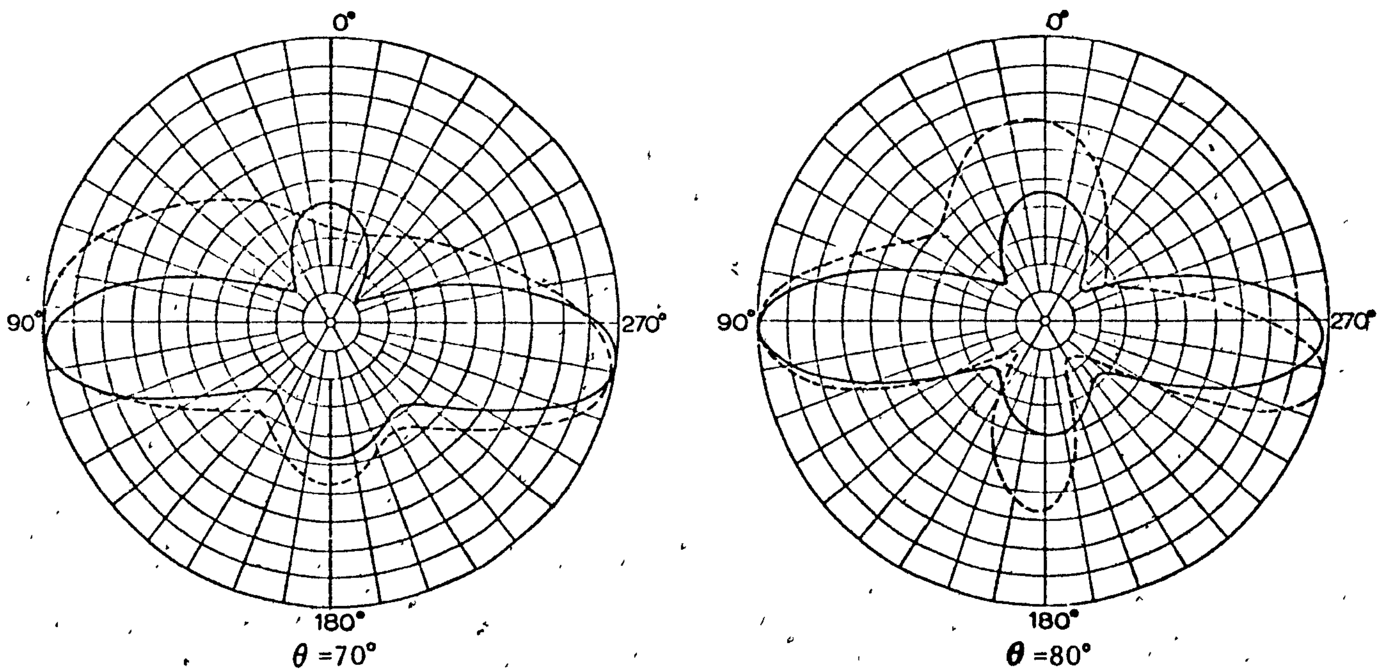

FIGURE 4.31 COMPUTED RADIATION PATTERNS - 203 ELEMENTS, E_{θ}^{2} vs ϕ, f = 675 MHz

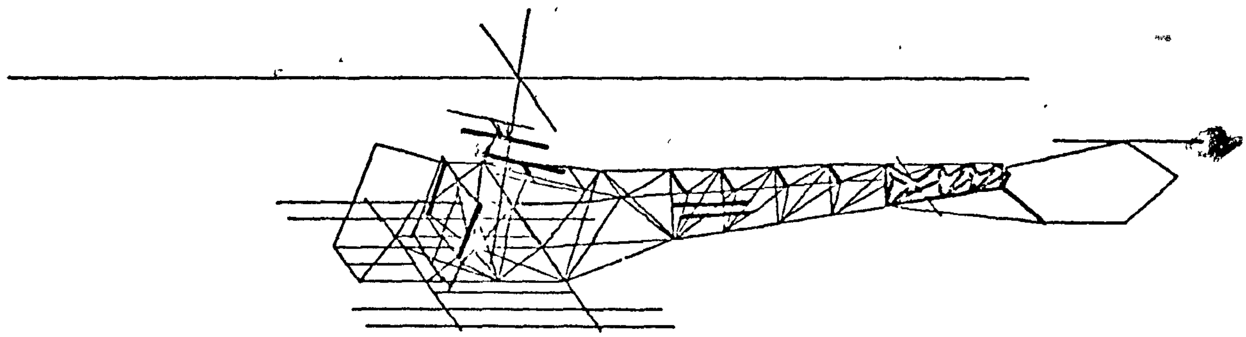

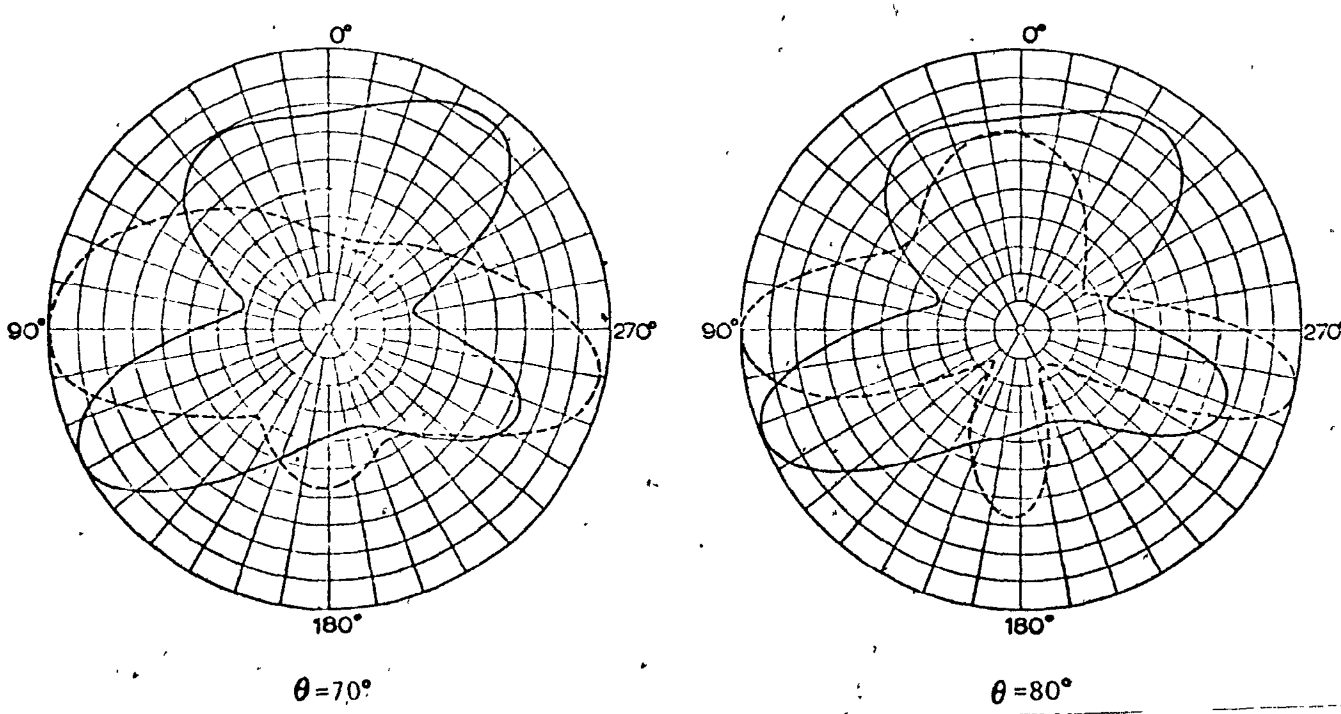

FIGURE 4.32 COMPUTED RADIATION PATTERNS - 206 ELEMENTS (CORRECTED)

E_{θ}^{2} vs ϕ, f = 675 MHz

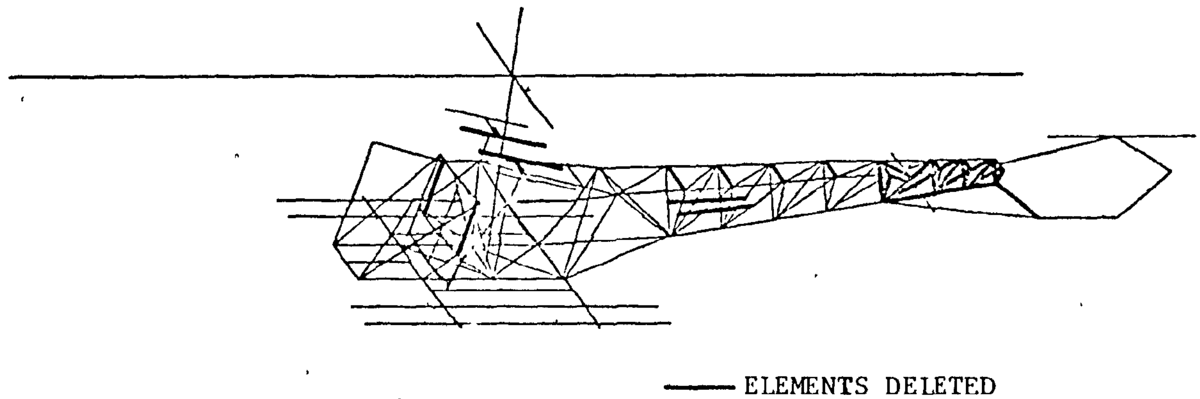

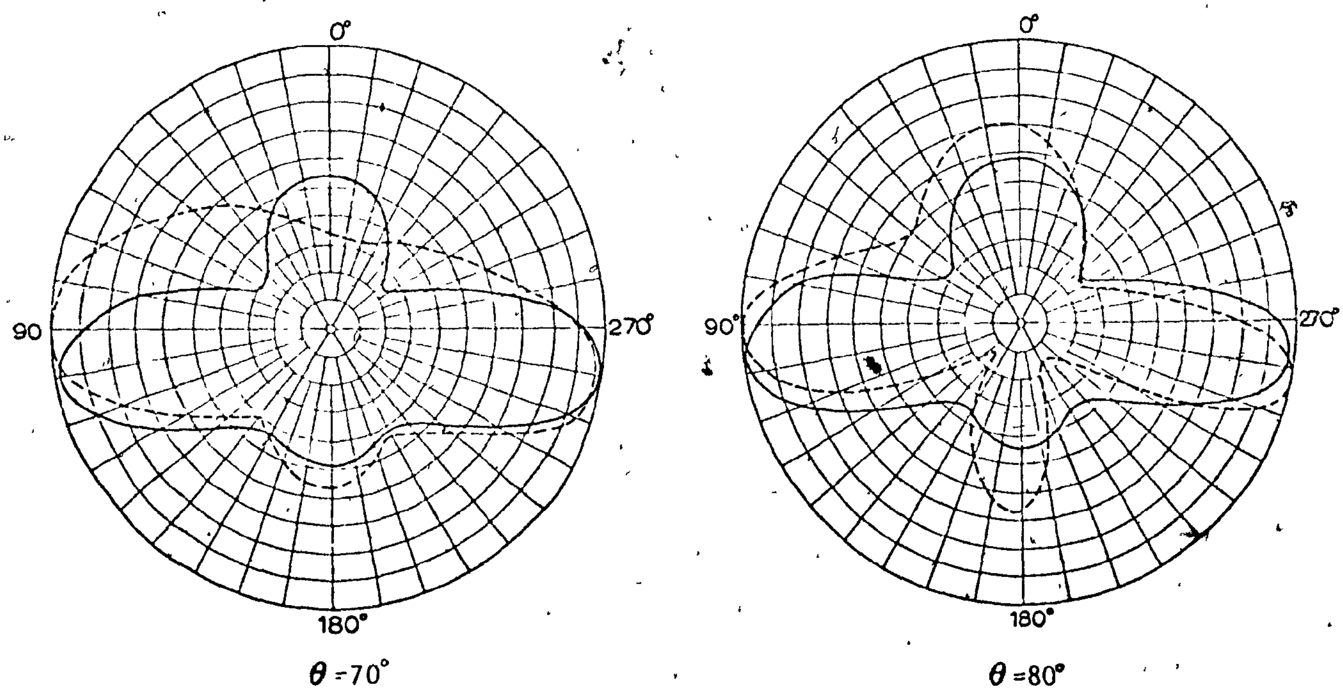

FIGURE 4.33 COMPUTED RADIATION PATTERNS - 208 ELEMENTS, E_θ^2 vs ϕ, f = 675MHz

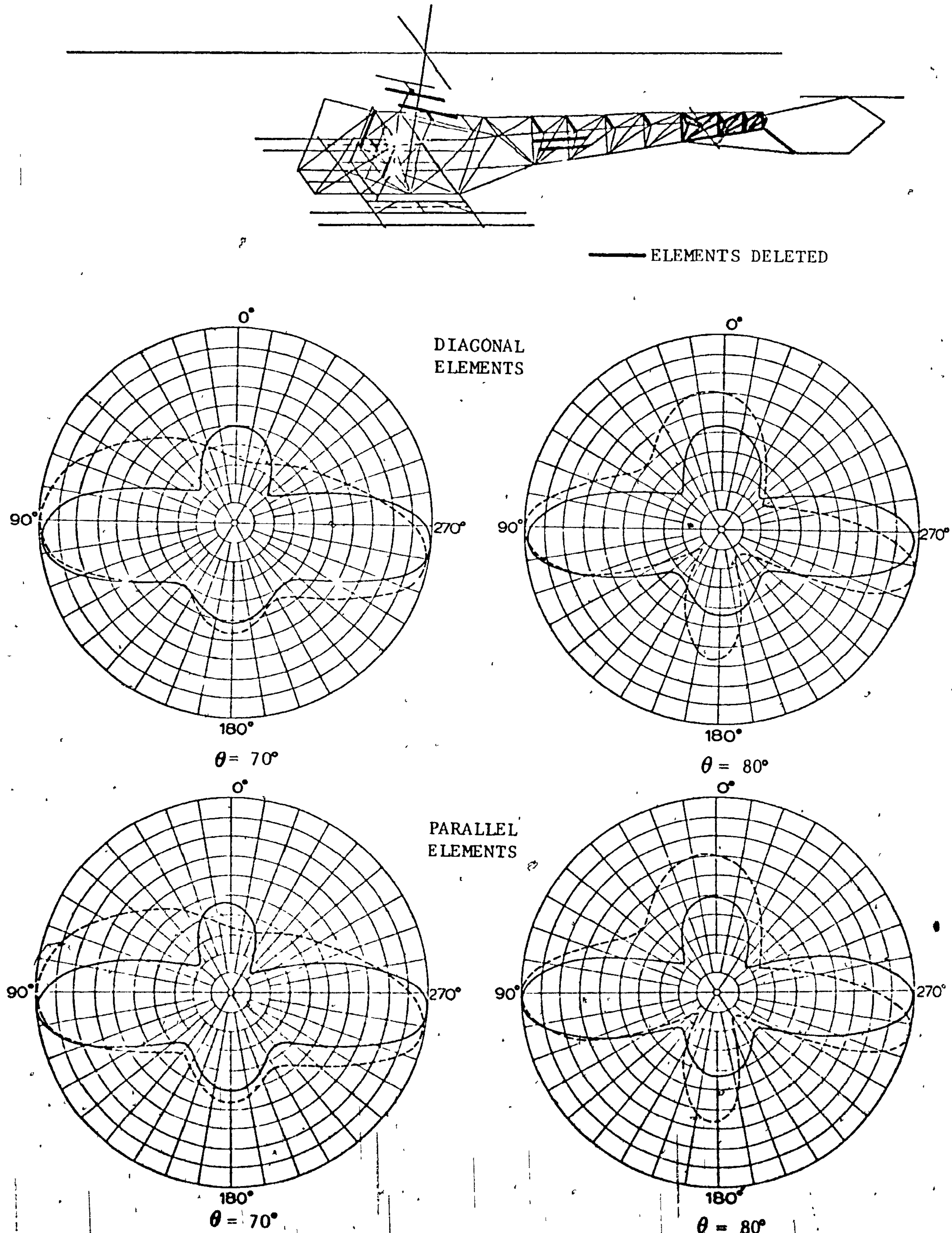

FIGURE 4.34 COMPUTED RADIATION PATTERNS, DIAGONAL & PARALLEL ELEMENTS IN LANDING GEAR, E_θ^2 vs ϕ, f = 675MHz

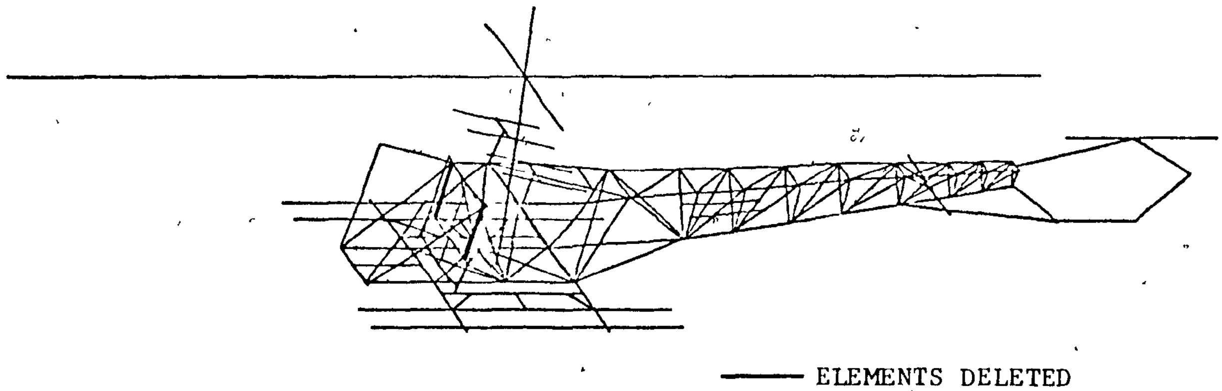

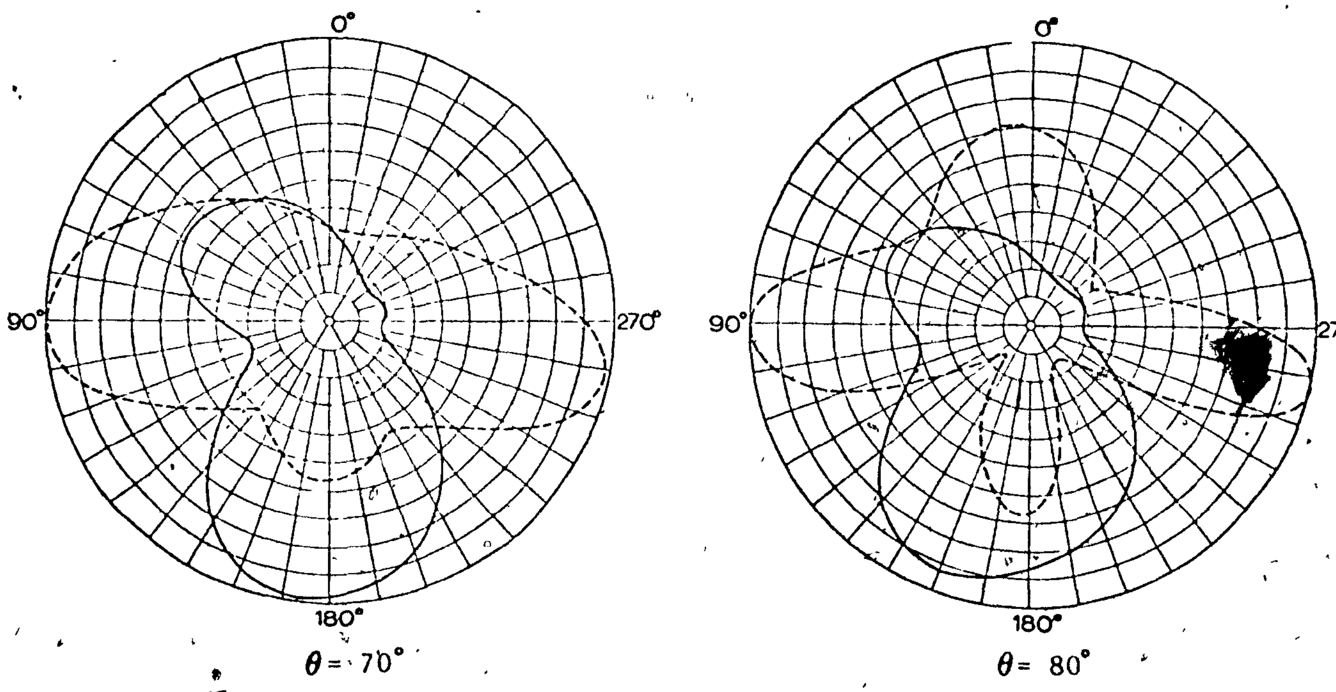

FIGURE 4.35 COMPUTED RADIATION PATTERNS - 254 ELEMENTS, E_{θ}^{2} vs ϕ, f=675MHz

generally whether the current distributions themselves were reasonable. Based on such an examination it was found that an unusually high current concentration was computed for segments of the tail near the horizontal stabilizer. Elements were placed along the leading and trailing edges of the horizontal stabilizer and different representations of the rudder section were tried as shown in Figure 4.36.

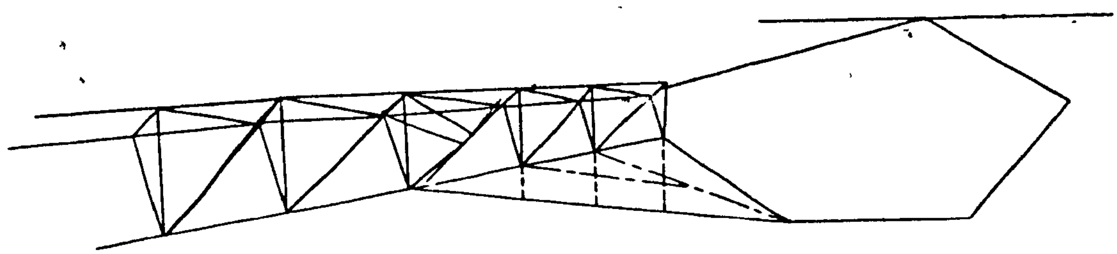

FIGURE 4.36. TAIL SECTION REPRESENTATION.

None of these produced pattern convergence. A series of tests was then undertaken to remove elements orthogonal to the longitudinal elements of the tail section, working back towards the representation used in Figure 4.34.

(6) The progressive removal of orthogonal elements produced convergence to the measured patterns once more. This is illustrated in Figure 4.37. The test of leading and

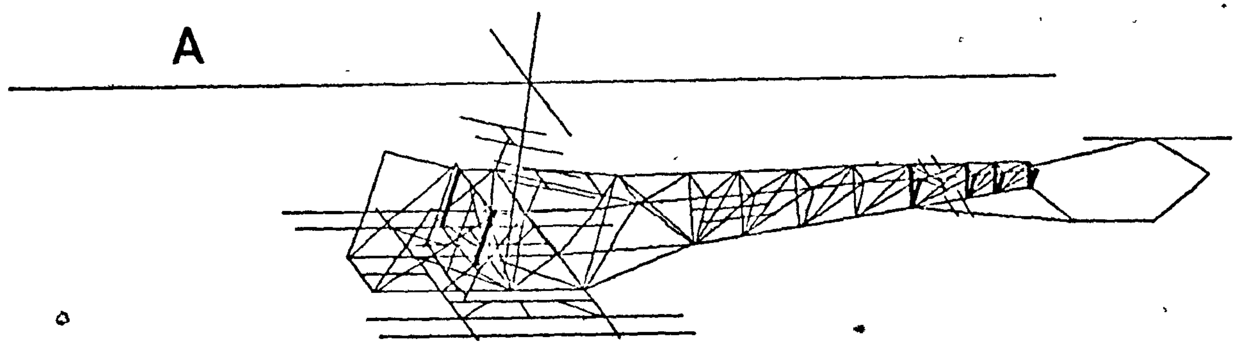

ELEMENTS DELETED

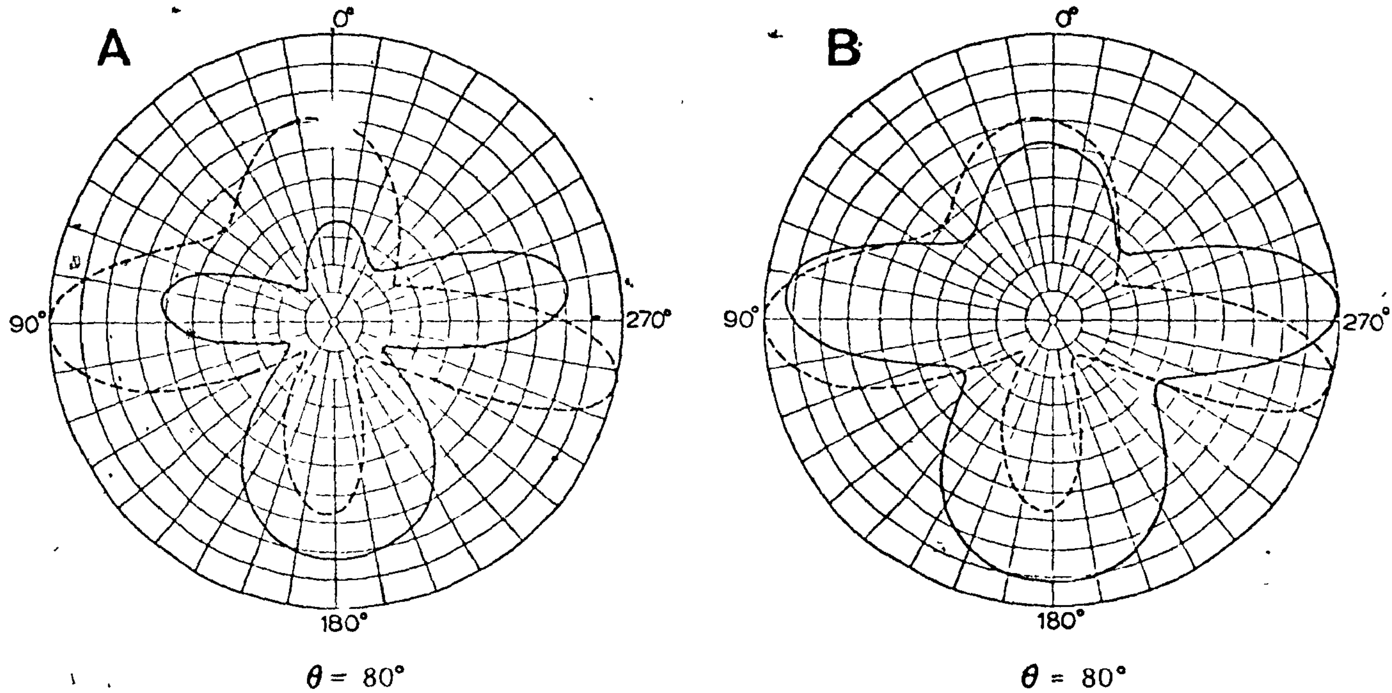

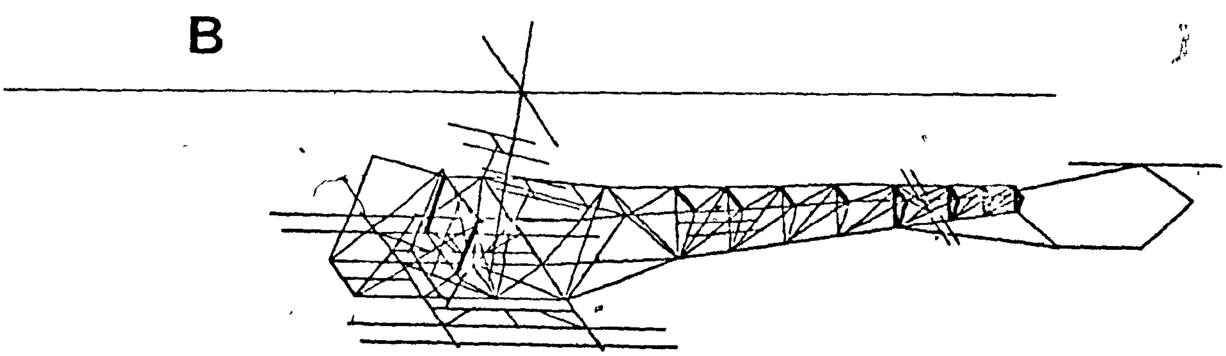

ELEMENTS DELETED

FIGURE 4.37 EFFECT OF DELETING ORTHOGONAL ELEMENTS.

trailing edge elements on the main rotor blades was tried when the E_θ patterns were divergent, hence no positive conclusion could be drawn. However, the E_ϕ patterns were generally at the same level as measured values and of the same form.

Further experimentation was not possible at this stage for practical and economic reasons. Therefore, the results of Figure 4.34 represent the closest convergence in modelling at this time.

4.5.3 Rotor Modulation

The wire-grid model of 214 elements which gave the results of Figure 4.34 was also used with the rotor perpendicular to the fuselage in order to determine whether this change would produce a pattern change. The results are shown in Figure 4.38 together with measured values for $\theta = 70^\circ$ and $\theta = 80^\circ$. A pattern change is obtained and it is comparable to the change in measured patterns.

The current output of the computer program allows the examination of the change in amplitude and distribution of current values. They are shown plotted on selected elements of the model in Figure 4.39. Comparison of these values also improves the appreciation of the current change needed to produce the pattern differences noted. Examination of the current distribution on the

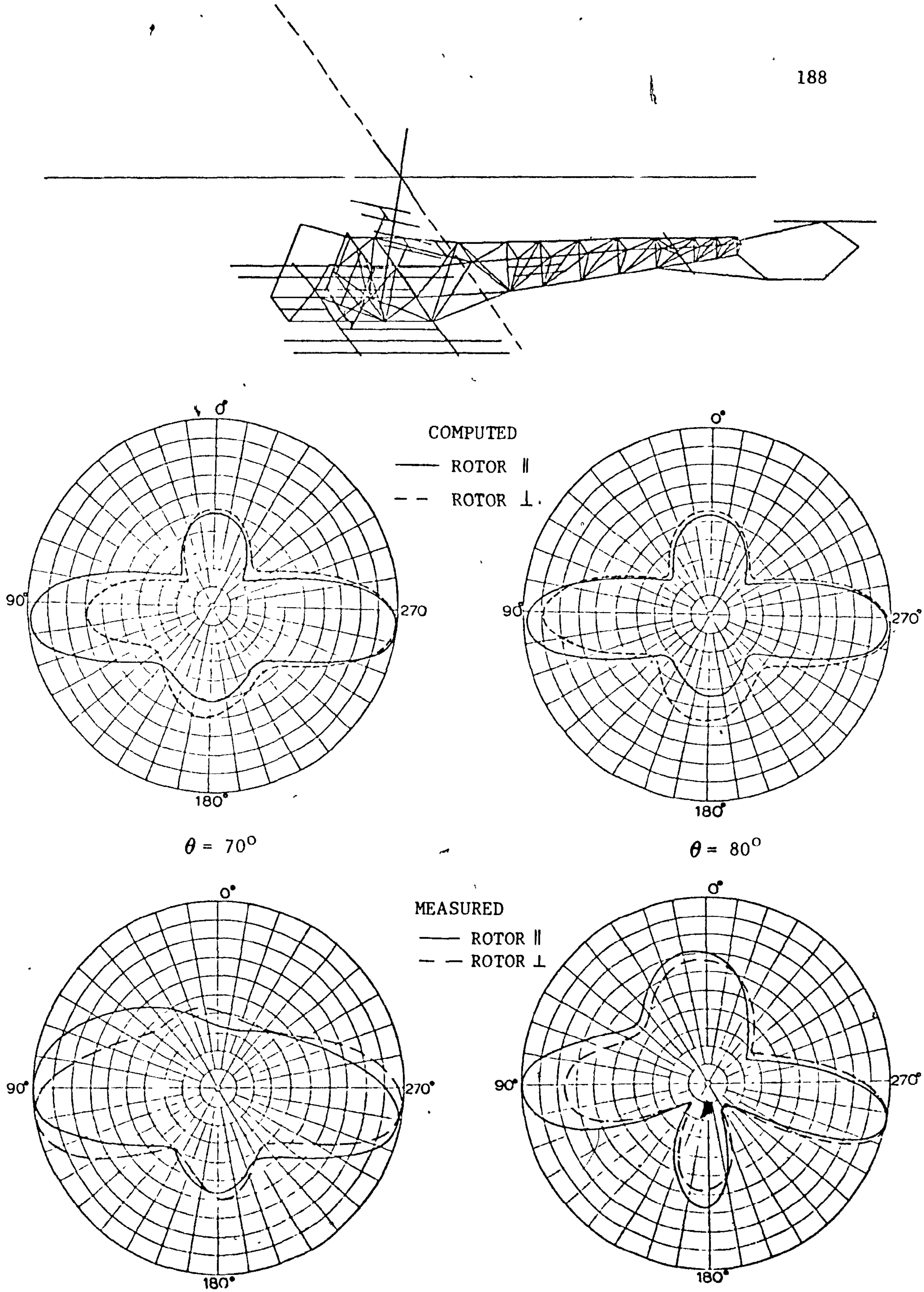

FIGURE 4.38 EFFECT OF ROTOR MODULATION

ROTOR $\parallel$

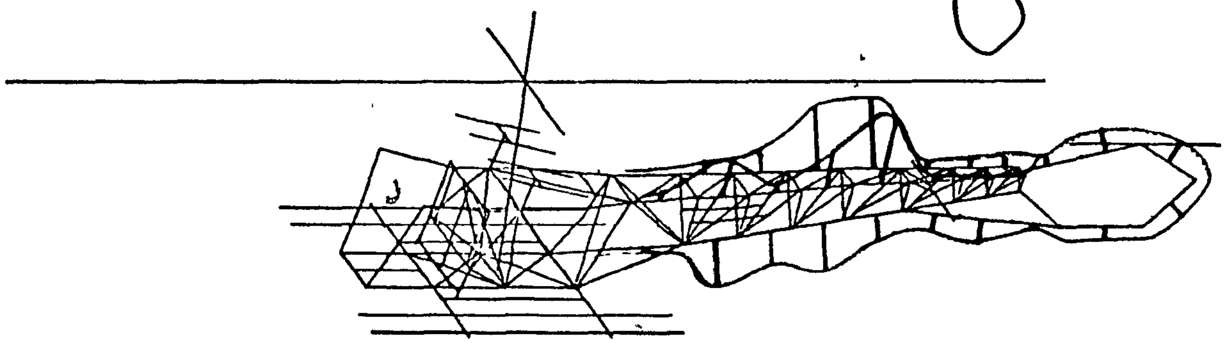

MAX. VALUE (ELEMENT No. 41)
= 0.2928 mA

ROTOR $\perp$

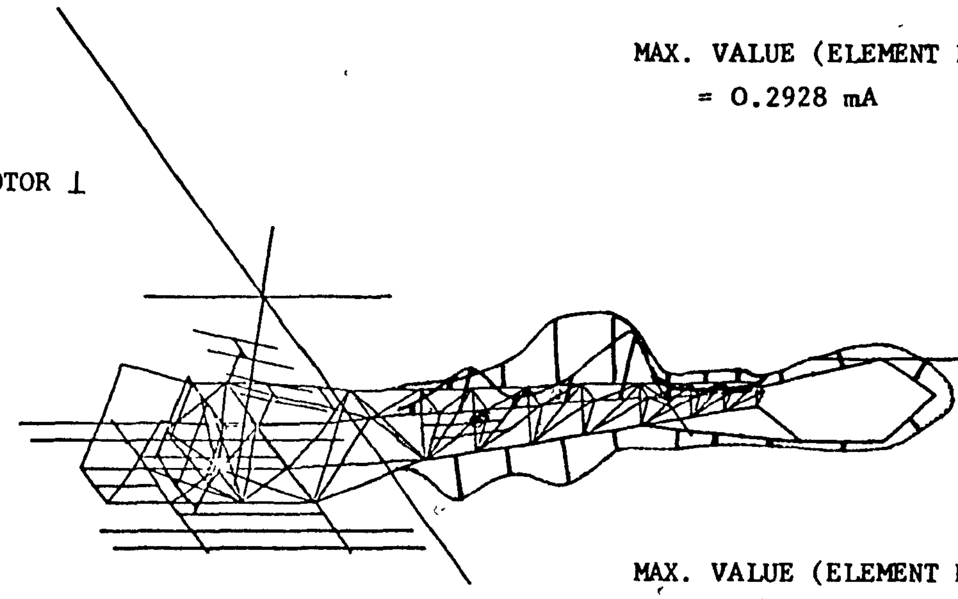

MAX. VALUE (ELEMENT No. 41)
= 0.278 mA

MONOPOLE

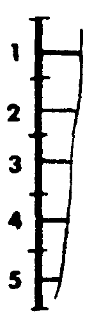

Segment Number	Current Magnitude (mA)		Current Phase (deg)	
	Rotor $\parallel$	Rotor $\perp$	Rotor $\parallel$	Rotor $\perp$
1	.191686	.193060	-43.634	-42.349
2	.168142	.169888	-39.678	-38.298
3	.157036	.158459	-43.446	-42.066
4	.128380	.129462	-45.783	-44.396
5	.080695	.081331	-48.048	-46.654

FIGURE 4.39 CURRENT DISTRIBUTION, TWO ROTOR POSITIONS.

monopole shows whether an impedance change should be anticipated. Here it can be seen that an impedance change is likely to be small.

Current plots of this type are extremely useful both for the assessment of rotor modulation as well as for the guidance of the finite element representation as noted above. The CALCOMP three-dimensional plotting program modification to incorporate this current line plot at each element was not incorporated in time for this work, but could be a distinct aid in making further research more effective and efficient.

4.5.4 Essential Factors and Limitations

The factors associated with the determination of the finite element model which produced satisfactory pattern convergence can be listed and summarized as follows:

(a) The segment lengths used were comparable to those used previously and by other investigators [79]. They ranged above .1λ only in a few cases in order to limit matrix size.

(b) The actual radii of rod elements were used or diameters corresponding to sheet metal thicknesses. This should not be construed to signify that this is considered the best choice say, in the case of the thick elements (.15 λ) of the landing gear structure. (see discussion in Chapter V).

(c) Elements were placed along all edges and lengths corresponding to possible resonant path lengths along the helicopter fuselage.

The above represent extensions of the introductory work presented here and elsewhere by others [45], [79].

(d) Elements were not placed, even though physical elements are present, in directions orthogonal to likely lines of current flow. These directions were not estimated so much from current distributions on elementary antenna forms, as from the complex measurements of Carswell [43] and Granger and Morita [42]. The influence of deliberately omitting such elements is believed to result only to a minor degree from round-off error considerations.

The results strongly demonstrate that extension of the number of arbitrary elements does not assure pattern convergence but will just as likely produce the opposite effect.

Computation time and cost, together with the limitations of core size or the difficulties in handling large matrices are serious limitations to effective research. The highest possible degree of physical insight must be progressively developed, and graphical aids used to accelerate and improve the analysis of results, in order to avoid errors or to minimize the number of computer runs.

The matching of a few experimental conical cuts is not as efficient as the matching of principal plane patterns. This can be seen by comparing the results with those obtained for the folded dipole and ground rod antenna. The availability of data free of possible detector effects would also be an asset. In closed fuselage structures, this is automatically obtained, but in open structures a refinement in model design is necessary to take this into account. The identification of this effect and support by wire grid modelling results appears to be the first documented description of this problem.

CHAPTER V

EVALUATION OF RESULTS, CONCLUSIONS & RECOMMENDATIONS

5.0 Introduction

In this concluding chapter comments are made about the possible extension of the results and about some of the hazards of such extensions. Recommendations are made for improvements of the experimental facility and some of the techniques used. Once again the topics are covered in the order of their earlier presentation to lend final emphasis to the purpose of the work and to the value of a comprehensive systems study using the proposed computer-aided analysis and design techniques.

5.1 Integrated System Analysis

It is believed that the proposed antenna evaluation method of Chapter II is well supported by the results presented. Its direct implications are that all future measurements on antenna systems should be complete and digitized to allow immediate application in vehicle antenna design. In this way, an awareness of performance in relation to operational specifications can be maintained from the conceptual stage onward through flight testing until full operation.

The comparative evaluation of the five antennas in Chapter II has shown:

(a) that the proposed evaluation method produces a different rating of the antennas than present methods,

(b) that the method improves the differentiation in performance between similar antennas,

(c) that the differences in performance are clearly and directly related to an operational performance parameter, namely range at each frequency of operation,

(d) that the method inherently distinguishes between antennas having different azimuth pattern distributions,

(e) that the application of the method makes it relatively easy to specify critical communications conditions, identify limiting factors and thus design efficient flight test and evaluation programs.

The identification of the rotor modulation effect and all main features of the antenna patterns by the wire grid modelling technique, shows that it could be used effectively to support and complement scale model pattern measurements in the generation of data for such an evaluation.

Since the wire grid model does not depend primarily on the radiator used, once developed, it becomes a powerful device for the study of performance of antennas in different locations or different antenna forms on the same vehicle.

5.2 Experimental Results and Antenna Test Facility

The automatic generation of principal plane patterns or conical cuts on a CALCOMP plotter from computer generated data contrasts sharply at this time, with the manual adjustment of the probe and manual data reduction necessary during the experimental work. The on-line connection of the instrumentation used to a process control computer for automatic data logging, correction for power level fluctuations and for automatic plotting of the reduced output, would improve the productivity of the antenna test facility significantly.

It is clear from the data of Chapter III that much more extensive testing of the anechoic chamber remains to be done to determine its lower and upper frequency limits. The free-space VSWR technique illustrated in Figure 3.31 using the low dielectric constant support structure but applied closer to the chamber walls should define more precisely the quiet zone of the chamber and the perturbations in the field near the outer absorber walls.

Some variations in patterns were noted with changes in humidity. The absorber used was intended for outdoor application and hygroscopic effects are possible. Although critical measurements can always be deferred to dry sunny days as was done in this work, the isolation and better definition of this phenomenon would be useful. Application of the free space VSWR technique under sharply different weather conditions should prove most productive. Isolation of reflections from a wet roof is possible by the suspension of absorber from an apex hook, installed for such purposes.

The difficulties described with helicopter measurements in Chapter III and the usefulness of having good measured results evident in Chapter IV suggests that most efficient and productive research would result from an even closer co-ordination between the experimental and computational work. The need for an opportunity to remeasure under various conditions while developing a finite element model cannot be overemphasized. In this work, this was especially true with regard to the isolation of the detector effect in the open grid of the tail structure. However due to high cost, modification of an experimental model which was obtained on a short term loan and which was designed for higher frequency use could not be comtemplated, and the structure was too small to house a self-contained oscillator. The results of Figures 3.28 to 3.30 and the patterns of Chapter IV emphasize the need for careful design of the model to minimize this effect.

The overwhelming conclusion of the research presented in Section 4.5 is that most productive further research into the development of guidelines for the wire-grid-modelling of complex bodies would result from an ability to measure the actual current distributions. It is believed that this compact anechoic chamber with its close inner arch could easily be adapted for such a purpose. The small loops of Figure 3.13 could serve as the transmitting probes in an adaptation of the technique used by Carswell [43]. Results of such measurements would corroborate or negate the intuitive reasoning used in this work and further improve the basis for its application to other complex problems. The highest priority should be given to such physical research in order to guide computer experimentation on the general problem.

5.3 Wire Grid Modelling and Numerical Techniques

Special emphasis has not been placed in this work on the numerical analysis portion of the wire grid modelling technique although it is shown as being central in the structural diagram of the technique shown in Figure 4.1. However, since these aspects are treated well in the literature and especially in view of the results obtained, the priority given to the other fundamental aspects of the complex body problem was justified. This should not be construed to suggest that further research into this aspect is unimportant or unnecessary. For example, a critical examination of munerical integration techniques in radiation problems has been presented by Richmond [102], Allen [103], Wexler [104] and others. The sequential use of subroutines with techniques from the trapezoidal rule to Chebyshev-Gauss quadrature could produce corresponding guidelines as to which technique is most pertinent to each antenna problem and each moment method in terms of both computation efficiency and convergence. A similar approach might be considered for matrix inversion or factorization algorithms. Miller [73] presents a comparison of Gaus-Jordan and Gauss-Doolittle techniques and recently Preis [105] derived a rapid inversion algorithm for a Toeplitz matrix[1] and suggested its use when the matrix occurs in antenna problems.

The results of Section 4.4 concerning the pattern variation with source locations explain some of the minor discrep-

---

[1]The elements Z_{ij} of a Toeplitz matrix depend upon the difference i-j and the matrix is symmetric about a cross-diagonal.

ancies in side lobe level between the results of Wolde-Ghiorgis [45] and Tesche and Neurether and experimental results for the monopole mounted on a sphere. The finite segmentation used in the point matching calculations distribute the source over one segment cell as shown in Figure 5.1. Hence the source is effectively displaced from its precise physical location on the test model.

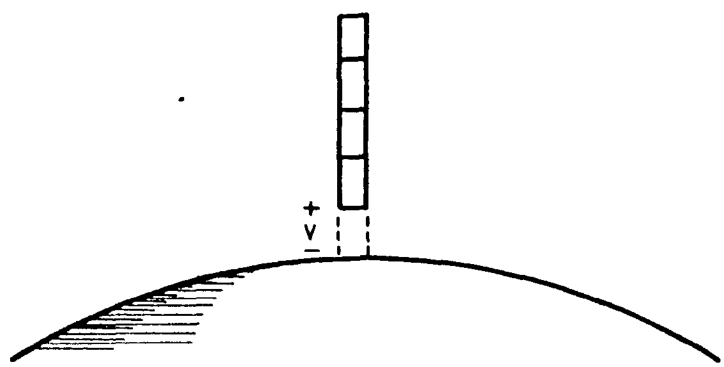

FIGURE 5.1

On the other hand Tesche [105] has recently pointed out that if a calculation of input current with frequency is carried out for a dipole and the source gap is allowed to become smaller as the frequency increases, the calculation for the current diverges especially for the thin wire kernel. Tesche recommends a distribution of the source over more than one cell although this makes the input current difficult to define. It should be pointed out that the magnetic current frill source representation used by Wolde-Ghiorgis [45] for other antennas produces voltage values distributed over the match points and would be interesting to apply to the problem raised by Tesche.

The question of what element radius should be used is first considered in Section 4.3 with the modelling of the folded dipole mounting mast. Both Wolde-Ghiorgis and Miller [73] use the actual wire radius in modelling structures composed of rod-like elements and this is also done in this work for the modelling of the helicopter structure. Imbriale and Ingerson [106] also claim the actual radius to be the correct value to use when the radius to length ratio (a/l) is small. When it is not small however, they claim another effective value from an expansion of a/l terms. These requirements arise of course, because of the approximations made in equation 4.23 where the Green's function,

$$G(z,z') = \frac{1}{2\pi}\int_0^{2\pi} \frac{e^{-jkR}}{R}\, d\phi \approx \frac{e^{-jkr}}{r}$$

If indeed the actual current distribution on the other elements were known, a more appropriate Green's function might be found. However in the radiation pattern problem of Section 4.3 the pattern arises physically from the actual surface currents. Hence placing an element on the axis of the mast and by some mathematical stratagem arriving at a current value which would produce a satisfactory match to measured values seems a more artificial analog of the physical problem than the placing of thin elements on the periphery. This of course is what was done by Wolde-Ghiorgis for thick cylinders. But why do two elements produce such good results? An explanation suggests itself from an analysis of the current distributions on peripheral elements used to model thick masts by Wolde-Ghiorgis. Figure 5.2 shows the modelling of a thick mast by six and eight elements together with a plot of the currents on these elements at their center. Note the concentration of current on the axis. It is interesting to note that Howarth [107] shows such a concentration using other methods based on a multi-pole expansion technique. Thus for directive arrays of elements with thick members not only an effective radius but also 'location' would be necessary for good radiation pattern results. Therefore the use of peripheral thin elements is more appropriate and more likely to give convergence, as evidenced by the results of Section 4.3.

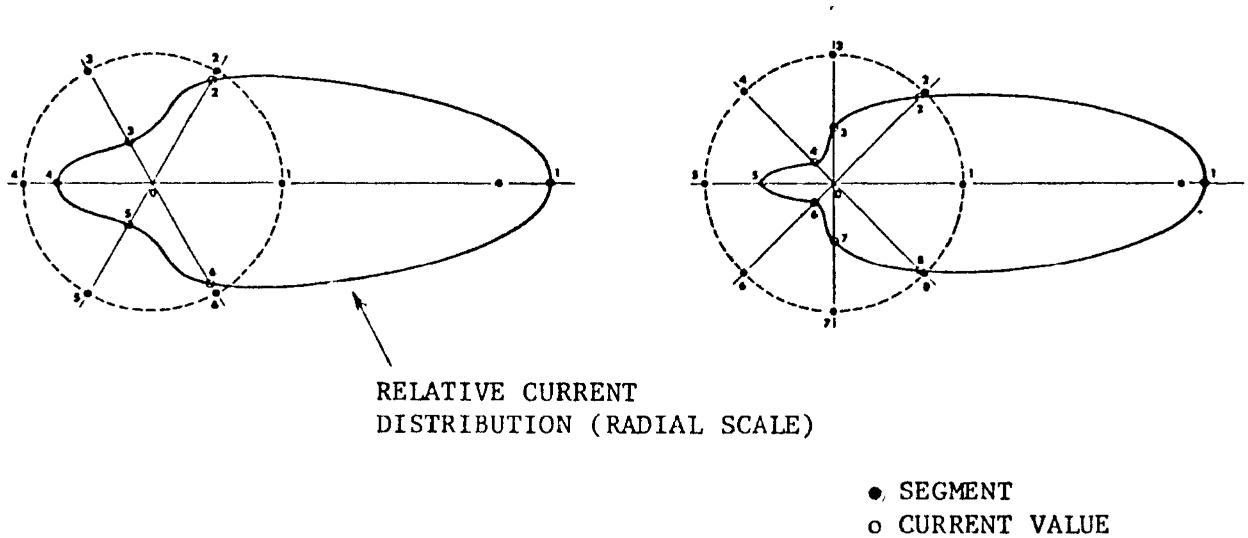

FIGURE 5.2

The above observations and arguments have relevance also to the modelling of the helicopter. For example, in the light of the above, since the radius of the rods in the landing gear is substantial (>.01λ), the argument for the use of the actual radius is weak, especially since the combination of cabin and landing gear acts as a counterpoise and the thick elements can be expected to support higher current concentrations on their outer surfaces. An awareness of these considerations should be used in the pursuance of further research on the complex body problem.

The location of wire grid elements along edges where current concentrations are likely to occur has been one of the important guidelines in the helicopter modelling research. The facility with which this can be done with the wire grid method is no doubt the reason for Goldhirsh and Knepp's [76] recommendation to use it after they had tried the surface element approach on the CH-47 helicopter.

The effect of removal of orthogonal elements in critical sections does not have its counter part in the surface element method since there is no de facto constraint on the current direction. The occurrence of this effect in the wire grid method is most interesting. Currents computed on such elements were much too large to be due to round off errors alone. Are there in fact currents flowing in these members in the helicopter modelled? Is there in fact a physical as well as a mathematical reason why divergence occurs when these elements are included? Does divergence also occur when a junction constraint is applied to the element currents? These questions should provide a substantial base for future research.

5.4 Epilogue

In this work the first emphasis has been on antennas as a part of systems and the need to evaluate them in this context. Such an evaluation has a degree of complexity which requires the application of new and specialized computer techniques to become tractable and useful.

Radiation pattern data necessary for such evaluations and for the model antennas themselves when scale-modelling is used, can be obtained by the use of the computer-based finite element technique of wire-grid modelling. It has been shown however, that at this time, this can only be achieved by the use of the guidelines developed here, based on physical insight and experimental results. To this extent it remains a practicing engineering art. It is hoped that this art has been defined better by this work for use by other practitioners.

The progress in research and development of the individual topics of this thesis, such as the evaluation method, wire grid modelling, computer graphics for pattern and current plotting, and complex body display, presents the possibility of the comprehensive combination of these components with the use of multicolor computer graphics terminals where, once the shape and radiator would be specified, the object could be displayed in its actual or wire grid model form, the computed currents could be plotted on the individual elements, the radiation patterns could be displayed in comparison with measured patterns, and the results of a system evaluation all could be presented simultaneously. The vehicle antenna designer would then have all the relevant factors at his disposal for a better understanding and optimization of the design. In fact a closer examination of the figures of Chapter IV shows that a number of the above features have already been combined.

APPENDIX I

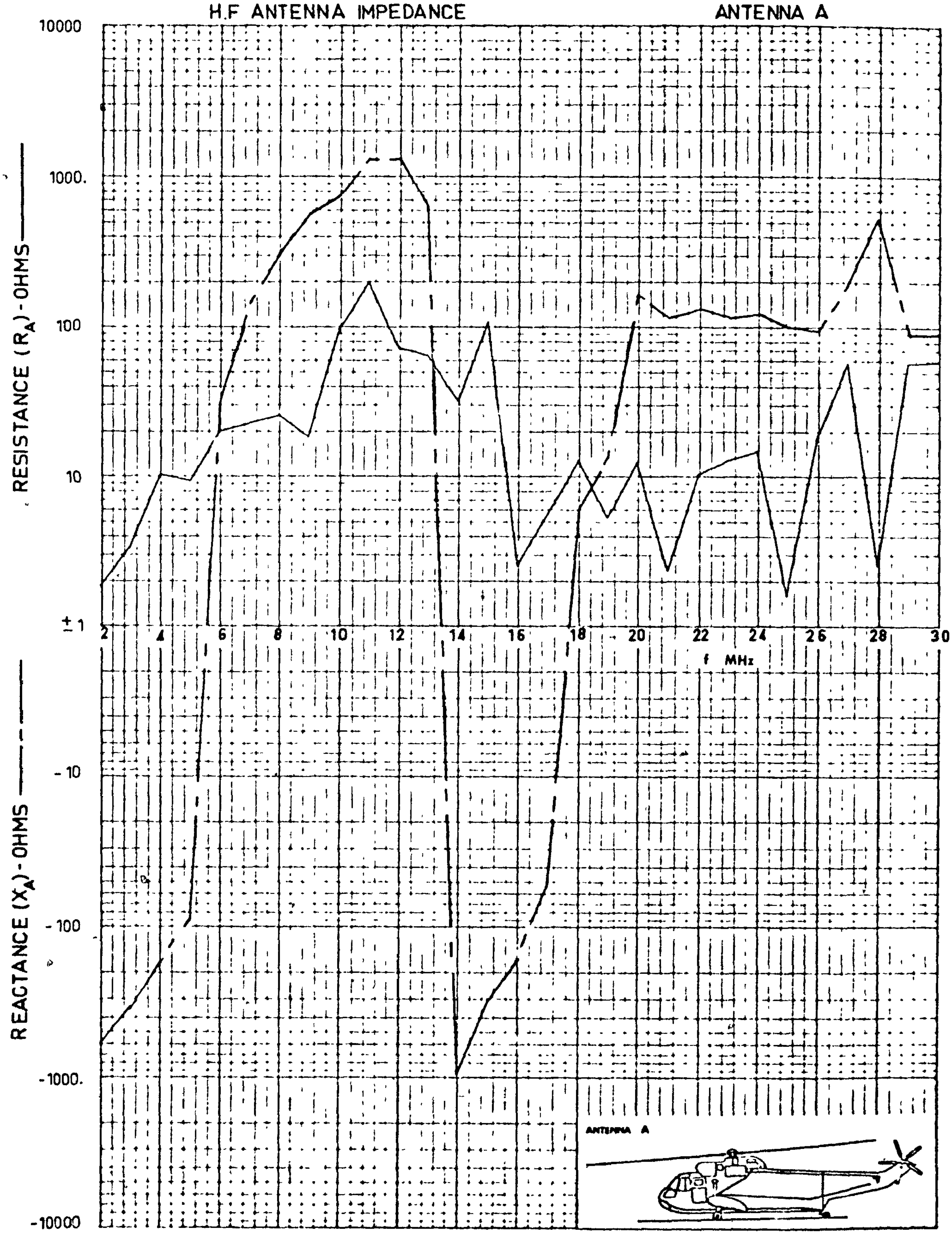

H.F ANTENNA IMPEDANCE
ANTENNA A
RESISTANCE (R_A) - OHMS
REACTANCE (X_A) - OHMS
10000
1000.
100
10
±1
-10
-100
-1000.
-10000
2
4
6
8
10
12
14
16
18
20
22
24
26
28
30
f MHz
ANTENNA A

H.F ANTENNA IMPEDANCE ANTENNA B

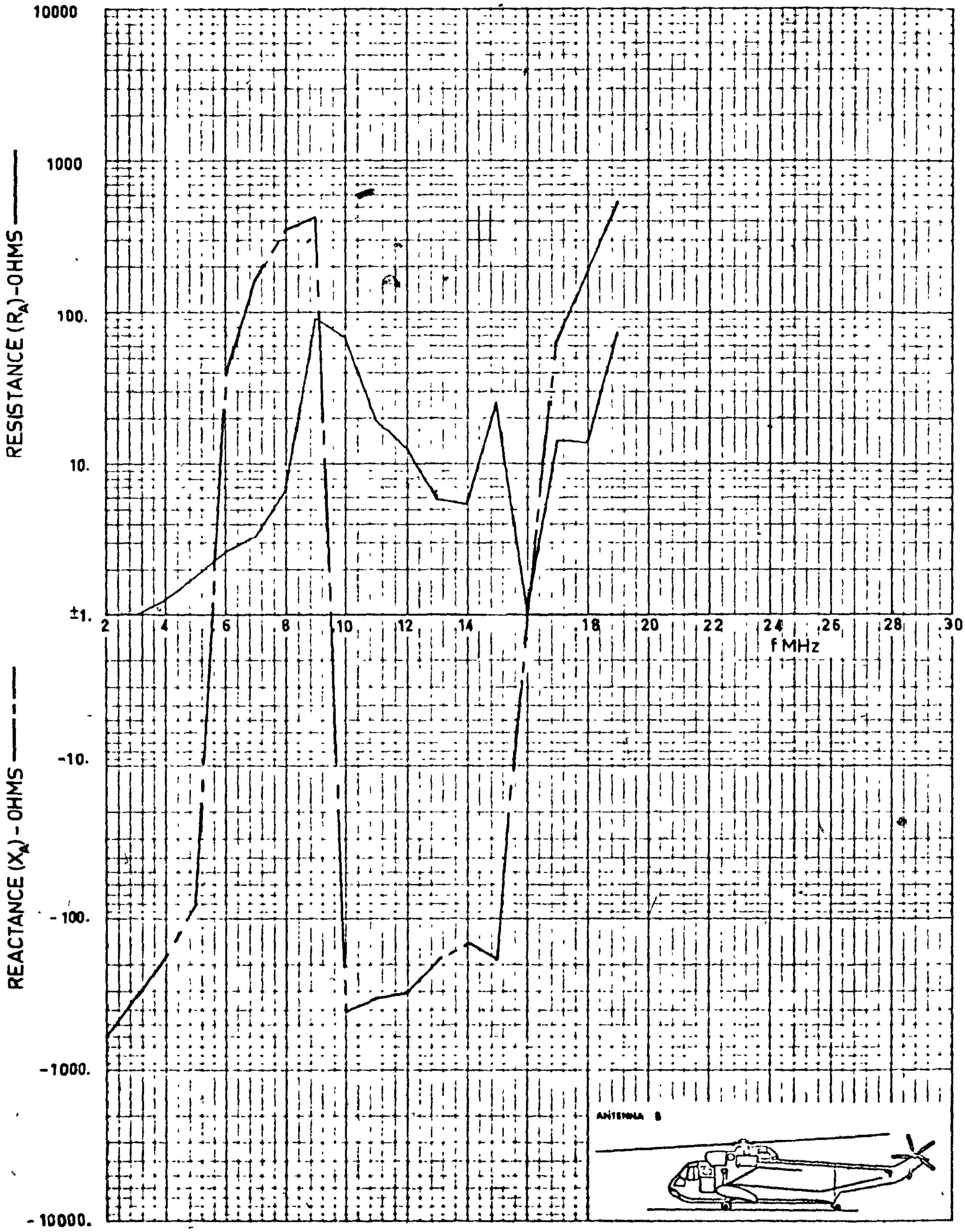

H.F ANTENNA IMPEDANCE ANTENNA C&E

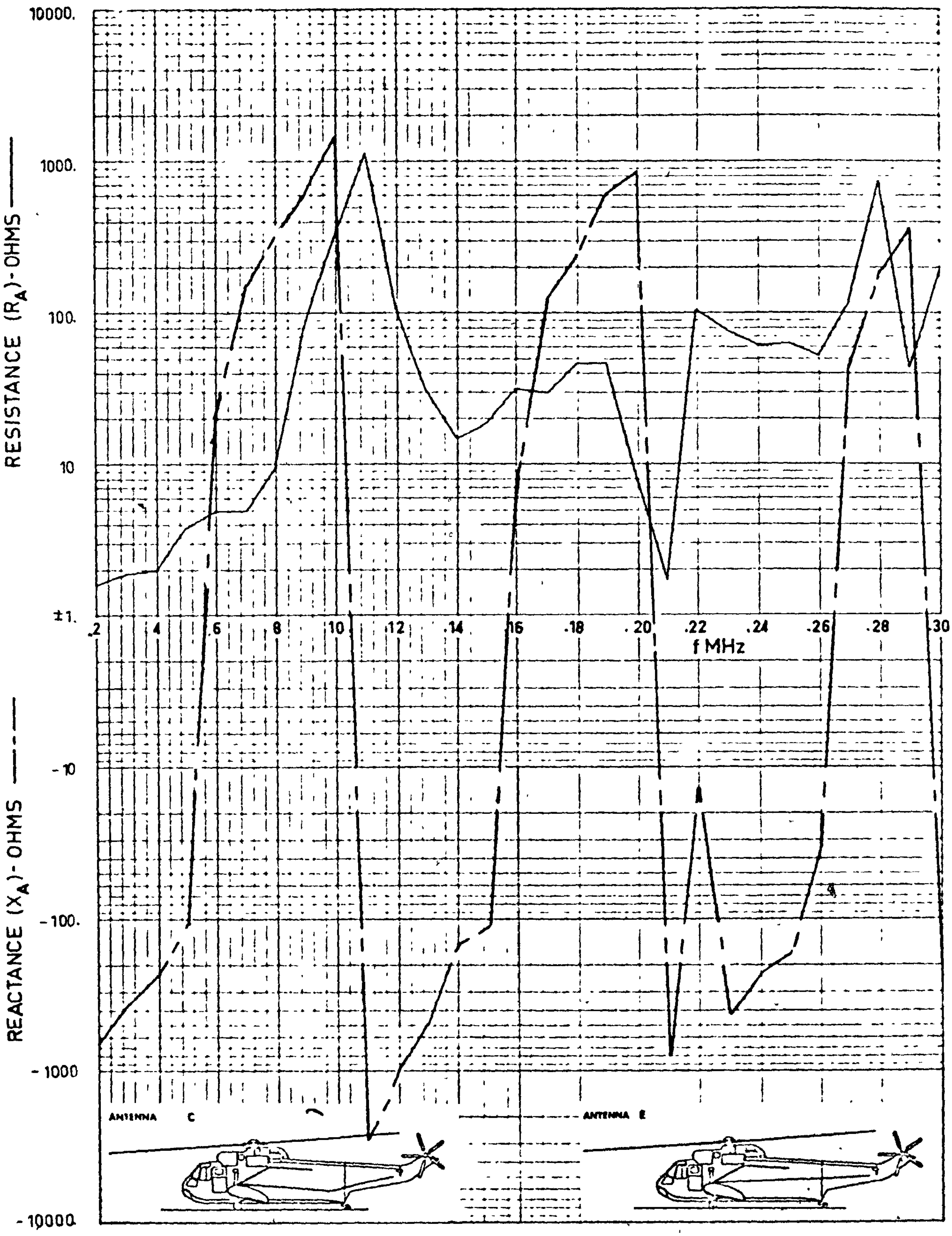

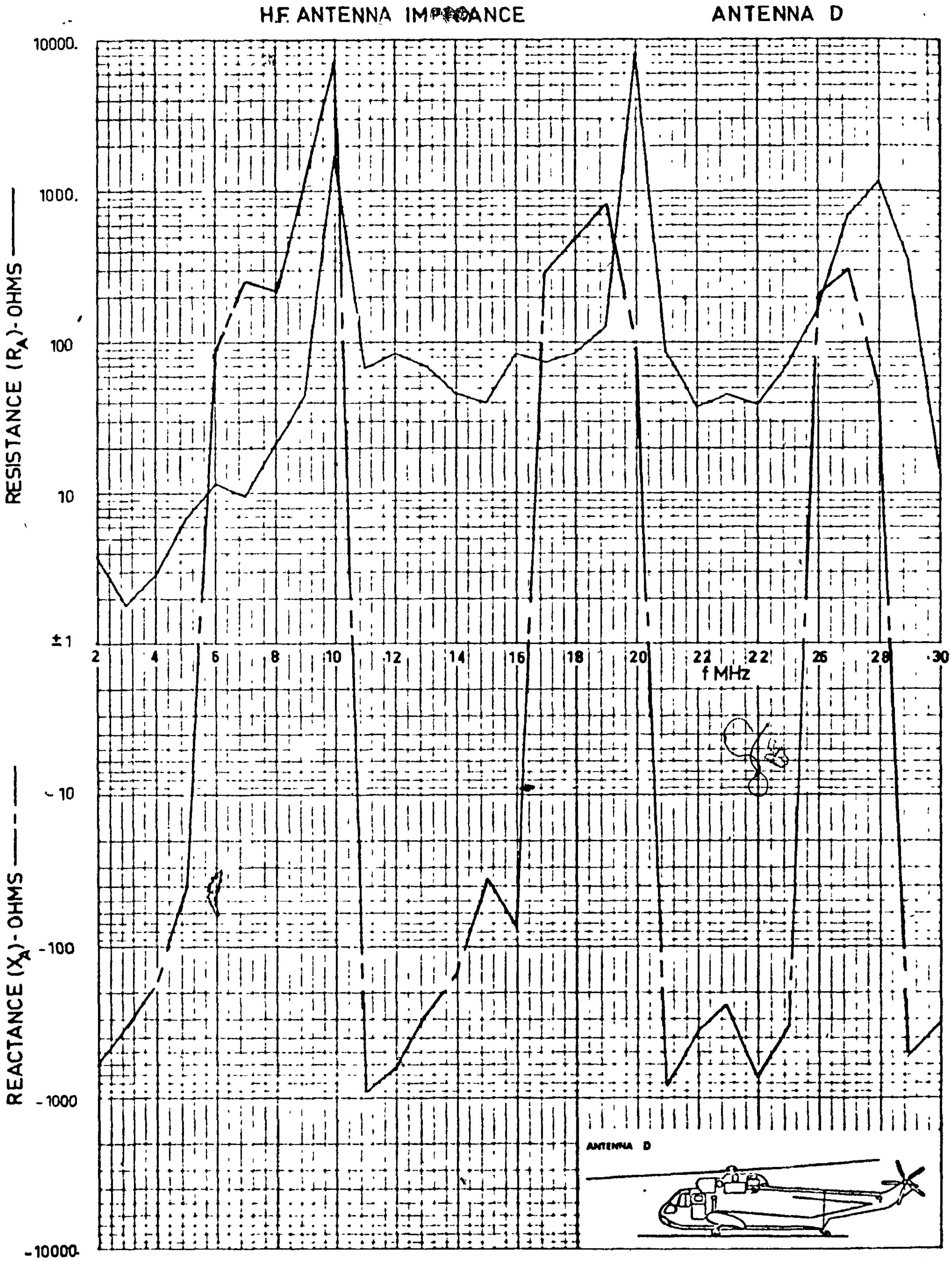
H.F. ANTENNA IMPEDANCE
ANTENNA D
RESISTANCE (R_A) - OHMS
REACTANCE (X_A) - OHMS
10000.
1000.
100
10
±1
- 10
-100
- 1000
-10000
2
4
6
8
10
12
14
16
18
20
22
22
26
28
30
f MHz
ANTENNA D

APPENDIX II

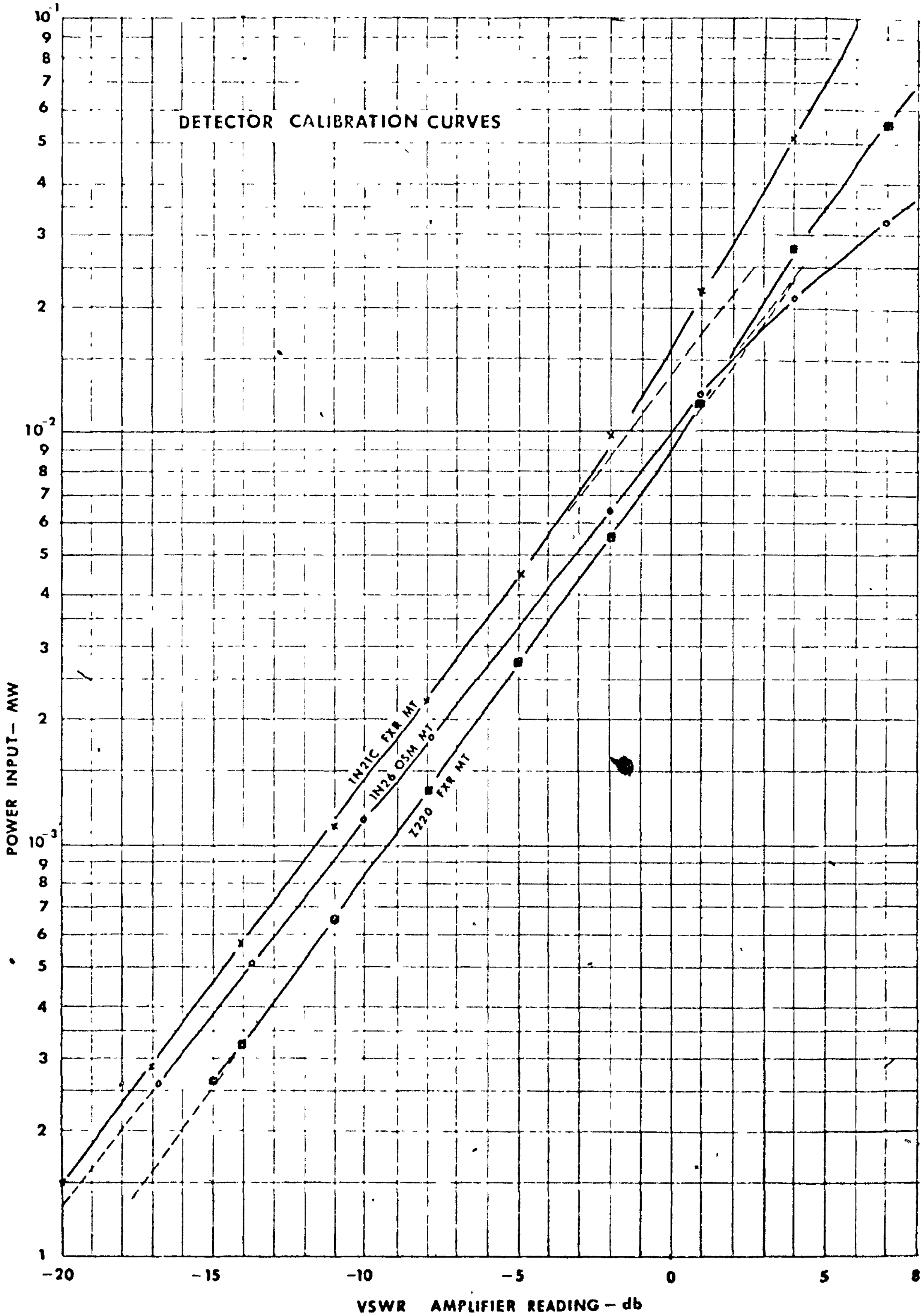
DETECTOR CALIBRATION CURVES
1N21C FXR MT
1N26 OSM MT
Z220 FXR MT
POWER INPUT— MW
VSWR AMPLIFIER READING — db
10^{-1}
9
8
7
6
5
4
3
2
10^{-2}
9
8
7
6
5
4
3
2
10^{-3}
9
8
7
6
5
4
3
2
1
−20
−15
−10
−5
0
5
8

BIBLIOGRAPHY

[1] J.V.N. Granger and J.T. Bolljahn, "Aircraft antennas", Proceedings of the I.R.E., Vol. 43, No. 5, pp. 533-550; May, 1955.

[2] George Sinclair, E.C. Jordan, and Eric W. Vaughan, "Measurement of aircraft-antenna patterns using models", Proceedings of the I.R.E., Vol., 35, pp. 1451-1462; December, 1947.

[3] S.J. Kubina, "Evaluation of the communications systems on the CL-28/ARGUS aircraft", paper No. 19, I.R.E. Symposium on Communications, Montreal, November 4, 1960.

[4] S.J. Kubina and T.J.F. Pavlasek, "Modelling development of helicopter antenna system for airborne field strength measurement and propagation path testing", Electrical Engineering Dept., McGill University; July, 1972.

[5] J.V.N. Granger, "Systems considerations in aircraft antenna design", I.R.E. Trans. on Airborne Electronics, Vol. AE-1, pp. 1-12; December, 1951.

[6] MIL-A-9080, Antennas, Liaison Communications Equipment, General Specifications for Design of; 2 February, 1954.

[7] E.J. Moore, "Factor of merit for aircraft antenna systems for the frequency range from 3 to 30 MC", I.R.E. Trans. on Antennas and Propagation, Vol. AP-3, pp.67-74; August, 1952.

[8] E.J. Moore, "Performance evaluation of HF aircraft antenna systems", I.R.E. Trans. on Antennas and Propagation, Vol. AP-6, pp. 254-260; July, 1958.

[9] W.S. Lucke, "Antenna evaluation methods", I.R.E. Trans. on Antennas and Propagation, Vol. AP-6, pp. 251-254; July, 1958.

[10] O.C. Boileau, Jr., "An evaluation of high frequency antennas for a large airplane", I.R.E. Transactions on Aeronautical and Navigational Electronics, Vol. ANE-3, No. 1, pp. 28-32; March, 1956.

[11] J.Y. Wong, "Radiation pattern efficiencies of some suppressed HF antennas", I.R.E. Transactions on Aeronautical and Navigational Electronics, Vol. ANE-5, No. 1; March, 1958.

[12] C.E. Shannon, "A mathematical theory of communications", Bell Sys. Tech. J., Vol. 27, pp. 379-423, July, 1948; pp. 673-656, October, 1948.

[13] A. Ellis, "Study of external navigation antennas on Lockheed Constellation aircraft", Airborne Instr. Lab., Mineola, N.Y., Rep. 726-IT; August, 1949.

[14] R.W. Silberberg and P.L. Hsu, "Automatic data reduction and analysis of omnidirectional antenna radiation patterns on space vehicles", Electronic Communicator, Vol. 1, No. 2, pp. 14-15, March/April, 1966.

[15] J.Blass, "A method for evaluating antennas", I.R.E. Trans. on Antennas and Propagation, Vol. AP-6, pp. 95-96; January, 1958.

[16] J.Y. Wong, "A proposed method for evaluating the performance of an HF shipborne transmitting antenna", N.R.C. Report ERB-647; September, 1963.

[17] J.F. Cline and R.L. Tanner, "A new approach to the evaluation of HF aircraft antennas", N.R.C. Report ERB-647; September, 1963.

[18] C.K. Adkar, "Radiation pattern measurements on nine HF antennas for the Sikorsky CHSS-2 helicopter", Canadair Report No. RAR-00-103; 16 April, 1964.

[19] K.A.Norton,"The Calculation of ground-wave field intensity over a finitely-conducting-spherical earth", Proc. I.R.E., Vol. 29, pp. 623-639; December, 1941. (and recent N.B.S. data)

[20] I.H. Gerks, "Use of a high-speed computer for groundwave calculations", I.R.E. Transactions on Antennas and Propagation, Vol. AP-10, pp. 292-299; May, 1962.

[21] J.R.Wait and L.C.Walters,"Curves for ground wave propagation over mixed land and sea paths", I.E.E.E. Transactions on Antennas and Propagation, Vol. AP-4, pp. 38-45; January, 1963.

[22] Allen R. Ellis, "Helicopter antenna design considerations", Proceedings of I.R.E. National Conference on Aeronautical Electronics, Dayton, Ohio; May, 1955.

[23] J.Y. Wong and C.A. Muilwyk, "Rotor modulation studies of an HF wire antenna for the CHSS-2 helicopter", N.R.C. Report ERB-710; July, 1965.

[24] J. Andrews, "Final report on the investigation to develop an HF-SSB system for an HUS-1 USMC helicopter utilizing a tuned monopole antenna", Collins Radio Co. Engineering Report 523-0756680-0211 M; 1 October, 1964.

[25] "Report on revision of atmospheric noise data", National Bureau of Standards , Boulder Colo., C.C.I.R. Study Group VI Report; July, 1956.

[26] George Sinclair, "Theory of models of electromagnetic systems", Proceedings of the I.R.E., Vol. 36, pp., 1364-1370; November, 1948.

[27] George Sinclair, E.C. Jordan and Eric W. Vaughan, "Measurement of aircraft-antenna patterns using models", Proceedings of the I.R.E., Vol. 35, pp. 1451-1462; December, 1947.

[28] W.A. Cumming, "Radiation measurements at radio frequencies: a survey of current techniques", Proceedings of the I.R.E., Vol. 47, pp. 705-735; May, 1959.

[29] L. Peters, Jr., "Use of high resistance audio cable for pattern measurements", Research Foundation, The Ohio State University, Columbus, Ohio, Eng. Report No. 487-4; September, 1953.

[30] Robert E. Webster, "20-70 MC monopole antennas on ground-based vehicles", I.R.E. Transactions on Antennas and Propagation, Vol. AP-5, pp. 363-368; October, 1957.

[31] J.Y.Wong and J.C. Barnes, "Design and construction of a pattern range for testing high frequency shipborne antennas and the low-frequency antennas", Trans. Eng. Institute of Canada, Vol. 2, pp. 15-21; January, 1958.

[32] J.T. Bolljahn and R.F. Reese, "Electrically small antennas and the low-frequency antenna problem", Trans. of the I.R.E. on Antennas and Propagation, Vol. AP-1, pp. 46-54; October, 1953.

[33] A. Stembridge, "Measurement of antenna radiation patterns on spacecraft", AGARD Conference Proceedings No. 87-71, 22nd Technical Symposium of Avionics Panel of AGARD, Rome, Italy; 31 May/4 June, 1971.

[34] E.D. Sharp and R.L. Tanner, "Scale modelling of high-frequency antennas", I.E.E.E. Transaction on Antennas and Propagation, Vol.AP-17, pp. 810-811; November, 1969.

[35] J.V.N. Granger, "Wing-cap and tail-cap aircraft antennas", Tech. Rep. 6, S.R.I. Proj. 188, SRI , Menlo Park, Calif.;March,1950.

[36] J.T. Bollhahn and J.V.N. Granger, "The use of complementary slots in aircraft antenna impedance measurements", Proceedings of the I.R.E., Vol.39, pp. 1445-1448; November, 1951.

[37] H.G. Booker, "Slot aerials and their relation to complementary wire aerials", Jour. I.E.E.,part IIIA, Vol. 93, pp. 620-626; March, 1946.

[38] J.Y. Wong, "A suppressed HF nose-cap antenna for aircraft", National Research Council of Canada Report ERB-478; June, 1958.

[39] T. Morita, "Current distributions on transmitting and receiving antennas", Proceedings of the I.R.E., Vol. 38, pp. 898-904; August, 1950.

[40] T. Morita and C.E. Faflick, "The measurement of current distributions along coupled antennas and folded dipoles", Proceedings of the I.R.E., Vol.39, pp. 1561-1565; December, 1951.

[41] J.V.N. Granger, "Shunt-excited flat-plate antennas with applications to aircraft structures", Proceedings of the I.R.E., Vol.38, pp. 280-287; March, 1950.

[43] J.V.N. Granger and T. Morita, "Radio-frequency current distributions on aircraft structures", Preceedings of the I.R.E., Vol. 39, pp. 932-938; August, 1951.

[43] Irene Carswell, "Current distribution on wing-cap and tail-cap antennas", Transactions of the I.R.E., on Antennas and Propagation, Vol.AP-3, pp. 207-212; October, 1955.

[44] L. Aharoni, "Antennas: An introduction to their theory", Clarendon Press, Oxford, England, pp. 127ff; 1946.

[45] Woldermariam Wolde-Ghiorgis, "Wire-grid analysis of antennas near conducting surfaces", PH.D. Thesis, Dept. of Electrical Engineering, McGill University, Montreal, Quebec; March, 1972.

[46] George W. Leopard, "The flight evaluation of aircraft antennas", Transactions of the I.R.E. on Antennas and Propagation, Vol.AP-8, pp. 158-166; March, 1960.

[47] H.R.Reed and C.M. Russell, "UHF Propagation", John Wiley and Sons Inc., New York, N.Y.; 1953.

[48] Erwin Meyer, "Experiments in cm. waves in analogy with acoustic techniques made in Gottingen", Jour. of the Acoustical Society of America, Vol. 30, pp. 624-632; July, 1958.

[49] Hans Severin, "Nonreflecting absorbers for microwave radiation", Transaction of the I.R.E. on Antennas and Propagation, Vol. AP-4, pp. 385-392; July, 1956.

[50] Steven Galagan, "Understanding microwave absorbing materials and anechoic chambers",

Part I: Microwaves, Vol. 8, pp. 38-41; December, 1969.

Part II: Microwaves, Vol. 9, pp. 44-49; January, 1970.

Part III: Microwaves, Vol. 9, pp. 47-50; April, 1970.

Part IV: Microwaves, Vol. 9, pp. 69-73; May, 1970.

[51] W.H. Cady, M.B. Karelitz and Louis A. Turner, "Radar scanners and radomes", Vol. 26, M.I.T. Radiation Laboratory Series, McGraw-Hill Book Co. Inc., New York, N.Y.; 1949.

[52] T.J.F. Pavlasek and S.J. Kubina, "Influence of timevarying geometry on HF antennas", Annual Report 1969, D.R.B. Grant No. 5540-32, Department of Electrical Engineering, McGill University, Montreal, Quebec.

[53] O.M. Woodward, Jr., "Balance measurements on balun transformers", Electronics, Vol. 26, pp. 188-191; September, 1953.

[54] Haven Whiteside, "Electromagnetic field probes", Technical Report 377, Crugt Laboratory, Havard University; October 25, 1962.

[55] H.Whiteside and R.W.P. King, "The loop antenna as a probe", I.E.E.E. Transactions on Antennas and Propagation, Vol.AP-12, pp. 291-297; May, 1964.

[56] W.V. Tilston and A.H. Secord, "The radiation patterns of ground rod antennas", Electronics and Communications, Vol.15, pp. 27-30; August, 1967.

[57] T.J.F. Pavlasek, S. Kubina and W. Wolde-Ghiorgis, "An experimental study on rotor modulation effects in radiation

patterns of helicopter antennas", Department of Electrical Engineering , McGill University; October 26, 1970.

[58] David J. Frediani, "Anechoic chamber evaluation techniques", Paper 1-3, 1971 U.R.S.I. Fall Meeting, University of California, Los Angeles.

[59] Sergei A. Schelkunoff, "Advanced Antenna Theory", John Wiley and Sons, New York; 1952.

[60] R.B. Mack, "A study of circular arrays", Cruft Lab., Harvard University, Cambridge, Mass., Tech. Reports 381-386;May,1963.

[61] H.C. Pocklington, "Electrical oscillations in wires", Cambridge Phil. Soc. Proc., Vol. 9, pp. 324-332; October 25,1897.

[62] E. Hallen, "Theoretical investigation into transmitting and receiving antennas", Nova Acta Regiae Soc. Sci. Upsaliensis, Ser. 4, Vol. 2, pp. 1; 1938.

[63] R.W.P. King, "The theory of linear antennas", Harvard University Press, Canbridge, Mass.; 1956.

[64] R.W.P. King, "The Linear Antenna: eighty years of progress", Proceedings of the I.E.E.E., Vol. 55, pp. 1-16; January, 1950.

[65] R.W.P. King, "Asymmetrically driven antennas and the sleeve dipole", Proc. I.R.E., Vol. 38, pp. 1154-1163; October, 1950.

[66] C.K. Adkar, "Study of HF criteria for a composite nose-cap antenna", Master of Engineering Thesis, Department of Electrical Engineering, McGill University; August, 1961.

[67] L.J. Chu and J.A. Stratton, "Steady-state solutions of electromagnetic problems: III forced oscillations of a prolate spheroid", J. Appl. Physics, Vol. 12, pp. 241-248; March, 1941.

[68] James R. Wait, "Theories of prolate spheroidal antennas", Radio Science 1 (New Series), No. 4, pp. 475-512; April, 1966.

[69] H.A. Myers, "Radiation patterns of unsymmetrically fed prolate spheroidal antennas", I.R.E. Transaction on Antennas and Propagation, Vol. AP-4, pp.58-64; January, 1958.

[70] C.P. Wells, "The prolate spheroidal antenna: Current and impedance", I.R.E. Transaction on Antennas and Propagation, Vol. AP-6, pp. 125-128; January, 1958.

[71] S.A. Schelkunoff, "Theory of antennas of arbitrary shape and size", Proc. I.R.E , Vol, 29, pp. 493-521; September, 1941.

[72] C.T. Tai, "Application of a variational principle to biconical antennas", Jour. Appl. Phys., Vol. 20, pp. 1076-1084; November, 1949.

[73] A.J. Poggio and E.K. Miller, "Integral equation soultions of three-dimensional scattering problems", Computer Techniques for Electromagnetics and Antennas, Part II. R. Mittra (ed.), University of Illinois; October, 1970.

[74] F.K. Oshiro and K.M. Mitzner, "Digital computer solution of three-dimensional scattering of problems", Presented at 1967 I.E.E.E. International Antennas and Propagation Symposium, Ann Arbor, Symposuim Digest, pp. 257-263; October, 1967.

[75] J. Goldhirsh, D.L. Knepp and R.J. Doviak, "Radiation from a dipole near a conducting cylinder of finite length",

I.E.E.E. Transactions on Antennas and Propagation, Vol. AP-18, pp. 96-105; August, 1970.

[76] Dennis L.Knepp and Julius Goldhirsh, "Numerical analysis of electromagnetic radiation properties of smooth conducting bodies of arbitrary shape", I.E.E.E. Trans. on Antennas and Propagation, Vol. AP-20, pp. 383-388; May, 1972.

[77] J.H. Richmond, "A wire-grid model for scattering by conducting bodies", I.E.E.E. Transactions On Antennas and propagation, Vol. AP-14, pp. 782-786; November, 1966.

[78] R.L. Tanner and M.G. Andreasen, "Numerical solution of electromagnetic problems", I.E.E.E. Spectrum, Vol.4, pp. 53-61; September, 1967.

[79] E.K. Miller, J.B. Morton, G.M. Pjerrou and B.J. Maxum, "Numerical analysis of aircraft antennas", Proc. of Conf. on Environmental Effects on Antenna Performance, Vol. 1, edited by J.R. Wait, pp. 55-58; 1969.

[80] G.A. Thiele. "Wire Antennas", Computer Techniques for Electromagnetics and Antennas, Part I, R. Mittra (ed.), University of Illinois; September, 1970.

[81] Hu H. Chao and Bradley J. Strait, "Computer programs for radiation and scattering by arbitrary configuration of bent wires", Scientific Report No. 7, Electrical Engineering Dept., Syracuse University; September, 1970.

[82] S.J. Kubina, T.J.F. Pavlasek and W.Wolde-Ghiorgis, "Applications of numerical techniques to the design of vehicle antennas", Conference Digest, pp. 58-59, International Electrical, Electronics Conference, October, 1971.

[83] P.D. Crout, "A short method for evaluating determinants and solving systems fo linear equations with real or complex coefficients", A.I.E.E. Transactions (Supplement), Vol. 60, pp. 1235-1241; December, 1941.

[84] E.K. Miller, G.J. Burke and E.S. Selden, "Accuracymodeling guidelines for integral-equation evaluation of thin-wire scattering structures", I.E.E.E. Transactions on Antennas and Propagation, Vol. AP-19, pp. 534-553; July, 1971.

[85] John D. Kraus, "Antennas", McGraw Hill Book Co., New York, pp 415-419; 1950.

[86] S.A. Schelkunoff and H.T. Friis, "Antennas, theory and and practice", John Wiley and Sons, Inc., pp. 339; 1950.

[87] H. Jasik (ed.), "Antenna engineering handbook", McGraw Hill Book Co., New York, Chapter 3; 1961.

[88] P.S. Carter, "Simple television antennas", RCA Review, Vol. 4, pp. 168-185; October, 1939.

[89] W. Van B. Roberts, "Input impedance of a folded dipoles", RCA Review, Vol. 8, pp. 289; 1947.

[90] R. Guertler, "Impedance transformation in folded dipoles", I.R.E. Proceedings, Vol. 38, pp. 1042-1047; September, 1950.

[91] J.P. Germain, and F.E. Brooks, Jr., "The effects of the physical parameters on the bandwidth of a folded dipole", I.R.E. Transactions on Antennas and Propagation, Vol. AP-6, No. 2, pp. 186-190; April, 1958.

[92] C.W. Harrison,Jr., and R.P.W. King, "Folded dipoles and loops", I.R.E. Transaction on Antennas and Propagation, pp. 171-187, March, 1961.

[93] Ronold W.P. King, Harry Rowe Mimno and Alexander H. Wing, "Transmission lines antennas and waveguides", First Edition, McGraw Hill Book Co. Inc.; 1954.

[94] Carter, P.S. "Antenna arrays around cylinders", Proceedings of the I.R.E. Vol. 31, pp. 671-693; December, 1943.

[95] Lucke, W.S. "Electric dipoles in the presence of elliptic and circular cylinders", J. Applied Physics, Vol. 22, pp. 14-19; January, 1951.

[96] Wait, J.R. "Electromagnetic radiation from cylindrical structures",Pergamon Press, New York; 1959.

[97] Sinclair,G. "The patterns of antennas located near cylinders of elliptical cross section", I.R.E. Proceedings, Vol. 39, pp. 660-668; 1951.

[98] Adams, A.T. and Warren, D.E. "Dipole plus parasitic elements", I.E.E.E. Transactions on Antennas and Propagation, Vol. AP-19, No. 4, pp. 536-537; July, 1971.

[99] Brown, G.H. "Ground plane antennas", Electronics, Vol. 16, pp. 338-344; December, 1943.

[100] Bouwkamp C.J., "Calculation of the input impedance of a special antenna", Phillips Research Reports, Vol. 2, pp. 228; 1947.

[101] Turpin, R.H. " A basic transformation technique with application to scattering by wires", I.E.E.E. Transactions on Antennas and Propagation, Vol. AP-20, pp. 80-82, January, 1972.

[102] J.H. Richmond "The numerical evaluation of radiation integrals", I.R.E. Transactions on Antennas and Propagation, Vol.AP-9, pp. 358-360; July, 1961.

[103] C.C. Allen "Numerical integration methods for antenna pattern calculation", I.R.E. Transactions on Antennas and Propagation, Vol. AP-7, pp. S387-S401; December, 1959.

[104] Alvin Wexler "Computation of electromagnetic fields", I.E.E.E. Trans. on microwave theory and techniques", Vol. MTT-17, pp. 416-439; August, 1969.

[105] F.M. Tesche "The effect of the thin-wire approximation and the source gap model on the high-frequency integral equation solution of radiating antennas", I.E.E.E. Transaction on Antennas and Propagation, Vol.AP-20, pp. 210-211; March, 1972.

[106] W.H. Imbriale and P.G. Ingerson, "On numerical convergence of moment solutions of thick wire antennas using sinusoidal basis functions", Paper VI 5-6, U.R.S.I. Fall Meeting, University of California, Los Angeles; September, 1971.

[107] Barry A. Howarth, "Application of multipole induction coefficients to multiple scattering of electromagnetic waves", Ph.D. Thesis, Dept. of Electrical Engineering, McGill University; March,1972.

[108] R. F. Harrington, "Matrix Methods for field problems", I.E.E.E. Proceedings, Vol.55, pp.136-149; February,1967.

[109] R.F. Harrington, "Field computation by moment methods", The Macmillan Co., New York; 1968.

[110] Francis Hugh Fenlon, "Calculation of the acoustic radiation field at the surface of a finite cylinder by the method of weighted residuals", Proceeding s of the I.E.E.E., Vol. 57,pp.291-306; March,1969.

[111] W.F. Ames,"Nonlinear partial differential equations in engineering, Academic Press, New York;1965.

[112] M. Becker, "The principles and applications of variational methods", M.I.T. Press, Cambridge, Mass.;1964.

[113] Jack H. Richmond, "Digital computer solutions of the rigorous equations for scattering problems", I.E.E.E. Proceedings, Vol.53, pp.796-804; August,1965.

[114] G. L. Albert and J. L. Synge, The general problem of antenna radiation and the fundamental integral equation, with application to an antenna of revolution", Part I, Quart.Appl. Math., Vol.5,pp.117-131;1948 and Part II, pp.133-156.

[115] R.F. Harrington, "Time-harmonic electromagnetic fields", McGraw-Hill, New York;1961.

[116] L.L. Tsai, "Analysis and measurement of a dipole antenna mounted on a conducting sphere or cylinder", Ph.D. Dissertation, Ohio State University, Columbus,Ohio;1970.